Investigation on advanced active materials for lithium-ion batteries

Yao Chen
University of Wollongong

Investigation on Advanced Active Materials for Lithium-ion Batteries

A thesis submitted in fulfilment of the requirements for the award of the degree

Doctor of Philosophy

from

University of Wollongong

by

Yao Chen, M. Sc., B. Sc.

Institute for Superconducting & Electronic Materials, Faculty of Engineering

2006

Dedicated to

My Parents, Shaoying Diao and Shanliang Chen

My husband, Jiangfeng Wu

My lovely Son, David Sichen Wu

Candidate's Certificate

I hereby declare that the research work presented in this thesis is original and was performed by the candidate in the laboratories in Institute for Superconducting & Electronic Materials and in the Faculty of Engineering at the University of Wollongong, New South Wales, Australia. This thesis has not been submitted for a degree to any other University or Institution.

_____

Yao Chen

Acknowledgements

I would like to express my deep gratitude to my supervisors, Professor. H.K. Liu, S.X. Dou and Dr. G.X. Wang for their academic guidance, financial support and constant encouragement throughout the project.

I wish to thank technical officers, Mr. N. Mackie and Mr. G. Tillman for their invaluable help with my experimental procedures. My sincere thanks should also go to Dr. Z.P. Guo, Dr. J.Z. Wang, Dr. K. Konstantinov, Dr. C.Y. Wang, Dr. Xiaolin Wang, Ms Aihua Li and Ms Jane Yao for their technical support and suggestions in carrying out all of my experimental work.

I would also like to express sincere gratitude to T. Silver for providing help in proof reading my papers and this thesis. Thanks are also go to Mrs. B.M. Allen for her help in official matters.

Thanks to the Australian government for providing an Overseas Postgraduate Research Scholarship and to the University of Wollongong for providing a University Postgraduate Award.

Finally, I would like especially to express my deep gratitude to my husband, Jiangfeng Wu and my son, David Sichen Wu for their love, understanding, patience, and constant support. I also wish to express my deep respect to my parents and parents-in-law for their encouragement during my Ph.D. study.

CONTENTS

ABSTRACT

The objectives of the Ph.D project were: (1) to prepare and study advanced active materials with high capacity and long cycle life for rechargeable lithium ion batteries; (2) to understand the relationship between the structural, physical, and electrochemical properties of the electrode materials; (3) to identify the main parameters which are responsible for the differences in electrochemical behaviour. In this study, several methods have been used to improve the performance of electrodes, including element substitution, synthesis methods, carbon-enriching, etc.

A starting point for the study was a survey of the literature pertaining to the cathode and anode materials for lithium ion batteries. Many different electrode materials are described. The thesis provides a detailed description of the status of current research and development in electrode materials for lithium ion batteries.

A variety of cathode materials have been investigated. Some of them have shown good electrochemical performance when used in lithium ion cells. Electroactive $LiCo_xMn_yNi_{1-x-y}O_2$ powders were prepared from lithium compounds and $Co_xMn_yNi_{1-x-y}(OH)_2$ precursor by heating at 850-900 °C.

High density spherical $LiCo_{0.25}Ni_{0.75}O_2$ compounds were synthesized from lithium compounds and spherical $Co_{0.25}Ni_{0.75}(OH)_2$ precursor by heating in oxygen at 750°C and 800°C for 12 hrs. The structural characteristics of the compounds were determined by x-ray diffraction. The best sintering temperature was found to be 800 °C, in terms of

stabilising the layered structure and improving the cycle life. It was found that the spherical $LiCo_{0.25}Ni_{0.75}O_2$ compounds sintered at 800 °C have a highly ordered layered structure with reduced cation mixing.

Carbon-enriched nanocrystalline $LiFePO_4$ compounds were prepared by the sol-gel method and the R/F carbon gel method, respectively. A layer of carbon was laid down as a coating on the surface of the lithium crystals, which dramatically enhanced the electronic conductivity of the $LiFePO_4$ compounds. A high capacity of 160 mAh/g at the C/5 rate has been demonstrated for the $LiFePO_4$ electrode. These electrodes also exhibited good cyclability at different charge/discharge rates.

A variety of anode materials have also been investigated to search out alternative anode materials to replace graphite for lithium ion batteries. Five types of cobalt oxides were prepared by high temperature decomposition, low temperature decomposition, high energy ball-milling, and the chemical decomposition of cobalt octacarbonyl in toluene, respectively. The LT-Co_3O_4, the CoO, and the nanosize Co_3O_4 powders prepared by decomposing organo-cobalt compounds at low temperature show good capacity retention on charge/discharge cycling, which is promising for their use as anode materials in Li-ion cells. It was found that the electrochemical properties of cobalt oxides are sensitive to the crystallinity, morphology, and particle size.

Nanosize Ag powders were prepared via a reverse micelle approach. The size of Ag nanoparticles can be influenced by the concentration of the reduction agent. In addition, SnO_2 nanopowders were synthesized by using the same method. 1D structured SnO_2

nanorods were observed in the SnO_2 nanopowders. The SnO_2 nanopowder electrodes show high electrochemical reactivity toward lithium in Li-ion cells.

The synthesized materials were characterized by x-ray diffraction, SEM and TEM, through which the phase composition and microstructure were observed. The capacity and cycle life of the cathode materials were obtained from charge/discharge cycling tests. The kinetic characteristics and kinetic parameters of lithium ion insertion and extraction within the electrode materials were determined by a.c. impedance spectroscopy and cyclic voltammograms.

In summary, the investigations in this project have produced several types of electrode materials with high capacity and long cycle life. In particular, the study focuses on the preparation of cathode materials with high density and ordered structure, and anode materials with ultrafine particles. Analysis of the electrochemical processes in lithium ion cells was conducted by various techniques. All of these studies provide a fundamental basis for the development of high energy density electrode materials.

Introduction

Lithium-ion batteries currently represent state-of-the-art power sources for modern consumer electronics due to their high voltage, high energy density, and long cycle life. The present lithium ion batteries use expensive materials, such as $LiCoO_2$, which are not in sufficient supply to allow the industry to grow at the same rate in the next decade. Moreover, the safety of the system is questionable for the large-scale batteries needed for hybrid electric vehicles (HEV). Intensive research activities have been carried out worldwide to reduce the cost, as well as improving the energy density, cycle life and safety of lithium ion batteries. Therefore, this study focuses on the synthesis and performance improvement of electrode materials for lithium-ion batteries.

Chapter 1 gives an overview of the cathode and anode materials for lithium-ion batteries, based on a literature survey. Some common cathode materials such as $LiCoO_2$, $LiNiO_2$, $LiFePO_4$, and their derivatives, and anode materials such as carbon-based, tin-based, and silicon-based anode materials, as well as transition metal oxides, have been reviewed in terms of their advantages, disadvantages, and structure, as well as their electrochemical properties.

In Chapter 2, a description is provided of the materials and chemicals used in this project, and the experimental methods and procedures are described in detail.

Chapter 3 presents the synthesis, structures and electrochemical properties of $LiCo_xMn_yNi_{1-x-y}O_2$ prepared from lithium compounds and the precursor $Co_xMn_yNi_{1-x-}$

$_y(OH)_2$ by heating at 850-900 °C. The synthesized $LiCo_xMn_yNi_{1-x-y}O_2$ has good micromorphology and uniform particle size. $LiCo_{0.2}Mn_{0.2}Ni_{0.6}O_2$ has the best electrochemical characteristics among the three materials studied and has an initial discharge capacity of 150 mAh/g.

Chapter 4 presents studies of high density spherical $LiNi_{0.75}Co_{0.25}O_2$ cathode material prepared by sintering $LiOH{\cdot}H_2O$ and spherical $Ni_{0.75}Co_{0.25}(OH)_2$ precursors at high temperature.. The structure, magnetic properties, and electrochemical behaviour of $LiNi_{0.75}Co_{0.25}O_2$ are described. Spherical $LiNi_{0.75}Co_{0.25}O_2$ cathode materials that were heat-treated at 800 ˚C demonstrated a high reversible capacity of 167 mAh/g and stable cyclability.

Chapter 5 presents the results of a systematic investigation of $LiFePO_4$ cathodes. Improvement of the electrochemical properties of $LiFePO_4$ by carbon-enriching and the use of ultra-fine material is demonstrated. The electronic conductivity of $LiFePO_4$ materials was dramatically enhanced via carbon inclusion. A high capacity of 160 mAh/g at the C/5 rate has been demonstrated for $LiFePO_4$ electrode.

In Chapter 6, an investigation of cobalt oxides as anode materials for lithium ion batteries is described. Five different types of cobalt oxides were prepared by high temperature decomposition, low temperature decomposition, high energy ball-milling, and the chemical decomposition of cobalt octacarbonyl in toluene at low temperature, respectively. The LT-Co_3O_4, the CoO, and the nanosize Co_3O_4 powders prepared by decomposing organo-cobalt compounds at low temperature show good capacity retention

on charge/discharge cycling, which is promising for their use as anode materials in Li-ion cells.

The reverse-micelle synthesis technique is a universal approach for preparing nanocrystalline metals, oxides and inorganic compounds. In Chapter 7, characterization studies of nanosized Ag and SnO_2 synthesized by the reverse-micelle technique are presented. The influence of synthesis parameters on the physico-chemical properties of the materials is investigated. The electrochemical properties are also described.

Finally, an overview and summary of the study is presented in Chapter 8. Suggestions for future work are also proposed.

Chapter 1

Literature review

1.1 Introduction to Lithium-ion Batteries

The lithium battery industry is undergoing rapid expansion and now represents the largest segment of the portable battery industry, dominating the computer, cell phone, and camera power source industry. However, the present lithium ion batteries use expensive materials, such as $LiCoO_2$, which are not in sufficient supply to allow the industry to grow at the same rate in the next decade. Moreover, the safety of the system is questionable for the large-scale batteries needed for hybrid electric vehicles (HEV). Intensive research activities have been carried out worldwide to reduce the cost, as well as improving the energy density, cycle life and safety of lithium ion batteries.

A lithium ion battery contains an anode, a cathode, and an electrolyte. The anode is the source of lithium ions, while the cathode is the sink for the lithium ions. The electrolyte provides for the separation of ionic transport and electronic transport, and in a perfect battery the lithium ion transport number will be unity in the electrolyte. The electrode system must allow for the flow of both lithium ions and electrons. That is, it must be both a good ionic conductor and an electronic conductor. Many electrochemically active materials are not normally good electronic conductors; therefore it is necessary to add an electronically conductive material such as carbon black. In addition, to physically hold the electrode together, a binder is also added. In such cases, the electrochemical reaction can only occur at those points where the

active material, the conductive agent, and the electrolyte meet. Thus, most electrodes are complex porous composites.

Almost all of the research and commercialization of cathode materials have focused on two classes of materials. The first is layered $LiMO_2$ (M = Co, Mn, Ni) with an anionic close-packed or almost close-packed lattice in which alternate layers between the anion sheets are occupied by a redox-active transition metal, and lithium then inserts itself into the essentially empty remaining layers. This structure is depicted in Fig. 1-1 [Spahr, Novak, et al 1998]. The spinels ($LiMn_2O_4$) may be considered as a special case where the transition-metal cations are ordered in all the layers. Another group of cathode materials have more open structures, such as vanadium oxides, the tunnel compounds of manganese dioxide and transition-metal phosphates, such as $LiFePO_4$. These materials are particularly attractive because of their potentially much lower cost.

The principal characteristics required for cathode materials in lithium ion batteries are as follows:

1. The discharge reaction should have a large negative Gibbs free energy (high discharge voltage).
2. The host structure must have a low molecular weight and the ability to intercalate large amounts of lithium (high energy capacity).
3. The host structure must have a high lithium chemical diffusion coefficient (high power density).
4. The structural modifications during intercalation and deintercalation should be as small as possible (long cycle life).

5. The materials should be chemically stable, non-toxic and inexpensive.

6. The handling of materials should be easy.

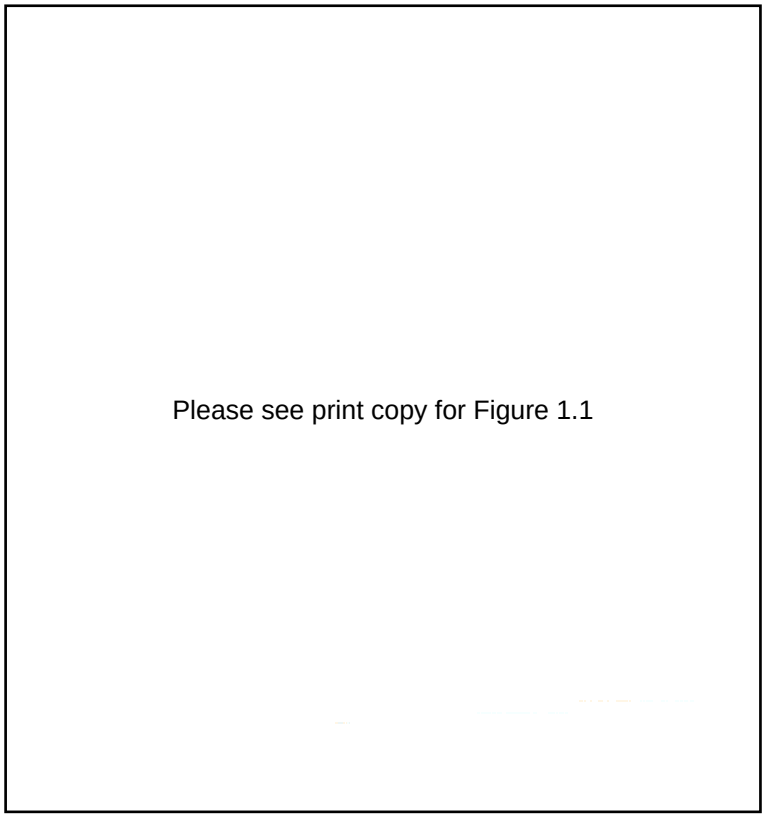

Fig. 1-1 Layered structure of $LiTiS_2$, $LiVSe_2$, $LiCoO_2$, $LiNiO_2$, and $LiNi_yMn_yCo_{1-2y}O_2$, showing the lithium ions between the transition-metal oxide/sulfide sheets. The actual stacking of the metal oxide sheets depends on the transition metal and the anion [Spahr, Novak, et al 1998].

With respect to the anode materials, graphitic or graphitization carbons have been used extensively as negative electrode materials for lithium-ion batteries. However, the lithium storage capacity of graphite is limited to 372 mAh/g, as associated with its maximum LiC_6 stage [Dahn, Zheng, et al. 1995]. Metals that store lithium are among the most appealing and competitive candidates for new types of anodes in lithium-ion

batteries. A number of metals and semiconductors, such as Al, Sn and Si, react with lithium to form alloys by electrochemical processes that are partially reversible, of low voltage versus lithium, involve a large number of atoms per formula unit, and in particular provide a specific capacity much larger than that offered by graphite. For example, $Li_{4.4}Si$ has a theoretical capacity of 4200 mAh/g [Sharma, Seefurth 1976]. However, lithium alloys are brittle and hence easily pulverized by the large volume change in charge and discharge reactions. The resulting loss of connectivity with the conducting additive particles causes poor cyclability in practice [Huggins 1998]. A popular approach to counter particle pulverization is to reduce the Si particle size to give a small absolute volume change in the local environment. Alternatively, the active particles may be embedded in a less active or inactive matrix to cushion the expansion and contraction in charge and discharge reactions.

A group of internally nanostructured anodes based on transition metal oxides has also recently been reported. The full electrochemical reduction of oxides such as CoO, Fe_2O_3, NiO, Co_3O_4 and MnO versus lithium, was shown to lead to composite materials consisting of nanometer-scale metallic clusters dispersed in an amorphous Li_2O matrix. Due to the nanocomposite nature of these electrodes, the reactions are highly reversible, providing reversible capacities two- to three-times higher than that use graphite as the anode materials [Poizot, Laruelle, et al. 2000].

Progress in lithium batteries relies as much on improvements in the electrolyte as it does on the electrodes. The electrolyte solution commonly comprises a lithium salt dissolved in a mixture of organic solvents, for example, $LiPF_6$ or LiBOB (where the BOB is the anion with the boron coordinated by two oxalate groups) in an ethylene

carbonate/dimethyl carbonate solvent. Solid polymer electrolytes represent the ultimate in terms of desirable properties for batteries because they can offer an all-solid-state construction, simplicity of manufacture, a wide variety of shapes and sizes, and a higher energy density. No corrosive or explosive liquids can leak out, and internal short-circuits are less likely, leading to greater safety. However, the conductivity reported in polymer electrolyte studies is still too low, and so they are only used when a liquid is added to give a gel state.

In this chapter, I will mainly focus on the cathode and the anode materials. Some aspects of the chemical and electrochemical behavior of a series of cathode and anode materials will be considered and compared.

1.2 Cathode materials for lithium ion batteries

1.2.1 Layered oxides

1.2.1.1 Lithium cobalt oxide, $LiCoO_2$

The most common cathode material for lithium ion batteries is layered-structure lithium cobalt oxide, $LiCoO_2$, which in fact is still the dominant cathode material in commercial lithium ion battery production. Although the theoretical capacity of $LiCoO_2$ is 248 mAh/g, the material delivers only 120-180 mAh/g due to structural restrictions. $LiCoO_2$ crystallizes in the space group R3m with the oxygens in a cubic close-packed arrangement (Fig. 1-2) [Hewston, Chamberland, 1987].

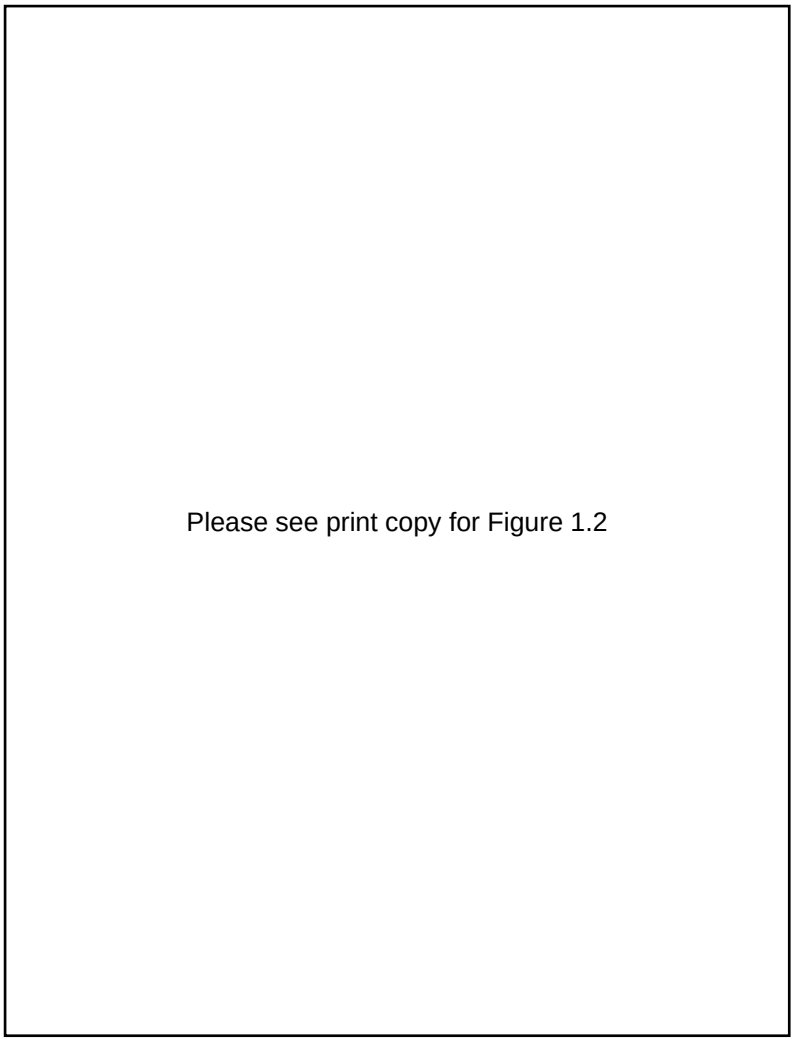

Fig. 1-2 Structure of α-$NaFeO_2$ [Hewston, Chamberland 1987].

The lithium ion reversibly intercalates into or deintercalates from the van der Walls gap between the CoO_2 layers. Between $LiCoO_2$ and CoO_2 composition limits, several phases are formed with varying degrees of distortion of the ccp oxygen lattice. The composition $Li_{0.5}CoO_2$ can also take on the spinel form, though it appears to be metastable and is not normally formed during the cycling of the Li_xCoO_2 electrode

[Rossen, Reimers, et al. 1993]. However, the spinel phase has been observed on the surface of heavily cycled $LiCoO_2$ cathodes in a recent TEM study [Gabrisch, Yazimi et al. 2004].

Many synthesis routes have been used to prepare electrochemically active $LiCoO_2$ compounds, including the conventional sintering of carbonate mixtures [Ohzuku, Kitagawa, et al. 1990, Fey, Hsieh, et al. 1993], nitrate mixtures [Antaya, Dahn, et al. 1993], and LiOH together with a carbonate [Antaya, Dahn, et al. 1993], an oxide [Broussely, Perton, et al. 1993, Lecerf, Brpisse, et al. 1989], or a nitrate of cobalt [Yoshio, Noguchi, et al. 1992]. The general trend suggests that the high temperature synthesis methods have little or no influence on the electrochemical performance of the $LiCoO_2$ material. However, most reports on materials prepared at low temperature show a high initial capacity, which unfortunately fades very quickly with cycling. Experimental results show that the structures of HT-$LiCoO_2$ ($LiCoO_2$ prepared by a high temperature synthesis method) and LT-$LiCoO_2$ [Garcia, Farcy, et al. 1995, Yazami, Lebrun, et al. 1995, Gummow, Tackeray 1993] (prepared by a low temperature synthesis route, usually one of the solution approaches) are quite different. HT-$LiCoO_2$ crystallizes in a layered structure isomorphic with α-$NaFeO_2$. It is based on a close-packed network of oxygen atoms with Li^+ and Co^{3+} ions ordered on alternating (111) planes of the cubic rock-salt structure, while LT-$LiCoO_2$ shows partial disordering of the Co and Li planes resulting in a different structure from HT-$LiCoO_2$. In LT-$LiCoO_2$ the deintercalation/intercalation reactions of Li are at lower potential than for HT-$LiCoO_2$. LT-$LiCoO_2$ is highly reactive with electrolytes and has slower Li transport than HT-$LiCoO_2$.

The capacity of the $LiCoO_2$ could be improved by coating a metal oxide or phosphate on the surface of the $LiCoO_2$ particles [Cho 1999, 2000, 2001]. Cho et al. reported that the capacity of coated $LiCoO_2$ could be increased to 170 mAh/g, without capacity fading over 70 cycles when cycled between 2.75 and 4.4 V. The protective mechanism depends on minimizing the reactivity of Co^{4+} on charge with the acidic HF in the electrolyte, which results from the interaction of moisture with the electrolyte salt $LiPF_6$ [Cho, Park 2003]. The capacity and cyclability of $LiCoO_2$ could also be improved by replacing the $LiPF_6$ salt by LiBOB or by completely drying the $LiCoO_2$ by heating to over 550 °C [Chen, Dahn 2004]. It was found that the reversible capacity could reach 180 mAh/g at a 4.5 V cutoff. Above this 4.5 V level, the cubic close-packed Li_xCoO_2 converts to the hexagonal close-packed structure of CoO_2; this requires substantial movement of the oxygen layers, which will eventually significantly disrupt/disorder the structure. Thus, capacity of $LiCoO_2$ much above 180 mAh/g is not attainable over hundreds of cycles.

The diffusion of lithium in $LiCoO_2$ is about 5×10^{-9} cm^2/s [Goodenough, Mizuchima 1981]; such a high diffusivity value is consistent with the ability to cycle this cathode at 4 mA/cm^2. However, the conductivity of Li_xCoO_2 remains a challenge, as it is reported to change dramatically with composition, behaving as in a metal at x = 0.6 and as in a typical semiconductor at x = 1.1 (the typical lithium-rich material used in commercial cells), changing with x by 2 [Levasseur, Menetrier, et al. 2000] to 4 [Imanishi, Fujiyoshi, et al. 1999] orders of magnitude at ambient temperatures and up to 6 orders of magnitude at lower temperatures [Levasseur, Menetrier, et al. 2000].

Although the $LiCoO_2$ cathode dominates the rechargeable lithium battery market,

$LiCoO_2$ has various drawbacks, including high cost due to the high price and the toxicity of Co. Thus, various alternative materials have been proposed within the last few years. Considerable work worldwide has been dedicated to partial substitution of cobalt by other metals such as nickel, iron, and manganese [Delmas, Saadoune 1992, Gummow, Thackeray 1992, Alcantara, Lavela, et al. 1998]. More recently, substitution of cobalt with aluminium [Ceder, Chiang et al. 1998, Yoon, Kee, et al. 2001] has resulted in an increase in the average discharge voltage. It has also been demonstrated that a very small amount of magnesium has an impact on the fading behaviour during cycling [Honbo, Muranaka, et al. 1998].

1.2.1.2 Lithium nickel oxide, $LiNiO_2$

Lithium nickel oxide, $LiNiO_2$, is isostructural with lithium cobalt oxide but has not been pursued in the pure state as a battery cathode for a variety of reasons, even though nickel is more readily available than cobalt. First, it requires utmost care in the synthesis process, since the resulting $LiNiO_2$ samples often suffer from twin complications, namely cation mixing and off-stoichiometry. Cation mixing in general leads to a composition of $Li_{1-x}Ni_{1+x}O_2$ with $x \sim 0.02$. Second, compounds with low lithium contents appear to be unstable due to the high effective equilibrium oxygen partial pressure, so that such cells are inherently unstable and therefore dangerous in contact with organic solvents. Furthermore, studies reveal that the electrochemical properties of $LiNiO_2$ cathode are extremely dependent upon the synthesis conditions, and hence the optimization of preparation conditions [Kalyani, Kalaiselvi et al. 2004] is essential for $LiNiO_2$ in order to minimize the said constraints.

A qualitative picture of the battery activity can be obtained from the nature of the XRD patterns of Li_xNiO_2. A typical XRD pattern of $LiNiO_2$ is presented in Fig. 1-3. The (003) peak results from the diffraction of the layered rock-salt structure (R-3m), whereas the (104) peak appears from the diffractions of both the layered and the cubic rock-salt structures [Morales, Perez-vicente, et al. 1990]. The crystal quality of the synthesized $LiNiO_2$ can be evaluated by measuring the integrated intensity ratio of the (003) to the (104) peak, with a decrease in the $I_{(003)}/I_{(104)}$ ratio indicating the formation of the cubic $LiNiO_2$ structure due to the displacement of nickel ions into the lithium layer. Ohzuku and Ueda et al. [1993] found that $LiNiO_2$ with an $I_{(003)}/I_{(104)}$ ratio ranging from 1.32 to 1.39 exhibit high electrochemical activity, and they assume that the exact chemical composition of the compound, i.e. x, is not the main factor in determining its electrochemical performance when the Li/Ni ratio is close to unity. However, Moshtev and Zatilova et al. [1995] have revealed a clear linear dependence of the $I_{(003)}/I_{(104)}$ ratio on x in the range of $0.91 < x < 0.99$. Likewise, Nitta and Okamura et al. [1995] have reported that the integrated intensity ratio of the (006) to the (101) peak should be less than 1.0, in order to obtain better electrochemical properties from the synthesized $LiNiO_2$.

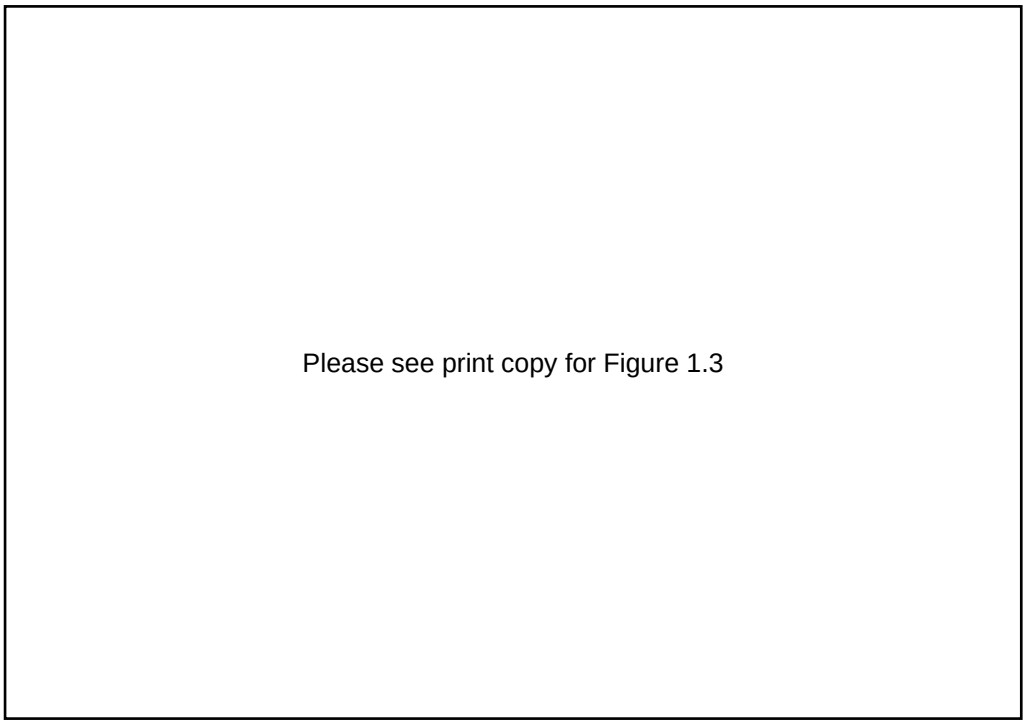

Fig. 1-3 Typical XRD pattern of $LiNiO_2$: a = 2.88 Å, c =14.19 Å; JCPDS # 9-063; rhombohedral structure ($R\text{-}3m$ -D_{3d}^5). Ref.: Lee et al., Solid State Ionics 118 (1999) 159.

Modification of $LiNiO_2$ by replacing a part of the nickel by other elements, such as cobalt, manganese, aluminum etc., could impact on the layered nature of the structure, the structural stability, and the retention of capacity on cycling. This aspect will be discussed in the next section.

1.2.1.3 Mixed nickel-cobalt dioxide, $LiNi_{1-y}Co_yO_2$

The $LiNi_{1-y}Co_yO_2$ system is one of the most promising candidate cathode materials of advanced lithium-ion batteries because of its lower cost, better rate capability and higher capacity compared with $LiCoO_2$, as well as its superior thermal stability compared to $LiNiO_2$ (following the tendency for $LiCoO_2$ to show good thermal stability). The good electrochemical performance of these compounds relies on a well

layered structure, in which Li and (Co/Ni) cations do not mix but occupy alternating fcc (111) planes [Ohzuku, Ueda et al. 1993].

From the synthetic point of view, these materials can be prepared by the traditional (and most often used) high temperature ceramic methods or by means of more recently introduced low-temperature wet chemistry routes. Interestingly enough, it has been shown that the synthetic conditions have a great impact on the electrochemical characteristics of the electrode materials and that a small particle size favors the rate capability on charging/discharging the electrochemical cells.

The structural details and physical properties of the $LiNi_{1-y}Co_yO_2$ system have been extensively studied. It has been proposed that there is increased ordering as the cobalt concentration increases [Zhecheva, Stoyanova 1993]. The c/3a ratio increases monotonically from 1.643 to 1.652 as y increases from 0 to 0.4, and there are no excess nickel ions in the interslab space (lithium sites) for $y \geq 0.3$. Therefore, cobalt suppresses the migration of nickel to the lithium sites in the mixed Li nickel/cobalt compounds. Studies have also shown that the cobalt substitution could improve the stability of $LiNiO_2$, and thus the chances for oxygen loss become less than in the pure nickel oxide. Partial aluminum substitution has a positive effect on the thermal stabilization of $LiNiO_2$ in its charged state [Ohzuku 1995, 1997]. This thermal stabilization could result from the stability of the Al^{3+} ions in tetrahedral sites, which disturbs the cationic migrations required by the phase transformations observed increasing temperature. Guilmard and Rougier et al. [2003] have found that less than 1% excess nickel ions are present in the interslab space when the composition is $LiNi_{0.7}Co_{0.15}Al_{0.15}O_2$, although they found that about 5% excess nickel was present on

lithium sites in the $LiNi_{1-y}Al_yO_2$ system [Guilmard, Pouillerie et al. 2003]. Thus partial cobalt substitution for nickel in the $LiNi_{1-y}Al_yO_2$ system could be a good means to combine two positive effects, i.e. an increasing lamellar character for the structure (induced by Co) and an increasing thermal stability (induced by Al). In fact, cobalt and aluminum substituted nickel oxides, $LiNi_{1-y-z}Co_yAl_zO_2$ are prime candidates for the cathode of advanced lithium batteries, especially for use in large-scale systems such as are required for hybrid electric vehicles. On charging, the nickel in the compound is oxidized first to Ni^{4+}, then the cobalt to Co^{4+} [Nakai, Nakagome 1998]. SAFT has constructed cells with these Co, Al-substituted $LiNiO_2$ compounds as cathode materials, and the cells have been cycled 1000 times at 80% depth of discharge with an energy density of 120-130 Wh/kg [Brouselly 2001]. Another redox-inactive doping element in $LiNiO_2$ is magnesium, which can reduce the capacity fading on cycling as in $LiNi_{1-y}Mg_yO_2$ [Pouileerie 2000, 2001]. Mg as an inert element, prevents the complete removal of all the lithium, thus minimizing possible structural collapse, as well as a high level of oxygen partial pressure, This is because NiO_2 itself is thermodynamically unstable at 25 °C, as the equilibrium oxygen partial pressure exceeds 1 atm.

Another issue with $LiNi_{1-y}Co_yO_2$ oxides is their electronic conductivity, which is not uniformly high across the lithium composition range. Cobalt substitution in $LiNiO_2$, as in $LiNi_{0.8}Co_{0.2}O_2$, reduces the conductivity [Saadoune, Delmas 1996]. However, as lithium ions were removed from $Li_xNi_{1-y}Co_yO_2$ [Saadoune, Menetrier 1997], the conductivity was found to increase dramatically by 6 orders of magnitude to around 1 S/cm from x = 1 to 0.6. The non-uniform conductivity demands that a conductive

diluent be added to the cathode-active materials, which unavoidably reduces the capacity and energy storage.

1.2.1.4 $LiMnO_2$ and $LiNi_{1-y}Mn_yO_2$

$LiMnO_2$ in layered α-$NaFeO_2$ structure is thought to be a promising material due to its low cost, nontoxic nature and high theoretical capacity. Despite all its promise, it is not thermodynamically stable at elevated temperature and thus can not be synthesized by the same methods as are used for materials like $NaMnO_2$. Instead, other approaches must be used. Armstrong and Bruce [1996] first reported the preparation of pure crystalline layered structure $LiMnO_2$ by an ion exchange reaction from α-$NaMnO_2$. The $NaMnO_2$ was synthesized by solid-state reaction between stoichiometric quantities of Na_2CO_3 and manganese (III) oxide at 700-730 °C for 18-72 hours under flowing argon. The layered $LiMnO_2$ was obtained by refluxing $NaMnO_2$ with an excess of LiCl or LiBr in n-hexanol at 145-150 °C for 6-8 hours. Mitsuharu and Kzauaki et al. [1996] reported that layered $LiMnO_2$ with trace impurities of orthorhombic-type $LiMnO_2$ and Li_2MnO_3 was synthesized directly from Mn_2O_3 by hydrothermal reaction at 220 °C using mixed solutions of LiOH and KOH or LiCl and KOH. This form of layered $LiMnO_2$ slowly transforms to tetragonal $Li_2Mn_2O_4$ and o-$LiMnO_2$ upon annealing at 150°C, indicating metastability of the monoclinic phase. It is usually difficult to get pure layered $LiMnO_2$ under high-temperature synthesis conditions and the firing environment has to be controlled (inert atmosphere). Nevertheless, Young-II Jang et al. [2002] recently reported that layered $LiMnO_2$ could be synthesized by high-temperature firing in an air atmosphere, without requiring reducing atmosphere as previously used. They found that control of the cooling conditions was crucial for avoiding oxidative decomposition into

$LiMn_2O_4$ and Li_2MnO_3.

Two approaches have been used to stabilize the layered $LiMnO_2$. In the geometric stabilization approach, non-ccp structures, such as tunnel structures, two block or other non-ccp close-packed structures [Chen, Whittingham 1997] or "pillars", are placed between the layers to provide the stabilization. Whittingham's group investigated the electrochemical behavior of pillared structure compounds, such as $KMnO_2$ [Chen 1996] and $(VO)_yMnO_2$ [Zhang, Ngala et al. 2000, Yang, Song et al. 2003], and found that the structure of $KMnO_2$ was stable at low current density, while $(VO)_yMnO_2$ showed excellent stability but poor rate capability. Dahn and Deoff's group [Doeff, Richardson et al. 1996, Lu, MacNeil et al. 2001] have pursued non-ccp structures by looking at tunnel structures such as $Li_{0.44}MnO_2$, and also at ion-exchanging layered sodium manganese oxide compounds without stacking of the oxygen sheets [Lu, MacNeil, et al. 2001, Eriksson 2003, Shaju, Subbarao, et al. 2003].

In the electroinic stabilization approach, the goal is to make the electronic properties of Mn more cobalt-like by replacing some of the Mn with more electron rich elements. $LiAl_xMn_{1-x}O_2$ was first successfully synthesized by Young-II Jang et al. in 1998. The compounds were prepared by firing homogeneous hydroxide precursors in a reducing atmosphere to control the manganese valence state. The composition $LiAl_{0.25}Mn_{0.75}O_2$ shows a first-charging voltage of 4 V against a lithium electrode, but develops 4 and 3V plateaus upon cycling, indicating a transformation to spinel-like cation ordering within the oxide. After that, they synthesized $LiAl_xMn_{1-x}O_2$ by a co-precipitation and freeze-drying route [Jang, Huang et al. 1998, Chiang, Jang et al. 1998] and studied the stability of $LiAl_xMn_{1-x}O_2$ as a function of temperature, oxygen

partial pressure, and Al content. Within the regime where Mn^{3+} is stable, the layered phase is the major phase at higher temperatures and oxygen partial pressures. For example, at 950 °C and $P_{o2} = 10^{-7}$ atm, nearly 100% layered phase is obtained. There is a maximum Al solid solubility due to the competing stability of γ-$LiAlO_2$. The maximum solubility is 5-7 % and is reached at 950 °C and $P_{o2} = 10^{-7}$ atm. Within the solid solubility limit, Al doping increases the fraction of layered phase.

Recently, Davidson and McMillan et al. [1999] and Ammundsen and Desilvestro et al. [2000] reported the preparation of layered $LiMnO_2$ by replacing a small fraction of the Mn with Al or Cr. The layered structure $LiMnO_2$ compounds obtained are well ordered with Al or Cr sharing the Mn sites and no detectable cation mixing between Mn and Li layers. Both Al- and Cr- substituted materials cycled between 4.4 and 2.0 V in Li cells show high stability of capacity. However the Al-substituted materials undergo a structural transformation to a spinel-type phase, accompanied by evolution of the discharge voltage curve to a two-plateau profile. Materials modified with small amounts of Cr show a different evolution of the discharge voltage. X-ray diffraction data for cycled $LiCr_xMn_{1-x}O_2$ cathodes show that these compounds do not undergo significant transformation to spinel on cycling, but retain the hexagonal structure established on first charge.

The groups of Ammundsen and Davidson [2000] also found that Li-Mn-Cr-O_2 mixed-metal compounds had the $NaFeO_2$ structure and cycled well when a substantial part of the transition metals were replaced by lithium as in Li_3CrMnO_5 or described in the layered form as $Li[Li_{0.2}Mn_{0.4}Cr_{0.4}]O_2$. They found that the Mn has the 4^+ oxidation state and that all the lithium can be removed giving Cr(IV). Increasing the

temperature from 20 to 55 °C increased the cell capacity from around 125 to 165 mAh/g. When the cells were charged/discharged in the voltage range of 2.5 to 4.5 V at low rates, capacities as high as 220 and 200 mAh/g could be obtained. The lithium ions in the transition-metal layer were found clustered around the manganese ions as in Li_2MnO_3, and the system can be considered as a solid solution of Li_2MnO_3 and $LiCrO_2$.

Furthermore, it has been reported that doping $LiMnO_2$ with Co also tends to stabilize the layered rhombohedral form without giving any evidence of a monoclinic Jahn-Teller distortion. Substitution of ~10 at.% Mn by Co leads to a 50% increase in the amount of lithium that can be removed and reinserted into the oxide framework, thereby improving the capacity retention from 130 to 200 mAh/g when the oxide electrode is cycled at 100 mA/cm^2. However, as with Al doped compounds, the Co doped $LiMnO_2$ is transformed to the spinel form upon electrochemical cycling, and the rate of conversion appears to be controlled by the cobalt content. For example, the layered $LiMn_{0.9}Co_{0.1}O_2$ converts to spinel within the first cycle, but $LiCo_{0.3}Mn_{0.7}O_2$ displays only some conversion after 30 cycles [Armstrong, Robertson et al. 1999].

Although of little commercial interest because of the toxicity of Cr and Co, this research provoked much thinking about other multi-electron redox reactions systems, such as the $LiNi_{1-y}Mn_yO_2$ phase system. The first studies on $LiNi_{1-y}Mn_yO_2$ were done by Dahn's group in 1992 [Rossen, Jones et al. 1992]. They reported a solid solution for $0 < y \leq 0.5$ but with low capacities and poor reversibility. However, Spahr and Novak et al. [1998] repeated the work, and they demonstrated a high capacity and reversibility for $LiNi_{0.5}Mn_{0.5}O_2$ with a discharge curve typical of $LiNiO_2$. They also

reported XPS and magnetic data that are consistent with the present interpretation of Ni^{2+} and Mn^{4+} ions rather than Ni^{3+} and Mn^{3+}. Ohzuku and Makimura et al. [2001] restudied the $LiNi_{0.5}Mn_{0.5}O_2$ system in 2001, and demonstrated very good electrochemical data. Their results were reconfirmed by Dahn's group almost immediately. These papers ignited a substantial amount of work on this composition. It was found that manganese shows no significant layer stabilization capability as up to 9.3% of the nickel was found on the lithium sites when the sample was formed at 1000°C, and 11.2% for a sample formed at 900 °C [Arachi, Kobayashi et al. 2003; Venkatraman, Manthiram 2003]. Nickel is expected to reduce the rate capability of the electrode. The $LiNi_{0.5}Mn_{0.5}O_2$ phase has a hexagonal lattice with slightly different α and c values from different reports (Table 1-1).

Table 1-1 Lattice parameters of $LiNi_{0.5}Mn_{0.5}O_2$ from different reports.

Please see print copy for Table 1.1

There is some disagreement about the structure formed on lithium removal. Yang and McBreen et al.[2002] reported that on delithiation a second hexagonal phase with a = 2.839 Å and c = 14.428 Å was formed; this is in contrast to the pure $LiNiO_2$, where a

third hexagonal phase is also found. They also reported that excess lithium could be intercalated with a slight expansion of the hexagonal cell to a = 2.908 Å and c = 14.368 Å; this is possibly the phase $LiNi_{0.5}Mn_{0.5}O_2$. However, Venkatraman and Manthiram et al. [2003] reported a single phase for $0 < x < 1$ with continuously varying lattice parameters. Arachi and Kobayashi et al. [2003] reported the formation of a monoclinic phase for $LiNi_{0.5}Mn_{0.5}O_2$ with a = 4.924 Å, b = 2.852 Å, c = 5.0875 Å and $\beta = 108.81°$.

The electrochemical data from different reports are also different. Spahr and Novak et al. [1998] reported in 1998 a capacity of 150 mAh/g, falling to 125 mAh/g after 25 cycles and to 75 mAh/g after 50 cycles for a $LiNi_{0.5}Mn_{0.5}O_2$ sample prepared at 700°C; they also found that the capacity and the cyclability of electrodes increased as the synthesis temperature increased from 450 to 700 °C, which we now know to be too low for optimum electrochemical behavior. Ohzuku and Makimura et al. [2001] synthesized a $LiNi_{0.5}Mn_{0.5}O_2$ sample at 1000 °C and reported a constant 150 mAh/g at 0.1 mA/cm^2 for 30 cycles. Lu and Dahn et al. [2001] prepared $LiNi_{0.5}Mn_{0.5}O_2$ compound at 900 °C and quenched to room temperature; they claimed a capacity exceeding 150 mAh/g for over 50 cycles in a thin film configuration. Shaju and Subbarao et al. [2004] charged/discharged their $LiNi_{0.5}Mn_{0.5}O_2$ electrodes with a 4.4 V top-up constant potential charge after a constant current charge to 4.4 V and reported an initial capacity exceeding 170 mAh/g, but which decayed over 20 cycles to less than 150 mAh/g. The electrodes that were also charged to just 4.2 V only had a capacity of 130 mAh/g, but with much better capacity retention. Increasing the temperature to 50 °C increased the capacity fading rate except where the maximum charge potential was limited to 4.2 V. However, Sun and Yoon et al. [2003] reported

that $LiNi_{0.5}Mn_{0.5}O_2$ shows good cycling stability at 0.1 mA/cm^2 even when charged to 4.6 V, with the capacity increasing from 150 to 190 mAh/g as the charging cutoff potential is raised from 4.3 to 4.6 V. Kang and Kim et al. [2002] prepared $LiNi_{0.5}Mn_{0.5}O_2$ compounds at 1000 °C and tested their electrochemical performance as cathode materials for lithium ion batteries; the $LiNi_{0.5}Mn_{0.5}O_2$ electrodes showed a lower capacity of around 120 mAh/g at 0.1 mA/cm^2. The capacity could be increased to about 140 mAh/g by adding 5% cobalt, aluminum, or titanium. These results suggest that the synthesis temperature of 1000 °C may be too high, which probably leads to excess nickel in the lithium layer. Lu and Dahn et al. [2001] proposed that the capacity could be increased from 160 to 200 mAh/g at 30 °C by substituting a part of the transition metals by lithium, giving compounds such as $Li[Ni_{1/3}Mn_{5/9}Li_{1/9}]O_2$, while Johnson and Kim et al. [2002] found that $LiNi_{0.5}Mn_{0.5}O_2$ compound could intercalate a second lithium, particularly when titanium was added. Recently, Cushing and Goodenough [2002] reported that conductive carbon coatings could raise the capacity of $LiNi_{0.5}Mn_{0.5}O_2$. The rate capability has also been studied by Ohzuku's group. It was found that the capacity approached 200 mAh/g at 0.17 mA/cm^2, falling off to 130 mAh/g at 6 mA/cm^2 (All cells were charged at 0.17 mA/cm^2, then held at 4.5 V for 19 h; cathode loading was around 15 mg/ cm^2.) [Makimura, Ohzuku 2003]

Koyama and Makimura et al. [2004] investigated the electronic and crystal structures and the phase stability of the $LiNi_{1-x}Mn_xO_2$ system by using first-principles calculations. Straight and zigzag models have been used to calculate the total energy of $LiNi_{1-x}Mn_xO_2$. They found that the relative energy of $LiNi_{1-x}Mn_xO_2$ is negative, especially at the midpoint between $LiNiO_2$ and $LiMnO_2$. The minimum value observed for $LiNi_{0.5}Mn_{0.5}O_2$ and its large stabilization energy indicate that it is

difficult to explain $LiNi_{1-x}Mn_xO_2$ in terms of a solid solution between $LiNiO_2$ and $LiMnO_2$. By comparing the relative energy value of $LiNi_{0.5}Mn_{0.5}O_2$ with that of NiO and Li_2MnO_3, they proposed that $LiNi_{0.5}Mn_{0.5}O_2$ contains Ni and Mn as Ni^{2+} and Mn^{4+}, concluding that Ni-rich phases of $LiNi_{1-x}Mn_xO_2$ ($0 \leq x \leq 0.5$) consist of a solid solution of $LiNiO_2$ and $LiNi_{0.5}Mn_{0.5}O_2$. A Mn-rich phase of $LiNi_{1-x}Mn_xO_2$ ($0.5 < x \leq 1$) may be distorted into a monoclinic structure, as the Mn-rich phase contains Jahn-Teller Mn^{3+} ions in a solid matrix. The unit cell of $LiNi_{0.5}Mn_{0.5}O_2$ is close to an ideal hexagonal one. However, the c-axis parameter for $LiNi_{0.5}Mn_{0.5}O_2$ is expected to be the longest value among nickel-based lithium insertion materials reported so far, while the a-axis lattice parameter is almost the same as that of $LiNiO_2$. The electronic structure of $LiNi_{0.5}Mn_{0.5}O_2$ is quite different from that of $LiNiO_2$, therefore, the solid-state redox reaction of $LiNi_{0.5}Mn_{0.5}O_2$ is expected to be different from that of $LiNiO_2$, i.e. Ni^{2+}/Ni^{4+} with Mn^{4+} vs Ni^{3+}/Ni^{4+} for an overall reaction with almost the same theoretical capacity of 280 mAh/g.

Ceder and Gray [2004] investigated $Li_xNi_{0.5}Mn_{0.5}O_2$ by experiments and calculations. They believe that the composition of the transition-metal layer requires 0.5/6 lithium (~8%). The manganese ions are surrounded by nickel ions on the hexagonal lattice, leading to a $2\sqrt{3} \times 2\sqrt{3}$ superlattice. On charging, the lithium is removed from the lithium layer first, which leads to vacancies in lithium sites, then the Li^+ in the transition-metal layer can drop down from its octahedral site into the vacant tetrahedral site. Thus, the tetrahedral lithium is only removed at the highest potential, i.e., only after all the octahedral lithium is removed.

1.2.1.5 $LiNi_{1-y-z}Mn_yCo_zO_2$

Based on the above review, it is obvious that cobalt additions in the $LiNi_{1-x}Mn_xO_2$ system can reduce the level of nickel in the lithium layer, thereby reducing the structural instability of $LiNi_{1-x}Mn_xO_2$. Mixed nickel-manganese-cobalt (Ni, Mn, Co) compounds were first reported by Liu et al. in 1999 and by Yoshio et al. in 2000. Liu and Yu et al. [1999] found that the partial substitution of Ni by Co and Mn has a positive effect on the maintenance of lithium stoichiometry, although lithium deficiency is still noticeable when extended thermal treatments (24 h) are used in the synthesis. Compared to pure $LiNiO_2$ cells, cells that are constituted from $LiNi_{0.7}Co_{0.2}Mn_{0.1}O_2$ shows good capacity and cycle life, but excessive Mn doping as in the case of $LiNi_{0.5}Co_{0.2}Mn_{0.3}O_2$ returns a cycle life as poor as that of pristine $LiNiO_2$. Yoshio et al. [2000] found that excess lithium and the Co doping level ($0.05 \leq y \leq 0.2$) did not significantly affect the discharge capacity of $Li_zCo_yMn_{0.2}Ni_{0.8-y}O_2$. The doping of Co into $LiNi_{0.8}Mn_{0.2}O_2$ accelerated the oxidation of the transition metal ions and suppressed partial cation mixing. Ohzuku and Makimura [2001] studied the symmetric compound $LiNi_{1/3}Mn_{1/3}Co_{1/3}O_2$, synthesized at 1000 °C, and found that the capacities obtained were dependent upon voltage limits, with a capacity of around 150 mAh/g when cells were cycled between 2.5 and 4.2 V at 0.17 mA/cm^2 at 30 °C; raising the charge cut-off potential to 5.0 V increased the capacity to over 220 mAh/g, but capacity fade was significant.

1.2.1.5.1 Synthesis and structure of $LiNi_{1-y-z}Mn_yCo_zO_2$

$LiNi_{1-y-z}Mn_yCo_zO_2$ is usually synthesized by the mixed hydroxide method [Liu, Yu et al. 1999], in which a $M(OH)_2$ (M = Ni, Co, Mn) precursor is precipitated from a metal salt solution and is then reacted with a lithium salt at elevated temperature. This is not difficult in practice, but pH, temperature, flow conditions, concentrations, and other

factors influence the crystal structure, purity, and physical properties of the products, and must be carefully controlled for optimum electrochemical performance. Yoshio and Noguchi et al. [2000] prepared $LiNi_{1-y-z}Mn_yCo_zO_2$ by sintering a mixture of $LiOH{\cdot}H_2O$, $Ni(OH)_2$ and γ-MnOOH. Single–phase $LiNi_{1-y-z}Mn_yCo_zO_2$ ($0 \leq z \leq 0.3$) with discharge capacities greater than 155 mAh/g was obtained by heating at 830-900 °C. They found that the optimum heating temperatures were 850 °C for z = 0-0.1 and 900 °C for z = 0.2-0.3. More recently, Patoux and Doeff [2004] synthesized pure $LiNi_{1/3}Co_{1/3}Mn_{1/3}O_2$ samples directly from nitrate precursors and by a glycine–nitrate combustion (GNC) process. For the series of materials made directly from nitrates, the irreversible capacities were inversely correlated with the crystallite size and decreased as the calcination temperature increased (except for 1000 °C). Somewhat surprisingly, the GNC sample did not follow this trend, exhibiting the lowest irreversible capacity in spite of the small crystallite size. $LiNi_{1/3}Co_{1/3}Mn_{1/3}O_2$ was only partially deintercalated when the cells were charged to 4.3 V. Higher discharge capacities can be obtained when the voltage limit upon charge is raised. Fig.1-4 shows first cycles for cells containing 900 °C-$LiNi_{1/3}Co_{1/3}Mn_{1/3}O_2$ charged to 4.3, 4.5, or 4.7 V. Although utilization is greater for cells charged to higher voltages, this comes at the expense of increased coulombic inefficiencies and more rapid capacity fading upon cycling (see inset).

Guo and Liu et al. [2003] synthesized $Li[Co_{1/3}Mn_{1/3}Ni_{1/3}]O_2$ by using a spray drying technique. They found that the intensity ratios of the (003) to (104) peaks in XRD patterns for the 800 °C and 900 °C samples were 1.21 and 0.83, respectively, which indicates that cation mixing emerged at the higher temperature. A discharge capacity of 154 mAh/g can be delivered in the range of 2.5-4.3 V at a specific current of 30

mA/g, and the rechargeable capacity for samples sintered at 800°C is more than 140 mAh/g.

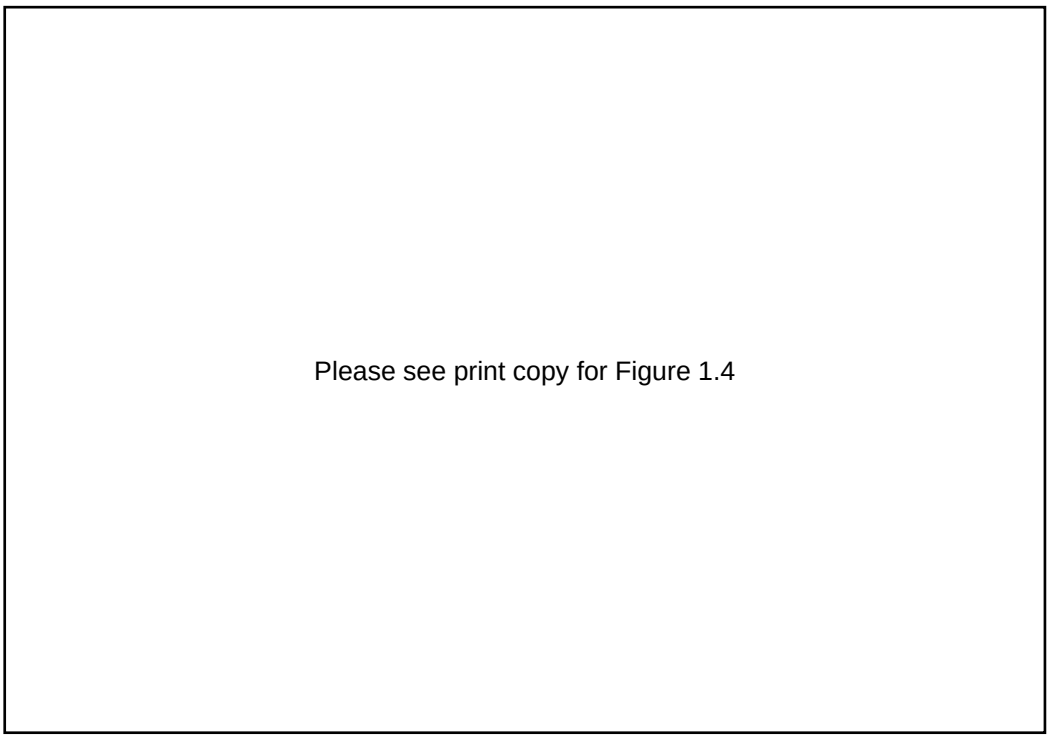

Fig. 1-4. First cycles of Li/900 °C-$LiNi_{1/3}Co_{1/3}Mn_{1/3}O_2$ cells at 0.055 mA/cm^2 charged to 4.3 V (o), 4.5 V (—), and 4.7 V (- - -). Inset shows discharge capacity as a function of cycle number [Patoux S., Deoff M.M., 2004].

All the synthesis above resulted in a single phase of $LiNi_{1-y-z}Mn_yCo_zO_2$ with a layered O3 structure. Typical diffraction patterns, as shown in Fig. 1-5, verified the R3m symmetry of the α-$NaFeO_2$ structure. This structure has Li-ions at the 3a sites, the transition metal ions (M = Mn, Co, and Ni) at the 3b, and the O ions at the 6c sites

(Fig. 1-6).

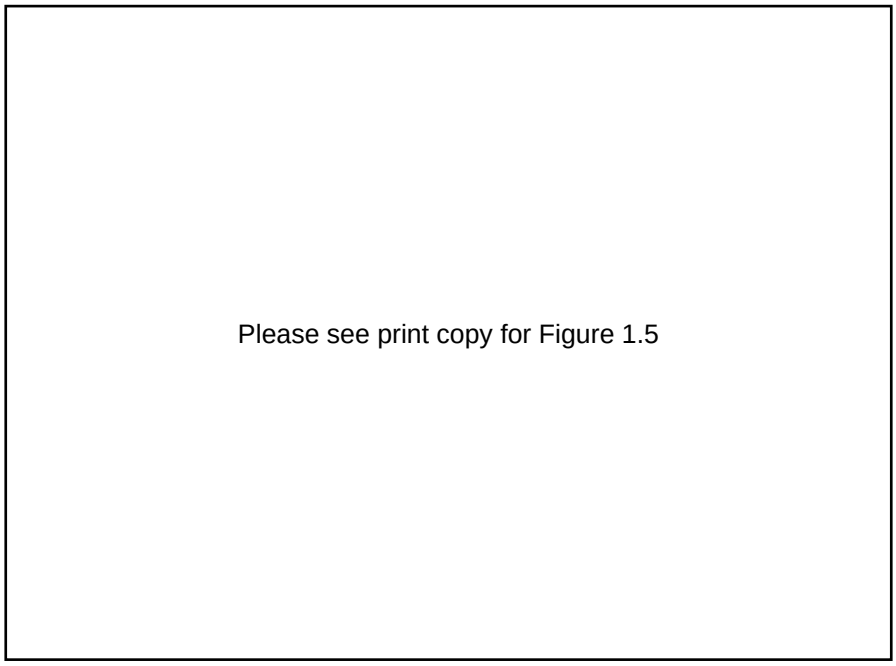

Fig. 1-5 X-ray diffraction patterns of $Li[Co_{1/3}Mn_{1/3}Ni_{1/3}]O_2$ powder. (a) Sintered at 800°C; (b) sintered at 900°C; (c) discharged electrode after 25 charge-discharge cycles (2.4-4.3 V) [Guo Z.P., Liu H. et al. 2003].

The cell parameters of $LiNi_{1-y-z}Mn_yCo_zO_2$ compound are slightly dependent on the transition metals. Macneil and Lu et al. [2002] found that as the concentration of Ni increased, there was an increase in both the *a* axis and the *c* axis parameters but a decrease in the *c*/*a* ratio. This is clearly demonstrated in Fig. 1-6. The increase in unit cell size might be caused by the substitution of the larger Ni^{2+} (r_{Ni}^{2+} = 0.69 Å) ion for Co^{3+} (r_{Co}^{3+} = 0.545 Å). The Mn^{4+} ion (r_{mn}^{4+} = 0.53 Å) is about the same size as the Co^{3+} ion, so they believe that the Ni ion is responsible for the changes observed.

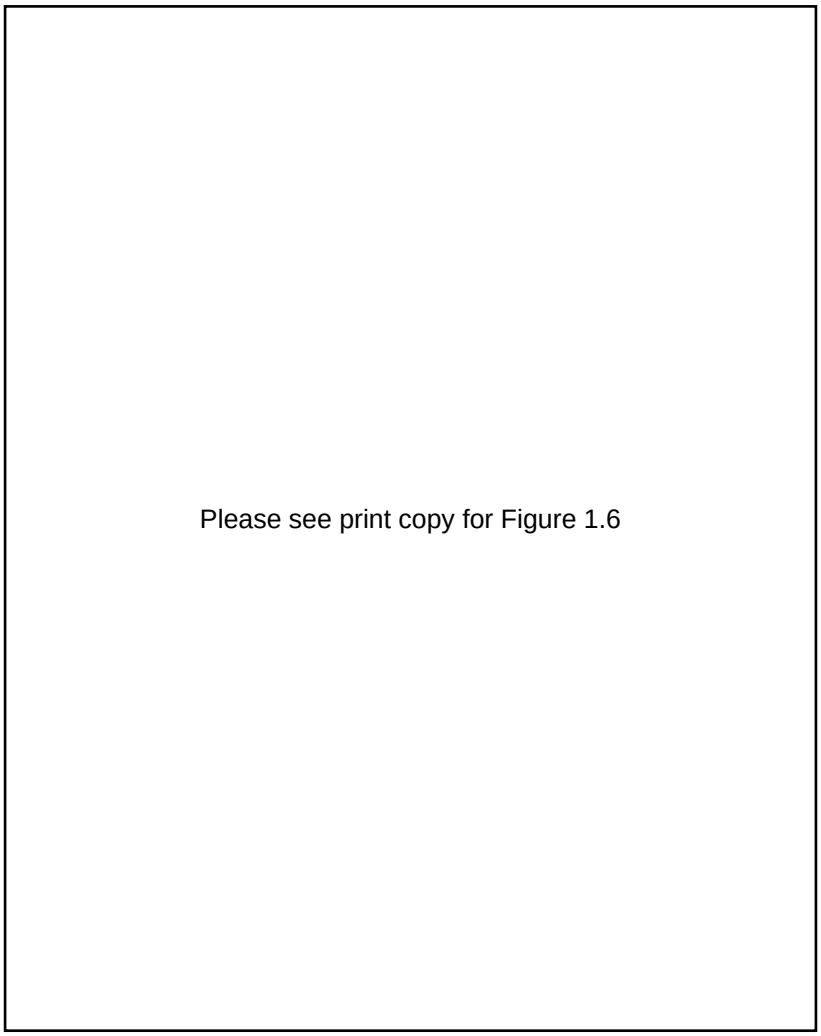

Fig. 1-6. Changes in lattice constants of $LiNi_xCo_{1-2x}Mn_xO_2$ as the Co content changes [Macneil D.D., Lu Z., et al. 2002].

Sun and Ouyang et al. [2004] found that the α and c parameters for compositions $LiNi_yCo_{1-2y}Mn_yO_2$ obey Vegard's law, decreasing linearly with increasing cobalt content. For constant nickel content, the α parameter is directly proportional to [Mn] and inversely proportional to [Co], indicating that the Mn ion is larger than the Co ion. This observation is contrary to the conclusion given by Macneil and Lu et al. [2002].

The ratio C/3a of the lattice constants is a direct measure of the deviation of the lattice from a perfect cubic close-packed structure, which can act as a measure of the "layeredness" of the lattice. An ideal ccp lattice has a c/3a ratio ratio of 1.633, and the closer the c/3a value is to 1.633, the greater the transition-metal content in the lithium layer. $LiNiO_2$ has a c/3a value of 1.639 [Spahr, Novak et al. 1998], while the c/3a ratio for $LiNi_{0.5}Mn_{0.5}O_2$ is 1.644-1.649 depending on the investigator [Lu, Dahn 2001; Kobayashi, Sakaebe et al. 2003]. Fig. 1-6 shows that this ratio becomes larger as the cobalt content increases, indicating that cobalt confers layer-like behavior on the lattice. The mean of all the data for the composition $LiNi_{1/3}Co_{1/3}Mn_{1/3}O_2$ is 1.657, which is more far from 1.633 than the average value (1.647) of the cobalt-free $LiNi_{1/2}Mn_{1/2}O_2$, indicating its more layered structure. For the $LiNi_{1/3}Co_{1/3}Mn_{1/3}O_2$ compounds, the c/3a value decreases as the sintering temperature increases, suggesting an increasing nickel content in the lithium layer with increasing temperature.

Rietveld refinement is usually used [Guilmard, Rougier et al. 2003] to determine the distribution of the transition-metal ions in the layered structure between the 3b and 3a sites; in a completely ordered layered structure, these sites should be fully occupied by transition metal and lithium, respectively. Kim and Chung et al. [2004] investigated the properties of $LiNi_{1/3}Co_{1/3}Mn_{1/3}O_2$ compounds, such as cation mixing and volume change during charging–discharging by X-ray and neutron diffraction Rietveld analysis (Fig. 1-7). They found that $Li[Ni_{1/3}Co_{1/3}Mn_{1/3}]O_2$ has as small as 6% cation mixing of all divalent nickel ions. When other transition metals such as cobalt and manganese were assumed to lie on the lithium sites in analysis, a very bad fitting outcome between calculated and measured results was obtained. This means that

cobalt and manganese reside on the transition metal sites, while only nickel ions can move to the lithium site. Similar conclusions were reached in other neutron studies on the Li-Ni-Mn-Co-O system.

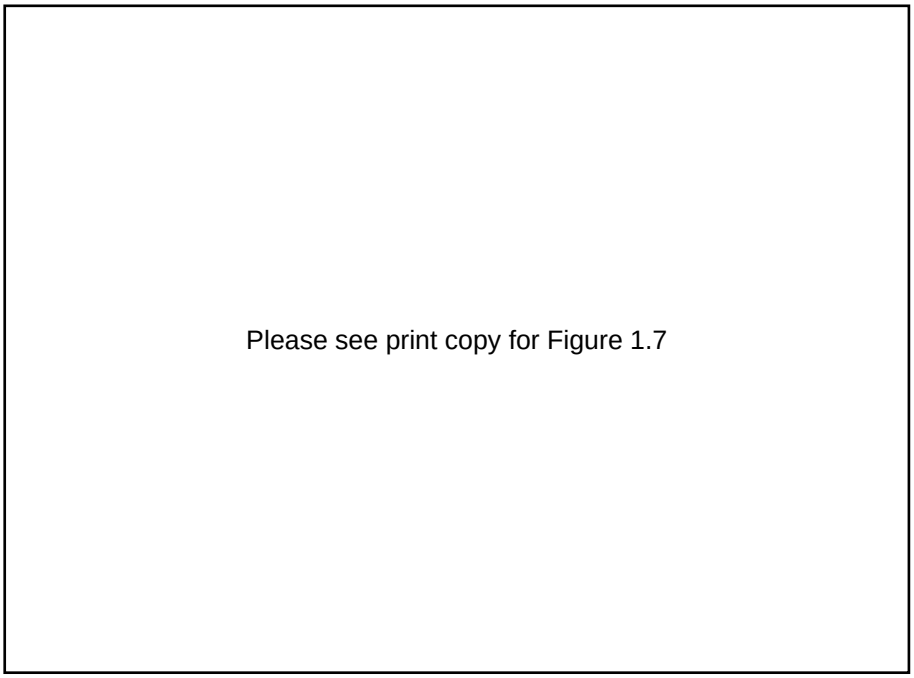

Fig. 1-7. The best Rietveld refinement results of neutron powder diffraction for $Li[Ni_{1/3}Co_{1/3}Mn_{1/3}]O_2$ based on *R*-3*m* [Kim, Chung et al. 2003].

However, the synthesis temperature has a significant effect on the cation mixing behaviour of the $Li[Ni_{1-y-z}Co_yMn_z]O_2$ composition. A sample prepared at 1000 °C then rapidly cooled to ambient temperatures had almost 10% Ni occupancy in the lithium layer [Kim, Chung et al. 2004]. A high Ni content of 5.9% on the Li sites was reported for a $Li[Ni_{1/3}Co_{1/3}Mn_{1/3}]O_2$ composite prepared at 950 °C. Only at 800 °C, did the nickel disorder drop to zero with increasing cobalt content. There is always considerable nickel disorder in the $Li[Ni_{1-y-z}Co_yMn_z]O_2$ composition when the synthesis temperature is higher than 900 °C, even with more cobalt than nickel in the

material. It was found that there was almost 2% more Ni in the lithium layer for samples sintered at 900 ˚C than for those sintered at 800 ˚C. It is obvious that the nickel ion disorder is increased by high temperature preparation; this effect may be reduced by a slow cooling of the sample in an oxidizing environment or a hold at 800 ˚C [Guo, Liu et al 2003].

There have been a number of studies of the physical and bonding behaviour of these tri-transition metal oxides. XPS studies have been made on a number of compositions of these materials, such as $Li[Ni_{1/3}Co_{1/3}Mn_{1/3}]O_2$ [Shaju 2002], $LiNi_{1/2}Mn_{1/2}O_2$ [Cushing, Goodenough 2002], and $Li[Ni_xCo_{(1-2x)}Mn_x]O_2$ (x = 1/4 and 3/8) [Lu, Dahn et al 2002], and all indicated predominantly divalent nickel. The cobalt is trivalent and the manganese is tetravalent. Thus, the electrochemically active species is predominantly nickel, with the cobalt playing an active redox role only in the later stages of lithium removal. The manganese is merely a spectator ion but a critical one as at a minimum it reduces the cost of the cathode.

The structural changes accompanying the removal of Li from $LiNi_{1-y-z}Mn_yCo_zO_2$ have also been intensively investigated. In the case of $Li[Ni_{1/3}Co_{1/3}Mn_{1/3}]O_2$, the change in cell volume is less than 2% as the lithium is removed [Kim and Chung 2004], much less than the 5% reported for $Li_xNi_{3/4}Co_{1/4}O_2$ [Ohzuku, Nakura et al 1999]. This small change in volume was associated with compensating changes in the a and c parameters. When the c parameter increased, the a parameter contracted and vice versa. For sample with the lowest lithium content, $Li_{0.05}Ni_{1-y-z}Mn_yCo_zO_2$, there was a trace amount of the one-block structure (H4) of CoO_2, in contrast to $LiCoO_2$ itself, where large amounts of this structure would be seen. Therefore, it seems that the

2-3% Ni on the lithium sites was impeding the structural reorganization, and thus might be very advantageous for capacity retention. The H4 phase was also found by Croguennec and Pouillerie et al [2000] in their studies on the NiO_2 phases. They found that the H4 phase was only formed for $Ni_{1.02}O_2$ but not for nickel contents above 1.07, suggesting that the NiO_2 slabs are pinned by the extra nickel and thus cannot slide to form the H4 form. They also found that at high potential, part of the H4 phase is irreversibly transformed into a new phase (called R′3) through Ni^{3+} ion migration in the interslab space. Thus, efforts should be made to prevent formation of the H4 structure in nickel-rich compounds to avoid capacity fading.

1.2.1.5.2 Magnetic behaviour of $LiNi_{1-y-z}Mn_yCo_zO_2$

Nalaga and Chernova et al. [2004] found that studies of the magnetic behavior of the $LiNi_{1-y-z}Mn_yCo_zO_2$ compounds could give information about the location of the nickel ions, but studies of the magnetic moment from the Curie-Weiss behavior do not give much information, as the combination Ni^{3+} + Mn^{3+} + Co^{3+} gives an almost the same moment as the combination Ni^{2+} + Mn^{4+} + Co^{3+} [Nagala, Chernova et al. 2004]. In the case of $LiNi_{0.4}Mn_{0.4}Co_{0.2}O_2$, the magnetic susceptibility increases as the temperature falls, and a small turn-down is observed at about 25 K (Fig. 1-8) The inverse magnetic susceptibility exhibits Curie–Weiss behavior above 150 K, while below 150 K the magnetic susceptibility deviates significantly from the Curie–Weiss law, and non-linear magnetization is observed.

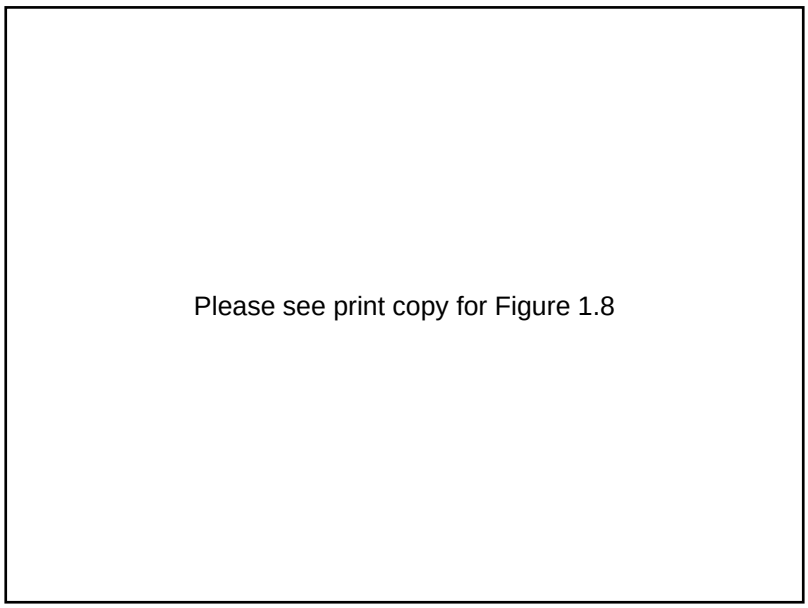

Fig. 1-8 Magnetic susceptibility of $LiNi_{0.4}Mn_{0.4}Co_{0.2}O_2$. The inset shows reciprocal susceptibility[Nagala, Chernova et al. 2004].

The value of the asymptotic Curie temperature, obtained by a fit of the high-temperature part of the $1/\chi_M(T)$ dependence to the Curie–Weiss law, is Θ = –86 ± 0.6 K. A negative Curie temperature indicates rather strong antiferromagnetic exchange. However, Guilmard and Pouillerie et al. [2003] found that the presence of nickel ions in the lithium layer results in a hysteresis loop in the magnetic moment for both the mixed materials $Li(NiMnCo)O_2$ and $Li(NiCoAl)O_2$ [Guilmard, Pouillerie et al. 2003]. They compared the magnetization hysteresis loops for $LiNi_{0.70}Co_{0.15}Al_{0.15}O_2$ with those of $(Li_{0.95}Ni_{0.05})Ni_{0.84}Al_{0.16}O_2$ and $(Li_{0.98}Ni_{0.02})NiO_2$, which were characterized by the presence of 5% and 2% extra-Ni^{2+} ions in the lithium sites, respectively. The residual magnetization observed at zero magnetic field was much smaller for $LiNi_{0.70}Co_{0.15}Al_{0.15}O_2$ than for $(Li_{0.95}Ni_{0.05})Ni_{0.84}Al_{0.16}O_2$ and $(Li_{0.98}Ni_{0.02})NiO_2$, indicating the quasi absence of ferromagnetic interactions for the former and confirming the very small amount of excess-nickel ions in the interslab space (as shown in Fig. 1-9).

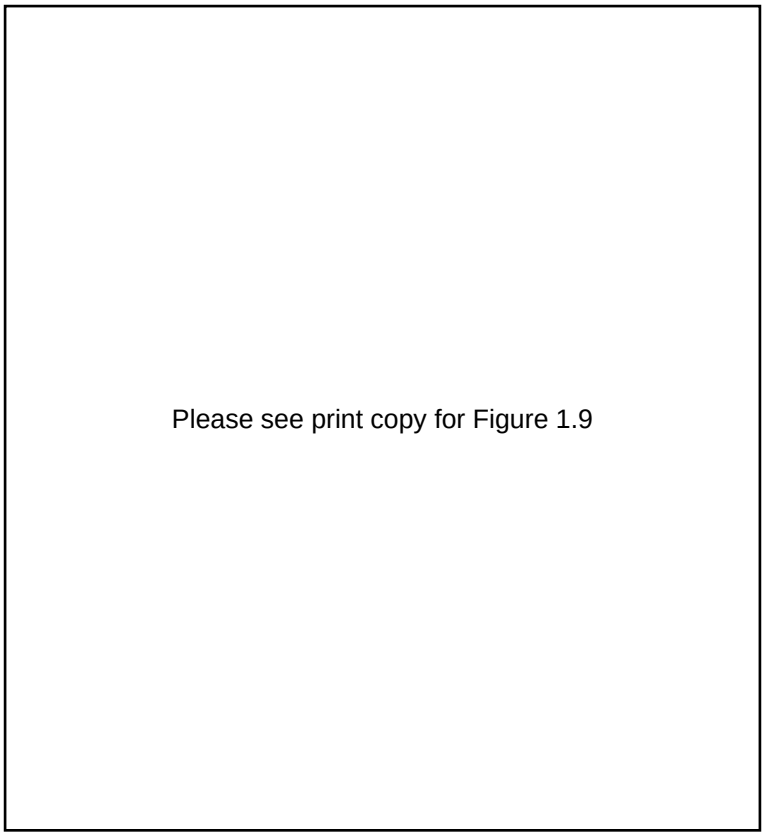

Fig. 1-9. Comparison of the hysteresis loops recorded at 5 K vs. magnetic field for $Li_{0.98}Ni_{1.02}O_2$, $Li_{0.95}Ni_{0.89}Al_{0.16}O_2$ and $LiNi_{0.70}Co_{0.15}Al_{0.15}O_2$. Thermal evolution of the inverse molar magnetic susceptibility (applied field = 10 G) is shown in the inset [Guilmard, Pouillerie et al. 2003].

1.2.1.5.3 Electrochemical behavior of $LiNi_{1-y-z}Mn_yCo_zO_2$

The electrochemical behaviour of a number of different compositions over a range of current densities has been studied. For example, Lu and Dahn et al. [2001] studied $Li[Ni_xCo_{1-2x}Mn_x]O_2$ with x = 1/4 or 3/8 and found that both compositions can deliver a stable capacity of about 160 mAh/g between 2.5 and 4.4 V *vs.* Li using a specific

current of 40 mA/g. If the upper potential of Li/Li[$Ni_xCo_{1-2x}Mn_x$]O_2 cells with x = 3/8 is reduced to 4.2 V *vs.* Li, its capacity retention behavior is improved, and it gives a capacity of 136 mAh/g, which is very close to that of $LiCoO_2$ in the same potential window. They [Lu, Dahn 2002] have also investigated Li[$Ni_xLi_{1/3-2x/3}Mn_{2/3-x/3}$]$O_2$ (900 °C) systems and found that the composition with x = 5/12 can deliver a stable capacity of about 160 mAh/g between 3.0 and 4.4 V *vs.* Li. An irreversible plateau could be observed at about 4.5 V during the first charge of Li/Li[$Ni_xLi_{1/3-2x/3}Mn_{2/3-x/3}$]$O_2$ cells, which was believed to correspond to the simultaneous removal of lithium and oxygen from the structure. After the plateau, Li[$Ni_xLi_{1/3-2x/3}Mn_{2/3-x/3}$]$O_2$ cells with x = 1/3 and 5/12 can deliver stable reversible capacities of about 230 and 225 mAh/g between 2.0 and 4.6 V. Li/Li[$Ni_xLi_{1/3-2x/3}Mn_{2/3-x/3}$]$O_2$ ($0 < x \leq 1/2$) synthesized at low temperatures (*i.e.,* 600 and 700 °C) shows dramatically different differential capacity *vs.* voltage behavior compared to the high temperature samples, which must be related to the structural differences between materials prepared above and below 750 °C. Another sample from Dahn's group [Macneil, Lu et al. 2002], which had only 3.2% Ni on the lithium sites had a lower capacity of 130-135 mAh/g over 50 cycles at 30 mA/g due to only being charged to 4.2 V; increasing the charging potential to 4.4 V increased the capacity by 20-30 mAh/g. This shows the critical effect of the charging potential. Kim and Chung [2004] charged Li[$Ni_{1/3}Co_{1/3}Mn_{1/3}$]O_2 compounds up to 4.7 V and found that there are two plateaus at around 3.75 and 4.54 V, which were responsible for the large charge capacity, ~ 250 mA h/g. They guessed that the lower voltage plateau at around 3.8 V might correspond to the oxidation of Ni ions, but they were not sure what reaction was related to the higher voltage plateau at 4.54 V. Guo and Liu et al. [2003] prepared Li[$Ni_{1/3}Co_{1/3}Mn_{1/3}$]O_2 compounds by using a spray drying technique and reported that the rechargeable capacity for Li[$Co_{1/3}Mn_{1/3}Ni_{1/3}$]O_2

sintered at 800 °C is more than 140 mAh/g, when cells were charged/discharged at current densities of 100 mA/g. The charge/discharge coulombic efficiencies are approximately 99% (as shown in Fig. 1-10).

Rate-capability testing was also done [Guo, Liu et al. 2003]. Fig. 1-11 shows the capacity fade of cathodes as a function of cycle number at different rates. As can be seen, the discharge rate affects the discharge capacity of the cathodes. For the first 25 cycles, capacity fade for cathodes cycled at 1, 2 or 3C remains much the same, but with further cycling, capacity fade diverges. The cell cycled at the 3C discharge rate lost almost 10.4% of its initial discharge capacity while the cells cycled at the 1C and 2C discharge rates, lost 6.9% and 8.7%, respectively, of their initial capacity after 100

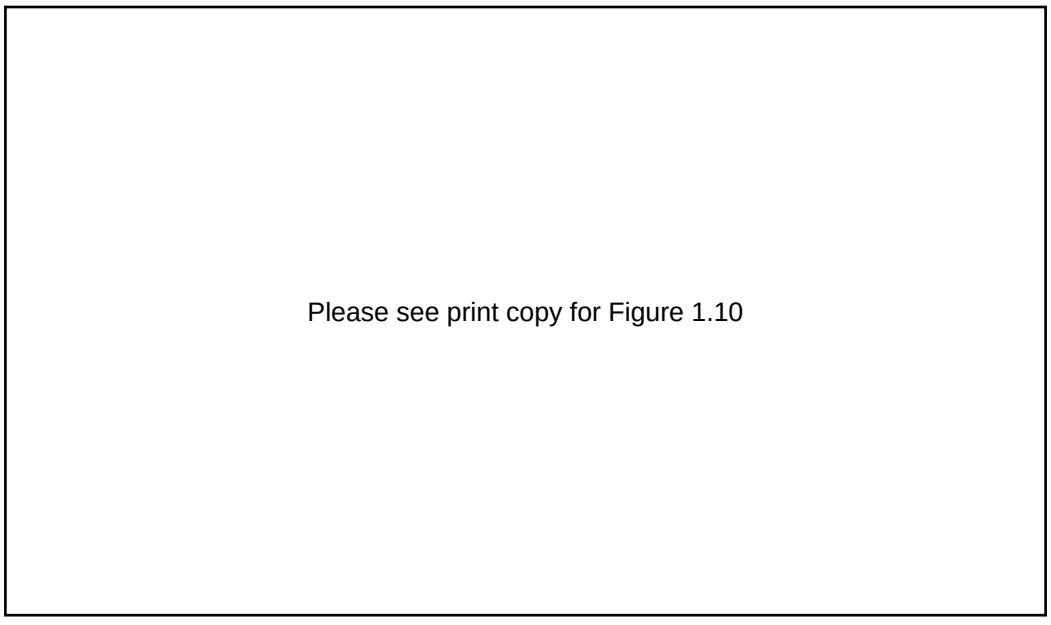

Fig. 1-10 Charge and discharge capacities as a function of cycle number for $Li[Co_{1/3}Mn_{1/3}Ni_{1/3}]O_2$ electrode [Guo, Liu et al. 2003].

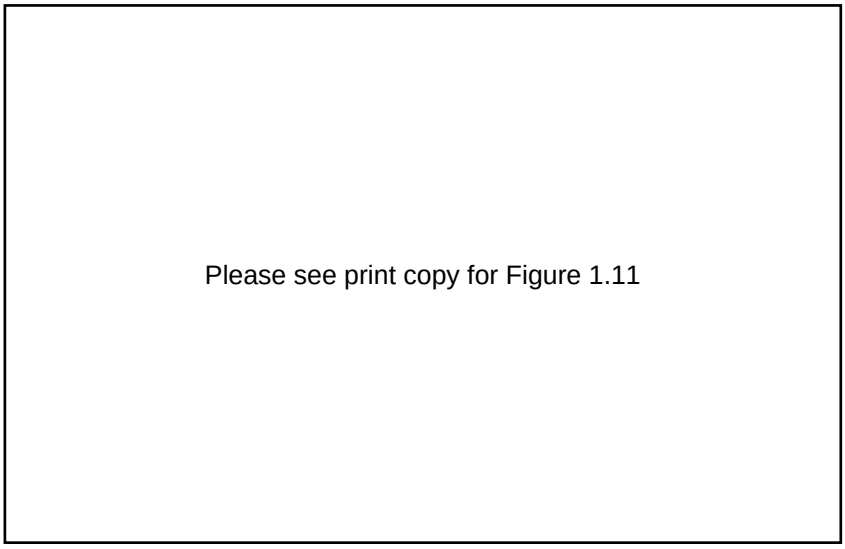

Fig. 1-11 Capacity fade of Li/ $Li[Co_{1/3}Mn_{1/3}Ni_{1/3}]O_2$ cells at different discharge rates. The discharge capacity was checked at the same discharge rate (1C) once every 25 cycles [Guo, Liu et al. 2003].

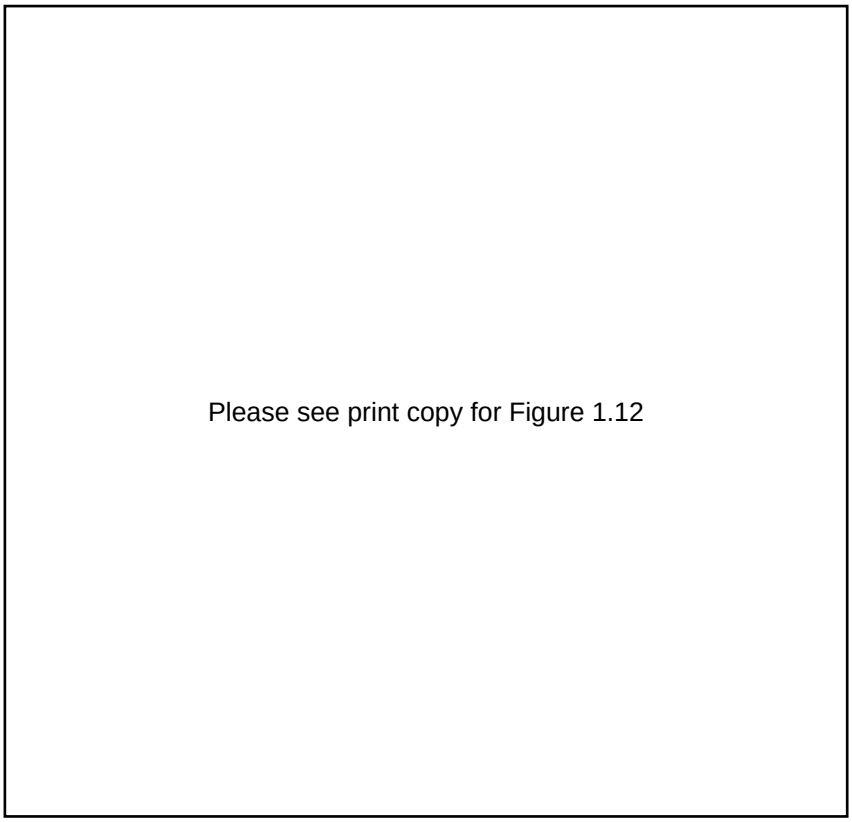

Fig. 1-12 The variation of the discharge capacity of $LiNi_{0.4}Mn_{0.4}Co_{0.2}O_2$ with discharge current density [Ngala, Chernova et al. 2004].

cycles. Further, it is clear from the slope between 50 and 100 cycles, that the rate of capacity fade is faster for 2 and 3 C discharge than for 1C discharge.

Nagala and Chernova et al. [2004] investigated the composition $LiNi_{0.4}Mn_{0.4}Co_{0.2}O_2$ and found that it gave the highest reversible capacity among the compositions studied. It shows excellent rate capability, giving reversible capacities ranging from 180 to 155 mA h/g at current densities from 0.1 to 2.0 mA /cm^2 (Fig. 1-12).

Nagala and Chernova et al. [2004] have also systemically investigated the electrochemical behaviour of the mixed metal oxides ($LiNi_{1-y-z}Mn_yCo_zO_2$), and the results are shown in Fig. 1-13 (current density: 0.1 mA /cm^2; potential window: 2.5–4.3 V; temperature: 22 °C). All the samples had an initial potential of around 3.8 V. The composition $LiNi_{0.4}Mn_{0.4}Co_{0.2}O_2$ showed the greatest capacity on charge, 205 mA h/ g, and one of the lowest capacity losses on recharge (20 mA h/ g at high lithium contents). Pure $LiNiO_2$ showed an initial low capacity of about 165 mA h/g, with a capacity loss on lithium insertion of around 40 mA h/g; the other high Ni content sample also showed a high capacity loss on lithium insertion. Furthermore, Ohzuku and Makimura et al [2001] found a constant capacity for the $LiNi_{0.4}Mn_{0.4}Co_{0.2}O_2$ composition of 175 mAh/g at 0.2 mA/cm^2 (20 mA/g or C/8) for 30 cycles within the potential window of 2.8-4.4 V; this capacity dropped slightly to 170, 165, and 162 mAh/g as the current density increased to 40, 80, and 160 mA/g.

In summary, the $LiNi_{1-y-z}Mn_yCo_zO_2$ compounds have the following cathode characteristics:

(1) The $LiNi_{0.4}Mn_{0.4}Co_{0.2}O_2$ composition has the highest capacity and maintains its capacity on cycling.

(2) Pure $Li_{1-y}Ni_{1+y}O_2$ has the lowest capacity.

(3) The temperature of synthesis is important, with the optimum capacity and capacity retention being found at 800-900 °C, while increasing the synthesis temperature to 1000 °C will induce a much lower capacity.

(4) The capacity increases with increasing charging potential, but in some cases there is marked capacity fade [Kim, Chung 2004]. Normally, a capacity of around 170 mAh/g for at least 50 cycles can be achieved, when cells were cycled between 2.8-4.4 V at 2 mA/cm^2.

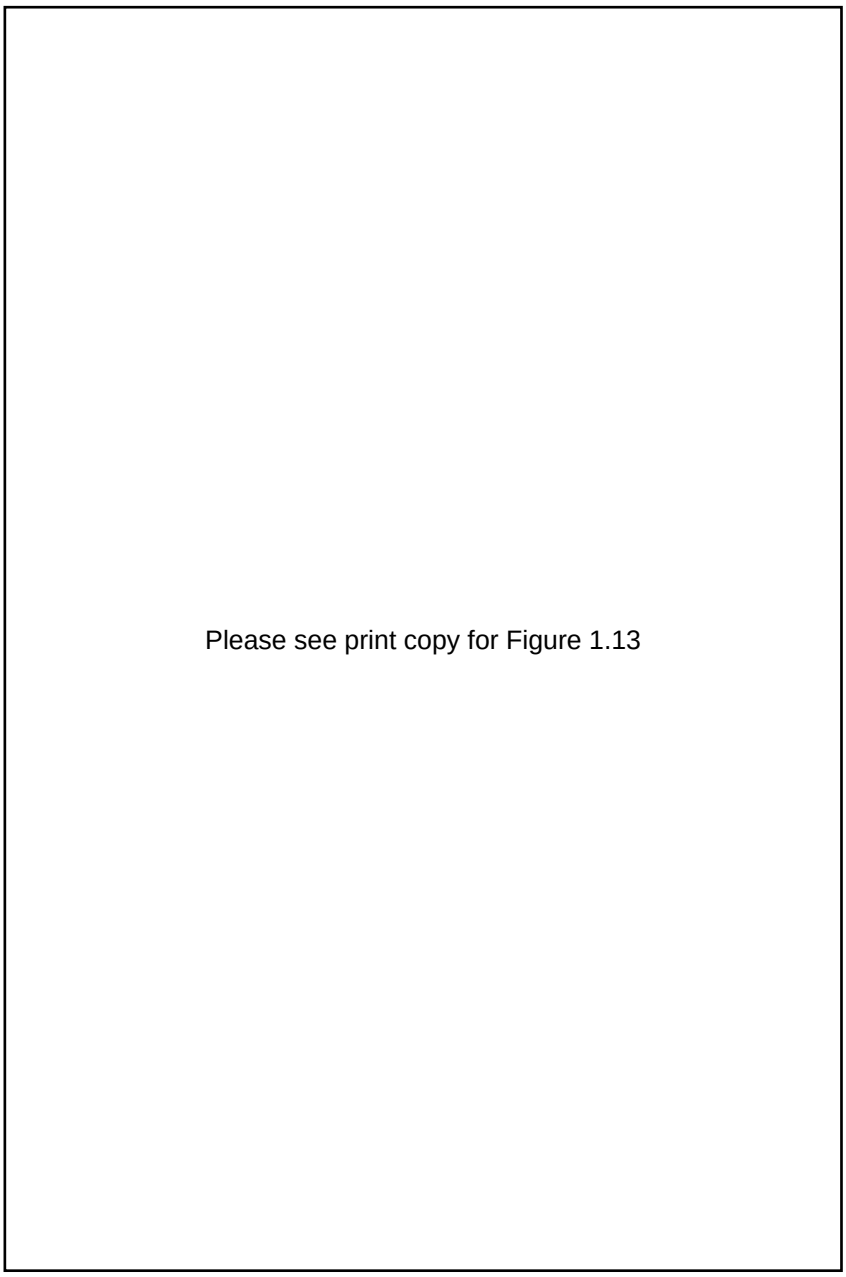

Fig. 1-13 Charge–discharge curves for the layered compounds $LiNi_{1-y-z}Mn_yCo_zO_2$ and $LiNiO_2$, synthesized at 800 °C, from 2.5–4.3 V at 0.1 mA cm^{-2} and 22 °C [Nagala, Chernova et al. 2004].

1.2.2 $LiFePO_4$ and related materials

In the search for new high energy density cathode materials for rechargeable lithium-ion batteries, an iron-based system has been discovered [Padhi, Najundaswamy et al. 1997]. Iron is the fourth most abundant element in the earth's crust, being outranked only by aluminum, silicon, and oxygen. It has been the most important metal in the development of civilization to the present time. From many different aspects, including practical considerations such as low toxicity and low cost, iron is a very attractive metal to use in the lithium battery field for realizing large size batteries for powering electric vehicles or for realizing dispersed electrical power sources. However, for a number of reasons, iron and its derivatives have not met with success as cathode materials. In fact, in the iron-based oxides containing O^{2-} as anion, the Fe^{4+}/Fe^{3+} redox energy tends to lie too far below the Fermi energy with respect to a lithium anode, while the Fe^{3+}/Fe^{2+} couple is too close to it. This problem is caused by the interaction between the electron and the relatively large nuclear charge of Fe and by the high spin configuration of Fe^{3+}. In order to overcome these difficulties, a series of compounds including large polyanions $(XO_4)^{y-}$ (X = S, P, As, Mo, W, y = 2 or 3) were explored by Goodenough's group, and the use of $(PO_4)^{3-}$ and $(SO_4)^{2-}$ has been shown to stabilize the structure and lower the Fe^{3+}/Fe^{2+} redox energy to useful levels [Padhi, Najundaswamy et al. 1997]. The emphasis changed radically in 1997 with the discovery of the electrochemical properties of the olivine phase, in particular $LiFePO_4$, by Padhi and Najundaswamy et al [1997]. This is the first cathode material composed of potentially low cost and plentiful elements that is also environmentally benign and thus could have a major impact in electrochemical energy storage. Its theoretical specific capacity (170 mAh/g) combined with a discharge voltage of 3.45 V vs Li^+/Li, leads to a very high energy density, and moreover, it is very stable during

discharge/recharge; no obvious capacity fading was observed even after several hundred cycles. These findings by Padhi et al. have spurred a great deal of interest in the scientific community, and a number of groups have started to work on this material [Anderson, Haffstrom et al 2000; Yamada, Chung 2001; Franger, Cras et al 2002; Prosini, Carewaka et al 2002].

$LiFePO_4$ compounds have, however, a fundamentally low conductivity at room temperature. It is possible achieve the theoretical capacity only at a very low current density [Yamada, Chung et al 2001] or at elevated temperatures [Anderson, Kalska et al 2000], which is associated with the diffusion-controlled kinetics of the electrochemical process [Croce, Epifanio et al 2001]. Four main ways have been used to bypass the above-mentioned kinetic limitations: the first method may consist in operating at medium-high temperatures. However, due to the obvious temperature constraints, this approach can not be practically extended to lithium ion batteries directed to a wider market. The second is that of improving the electronic conductivity by coating or adding an electronically conductive substance during the synthesis, such as carbon, Cu, Ag, etc. [Huang, Yin et al 2001; Croce, Epifanio 2001]. Third, since the slow lithium ion diffusion in $LiFePO_4$ is the main cause of the poor electrochemical performance, reduction of the grain size could be one of the possible routes to improving the performance of $LiFePO_4$ [Huang, Yin et al 2001]. The last method is that of doping $LiFePO_4$ material with metals supervalent to Li^+, which may increase the electronic conductivity by a factor of ~10^8 [Chung, Blocking et al 2002].

In the following paragraphs, the structure, synthesis, reaction mechanism, and electrochemical performance of $LiFePO_4$ will be described and discussed.

1.2.2.1 The structure and conductivity of $LiFePO_4$

$LiFePO_4$ has an ordered olivine structure in which the Fe cations occupy the M2 sites forming a corner-sharing network of octahedra in the (010) plane, while the Li cations are on M1 sites forming edge-sharing chains of octahedra in the (100) direction (Fig.1-14). The octahedra are connected so as to form the tunnel structure shown in Fig. 1-15. There are tunnels along the b axis, but they are not connected, so the lithium ions residing in the tunnels can not readily jump from one tunnel to another. Thus, the lithium ion diffusion is one-dimensional, which suggests that any blockage in the tunnel will deter the movement of the lithium ions. This is consistent with the pooor electrochemical performance of materials containing iron in these tunnels [Yang, Song et al 2002] and would also suggest that any attempts to dope these materials with aliovalent ions should ensure that these ions do not reside on the lithium sites, but rather on the iron sites.

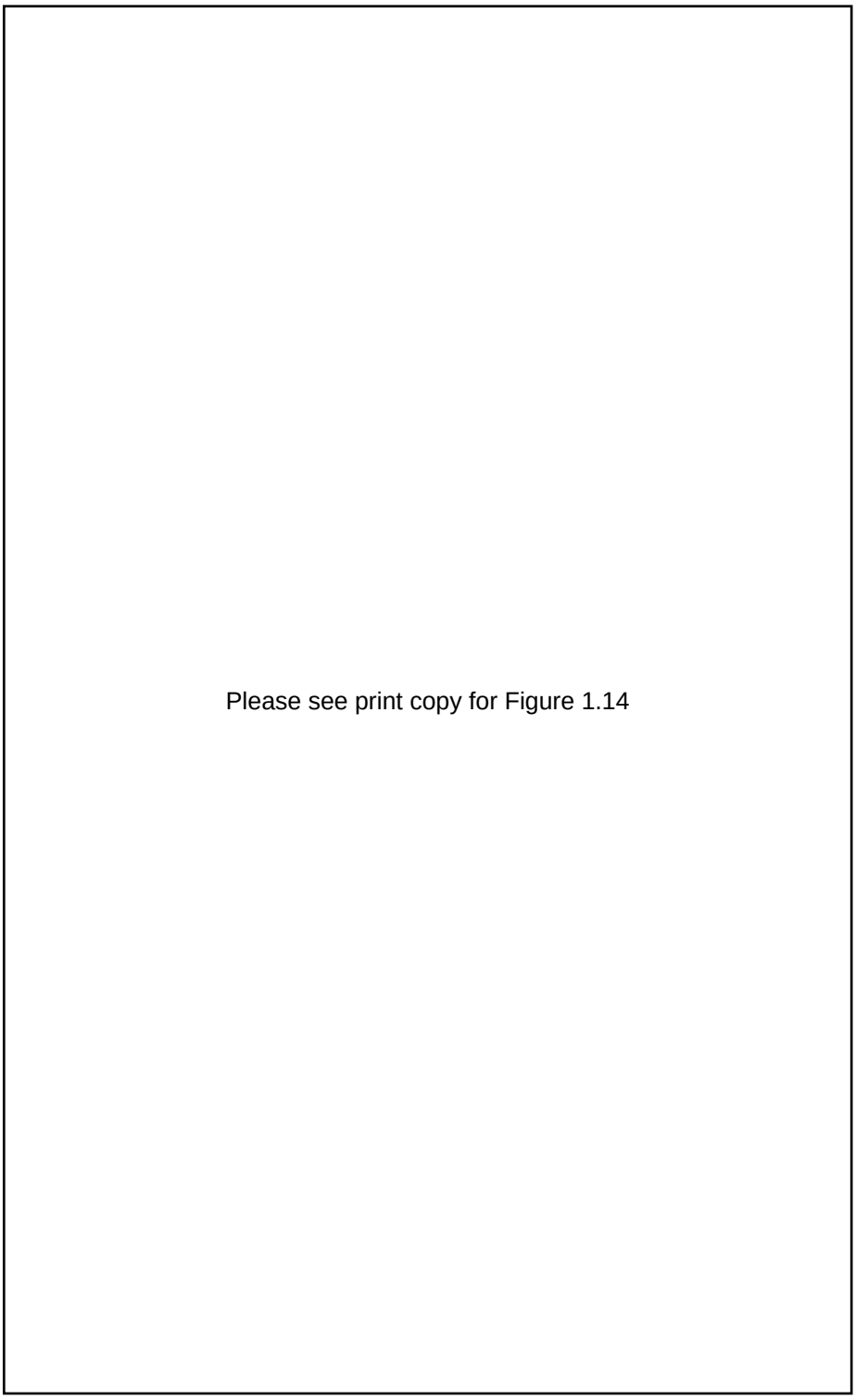

Fig. 1-14 Ordered-olivine structure of $LiFePO_4$: Pmnb space group, with Li in M1 site and Fe in M2 site. (a) Ball-stick model. (b) Depiction of polyhedral connectivity. [Chung, Blocking et al. 2002]

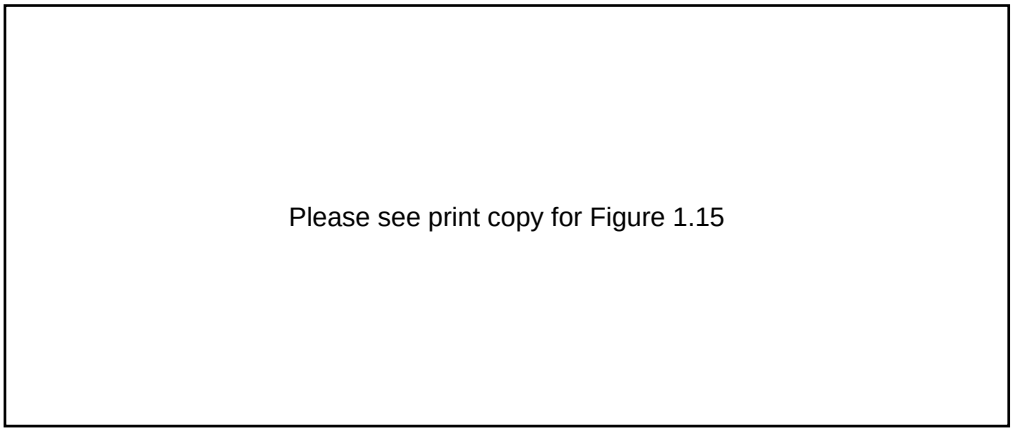

Fig. 1-15 Structures of $LiFePO_4$, $FePO_4$ and $LiMnPO_4$ [Rousse, Carvajal et al. 2003].

In a lithium cell, the electrochemical insertion-deinsertion of lithium ions into $LiFePO_4$ can be described as

$$LiFePO_4 \rightarrow Li_{1-x}FePO_4 + xLi^+ + xe^-$$

In this electrochemical reaction, the Fe^{2+} ions are oxidized to Fe^{3+}, leaving the olivine $FePO_4$ framework intact. Therefore, two separate phases, $LiFePO_4$ and $FePO_4$, exist in the $LiFePO_4$ electrode during charge and discharge of the cell. The exact mechanism of lithium ion motion in these olivine-type structures is still not known, but a general sense of its magnitude can be obtained from conductivity and diffusion coefficient measurements. In pure $LiFePO_4$, there are essentially no electronically conducting species present, so that the total conductivity is less than 10^{-9}S/cm [Chung, Blocking et al 2002]. This conductivity is probably at least partly due to the motion of the lithium ions. Two theoretical calculations have been carried out on the diffusion process in $LiFePO_4$ [Morgan, Vanderven et al 2004; Ouyang, Shi et al 2004], and the

key conclusion is that the activation energy for diffusion is much lower along the b axis, and much higher in other directions. Thus, lithium diffusion is essentially restricted to the tunnels along the b axis, i.e. these olivine structures are one dimensional ionic conductors. It is difficult to measure the diffusion coefficient by standard cathode methods because there is no compositional variation, so what is measured is the movement of the $LiFePO_4/FePO_4$ interface. One experimental study suggests a diffusion coefficient of 2×10^{-14} cm^2/s for $LiFePO_4$ [Prosini, Carewaka et al 2002], and another [Franger, Cras et al 2002] reported a value of around 10^{-13}–10^{-14} cm^2/s over the whole range of composition for $LiFePO_4$. These values are consistent with conductivity values of less than 10^{-9} S/ cm for pure compounds. A measurement of the intrinsic ionic conductivity would be desirable, probably using the methods appropriate for a solid electrolyte.

Many $LiFePO_4$ samples are prepared using carbon containing precursors, such as oxalates, acetates or carbonates, which result in some residual carbon in the reducing atmospheres used to prevent the formation of ferric ions. These samples typically have much higher conductivities, around 10^{-5}–10^{-6} S/cm [Yang, Song et al 2003], but these are still too low for high power battery applications. Ravet and Goodenough et al. [1999] showed that a carbon coating significantly improves the conductivity of this material; sucrose was proposed [2000] as one carbon precursor, and it was used on the initial hydrothermal samples [Yang, Zavalij et al 2001]. Silver and copper have also been used in improving the electronic conductivity of the $LiFePO_4$ particles [Herle, Ellis et al 2004; Croce, Epifinio et al 2002]. Inspired by the appreciable electronic conductivity at high temperatures in $(Mg, Fe)_2SiO_4$ and the existence of other corner-sharing transition metal oxides having high electronic conductivity near room

temperature and below, Chung and Blocking et al [2002] controlled cation nonstiochiometry in combination with solid-solution doping by metals supervalent to Li^+ to increase the electronic conductivity of $LiFePO_4$ (10^{-9} to 10^{-10} Scm^{-1}) by eight orders of magnitude to 10^{-2} Scm^{-1}. They proposed a two-phase model to explain the electronic behavior of doped $LiFePO_4$, in which the relative proportions of the two phases with Fe^{3+}/Fe^{2+} character (one with p-type conductivity and one with n-type conductivity) change according to the charge state of the cell. They propose that the cation and charge distribution would be $Li^+_{1-a-x}M^{3+}_x(Fe^{2+}_{1-a+2x}Fe^{3+}_{a-2x})[PO_4]$, in which x represents the amount of M^{3+} dopant on the lithium site, and the sum of a and x is the lithium deficiency. During charging of the cell, the extraction of lithium from the lattice would yield an electronically conducting phase, $M^{3+}_x(Fe^{2+}_{3x}Fe^{3+}_{1-3x})[PO_4]$, with mixed-valence $Fe^{3+/2+}$ character. However, a recent paper by Nazar et al. [Herle, Ellis et al 2004] has shown that the conductivity increase is related to the formation of a highly conductive iron phosphide, Fe_2P, surface film; this film is formed at high temperature, particularly in the presence of a reducing agent such as carbon.

1.2.2.2 Synthesis and electrochemistry of $LiFePO_4$

There have been an exponentially increasing number of papers describing the synthesis and electrochemistry of $LiFePO_4$. Traditionally, $LiFePO_4$ compound is made by using the solid-state reaction of $Fe(CH_3CO_2)$, $NH_4H_2PO_4$, and Li_2CO_3 [Anderson, Haffstrom et al 2000] in an inert gas atmosphere. The ingredients are thoroughly mixed and ground, then decomposed at low temperature (for example 300°C) to expel the gases. After regrinding, the mixture is sintered at high temperatures in the range of 400 °C to 800 °C. However, trivalent Fe_2O_3 or $Li_3Fe_2(PO_4)_3$ has been detected in samples synthesized below 700 °C. Researchers have reported that sintering above

800 °C is necessary to obtain single phase $LiFePO_4$. However, Yamada and colleagues found that homogeneity of the starting materials was critical for low temperature synthesis below 700 °C [Yamada, Chung et al 2001]. They dispersed the starting materials into acetone before thoroughly mixing and regrinding, and obtained single phase olivine from 320 to 800 °C. On the other hand, to improve the electronic conductivity of $LiFePO_4$, $LiFePO_4$/C composite was prepared by mixing precursors with carbon gel [Huang, Yin et al 2001], graphite, carbon black, partially oxidized carbon [Huang, Yin et al 2001], or organic compounds such as sucrose [Franger, Cras et al 2002]. Huang and Yin et al. [2001] proposed coating the material with carbon-gel during the synthesis step and found that the complete utilization of the $LiFePO_4$ could be achieved at low loadings; they also obtained 800 cycles at around 120 mAh/g at high rates. Masquelier proposed [2001] extensive milling of the material with carbon and then found high capacities at elevated temperatures. A nanocomposite consisting of monodispersed nanofibers of $LiFePO_4$ electrode material mixed with an electronically conductive carbon matrix delivered almost 100% of its theoretical discharge capacity at the high discharge rate of 3C, and 36% of its theoretical capacity at the enormous discharge rate of 65 C [Howing, Gustafsson et al 2003]. This new nanocomposite electrode shows such excellent rate capabilities because the nanofiber morphology mitigates the problem of slow Li^+ transport in the solid state, and the conductive carbon matrix overcomes the inherently poor electronic conductivity of $LiFePO_4$. Hence, what is needed is a good continuous conductive surface coating that does not reduce the effective packing density of the cathode material [Chen, Dahn et al 2002] and can allow the passage of lithium ions; thus, many approaches can lead to similar electrochemical reactivities [Yang, Song et al 2003].

The solution synthesis routes have also been investigated. Franger and Cras et al. [2002] obtained pure, well crystallized, and homogeneous small particles of $LiFePO_4$ via hydrothermal synthesis using $Fe_3(PO_4)_2.5H_2O$ and Li_3PO_4 as starting materials. To improve the efficiency of the electronic transfer, they also hea-treated the $LiFePO_4$ powder under nitrogen in the presence of an organic compound (typically a sucrose) to deposit a thin layer of carbon on the particles. Prosini and LiSi et al [2002] obtained amorphous $LiFePO_4$ material by lithiation of $FePO_4$ synthesized by spontaneous precipitation from equimolar aqueous solutions of $Fe(NH_4)_2(SO_4)_2.6H_2O$ and $NH_4H_2PO_4$ using hydrogen peroxide as the oxidizing agent. They then heat-treated the amorphous $LiFePO_4$ to obtain nanocrystalline $LiFePO_4$. Croce et al. [1997] prepared $LiFePO_4$ cathode material by a sol-gel route using either acetates or nitrates as precursors. For the synthesis of the $LiFePO_4$ material, a solution of LiOH and $Fe(NO_3)_3$ was added to ascorbic acid and then to H_3PO_4. The ascorbic acid is able to reduce Fe^{3+} to Fe^{2+}, thus avoiding the use of the generally very expensive Fe^{2+} precursors. To improve the kinetics of the $LiFePO_4$ material, they dispersed metal powder (copper or silver) at a very low concentration (1wt%) in the solution and obtained metal-added $LiFePO_4$ samples [Croce, Epifanio et al 2002].

As discussed above, a number of carbons have been studied to optimize carbon sources and carbon content, as well as the method of carbon coating. For carbon black, little difference was observed for carbon loadings from 6 to 15%, except that the polarization observed was slightly higher at low carbon content. The method of carbon addition, whether carbon black, carbon gel, sugar or aqueous gelation, [Dominko, Gaberscek, et al 2001] did not appear to be important. However, the temperature of sintering appears to be much more important as that determines the

amount of graphitic compound on the $LiFePO_4$ surface; sp^2 carbon was found to be much more effective than sp^3 carbon [Doeff, Hu et al 2003]. The particle size is also controlled by the temperature and carbon content in the reaction mixture.

The electrochemical properties of $LiFePO_4$ such as capacity and rechargeability vary with different synthesis routes. The typical electrochemical behavior of $LiFePO_4$ is shown in Fig. 1-16.

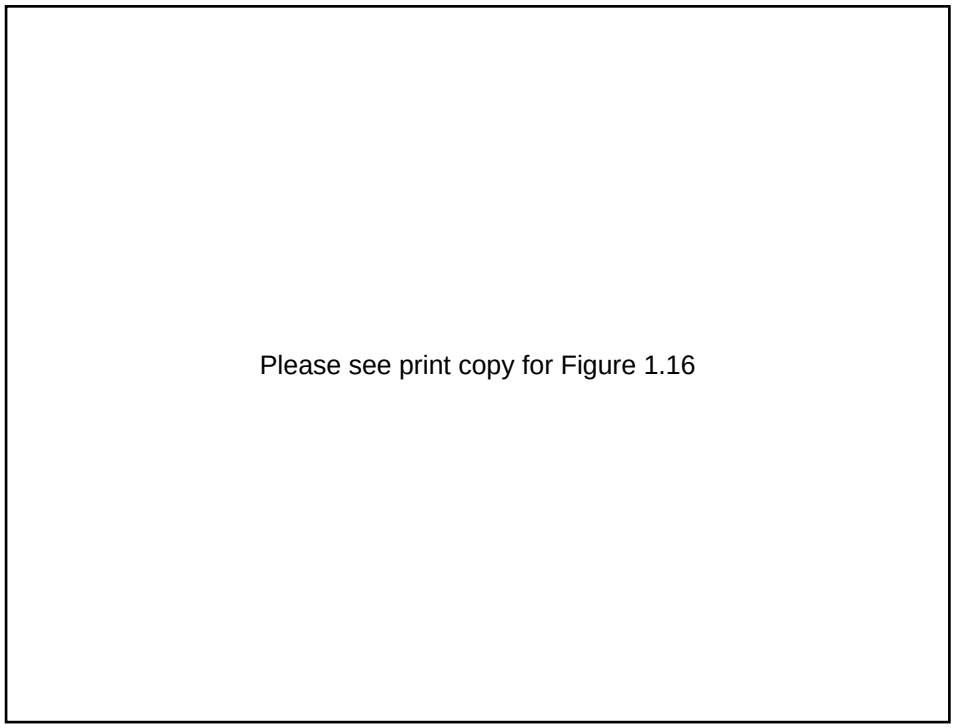

Fig. 1-16 Typical electrochemical behavior of $LiFePO_4$ [Whittingham, Song et al. 2005].

Capacities approaching the theoretical capacity can be obtained at either low rates or at slightly elevated temperatures around 60 °C. When $LiFePO_4$ is cycled between

limits of 2.5 to 4.0 V, excellent capacity retention is maintained over hundreds of cycles. However, outside of these limits other phases might be formed. For example, an electrochemical study [Yang, Song et al 2002] where the $LiFePO_4$ cathode was subjected to a discharge down to 1.0V confirmed that under these conditions lithium reacts to destroy the $LiFePO_4$ lattice, resulting in considerable loss of capacity. After five cycles the capacity had dropped by 80%. Thus lithium iron phosphate cells will require overdischarge protection in commercial applications.

1.2.2.3 $LiMn_yFe_{1-y}PO_4$

Driven by the result of Padhi and Goodenough et al. [1997] that the potential of the Mn^{3+}/Mn^{2+} transition is at 4.1 V vs Li^+/Li in the olivine compound $LiMn_yFe_{1-y}PO_4$, several research groups studied the cycling behavior of the pure $LiMnPO_4$ compound [Yamada, Chung et al 2001; Li, Azuma et al 2002]. The results are controversial: Yamada and Chung et al. [2001] related the inability to extract lithium from $LiMnPO_4$ electrochemically to the thermodynamic instability of olivine-type $MnPO_4$ due to the Jahn-Teller effect of Mn^{3+}. Delacourt and Poizot et al. [2004] prepared $LiMnPO_4$ by direct precipitation and obtained a reversible capacity of 70 mAh/g after carbon coating by ball milling the materials with carbon black. This suggests that $MnPO_4$ is thermodynamically stable. However, Li and Azuma et al. [2002] reported a reversible capacity of about 140 mAh/g for the reaction between $LiMnPO_4$ and $MnPO_4$. Song and Zavalij et al. [2005] studied $LiMnPO_4$ formed from the thermal decomposition of $LiMnPO_4$-(OH), and found that the Mn^{3+}/Mn^{2+} transformation occurs at about 4.1 V with a high polarization and low capacity; heating with carbon black did not result in any dramatic enhancement of the capacity. For the $LiMn_yFe_{1-y}PO_4$, there are two voltage plateaus in the discharge curve [Li, Azuma et al.

2002]. The 4.1 V plateau corresponds to the Mn^{3+}/Mn^{4+}potential, while the 3.4 V plateau relates to the redox potential of Fe^{3+}/Fe^{4+} vs Li/Li^{+}. Systemical study of the electrochemical charge and discharge characteristics of $LiMn_yFe_{1-y}PO_4$ (y = 0, 0.25, 0.5, 0.75) have shown that the width of the 4.1 V plateau (Mn^{3+}/Mn^{4+}) relative to that of the 3.4 V plateau (Fe^{3+}/Fe^{4+}) increases as the Mn content y is increased (Fig. 1-17). However, the total capacity decreases rapidly at y > 0.8 due to an abrupt increase in the polarization [Padhi, Goodenough et al. 1997]. $LiMn_yFe_{1-y}PO_4$ with high y value is obviously not suitable for use as a cathode material in lithium-ion batteries.

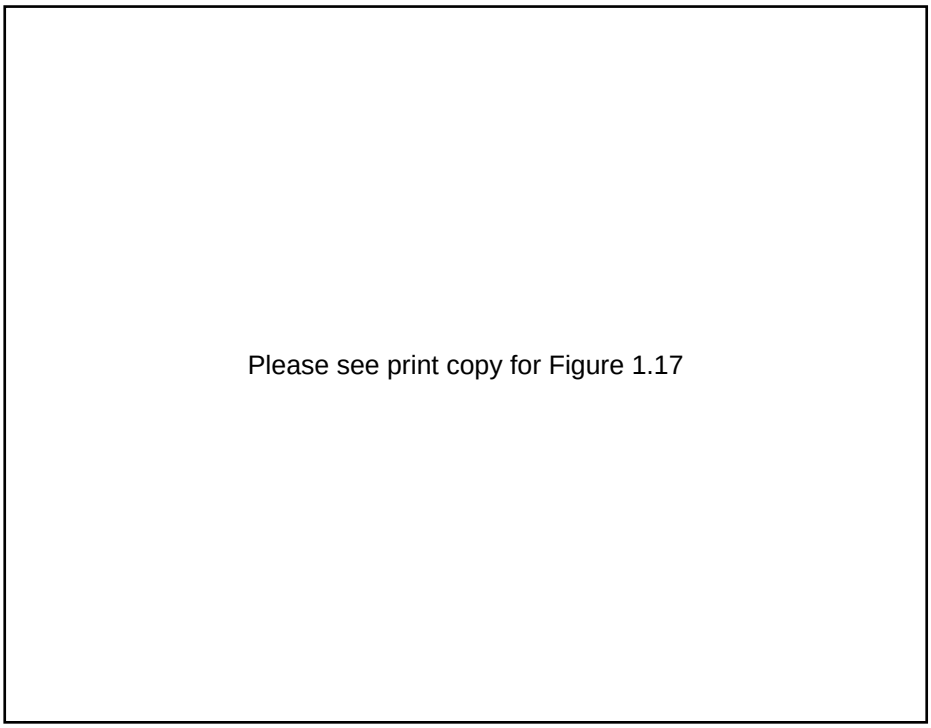

Fig. 1-17 The typical discharge curves of carbon-containing $LiMn_yFe_{1-y}PO_4$ (y = 0, 0.25, 0.5 and 0.75). [Li, Azuma et al. 2002]

Yamada and Chung et al. [2001] have interpreted this phenomenon from the structural aspect. They found that the unit-cell volume for $LiMn_yFe_{1-y}PO_4$ increases as y increases, while the volume is almost constant in the $Mn_yFe_{1-y}PO_4$ seires (Fig. 1-18).

In the $Mn_yFe_{1-y}PO_4$ system under constant volume conditions, strain energy is accumulated in the lattice and may induce lattice frustration, which makes the Mn-rich phase ($x > 0.8$) inaccessible [Yamada, Chung et al. 2001]. In addition, the larger effective mass of the polaronic electrons around Mn^{3+} would also increase the polarization and promote the inaccessibility [Shimakawa, Murata et al. 1997].

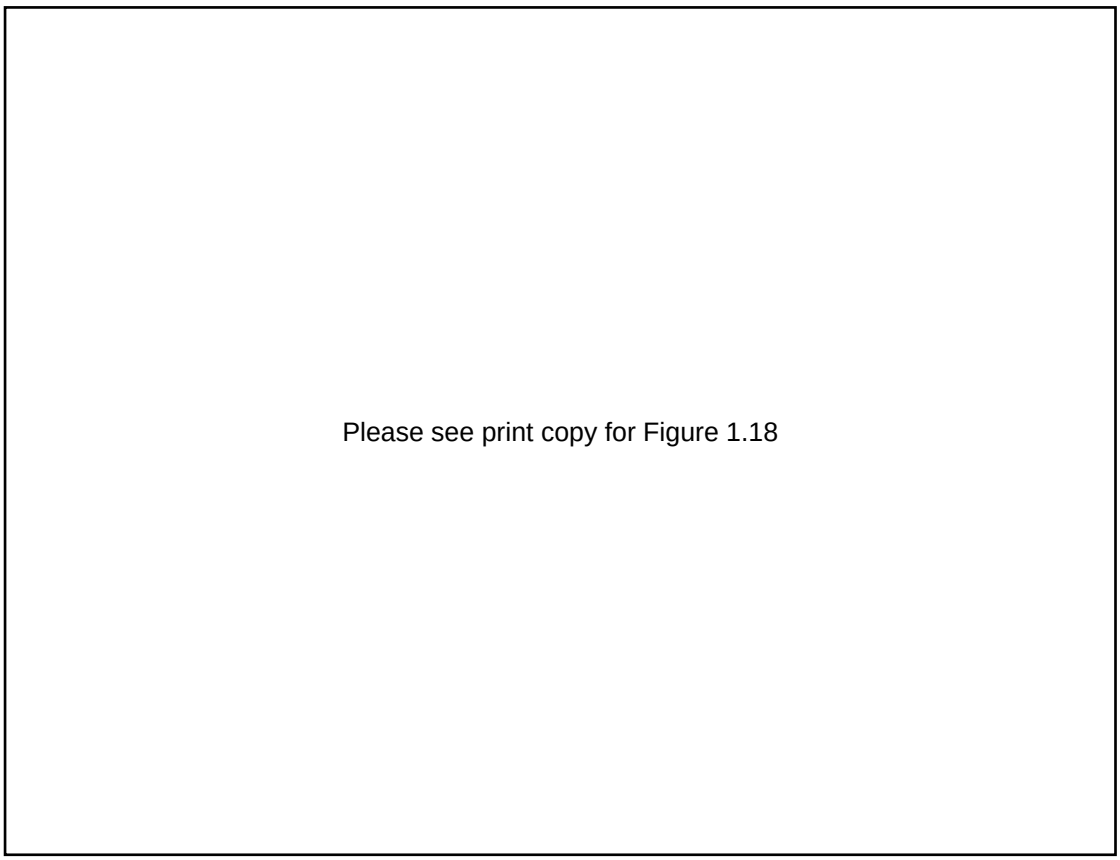

Fig. 1-18. Change in the unit cell volume as a function of Mn content *y* in $Li(Mn_y^{2+}Fe_{1-y}^{2+})PO_4$ (open circles, discharged state) and $(Mn_y^{3+}Fe_{1-y}^{3+})PO_4$(closed circles, charged state). The data for $(Mn_{0.8}^{3+}Fe_{0.2}^{3+})PO_4$ is not connected by a solid line because it includes non-olivine phase, which was observed by Mössbauer spectroscopy, but not by XRD. [Yamada, Chung et al. 2001]

Excellent $LiMn_yFe_{1-y}PO_4$ cathode performance can be achieved with strategic design consideration of the electrode powder and its composition [Hosoya, Takahashi et al.

2002; Yamada, Chung et al. 2001]. Li and Azuma et al. [2002] have synthesized $LiMn_yFe_{1-y}PO_4$-C using a solid-state reaction. They found that carbon-containing $LiMn_yFe_{1-y}PO_4$ has very good electrochemical performance. Even at the large Mn content of y = 0.75, a high capacity of 164 mAh/g has been achieved with an average discharge voltage of 3.63 V (595Wh/kg) at room temperature. Carbon additives have three important functions: (1) as a reducing agent to avoid formation of trivalent phases at moderately low sintering temperatures [Yamada, Chung et al. 2001]; (2) to block inter-particle contacts and disturb the consequent undesirable particle growth [Yamada, Chung et al. 2001]; and (3) to enhance the intra- and inter-particle electronic conductivity [Ravet, Goodenough et al. 1999]. As pointed out by Huang and Yin et al. [2001], a homogeneous electrode with minimum particle size and intimate carbon contact is required for efficient charge transport.

1.3 Anode materials for lithium ion batteries

Research in the field of ambient temperature rechargeable batteries has achieved significant growth in the last three decades. Lithium batteries provided an apparent solution to the energy density problem due to the low atomic weight of lithium metal and the high voltages obtained. However, rechargeable lithium batteries were unsuccessful in the early trials. The main reason was the safety problem caused by using a lithium metal anode. On discharge, the lithium atoms passing to the electrolyte in the form of Li^+ ions leave surface regions of the metal surface, which are not coincident with those in which lithium atoms are deposited during charge. This phenomenon leads to a marked complexity of the metal surface, with an increased growth in the areas exposed to the electrolyte. Increasing surface area leads to two unwanted effects: first an increase in the reactivity with the electrolyte, which in turn

leads to a larger consumption of the latter in side reactions, with a decreased cycling efficiency and cell capacity, while increasing the internal cell temperature. Second dendrite growth takes place towards the cathode after several tenths of cycles. The final result may be that dendrites perforate the separator and reach the cathode, leading to an internal short-circuit with a sudden increase in temperature, which may have explosive results.

The problems relating to the use of lithium metal anodes can be overcome by using lithium insertion anode materials. Scrosati and coworkers [Lazzari, Sacrosati 1980; Pietro, Patriarca et al. 1982] introduced the term "rocking-chair" batteries during 1980s. In this pioneering concept, both electrodes reversibly intercalate lithium and show a back and forth motion of their lithium-ions during cell charge and discharge. The most common anode materials are lithium-carbon-based materials (hard carbons, soft unorganised carbons and graphite or graphitised material), intermetallic lithium alloys and transition metal oxides. Some oxides such as $Li_4Ti_5O_{12}$ and lithium perovskites also can reversibly react with lithium at relatively low potentials (around 1.0 V versus lithium). These compounds may be used as anode materials in lithium-ion cells but with some sacrifice of the energy density.

The requirements for the anode materials are:

1. The potential must be as low as possible;
2. The amount of lithium which can be accommodated by the anode material should be as high as possible to achieve a high specific capacity;
3. The anode hosts should endure repeated lithium insertion and extraction without any structural damage to obtain long cycle life.

1.3.1 Carbon-based materials

There are hundreds of commercially available carbon types, including natural and synthetic graphite, carbon blacks, active carbons, carbon nanotubes and fibres, cokes, and various other carbonaceous materials prepared by the pyrolysis of organic precursors in inert gas atmosphere. For use as anode materials for lithium ion batteries, three groups of carbon can be considered, i.e. hard carbons, soft unorganised carbons, and graphite and graphitised material.

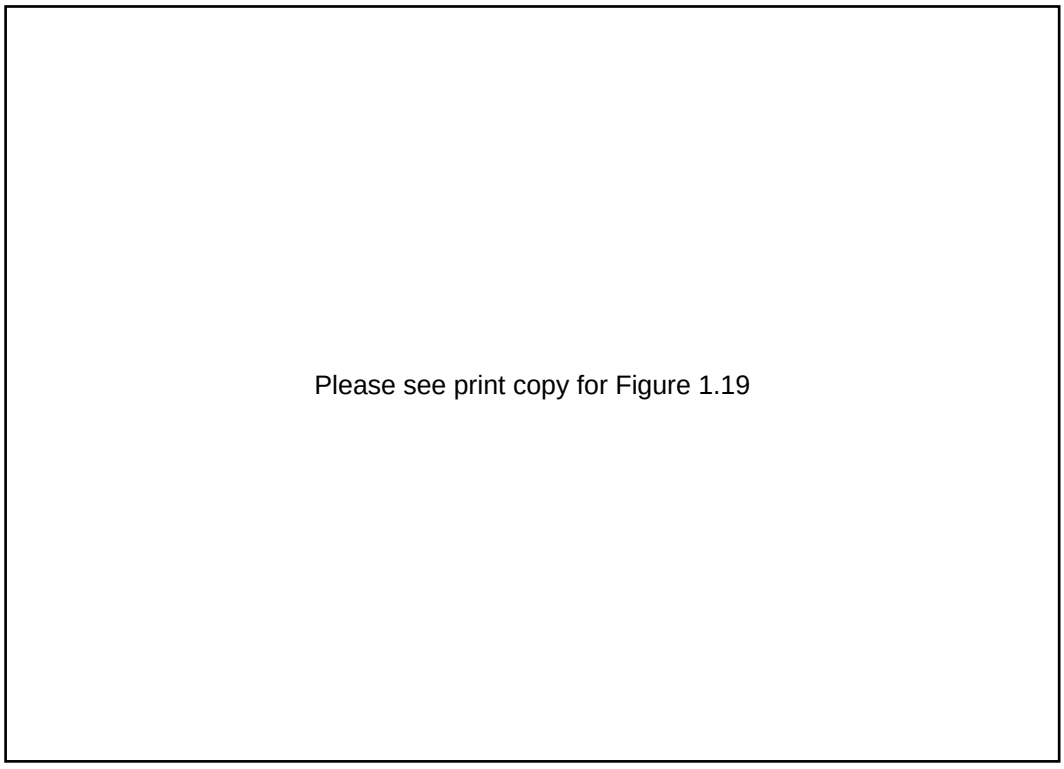

Fig. 1-19 Levels of organization in carbon-based materials: (a) stacking of graphene layers in two crystalline modifications; (b) stacking faults and turbostratic stacking; (c) falling cards model [Dahn, Xing et al. 1997] and curved layers [Tirado 2003].

Graphitic carbons are normally prepared by heating so-called soft carbon precursors

to temperatures above 2400 °C, where well graphitised materials result. Unorganised carbon is normally prepared by pyrolyzing organic precursors at different temperatures [Larcher, Beaulieu et al. 2000]. The structure and chemistry of carbons strongly depends on the procedures for heating the organic precursors. During the early stages of pyrolysis in inert gas (below 600 °C), organic compounds decompose and emit gases that contain carbon such as Co and CH_4. The remaining C atoms condense into planar aromatic structures (graphene sheets). If the decomposing precursor forms a semifluid state, then these planar sheets can align in a more parallel fashion that leads to easy graphitisation when heating to very high temperatures. Such precursors yield "soft" carbons. However, if the organic precursor is cross-linked, then the planar aromatic structure can not align during any further heating process. Therefore, these carbon materials are difficult to graphitize at high temperature and are called "hard" carbons. The level of disorder of the carbon has a direct effect on the mechanism of the reaction with lithium. A true intercalation only takes place in crystalline, hexagonal or rhombohedral forms of graphite (Fig. 1-19a). The theoretical capacity is 372 mAh/g based on the reaction to from the LiC_6 compound:

$$Li^+ + 6C + e^- \rightarrow LiC_6$$

However, the charge consumed in the first intercalation usually exceeds the theoretical capacity, i.e. 372 mAh/g for the formation of LiC_6. This is generally regarded as caused by a side reaction involving the decomposition of electrolyte. The decomposition of electrolyte has been attributed to the exfoliation of graphite, thus inducing irreversible capacity. A passivation layer is formed on the electrode surface during the first intercalation, which is called the solid electrolyte interface (SEI). The SEI layer is electronically insulating, but ionically conducting, which prevents further electrolyte decomposition while allowing ionic transfer. The formation of the

passivation layer is an essential effect in assuring the stability and cyclability of the carbon electrode, since it provides the conditions for the desired electrochemical reactions even at voltage levels which fall well below the limit of stability of the most common electrolyte. In addition, besides lithium intercalation, solvent co-intercalation may occur with large interlayer expansion, leading to the degradation of the graphite structure and loss of electrode performance. Fortunately, such a problem could be solved by choosing a good solvent for the electrolyte or by adding a lithium chelating reagent, such as one of the crown ethers.

For soft carbons heat-treated below graphitisation but above 1000 °C, a turbostratic structure can be obtained. Since there is disorder between the graphene layers, lithium can not be accommodated in the interlayer space, and only low capacities can be obtained for these materials (Fig 1-19b) [Dahn, Zheng et al. 1995; Alcantara 1996,2002].

Hard carbons and soft carbons heat-treated below 1000°C show a very different mechanism of reaction in which surface effects and pores (Fig. 1-19c) play a major role [Alcantara 1996, 2002; Dahn, Xing et al 1997]. In contrast to graphite, the cycling profile of these materials shows no evidence of staging plateaus but rather continuous charge/discharge curves sloping between 1.2 V and 0.2 V [Vaughey, Kelper et al. 2000]. It is believed that the intercalation of lithium in these materials corresponds to the filling of micro-pores in the carbon by clusters of lithium, thus producing weakly bound lithium and giving a very low plateau consistent with experimental results. These carbons consisted primarily of small single layers of carbon arranged more or less like a house of cards (Fig. 1-19c), so that lithium can be

absorbed on both surfaces of these single sheets, leading to more lithium per carbon than in intercalated graphite. For example, total capacity above 750 mAh/g has been reported. In addition, the intercalation process in these electrodes does not promote formation of the staging phases, and due to their lack of crystallinity, these electrodes are not as sensitive to the nature of the electrolyte as is the case for the graphite electrodes. Electroplating and passivation are less important factors for these materials.

As a result of numerous chemical (pyrolitic processing) or physical (mechanical milling) modifications, carbon negative electrodes display electrochemical performances that are continuously improving. In parallel, ongoing research efforts are focused on searching for carbon alternatives in the hope of finding materials with both larger capacities and slightly more positive intercalation voltages compared to Li/Li^+, so as to minimize any risks of high-surface-area Li plating at the end of fast recharge, which is associated with safety problems. A large number of alternative possibilities for the anode of the lithium ion cell have been recently reported in the literature. The diversity in chemical elements and reaction mechanisms clearly demands a systematic study.

1.3.2 Tin-based anode materials

Throughout the search for carbon alternatives, much effort has been devoted to the use of Li alloys. The first commercial cell was introduced in the 1980s by Matsushita: this was based on Wood's metal (a low-melting alloy of Bi, Pb, Sn and Cd), whose cycling performance was found to deteriorate with increased depth of discharge. The theoretical lithium uptake capacity of different elements can be referred to the

composition of the highest Li-content phase [Foster, Crouthamel et al. 1966; Wen, Huggins 1981]. As shown in Fig. 1-20, elements from groups 13–16 of the periodic table have capacity values well above LiC_6.

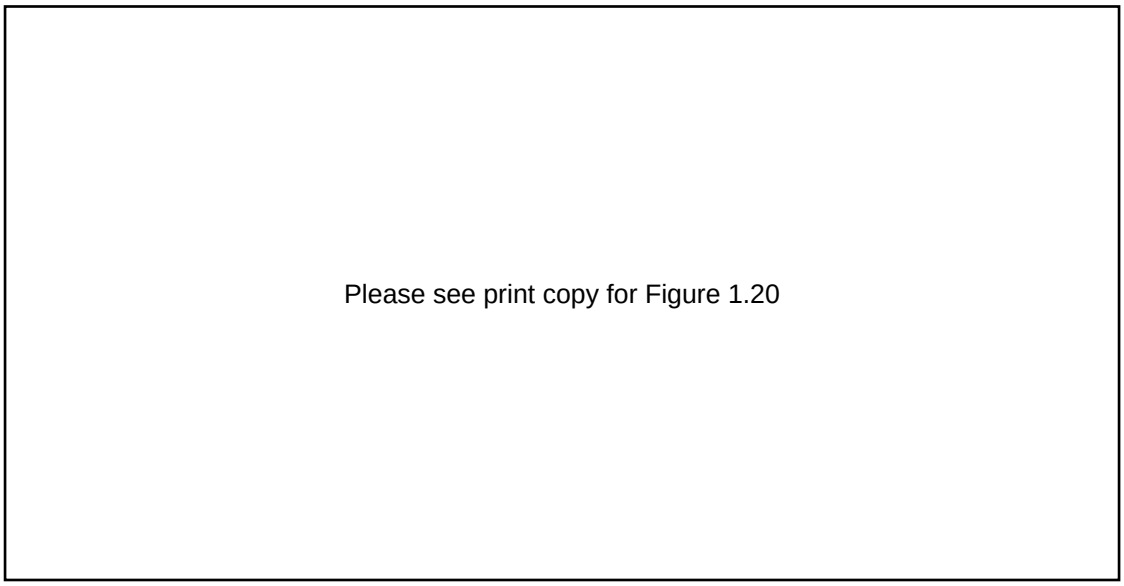

Fig. 1-20 Theoretical capacity resulting from the formation of end compounds of lithium with different elements of groups 13–16. For N and O, a third element to fix nitrogen or oxygen is needed (not included in the calculation). Volume expansion is from the solid elements [Beaulieu, Eberman et al. 2001].

The main problems associated with the use of lithium alloys instead of lithium in rechargeable batteries at room temperature are caused by the colossal changes [Beaulieu, Eberman et al. 2001] in volume from the pure metals to the intermetallic compounds (Fig. 1-20). The molar volume increases by a factor of three in some cases, while the difference with graphite is below 10% for LiC_6. In consequence,

successive charge–discharge cycles lead to mechanical stresses in the electrode and it finally fractures. The divided material loses electrical contact between the particles, which causes a sharp decrease in capacity. Although a reduction in alloy particle size clearly benefits the cyclability by increasing tolerance to stress cracking, so far the gains are not sufficient [Winter, Besenhard 1999]. However, it became clear that any physical or chemical means of overcoming the problem of reactant expansion should be beneficial, hence the use of composite negative electrodes. The basis behind this concept is the use of a 'buffer matrix' to compensate for the expansion of the reactants, so preserving the electrical pathway [Kim 2000, 2003]. Initially, such a buffer action was achieved by mixing two alloys that reacted at different potentials so that the electrochemically active phase was imbedded in a non-electrochemically active matrix. By using this concept, Sony successfully developed a new tin-based amorphous anode material, which consists of multiple elements such as tin, cobalt, and carbon, where the elements are mixed on a nanometer level. By adding several elements to the tin based compound, Sony has been able to minimize the change in particle shape during charge and discharge, solving the problem of cycling characteristics. The result is a 50% higher ratio per unit volume of lithium ion density compared to the conventional graphite anode, resulting in a dramatic increase in the density.

1.3.2.1 Tin

Research on tin-based anode materials was first initiated by Fuji Film Company in the middle 1990s [Idota 1995, 1997; Tomyama 1995], and later moved from oxides to alloys. Their advantages are easy preparation, such as heat-treatment below 1500 °C or simple mechanical milling, and high volumetric capacity, which can be twice that

of carbonaceous anode materials. From intensive studies, it is known that the binary lithium–tin system shows seven different phases: Li_2Sn_5, LiSn, Li_7Sn_3, Li_5Sn_2, $Li_{13}Sn_5$, Li_7Sn_2 and $Li_{22}Sn_5$. Their structures, which were described 30 years ago [Muller 1973, 1974; Frank, Muller et al 1975; Hansen, Chang 1978] can be visualized as in Fig. 1-21. From these structures, Courtney and Tse et al. [1998] calculated the total energies of the lithium–tin phase diagram using the ab initio pseudo-potential plane-wave method. From these results, they calculated the theoretical electrochemical voltage profile, which showed an excellent agreement with the experimental curve, the discrepancies being mostly associated with the departure from equilibrium conditions. The occurrence of the successive phases was shown to take place at decreasing voltage values, which were confirmed in Sn electrodes working versus lithium metal at room temperature [Chouvin, Fourcade et al. 1999; Dunlap, Small 1999].

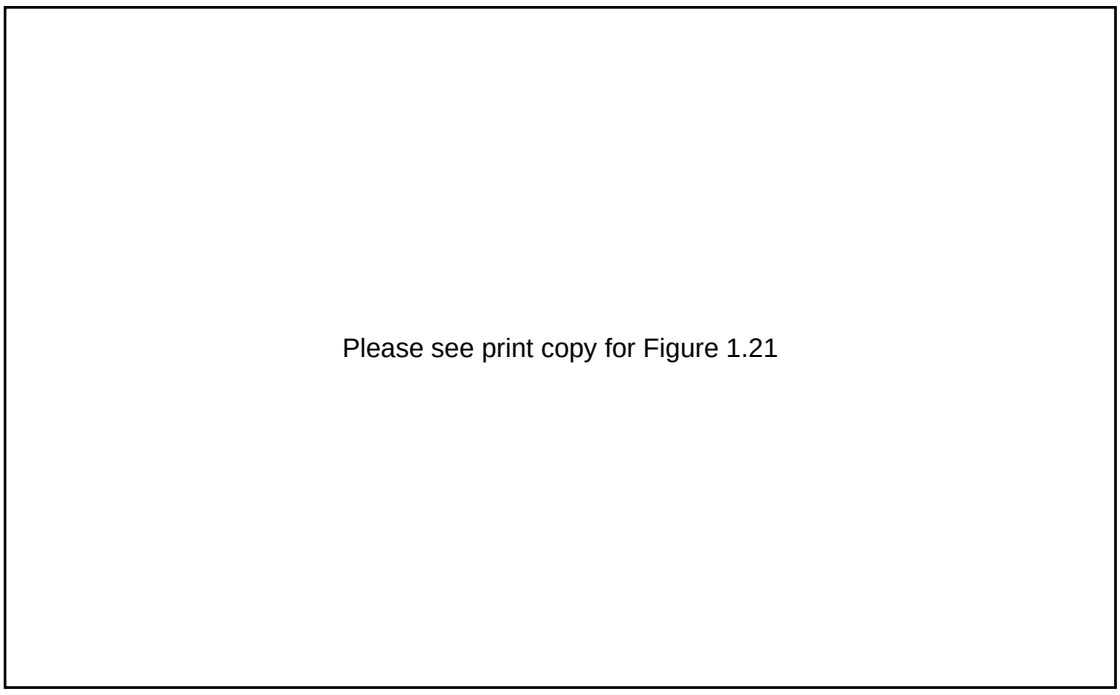

Fig. 1-21 Plot of the structure of different phases in the Li–Sn system [Muller, Schafer et al. 1973].

1.3.2.2 Tin oxides

Tin oxide and stannic oxide can be matrices for lithium storage since tin can form alloys with Li up to $Li_{22}Sn_5$. Cystalline tin monoxide possesses a layered structure in which Sn-O-Sn slabs are stacked together so that tin atoms protrude at both sides of the oxygen layers, while tin dioxide crystallizes in the rutile structure [Tirado 2003]. The first discharge curves of lithium cells using SnO or SnO_2 as active materials show a complex multistep shape that could be simply ascribed to Sn ions to Sn reduction with Li_2O formation, followed by the formation of Li-Sn phases, and ending with the approximate "$Li_{4.4}Sn$" composition:

$$6\ Li + SnO_2/SnO \rightarrow 2Sn + 3Li_2O$$

$$Sn + x\ Li \Leftrightarrow Li_xSn\ (x \leq 4.4)$$

The formation of a Li_2O matrix may act to retard the aggregation of tin atoms into large coherent regions. When large tin regions form, the large volume differences between coexisting bulk Li-Sn phases may introduce cracking and crumbling of the electrode structure, therefore, capacity will be lost. The reversible capacity on charge should then correspond to the formation of intermediate Li-Sn compositions and finally tin metal. An irreversible capacity in the first cycle is then expected. However, there is some extra irreversible capacity, which is induced by the formation of a passivating layer during the first steps of the discharge [Li, Huang et al. 1999].

X-ray diffraction has been used to study these materials, however, the quality of the diffraction effects resulting from small crystallite size and/or imperfections prevents a

clear picture. Different spectroscopic techniques have been applied to the study of tin oxides which reveal the intermediate local environments of the tin atoms. For example, EXAFS studies at the Sn-K edge [Goward, Leroux et al. 1999] gave evidence of an intense Sn-Sn peak at ~ 3.0 Å at a depth of discharge of 2Li/Sn. The Sn-O peak is visible until the end of the discharge. However, it is noticeable that the Sn-O peak was recovered after cell charge. Li MAS NMR studies showed two isotropic resonances in different field regions, which were ascribed to Li_2O and $Li_{4.4}Sn$. Sn MÖssbauer spectroscopy has proven a particularly sensitive indicator of the oxidation states and environments of tin in Li/SnO or SnO_2 cells, and the formation of tin and Li-Sn alloys close to the nominal phases was qualitatively confirmed [Wang, Sakamoto 1998; Chouvin,Branci et al. 1999; Courtney, Mckinnon et al. 1999]. In addition, XPS and XAS were also used to investigate the structure and valence states of these materials.

Comparing the electrode behaviour of SnO_2 with that of SnO, the irreversible capacity in the first cycle is higher than in SnO, while reversibility is restricted to 4.4Li/Sn, after complete reduction to tin metal (~ 600 mAh/g). A particular interest in tin dioxide has resulted from the different preparation routes described in the literature. Chemical vapour deposition and electron beam evaporation [Brousse, Retoux et al. 1998; Retoux, Brousse et al. 1999], spray pyrolysis [Arai 1960], sol–gel [Orel, Lavrebcuc-Strangar et al. 1994] and dip-coating [Takahashi, Wada 1990] procedures have been used in the preparation of coatings and films, while spray pyrolysis [Guo, Liu et al. 2003] and the sol–gel route using inorganic hydrosols [Davis, Chadwick et al. 1998; Santilli, Pulcinelli et al. 1999] and tin alkoxide [Mehrota 1990] have been used to obtain the powdered material. The different textures and microstructures resulting from each synthesis route may play an important role in the electrochemical behaviour and condition the ability of the oxide products to be used as the active

anode material in lithium-ion batteries. Recently, the metal–citrate method was used to prepare microcrystalline tin dioxide and aluminum-doped materials [Alcantara, Madrigal et al. 2000]. The thermal decomposition of the citrate precursors leads to rutile-type SnO_2 solids. For Al-containing oxide materials, ^{27}Al MAS NMR signals gave evidence that Al(III) ions occupy octahedral sites isomorphic to Sn(IV). XAS studies of the Al-doped material showed that the presence of Al atoms in the structure does not modify the relative positions of the different anti-bonding states in SnO_2. X-ray diffraction line broadening analysis indicated a large microstrain content in the ex-citrate products, which is released by successive thermal treatments at 450 °C.

FUJI Photofilm announced an amorphous tin composite oxide (ATCO) for use as a negative electrode material. The starting material was a non-crystalline solid: tin-based composite oxide (TCO). The stoichiometry of this solid is: SnM_xO_y, where M is the vitrifying element (B(III), P(V), As(III)) and $x \geq 1$. A typical composition was TCO-1, $Sn_{1.0}B_{0.56}P_{0.40}Al_{0.42}O_{3.6}$, which can be obtained by reaction of SnO, B_2O_3, SnP_2O_7 and Al_2O_3 at 1100 °C, followed by quenching to give a yellowish transparent glass. This non-crystalline structure consisting of electrochemically active centers of Sn---O and the surrounding amorphous network is stable during charge and discharge [Idota, Kubota et al. 1997]. The other oxides added to the amorphous network delocalize the Sn(II) active centers and enable effective storage of lithium. Reversible capacities larger than 600 mAh/g and 2200 Ah/l were described, which are significantly higher than 372 mAh/g and double the volumetric capacity of the best carbon-based material (~1200 Ah/l), respectively. In addition, the amorphous glass formed by the other added oxides enhances lithium diffusion in comparison with crystalline tin and stannic oxides, thus reversible intercalation and deintercalation are favored. The mechanism for lithium storage is as follows [Tomyama 1995]:

$$SnB_{0.5}P_{0.5}O_3 + 7–8\ Li \Leftrightarrow Li_{7–8}SnB_{0.5}P_{0.5}O_3$$

Lithium exists in the form of lithium ions in the composite. However, other researchers found that lithium first reacts with the composites to form Li_2O, and then forms an alloy with the reduced tin, as shown below, [Courtney, Dunlap et al. 1999]. As to its specific actions, further studies are still underway.

$$4\ Li + Sn_2BPO_6 \rightarrow 2\ Li_2O + 2\ Sn + 1/2\ B_2O_3 + 1/2\ P_2O_5$$

$$8.8\ Li + 2\ Li_2O + 2\ Sn + 1/2\ B_2O_3 + 1/2\ P_2O_5 \Leftrightarrow 2\ Li_{4.4}Sn + 1/2\ B_2O_3 + 1/2\ P_2O_5 + 2\ Li_2O$$

Besides ATCO, other investigations, such as those pursued by Mao and Dahn et al. [1999] on the Sn-Fe-C and Sn-Mn-C systems, have also revealed an appealing low-voltage reversible reactivity in composite materials developed as negative electrodes (in spite of initial irreversibility and short-lived capacities). The best experimental proof of the beneficial effects on cycle stability was obtained with a composite made by precipitating Sn metal at the grain boundaries of electrochemically inactive $SnFe_3C$ grains [Beaulieu, Dahn 2000]. However, the cycling performance was improved at the expense of the electrode electrochemical capacity.

1.3.2.3 Tin-based alloys

Metallic tin can form alloys with Li up to $Li_{22}Sn_5$, and its reversible capacity is very high. However, there is a drastic expansion and contraction during charge and discharge, and the Li_xM alloy that is formed is very brittle, resulting in pulverization

of the alloy and fast fading of capacity. In order to circumvent the problem of volume change upon lithium insertion, Sn and SnAg alloy powders with small particle size (typical grain size: 200-400 nm) have been synthesized by a chemical reaction method. These fine grained alloys have demonstrated excellent cycling performance [Besenhard, Yang et al. 1997]. A model for lithium insertion in alloys with small particle size has been proposed. Many pores and cavities exist in a loosely packed small particle size metallic matrix. During lithium insertion, even 100% volume expansion of individual particles will not crack the electrode as the absolute changes in dimensions are still small. In other words, the pores and cavities have a buffering effect on the volume expansion of individual particles. During the lithium extraction, the expanded particles do not contract very much, thus the overall dimensions of the electrode show little change. However, Wolfenstine [1999] proposed that the critical grain size must be less than the unit cell size for a single-phase materials, otherwise the microcracking still could not be avoided. This suggests that decreasing the particle/grain size can not fundamentally solve the mechanical instability problem associated with Li-alloys.

Some other solutions to solve the mechanical instability have been proposed. The basic concept is embedding the active particles in a less active or inactive matrix to cushion the expansion and contraction in charge and discharge reactions. The intermetallic alloys MM′, especially SnM′, have emerged as a new class of anode materials for lithium-ion batteries. In the intermetallic compound MM′, M is an "active" element such as Sn, which can react with lithium to form Li_xM; while M' is an "inactive" element such as Cd, Ni, Mo, Fe or Cu [Huggins 1999; Ehrlich, Durand et al. 2000; Morales, Sanchez et al. 1999; Crosnier, Brousse et al. 1999; Thackeray,

Johnson et al. 1999; Kepler, Vaughey et al. 1999]. The reaction is supposed to proceed as follows:

$$xLi^+ + SnM' + e^- \rightarrow Li_xSn + M'$$

These materials are promising alloy anodes for lithium ion batteries [Thackeray, Johnson et al. 1999]. The main reason is that addition of M′ results in ductile alloys with greatly reduced volume change [Besenhard, Yang et al. 1997; Yang, Wachtlwer et al. 1999].

Various SnM′ alloys show improved cycling performance compared to the pure Sn anode. A typical example is Cu_6Sn_5 [Kepler, Vaughey et al. 1999], which has been well studied and has demonstrated much improved cycling behaviour compared to pure Sn. When lithium ions are inserted into Cu_6Sn_5 alloys, a displacement reaction occurs in which the intermetallic structure is broken down to form a series of Li_xSn alloys within the inert Cu matrix. In this phase, the Li-rich phase $Li_{4.4}Sn$ and Cu coexist. The deintercalation also goes via multiple steps resulting in Cu_6Sn_5. At first Li deintercalates from $Li_{4.4}Sn$ to produce $Li_{4.4-x}Sn$. With progressive deintercalation, $Li_{4.4-x}Sn$ reacts with copper, producing Li_2CuSn. Later lithium deintercalates from Li_2CuSn forming $Li_{2-x}CuSn$, which contains vacancies. In situ x-ray diffraction studies combined with MÖssbauer spectroscopy have confirmed the formation of metallic Cu in Cu_6Sn_5 electrodes after cycling. An increase in the copper content in Cu_xSn alloys provides better cycling behavior at the expense of a lower capacity [Xia, Sakai et al. 2001].

Ni_3Sn_2 and Co_3Sn_2 are similar to η-Cu_6Sn_5 in structure, and the reversible capacity can be up to 327 or 2740 mAh/cm^3 [Ehrlich, Durand et al. 2000], much higher than that of currently available carbonaceous materials. When the utilized capacity is only

1500 mAh/cm^3, fading in capacity becomes slow. In the case of NiSn alloy, the reversible capacity is only 77 mAh/g, which is perhaps associated with a low diffusion coefficient of Li [Crosnier, Brousse et al. 1999]. Antimony is also added into tin forming multi-phase structures, and the cycling behavior is significantly improved [Yang 1996; 1999].

Nanocrystilline alloys provide an approach to further improve the electrochemical performance of Sn-based alloys. There are countless pores and cavities in the nanocrystalline Sn-based alloys, which provide free rooms for the volume expansion of the active element when reacting with lithium to form Li_xSn alloys. The generated inactive matrix is also nanocrystalline in nature, which will be compatible with the original Sn-based alloys if the starting materials are nanocrystalline.

1.3.3 Silicon-based anode materials

Silicon can also react with lithium to form Li_xSi up to a maximum of $Li_{22}Si_5$, whose theoretical capacity is 4200 mAh/g [Boukamp, Lesh et al. 1981]. However, there is also a drastic change in volume during charge and discharge processes, which leads to pulverization and results in a fast fading of capacity. To circumvent this problem, several research efforts have been focused on composites consisting of silicon and carbonaceous materials. For instance, Wilson and Dahn [1995] have synthesized nanodispersed silicon in carbon using chemical vapor deposition (CVD). Although the Si-C anodes demonstrated a reversible capacity of 500 mAh/g, it is difficult to control the morphology of Si and C when using the CVD approach. Yoshio and Wang et al. [2002] prepared carbon-coated silicon by a thermal vapor deposition (TVD) method, and a better cycle life than with the respective silicon has been achieved. Composites produced by mechanically mixing silicon and graphite (or acetylene black) show high

capacity, but their cycling is still poor [Li, Huang et al. 1999]. More recently, research work by many groups has demonstrated that silicon/disordered carbon (DC) composite, obtained by mechanically milling and pyrolyzing organic precursors, such as polyparaphenylene (PPP) or polyvinyl chloride (PVC), in an inert gas atmosphere can reversibly insert Li atoms with a capacity (> 500 mAh/g) greater than that of graphite (372 mAh/g) [Liu, Hanai et al. 2004; Zhang, Patil et al. 2004]. Although the electrochemical performance is significantly improved compared with the respective silicon electrodes, the silicon-disordered carbon systems still pose some problems, such as a relatively high capacity fading rate and a relatively low capacity contribution from disordered carbon (386 mAh/g from PVC-based disordered carbon; 451.3 mAh/g from PPP-based disordered carbon). Recently, it was reported that the disordered carbon prepared by pyrolyzing hexa(phenyl)benzene (HPB) demonstrated a stable capacity on the order of 500 mAh/g [Bonino, Brutti et al. 2005]. Carbon from pyrolyzed sugar under optimal conditions showed a large reversible capacity of 650 mAh/g [Xing, Xue et al. 1996]. Therefore, the optimization of the silicon-disordered carbon system and further improvement of the silicon-disordered carbon concept are necessary.

Alternatively, Si can be dispersed in a solid, conducting and electrochemically inactive matrix, such as TiN, TiB_2, TiC and SiC. Kim et al. [1999, 2000] and Guo and Zhao et al. [2005] have separately examined the role of silicon after dispersion in a nanostructured conducting, but electrochemically inactive matrix, by mechanical milling. They found that an increasing amount of the inactive portion of amorphous Si was observed by prolonged milling. For compositions with low Si ratios, good capacities (300-400 mAh/g) with little fade were observed. The stability of the

electrode was attributed to the positive effect of the electrochemically inactive matrix on a fine dispersion of silicon.

On the other hand, several silicon alloys and compounds have been reported so far that may produce the desired composite by an “in situ” electrochemical reaction with lithium. For example, the alloy SiAg exhibits a reversible capacity of about 280 or 1150 mAh/cm^3 and little fading in capacity within the first 50 cycles. When silicon is doped with chromium to form a composite, the reversible capacity is enhanced from the 550 of Li---Si to 800 mAh/g. Capacity is associated with the initial ratio of Li/Si. When the ratio of Li/Si is about 1:3.5, capacity is at the highest level and good in cycling [Weydanz, Wohlfahrt et al. 1999].

For the ternary Li–M–Si systems [Maleki, Deng et al. 1999; Huang, Rao et al. 1999; Jang, Huang et al. 1999], for example hexagonal Li_2ZnSi, a simpler behavior is characterized by a single phase mechanism of lithium insertion–extraction. However, loss of crystallinity during deep charge or discharge causes additional complexity. The charge and discharge voltage plateaus are at ~ 0.8 and 0.5 V, respectively. Such values are well above those of the lithium electrode to avoid the deposition of dendritic lithium metal on the surface of the anode on prolonged cycling. This may be an improvement in safety as compared with graphite electrodes but with a compensating loss of power.

1.3.4 Transition metal oxides

Rock salt structured MO-type (M = Fe, Co, Ni ,Cu……) transition metal oxides react reversibly with lithium in a lithium cell below 1.5 V [Poizot, Laruelle et al. 2000]. It has been reported that the MO type oxides demonstrate large capacity (700 mAh/g),

long cycle life, and high recharging rates. These brilliant properties make them promising candidates for use as anode materials for Li-ion batteries [Dolle, Poizot et al. 2002]. However, such simple transition metal oxides have long been overlooked, due to the lack of intercalation/deintercalation sites in their crystal structures and lack of existing Li-M alloys. In the mid 1980s, Thackeray and Backer et al. [1985] proposed a mechanism different from conventional lithium intercalation processes for the MO-type oxides. Their study of Li/Co_3O_4 and Li/CoO cells suggested that during discharge Co_3O_4 was reduced via CoO to Co metal. A detailed understanding of the intimate processes in the reaction of lithium and MO-type oxides was not obtained until recently. The Tarascon group [Poizot, Laruelle et al. 2000] started their research in this field by using CoO in lithium test cells. The electrochemical reduction of cobalt to the metallic state was reported together with the formation of lithium oxide. The main difference from previous reports was the fact that Li_2O becomes electroactive during the charge of the lithium cell. Such unexpected behavior was ascribed to the nanosized Co particles dispersed in the Li_2O matrix that were produced during the reaction and possess an enhanced reactivity. In addition, the complex Li_2O plus Co system are surrounded by a solid electrolyte interface.

Similarly, a good performance was found for NiO and FeO, in which reversible capacities close to 700 mAh g^{-1} were reported with high cycling efficiency, and later in Cu_2O prepared by the polyol process [Grugeon, Laruelle et al. 2001] with ~ 400 mAh g^{-1}. More recently, several independent groups re-examined the spinel Co_3O_4, as an anode material for lithium-ion batteries [Larcher, Sudant et al. 2002]. Yuan and Huang et al. [2003] synthesized Co_3O_4 through pyrolysis of the oxalate precursor, which was prepared with a rheological phase reaction from cobaltous hydroxide carbonate and oxalic acid. They found that the samples exhibited large

lithium storage capacities and that the reversible capacities were more than 900 mA h/g. The particle size of Co_3O_4 has a significant effect on the capacity and cycling stability. The sample with the average particle size of about 37 nm showed the best electrochemical performance. Pralong and Leriche et al. [2004] deposited cobalt oxide, Co_3O_4, thin films on a 1.37-cm^2 nickel substrate by pulsed laser deposition (PLD) and investigated their electrochemical properties. It was found that the first discharge process is characterized by a quasilinear potential decrease corresponding to the uptake of 10 lithium. Upon increasing the discharge rate, 1 or 10 Li^+/h, the voltage–composition profile curve evolves from a nice plateau toward a slow sloping voltage curve implying some kinetics limitations (Fig. 1-22a). The capacity rapidly decreased during the first 10 cycles and stabilized over the next 150 cycles to finally increase and reach 800 mA h/g after 350 cycles (Fig. 1-22b). Such a phenomenon was associated with the occurrence of a second redox process involving the electrolyte. More recently, Zhao and Guo et al. [2005] prepared crystalline Co_3O_4 powders with controllable morphology by using cobalt chloride and various alcohol precursors at different temperatures. Co_3O_4 particles have a dramatic tetragonal dipyramid structure when synthesized from benzyl alcohol and cobalt chloride. A stable and reversible storage capacity for lithium of 740 mAh g^{-1} within 50 cycles was achieved on electrochemical performance testing.

It was pointed out that the reaction of rock salt structured MO-type transition metal oxides in lithium ion batteries is based on two reversible faradaic processes : first the transition metal oxide reacts with lithum and is reduced into nanosized metallic particles dispersed in subsequently formed Li_2O matrix upon discharge. In the following cycles, the process is reversible according to the reaction:

$$MO + 2L^+ + 2e^- \leftrightarrows M + Li_2O$$

Obrovac and Dahn also confirmed the reaction in their study of ball-mill-synthesized Li_2O/Co and Li_2O/Fe nanocomposite electrodes. It was also found that the polymer-like solid-electrolyte interphase (SEI) layer forms and decomposes at low reduction potential, which is partially reversible in the charge-discharge cycles.

Other transition metal oxides used as anode materials for lithium ion battery include intercalation electrode materials, such as Fe_3O_4, Mn_3O_4, and TiO_2 etc. Among all the oxides that allow true lithium intercalation reactions, nanostructured titanium dioxide with the anatase structure has attracted great interest as a possible anode material in lithium ion batteries [Huang, Kavan et al. 1995]. The known polymorphs of TiO_2 incorporate lithium electrochemically in a very different extension. Rutile, hollandite and brookite show very poor lithium intercalation properties, while anatase shows much better electrochemical performance. The TiO_2-B polymorph is an excellent intercalation host for Li, accommodating up to $Li_{0.91}TiO_2$-B (305 mAh/g) at 1.5-1.6 V vs Li^+/Li and with excellent capacity retention on cycling. Another interesting metal oxide with spinel structure is $Li_4Ti_5O_{12}$. This material is called zero-strain insertion material and has a very stable structure for lithium insertion and extraction.

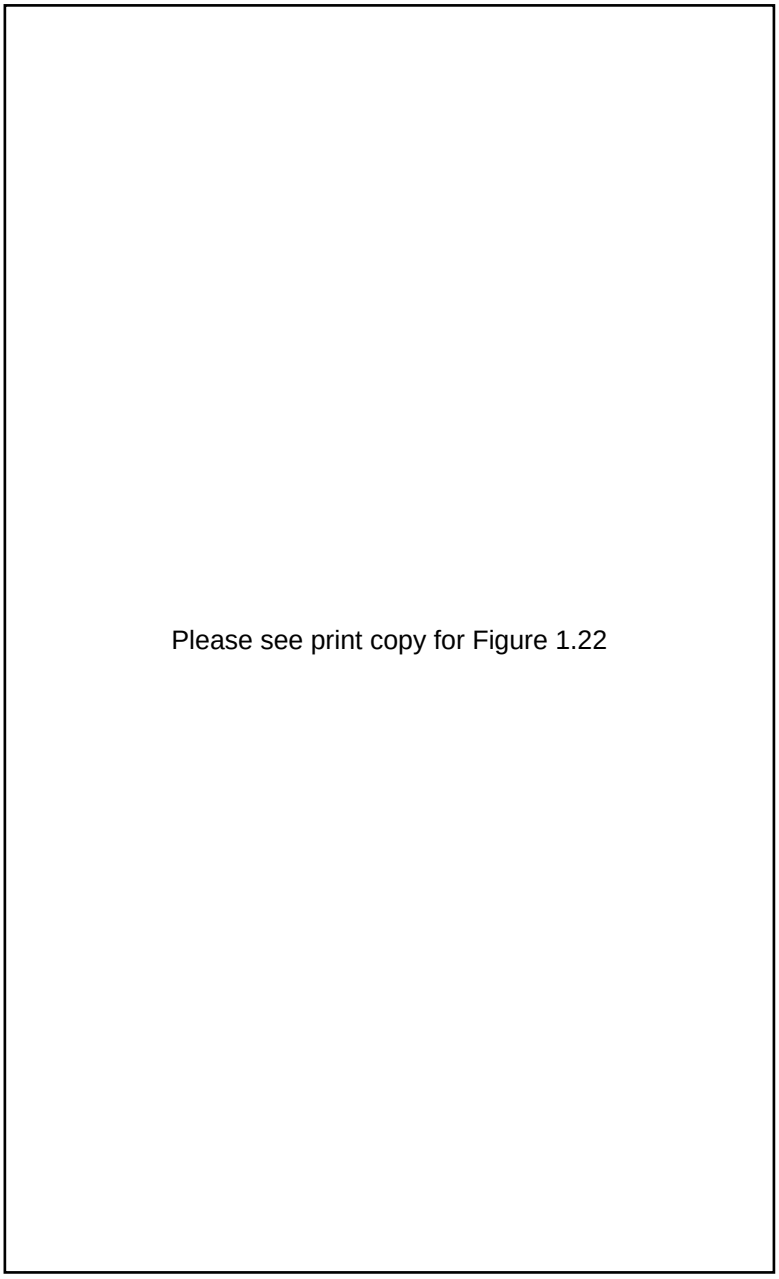

Fig. 1-22 (a) Voltage profile of a Co_3O_4/Li cell cycling at room temperature between 0.05 and 3 V versus Li/Li^+ with a 10 Li^+/h rate. Inset: comparison voltage–composition profile between two rates, 1 and 10 Li^+/h. (b) Capacity versus cycle number [Pralong, Leriche et al. 2004].

The electrochemical curves show a plateau at about 1.5 V and capacity values close to 150 mAh/g are preserved during 100 cycles. Thin-film electrodes obtained from nanocrystalline $Li_4Ti_5O_{12}$, which was prepared by a sol-gel route employing lithium ethoxide and Ti (IV) alkoxides, showed excellent electrochemical behaviour. However, all of the above oxide electrode materials exhibit a high average voltage versus metallic lithium for lithium intercalation and deintercalation. Some of them have limited reversible capacity. This results in low energy density when used as the anode in a whole cell.

1.4 Present status and remaining challenges

Lithium ion batteries have made substantial and significant gains as the power source of choice for consumer electronic devices such as cell phones and laptop computers due to their high energy density and long cycle life. However, the next market opportunities will be much tougher to conquer, as lithium-ion batteries are expected to be the power sources in the hybrid vehicle field. These demand batteries with higher power density but lower costs and enhanced safety. Accordingly, much research work is presently directed towards the exploration of different types of materials with high reversible capacity and long cycle life. For the cathode, the mixed transition metals layered oxides, such as ($LiCo_{1-x}Ni_xO_2$, $LiNi_{1-x-y}Mn_xNi_yO_2$) will, without doubt, continue their improvement and slowly displace the pure cobalt system ($LiCoO_2$). These mixed transition metal oxides appear to offer improved safety with larger capacity at lower cost. In addition, lithium iron phosphate ($LiFePO_4$) is a promising low-cost cathode material with enhanced safety.

With respect to the anode, the main goal is to replace the present carbon-based materials with larger specific capacity materials, i.e. metals or compounds that alloy with lithium (e.g. SnO_2, Co_3O_4, CoO, etc.).

Whatever the battery technology considered, measures of its performance (for example, cell potential, capacity or energy density) are related to the intrinsic properties of the materials that form the positive and negative electrodes. The cycle life and lifetime are dependent on the nature of the interfaces between the electrodes and electrolyte, whereas safety is built on a foundation of the stability of the electrode materials and interfaces. During the next decade, improvements should arise from changes in battery chemistry and cell engineering. Advances in active chemistry are left to the solid-state chemists creativity and innovation in the design and elaboration of new types of intercalation materials.

Chapter 2

Experimental

2.1 Materials and Chemicals

The materials and chemicals were supplied by several chemical companies. Most of were from the Aldrich Chemical Company Pty. Limited. The details are given in table 2-1.

Table 2-1 Description of materials and chemicals

Materials or Chemicals	Formula	Purity	Supplier
Lithium carbonate	Li_2CO_3	99.99%	Aldrich
Manganese oxide	Mn_2O_3		Aldrich
Lithium hydroxide	$LiOH{\cdot}H_2O$	99.9%	Aldrich
Nickel nitrate	$Ni(NO_3)_2{\cdot}6H_2O$	98+%	Aldrich
Manganese acetate	$Mn(CH_3CO_2)_2Mn{\cdot}6H_2O$	99%	Aldrich
Lithium nitrate	$LiNO_3$	99.98%	Aldrich
Cobalt nitrate	$Co(NO_3)_2{\cdot}6H_2O$	98+%	Aldrich
Cobalt carbonate	$CoCO_3$	99.5%	Aldrich
Cobalt octacarbonyl	$Co_2\ (CO)_8$		
Nitric acid	HNO_3	60%	Aldrich
Ethylene glycol	$C_2H_6O_2$	Extra pure	Aldrich
Lithium hexafluorophosphate	$LiPF_6$		Aldrich
EC (ethylene carbonate)			Aldrich
DEC (diethyl carbonate)	$(C_2H_5O)_2CO$		Aldrich
Iron oxalate	$FeC_2O_4{\cdot}2H_2O$	99%	Aldrich
Ammonium dihydrogenphosphate	$NH_4H_2PO_4$	99.999%	Aldrich
Silver nitrate	$AgNO_3$		Aldrich
Citric acid	$C_6H_8O_7$	99.5%	Aldrich

Cetyltrimethylammonium bromide	$C_{19}H_{42}BrN$	99%	Aldrich
1-Butanol	$CH_3(CH_2)_3OH$	>99%	Sigma
Octane	$CH_3(CH_2)_6CH_3$	98%	Aldrich
AOT	$C_{20}H_{37}NaO_7S$	>99%	Aldrich
n-heptane	C_7H_{16}		Fluka
methanol	CH_3OH	99.8%	Aldrich
Graphite	C	99.99%	Aldrich
Sodium borohydride	$NaBH_4$	98%	Aldrich
Tin(IV) chloride	$SnCl_4$	98+%	Aldrich
Ammonia	$NH_3 \cdot H_2O$		Aldrich
Manganese acetate	$Mn(CH_3COO)_2 \cdot 4H_2O$	99.5%	Aldrich
Lithium acetate	$Li(CH_3COO) \cdot 2H_2O$	99.5%	Aldrich
Polyvinylidene fluoride(PVDF)			Aldrich
Dimethyl phthalate (DMP)			Aldrich
Carbon black			Aldrich
LP30 electrolyte	EC:DMC 1:1 w/w		Merck
LP31	EC:DMC 2:1 w/w		Merck
Polypropylene separator			Celgard 2500, Hoechst, USA
Propylene carbonate		99.7%	Aldrich
CR2032 coin cell hardware			Hosen Corp., Japan
Cobalt acetate	$Co(CH_3COO)_2 \cdot 4H_2O$	99%	Aldrich

2.2 Experimental procedures

Various anode and cathode materials were synthesized and characterized in the present work. The synthesized active materials were then used for preparing test electrodes. Teflon test cells or CR2032 coin cells were assembled to examine the electrochemical properties. The overall experimental procedure is schematically illustrated in Fig. 2-1.

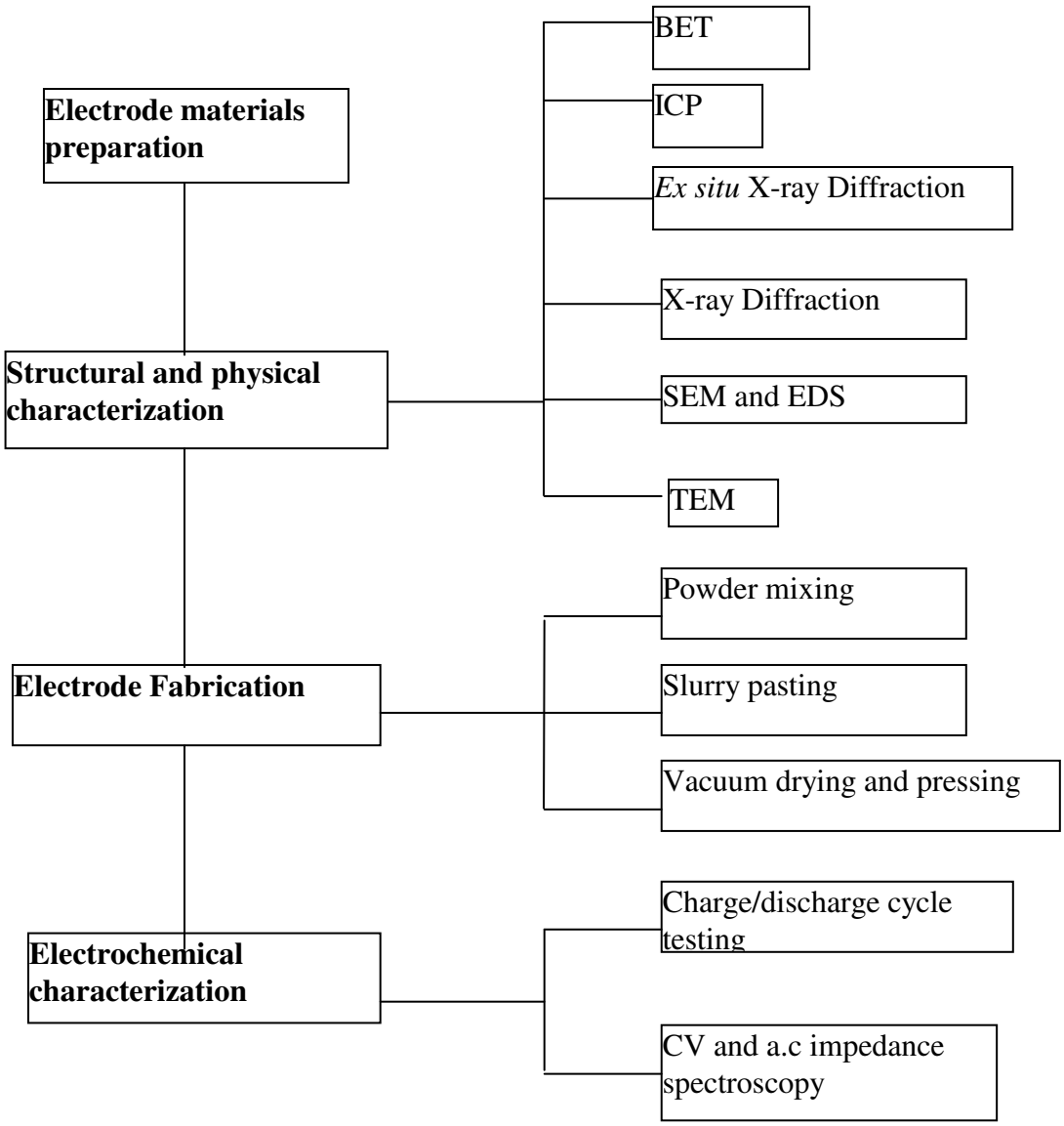

Fig. 2-1. The experimental procedure.

2.3 The preparation of cathode materials

The cathode materials investigated were spherical $LiCo_{0.25}Ni_{0.75}O_2$, $LiCo_xMn_yNi_{1-x-y}O_2$ ($0 \leq x \leq 0.3$, $y = 0.2$) compounds, nanocrystalline $LiFePO_4$ and carbon-coated $LiFePO_4$. These compounds were prepared by various synthesis routes, including the chemical coprecipitation method, the carbon aerogel synthesis process, and the sol-gel method.

2.3.1 Spherical $LiCo_{0.25}Ni_{0.75}O_2$ prepared by chemical coprecipitation method

The spherical $Ni_{0.75}Co_{0.25}(OH)_2$ precursor powders were synthesized by chemical co-precipitation and controlled crystallization. The reagents $NiSO_4 \cdot 6H_2O$ (99%, Aldrich) and $CoSO_4 \cdot 7H2O$ (99.9%, Aldrich) were dissolved in de-ionized water and homogeneously mixed. A mixture of NaOH and NH_4OH solution was added to precipitate the hydroxide. The pH (=10-11) value, temperature, and pressure were strictly controlled. The precipitate was then aged in a pressurized vessel at 60 – 80 °C for a few hours to allow the spherical crystals to grow. The resultant crystals were thoroughly washed using deionized water and then dried in a vacuum oven to yield spherical $(Ni_{0.75}Co_{0.25})(OH)_2$ powders. The spherical $(Ni_{0.75}Co_{0.25})(OH)_2$ and $LiOH \cdot H_2O$ precursor powders were intimately mixed by mortar and pestle with a molar ratio of $Ni_{0.75}Co_{0.25}$: Li = 1:1.04 (due to evaporation of Li during high temperature sintering). The mixture was then sintered at high temperature between 650 and 850 °C for 12 h under flowing oxygen to obtain spherical $LiNi_{0.75}Co_{0.25}O_2$ compounds. The non-spherical $LiNi_{0.75}Co_{0.25}O_2$ compounds were prepared by sintering the precursors Li_2CO_3, NiO, and CoO at 750 °C under flowing oxygen.

2.3.2 $LiCo_xMn_yNi_{1-x-y}O_2$ synthesized by a chemical coprecipitation process

$Co(NO_3)_2 \cdot 6H_2O$ (98%+, Aldrich), $Ni(NO_3)_2 \cdot 6H_2O$(98%+, Aldrich) and $(CH_3CO_2)_2Mn \cdot 6H_2O$ were used as the starting materials and were dissolved in stoichiometric amounts. The solution was slowly dripped into a 50 ml aqueous solution, which was maintained at 60 ºC while stirring. At the same time, a NaOH (6M) and NH_3OH (6.5M) solution mixture was slowly pumped into the original solution by a peristaltic pump to keep the pH of the solution at 11-12. The mixed hydroxide precipitate that was obtianed was first filtered and thoroughly washed with distilled water, then dried at 65 ºC overnight. The precursor powders of $(Co_xMn_yNi_{1-x-y})(OH)_2$ were thus obtained. The precursor and Li_2CO_3 in excess (Li:M = 1.04:1) were mixed and ground using a mortar and pestle. The mixture was then pressed at 800 kg/cm^2. The obtained disks were heated in oxygen at 700-900 ºC for 24 h.

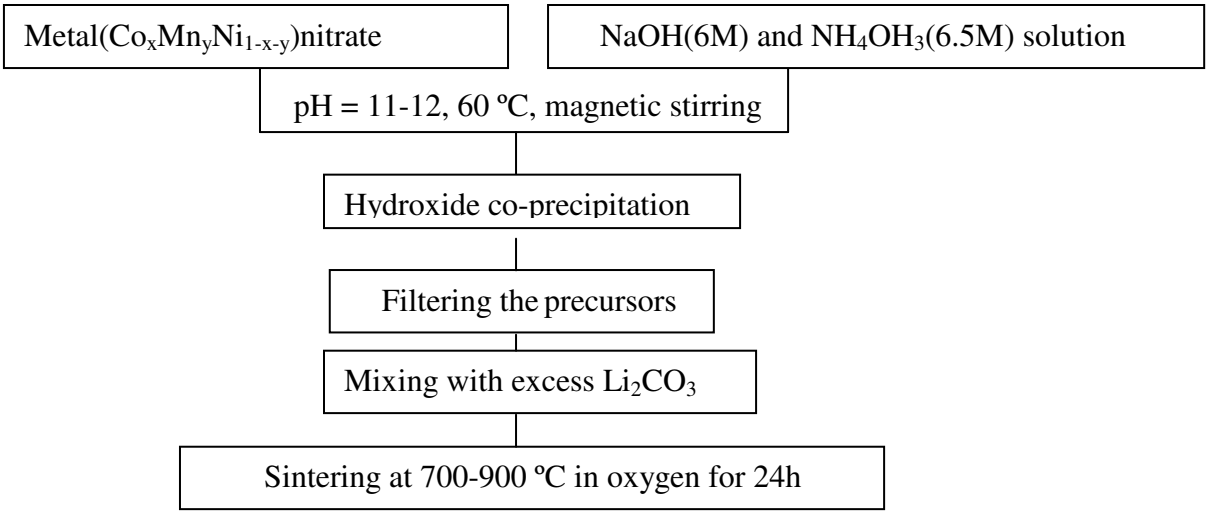

Fig. 2-2 Flow chart of the synthesis procedure.

2.3.3 Nanocrystalline $LiFePO_4$ prepared by a sol-gel method.

$FeC_2O_4 \cdot 2H_2O$, $Li(CH_3COO) \cdot 2H_2O$, H_3PO_4, and citric acid were used as the starting materials. The metal compounds were first dissolved in phosphoric acid and deionized water. This solution was mixed until homogeneous, and citric acid was added while stirring, until the molar ratio of citric acid to metal ions was 2:1. Ammonium hydroxide was added to the solution to adjust the pH to between 8 and 9. The solution was then heated to 80 ˚C under N_2 until a gel formed. After that, the gel was transferred to an alumina boat and heated at 500 ˚C for 10 hrs under flowing N_2. The resultant powders were then ground and heated at a rate of 2 ˚/min to 700 ˚C under a flow of N_2 gas for another 10 hrs.

2.3.4 Carbon-coated $LiFePO_4$ prepared by a carbon aerogel synthesis process.

$Li(OH) \cdot H_2O$ (99.9%, Aldrich), $FeC_2O_4 \cdot H_2O$ (99%, Aldrich), and $NH_4H_2PO_4$ (97%, Aldrich) were used as the raw chemicals. The stoichiometric reactants were dissolved in de-ionised water, to which diluted nitric acid was added to accelerate the dissolving of $FeC_2O_4 \cdot H_2O$. A typical carbon gel was formed by mixing 0.29 M resorcinol and 0.57 M formaldehyde. The $LiFePO_4$ reactant solution and the carbon gel solution were mixed, and the pH value was adjusted to be in the range of 6.5 – 7.4. Then, the mixture solution was put in an ampoule, sealed and heated on a hot plate. The temperature was maintained at 85 °C. When the solution became viscous, the ampoule was moved to an oven and kept at 85 °C for 10 h. The carbon aerogel was then formed with the reactants Li^+, Fe^{2+} and $[PO_4]^{3-}$ dispersed inside. The gel was first decomposed at 450 °C and then

sintered at 750 °C for 12 hours under flowing argon to yield carbon coated $LiFePO_4$. The carbon content was analysed by thermal gravimetric analysis (TGA) to be 20 wt %.

2.4 The preparation of anode materials

2.4.1 Synthesis of nanocrystalline Ag and SnO_2 via a reverse micelle approach.

Nanocrystalline Ag powders were synthesised using reverse micelles as nanoreactors. Reverse micelle A contains metal salts, while reverse micelle B contains a reduction agent for preparing Ag powders, and a hydroxylation agent for preparing SnO_2. The compositions of the reverse micelles are summarized in Table 2-2. Reverse micelles A and B were then mixed together using high speed mechanical stirring to form a single new type of reverse micelle. The reacted solutions were centrifuged and washed with methanol several times. The products were then dried in vacuum at 80 °C for 5 hours. Nanosize Ag powders were directly obtained. During the synthesis of SnO_2, we first obtained $Sn(OH)_4$ in the reverse micelles. The $Sn(OH)_4$ was further sintered at 450 °C to yield SnO_2.

Table 2-2 Compositions of the reverse micelle systems.

Compositions / Nanosize powders	Reverse micelle A	Reverse micelle B
Ag	15 wt % 0.5 M $AgNO_3$ + 42 wt % octane + 25 wt % CTAB ($C_{19}H_{42}BrN$) as surfactant + 18 wt% 1-butanol as co-surfactant	15 wt% 1 M $NaBH_4$ + 42 wt% octane + 25 wt % CTAB ($C_{19}H_{42}BrN$) as surfactant + 18 wt% 1-butanol as co-surfactant
SnO_2	24 wt % 0.1 M $SnCl_4$ + 48 wt % n-heptane + 28 wt % AOT ($C_{20}H_{37}NaO_7S$) as surfactant	24 wt % 1 M NH_4OH + 48 wt % n-heptane + 28 wt % 28 wt % AOT ($C_{20}H_{37}NaO_7S$) as surfactant

2.4.2 Preparation of CoO and Co_3O_4 by high temperature decomposition

CoO was synthesised by decomposition of $CoCO_3$ in an argon atmosphere at 850 °C for 12 hours, and Co_3O_4 was obtained by decomposition of $CoCO_3$ in air at 900 °C for 12 hours. This type of Co_3O_4 is called HT-Co_3O_4. Fine Co_3O_4 powders, called LT-Co_3O_4 were also prepared by heating $Co(OH)_2$ at the low temperature of 250 °C under oxygen flow for 20 hours. Superfine Co_3O_4 powders were prepared by high energy ball-milling. The ball milling was performed in a planetary ball milling machine (Pulverisette-5, LABTECHNICS, Australia) for 120 hours at a rotation rate of 200 rpm.

2.4.3 Nanosize Co_3O_4 powders prepared by a chemical decomposition approach

Nanosize Co_3O_4 powders were prepared by a chemical decomposition approach. Cobalt octacarbonyl ($Co_2(CO)_8$) compounds were initially dissolved in toluene to form a solution. The solution was heated at 130 °C in a glove box under flowing oxygen. Homogeneous nucleation and growth of nano cobalt oxide crystals were achieved by using oxygen gas to bubble through the solution during the heating process. The oxygen bubbling effect not only can enhance the oxidation of cobalt, but also disperse the cobalt oxide nanocrystals and prevent the formation of agglomerates. This technique is well known for preparing nanocrystalline self-assembled materials [Yin, Wang 1999; Chen 1995; Papirer, Horny et al. 1983]. For comparison, normal crystalline cobalt oxides (Co_3O_4) were also prepared by decomposition of $CoCO_3$ at high temperature.

2.5 Electrode preparation and test cell construction

2.5.1 Electrode preparation

The electrodes were made by dispersing a mixture of 85 wt% active materials, 13 wt% carbon black, and 2 wt% PVDF binder into dimethyl phthalate to obtain a slurry. (The ratio may be adjusted for certain cases.) The slurry was spread onto aluminium foil for cathode and onto copper foil for anode. After the electrode was dried at 140 °C for 2 hours, it was compressed at a rate of about 150 kg/cm^2. The electrodes were then dried in a vacuum furnace for 24 hours and finally transferred to a glove box. The electrode area is approximately 1 cm^2, and the typical thickness of an electrode is about 100 μm.

2.5.2 Test cell construction

The test cells were assembled in an argon filled glove box (Unilab, Mbraun, USA), in which moisture and oxygen were automatically controlled to be less than 5 ppm. In order to examine the electrochemical properties of the prepared electrode materials, lithium metal was used as a standard counter electrode in all test cells. The electrolyte was 1 M $LiPF_6$ in a solution of EC (ethylene carbonate) and DMC (dimethyl carbonate) (1:1 in volume). The separator was Celgard 2500 porous plastic film. There were two configurations of test cells, Teflon test cells and standard CR 2032 coin cells. A Teflon test cell is shown in Fig. 2-2. A reference electrode can be put on the side of this Teflon test cell to construct a three-electrode cell, which is used for CV and a.c. impedance measurements.

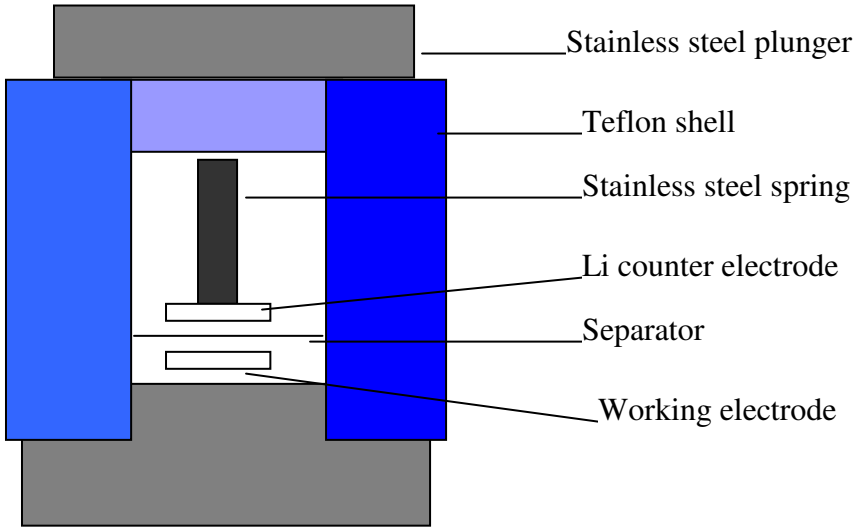

Fig. 2-3 Schematic of the configuration of the Teflon test cell.

Electrodes were initially tested using Teflon test cells. For long term cycle life testing, CR 2032 coin cells were assembled. The CV and a.c. impedance experiments were conducted on Teflon test cells with lithium metal as both counter electrode and reference electrode.

2.6 Structural and physical characterization of electrode materials

The synthesized cathode materials were thoroughly characterized by a variety of approaches. The structural characteristics were determined by x-ray diffraction using a MO3xHF[22] diffractometer (MacScience Co. Ltd, Japan) with a diffracted beam monochromator curved crystal (graphite 002) and Cu-Kα radiation.

The morphology and surface images of electrode materials were observed by SEM (Leica/Cambridge Stereoscan 440 scanning electron microscope equipped with an energy dispersive spectrometer), TEM (JEOL 2000FX transmission electron microscope), and high resolution TEM (300 kV JEOL JEM-3000F with field emission). The particle size of materials was determined with a particle size analyser (Mastersizer, Malvern Instruments Ltd.). The composition of materials was analysed using an inductively coupled plasma spectrometer (ICP).

2.7 Electrochemical testing

The assembled test cells were cycled galvanostatically at a constant current density with a certain cut-off voltage. The cycling tests were performed at different current densities for different electrode materials.

Cyclic voltammetry (CV) was performed to determine the characteristics of lithium insertion/extraction reactions for the electrodes investigated. The CV measurements were carried out with an EG&G electroanalyzer, with the sweep rate controlled. A.c. impedance measurements were used to analyse the interface behaviour between the active materials and the electrolyte, and to characterise the kinetic properties of the electrode materials with an EG&G Princeton Applied Electrochemical Impedance Analyser (Model 6310). Electrochemical impedance software (Model 398) was used to control a computer for conductivity and stability measurements. The a.c. impedance was measured potentiostatically with a 5 mV a.c. input signal applied between the working and reference electrodes over a frequency range from 100 kHz to 0.001 Hz at six points per decade of frequency.

Chapter 3

Synthesis and Characterization of $LiCo_xMn_yNi_{1-x-y}O_2$ as a Cathode Material for Lithium Secondary Batteries

3.1 Introduction

Rechargeable lithium-ion batteries are becoming increasingly important as power sources for portable consumer electronics. $LiCoO_2$ compound has been widely used as a cathode material in commercial lithium ion battery production because it is reasonably easy to synthesize and shows a stable discharge capacity. However, due to the high cost and toxicity of $LiCoO_2$, many efforts have been made to replace it. $LiNiO_2$ is an attractive material because of its low cost and its possibility of a high charge/discharge capacity. $LiNiO_2$ suffers two disadvantages, the difficulty in preparing of stoichiometric compounds and the poor cycle life. In an attempt to overcome the problems associated with $LiNiO_2$, a great deal of effort has been concentrated on doped materials that may possess properties superior to either $LiCoO_2$ or $LiNiO_2$. $LiCo_xNi_{1-x}O_2$ is the most attractive compound in this group, because Ni and Co can substitute for each other to form a solid solution of any percentage and without disturbance of the layer structure. Recently, there have been some studies of the $LiCo_xNi_{1-x}O_2$ series［Caurant, Baffier et al.1996; Banov, Bourikov et al. 1995］. These materials showed a higher capacity and energy density than

conventional $LiCoO_2$, while the presence of some low cost Mn in the samples leads to an oxide network favorable for good lithium intercalation［Nayoze, Ansart et al. 2001; Yoshio, Noguchi et al. 2000］. This chapter gives a synthesis method for $LiCo_xMn_yNi_{1-x-y}O_2$ (y = 0.2) that uses $Co_xMn_yNi_{1-x-y}(OH)_2$ precursor and Li_2CO_3 as the starting materials. The resulting compounds have demonstrated good battery performance.

3.2 Synthesis and physical characterization of $LiCo_xMn_yNi_{1-x-y}O_2$

$Co(NO_3)_2 \cdot 6H_2O$ (98%+, Aldrich), $Ni(NO_3)_2 \cdot 6H_2O$ (98%+, Aldrich) and $(CH_3CO_2)_2Mn \cdot 6H_2O$ were used as the starting materials and were dissolved in distilled water in stoichiometric amounts. The solution was slowly dripped into a 50 ml aqueous solution that was heated to 60 ºC while stirring. At the same time, a NaOH (6M) and NH_3OH (6.5M) solution mixture was slowly pumped into the original solution by a peristaltic pump to maintain the pH value of the solution at 11-12. The obtained mixed hydroxide co-precipitate was first filtered and thoroughly washed with distilled water, then dried at 65 ºC overnight. The precursor powders of $(Co_xMn_yNi_{1-x-y})(OH)_2$ were thus obtained. The precursor and Li_2CO_3 were mixed and ground using a pestle and mortar. The mixture was then pressed into a pellet at 800 kg/cm^2. The obtained disks were heated in oxygen at 700-900 ºC for 24 h

The $LiCo_xMn_yNi_{1-x-y}O_2$(x = 0.05,0.1 and 0.2, y = 0.2) powders were characterized by X-ray and SEM observation. Fig. 3-1 shows typical X-ray diffraction patterns of $LiCo_xMn_yNi_{1-x-y}O_2$. A pure phase of $LiCo_xMn_yNi_{1-x-y}O_2$ could be identified. All of the peaks can be indexed based on hexagonal α-$NaFeO_2$, in which the transition metal ions are surrounded by six oxygen atoms. Table 3-1 gives the computed values of the lattice parameters of the hexagonal cell. The lattice parameters, *a* and *c*, and the volume decreased with increasing cobalt content. The unit cell dimensions in a hexagonal setting shrink with an increase in the Co doping level because of the difference in size between trivalent cobalt and divalent nickel ions (since r^{2+}_{Ni} = 0.69 Å and r^{3+}_{Co} = 0.545 Å)[Yoshio, Noguchi et al. 2000; Shannon, Prewitt et al. 1969; Delmas, Saadoune et al. 1996].

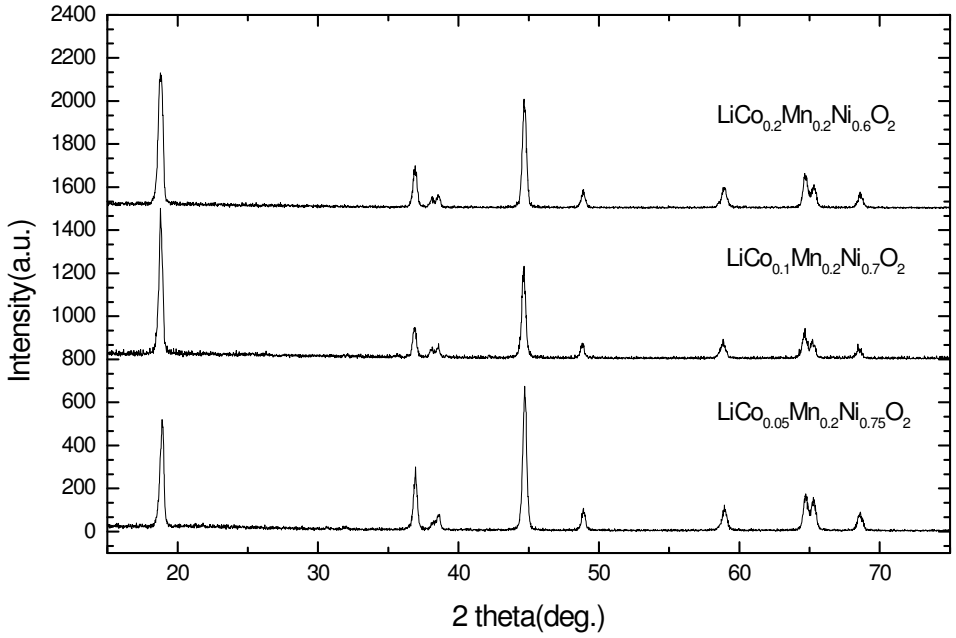

Fig. 3-1 XRD patterns of $LiCo_xMn_yNi_{1-x-y}O_2$.

Scanning electron micrographs of $LiCo_xMn_yNi_{1-x-y}O_2$ powders are shown in Fig.3-2. The powders consist of cubic grains with sizes in the range of 0.1-1 μm together with larger agglomerates.

Table 3-1 Lattice parameters and volume of the $LiCo_xMn_yNi_{1-x-y}O_2$ unit cell, and the intensity ratio I(003)/I(104).

Composition	a(Å)	c(Å)	Volume(Å)^3	Intensity ratio of I(003)/I(104)
$LiCo_{0.05}Mn_{0.2}Ni_{0.75}O_2$	2.8536	14.1540	99.7363	
$LiCo_{0.1}Mn_{0.2}Ni_{0.7}O_2$	2.8516	14.1426	99.5138	
$LiCo_{0.2}Mn_{0.2}Ni_{0.6}O_2$	2.8479	14.1313	99.4154	702/432

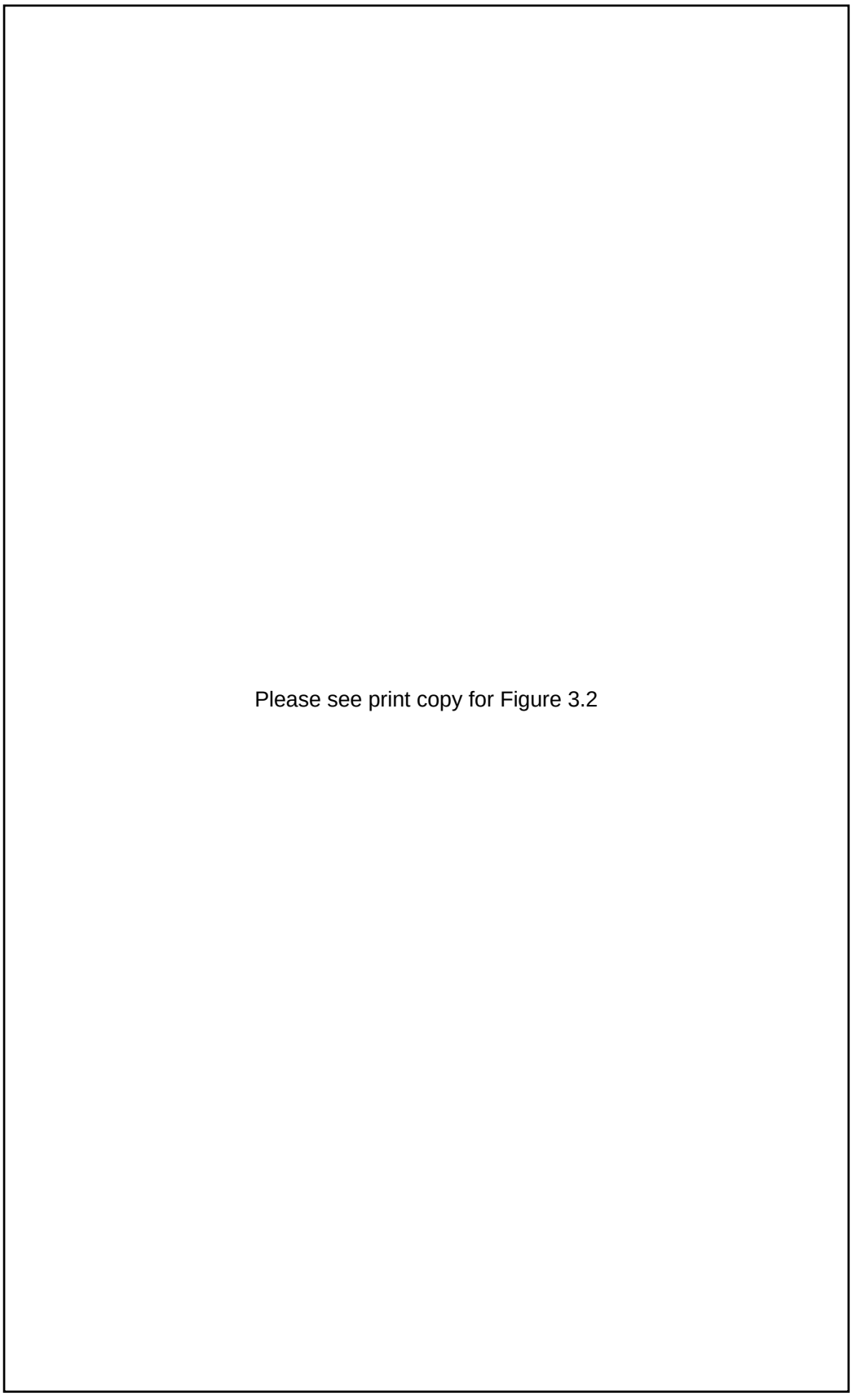
Please see print copy for Figure 3.2

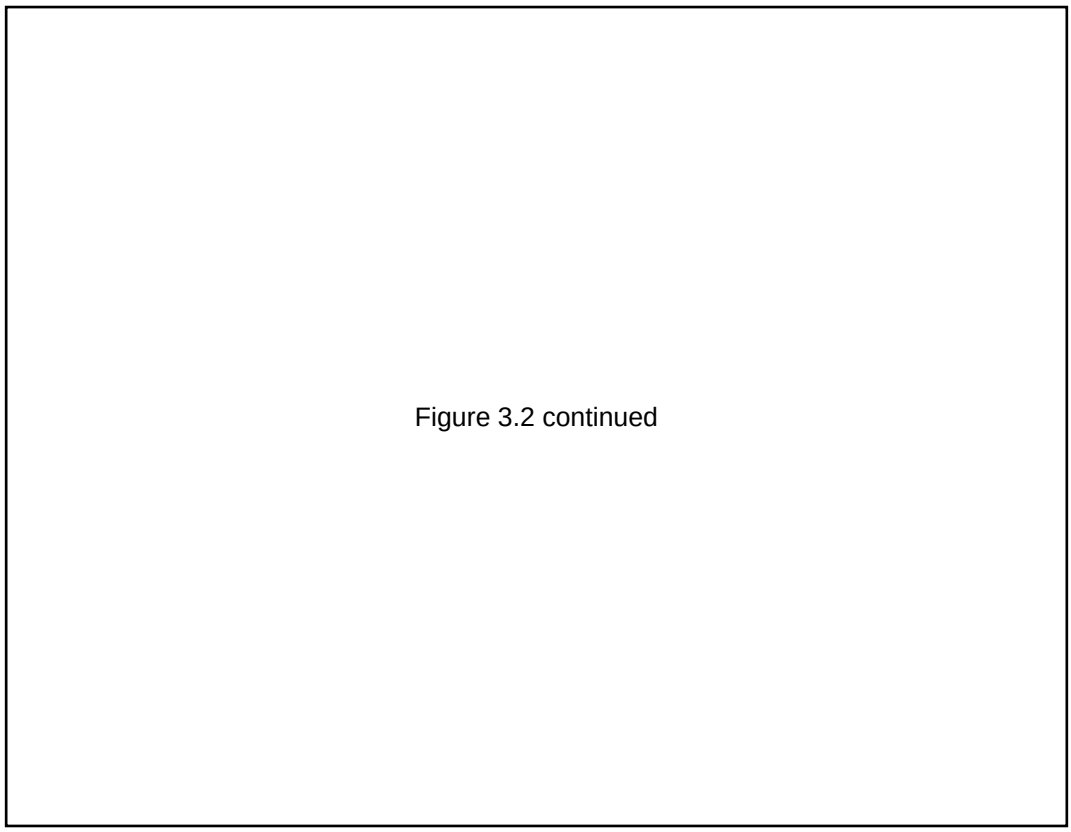

Fig. 3-2 SEM image of (a) $LiCo_{0.05}Mn_{0.2}Ni_{0.75}O_2$, (b) $LiCo_{0.1}Mn_{0.2}Ni_{0.7}O_2$, (c) $LiCo_{0.2}Mn_{0.2}Ni_{0.6}O_2$ powders.

3.3 Electrochemical characteristics of $LiCo_xMn_yNi_{1-x-y}O_2$

Teflon cells, using Li/ $LiCo_xMn_yNi_{1-x-y}O_2$ (x = 0.05, 0.1 and 0.2, y = 0.2) electrodes, were cycled in the voltage window of 3.0 to 4.3 V at 0.4 mA/cm^2. Figs. 3-3 and 3-4 show the initial charge/discharge profiles. The charge capacities of $LiCo_{0.1}Mn_{0.2}Ni_{0.7}O_2$ and $LiCo_{0.2}Mn_{0.2}Ni_{0.6}O_2$ were smaller than that of $LiCo_{0.05}Mn_{0.2}Ni_{0.75}O_2$. Their irreversible capacities in the first cycle were also higher than for $LiCo_{0.05}Mn_{0.2}Ni_{0.75}O_2$. The discharging potentials increase with increasing Co doping level. However, the curve shapes of $LiCo_{0.1}Mn_{0.2}Ni_{0.7}O_2$ and $LiCo_{0.2}Mn_{0.2}Ni_{0.6}O_2$ were very similar to each other. The three materials showed large

initial discharge capacities of 140-170 mAh/g. The initial discharge capacity of $LiCo_{0.05}Mn_{0.2}Ni_{0.75}O_2$ was the highest, but with a lower (average) discharge potential compared to the two other materials due to its high Ni content. The charging capacities of $LiCo_{0.1}Mn_{0.2}Ni_{0.7}O_2$ and $LiCo_{0.2}Mn_{0.2}Ni_{0.6}O_2$ were similar. However, $LiCo_{0.2}Mn_{0.2}Ni_{0.6}O_2$ demonstrated the highest discharge potential.

Cyclic voltammetry measurements were performed on $LiCo_{0.05}Mn_{0.2}Ni_{0.75}O_2$ and $LiCo_{0.2}Mn_{0.2}Ni_{0.6}O_2$ electrodes at a sweep rate of 0.1 mV/s over a voltage of 3.0 to 4.4V. Fig. 3-5 (b) shows that well-defined anodic and catholic peaks are observed at 3.88 and 3.73 V, respectively. This means that the extraction of Li^+ occurs easily from an ordered and stabilized layer structure and that the difference between the cathode and anode peaks is less than 200 mV, which resembles the situation for the pure $LiCoO_2$.

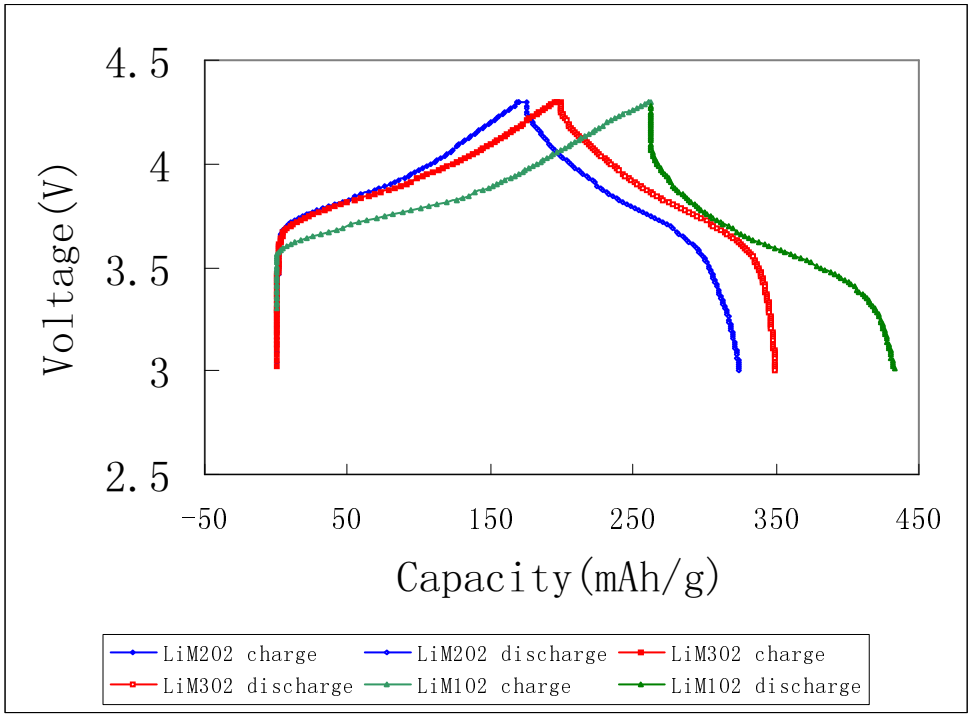

Fig. 3-3 $LiCo_xMn_yNi_{1-x-y}O_2$ charge-discharge curves. (LiM_1O_2 is $LiCo_{0.05}Mn_{0.2}Ni_{0.75}O_2$, LiM_2O_2 is $LiCo_{0.1}Mn_{0.2}Ni_{0.7}O_2$ and LiM_3O_2 is $LiCo_{0.2}Mn_{0.2}Ni_{0.6}O_2$.)

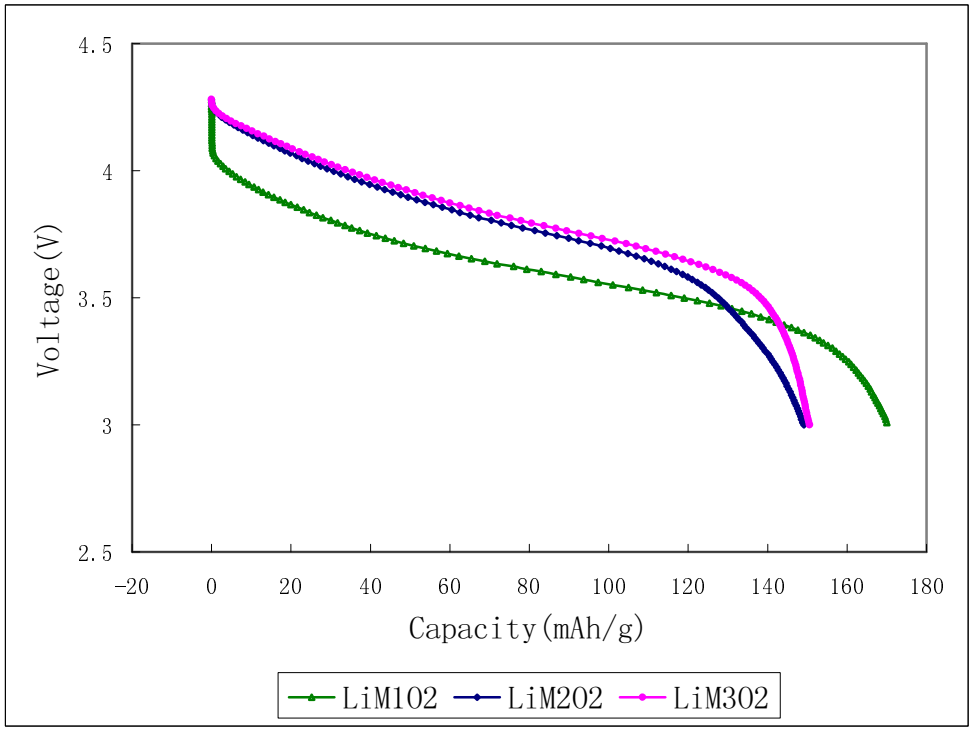

Fig. 3-4 $LiCo_xMn_yNi_{1-x-y}O_2$ discharge curves. (LiM_1O_2 is $LiCo_{0.05}Mn_{0.2}Ni_{0.75}O_2$, LiM_2O_2 is $LiCo_{0.1}Mn_{0.2}Ni_{0.7}O_2$ and LiM_3O_2 is $LiCo_{0.2}Mn_{0.2}Ni_{0.6}O_2$.)

In Fig. 3-5 (a), two reduction peaks at 3.74 and 4.16 V are observed during the discharge process. The reduction peak at 4.16 V is possibly associated with the participation of Mn in the lithiation reaction.

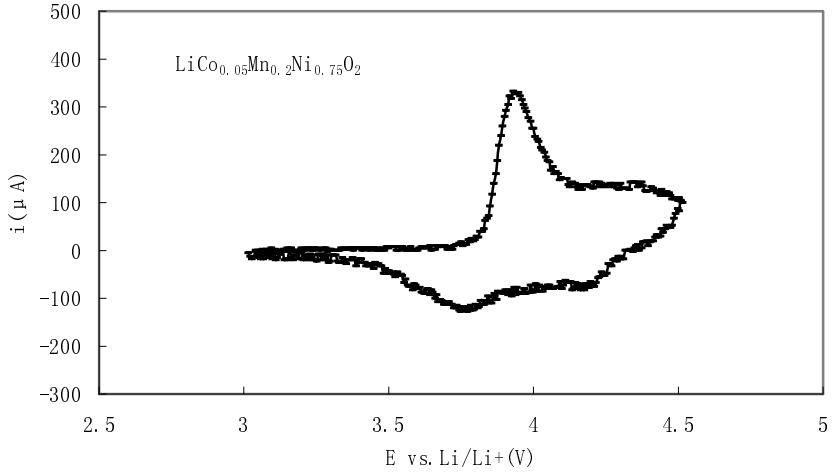

(a)

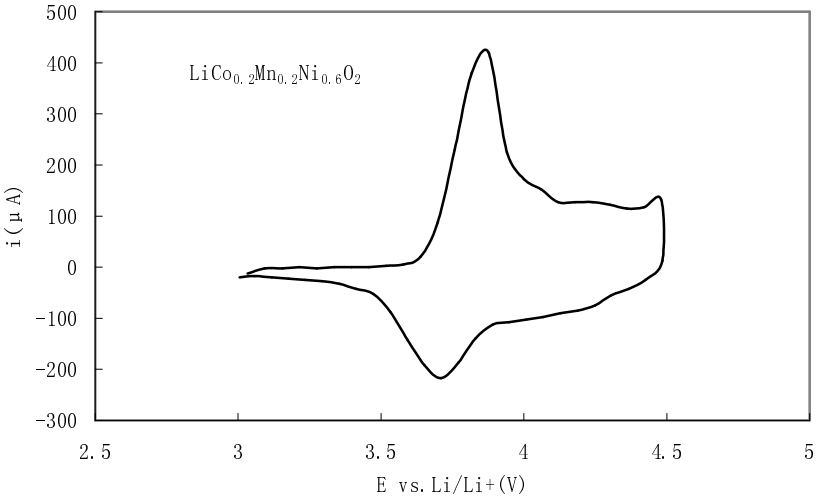

(b)

Fig. 3-5 Cyclic voltammograms of (a) $LiCo_{0.05}Mn_{0.2}Ni_{0.75}O_2$ and (b) $LiCo_{0.2}Mn_{0.2}Ni_{0.6}O_2$ electrodes.

In order to investigate the kinetics of the electrode process, ac impedance spectra were measured after one charge-discharge cycle for $LiCo_{0.1}Mn_{0.2}Ni_{0.7}O_2$ electrode. The 99999999Nyquist plots obtained at different potentials under different conditions for $LiCo_{0.1}Mn_{0.2}Ni_{0.7}O_2$ are shown in Fig. 3-6.

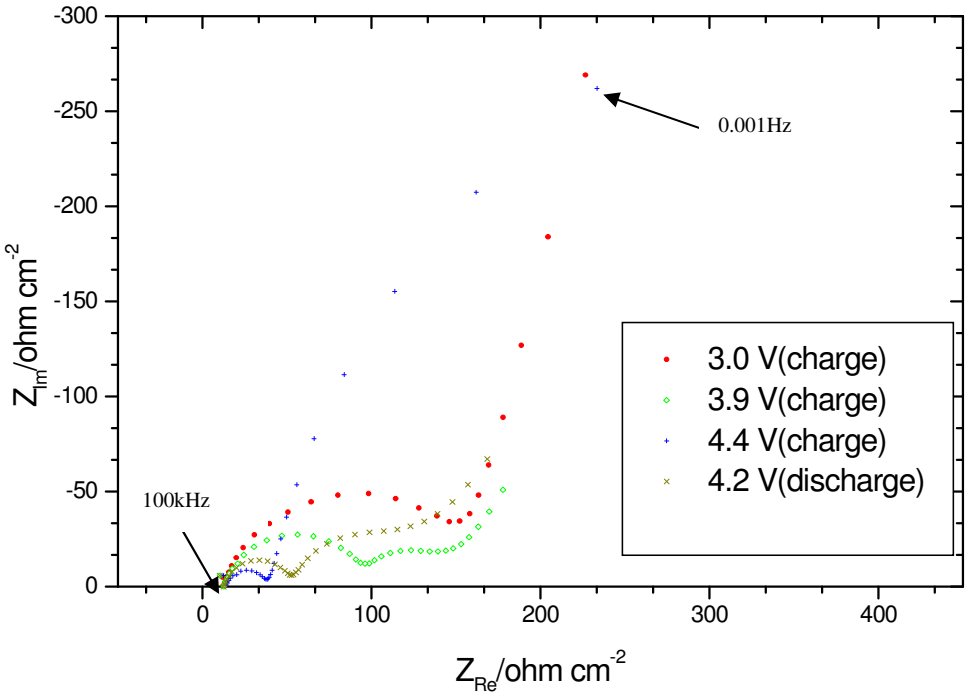

Fig. 3-6 Impedance spectra for $LiCo_{0.1}Mn_{0.2}Ni_{0.7}O_2$/Li cell during charge-discharge cycling.

Initially, EIS experiments were performed on working electrodes in the OCV state, then potentiostatically charged to 4.4 V and discharged to 3.0 V. Only one semicircle was observed in the lower voltage state during charge and discharge, while two semicircles were observed in the higher voltage charged and discharged states,

which generally correspond to the migration within the surface layer and the charge transfer process, respectively. The reason for only one semicircle at 3.0 V (OCV) is that a passivation film has not been formed on the surface of cathode, while the single semicircle for the electrode charged to 4.4 V is because the passivated film on the cathode surface is partly destroyed by the deintercalation of lithium ions, so that the resistance of the SEI film decreases very rapidly. The two semicircles in the high and intermediate frequency regions overlap and appear to be one. The 45° line in the low-frequency region presents the typical characteristics of the Warburg impedance, Z_w, which generally reflects the diffusion process of lithium within the bulk electrode. A comparision of the EIS Nyquist complex plots (Fig. 3-6) shows that the size of the semicircle drastically decreases with charging, then it starts increasing with discharging. Zview 2.3 C software was used to quantitatively analyze the condition of the cathodes, and the situation at the cathodes can be approximately represented by the equivalent circuit in Fig. 3-7. In this circuit a constant phase angle element, Z_w', rather than the true double capacitances, is taken into account due to the depressed nature of the semicircles. For rough or porous electrodes, such as the electrodes being analyzed here, the ac signal penetration depth is comparable to the depth of the pores, especially at high frequencies, and the frequency dispersion of the impedance is analogous to a nonuniform transmission line. Therefore, such a nonfaradaic response can be represented by a constant phase angle element, Zw', with the form

$$Z_w' = A_w' (j\omega)^{-m} = A_w'\omega^{-m}[\cos(m\pi/2)-j\sin(m\pi/2)] \qquad 0 < m < 1$$

where A is termed the Z_w' factor, and m is the Z_w' exponent.

Across the surface layer, the ion transport may be represented by the insertion-ion resistance, R_{sl}, and the surface-layer capacitance, C_{sl}. R_e is the solution resistance of the cell, R_{ct} is the cathode charge-transfer resistance, and Z_w is the Warburg impedance. Table 3-2 lists the results calculated from ac impedance spectra based on the equivalent circuit shown in Fig. 3-7 using ZView 2.3C software.

From Table 3-2, it is obvious that the solution resistances (R_e) of the cell at all voltages are similar, while the charge transfer resistance (R_{ct}) and the insertion-ion resistance (R_{sl}) significantly decrease with charging. Generally, for the cathode of a lithium ion battery, the value of R_{ct} reflects the ion transfer in the composite cathode and relates to the electronic conductivity of the electrode. R_{sl} is the resistance that occurs while ions transfer through the surface layer, i.e. the passivation film caused by the reaction between the electrode and electrolyte. Therefore, the increase in the diameter of the semicircle with charging is mainly ascribed to an increase in the electronic conductivity, which is induced by lithium ion deintercalation during cycling. It has been reported that the conductivity of Li_xCoO_2 changed dramatically with composition [Levasseur, Menetrier et al. 2000; Imanishi, Fujiyoshi et al. 1999]: it behaves like a metal at x = 0.6 and a typical semiconductor at x =1.1, changing by 2 to 4 orders of magnitude at ambient temperature.

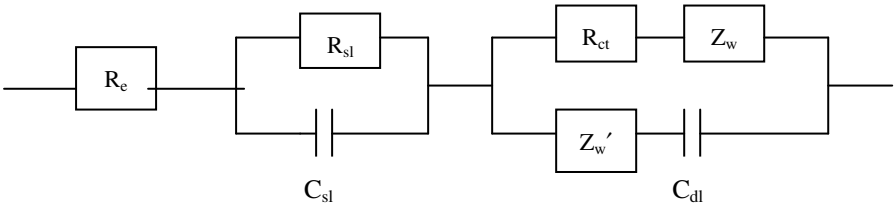

Fig. 3-7 Equivalent circuit for the $LiCo_{0.1}Mn_{0.2}Ni_{0.7}O_2$ electrode. R_{sl} is the insertion-ion resistance, and C_{sl} the surface-layer capacitance, R_e is the solution resistance of the cell, R_{ct} is the cathode charge-transfer resistance, and Z_w is the Warburg impedance.

Table 3-2 Results of AC impedance analysis of $LiCo_{0.1}Mn_{0.2}Ni_{0.7}O_2$ compound during charge-discharge cycling. (R_{sl} is the insertion-ion resistance, R_e is the solution resistance of the cell, R_{ct} is the cathode charge-transfer resistance.)

	R_e (Ω)	R_{ct}(Ω)	R_{sl}(Ω)
3.0V (Charge)	12.17	121.35	106.12
3.9V (Charge)	11.61	91.26	78.41
4.4V (Charge)	13.59	17.98	19.24
4.2V (Discharge)	11.83	44.25	102.36

On the other hand, when Li^+ ions are electrochemically extracted from Li $Co_{0.1}Mn_{0.2}Ni_{0.7}O_2$, Ni^{2+} or Co^{3+} ions are oxidized to Ni^{4+} or Co^{+4}. Ni^{4+} or Co^{+4} ions are very reactive in nature and tend to react with the organic electrolyte, causing the decomposition product deposited on the surface of the electrode to form a passivationfilm [Arova, Popov et al. 1998; Bohnke, Bohnke et al. 1997]. However, with further lithium ion deintercalation, the passivation film formed could be partly destroyed, leading to a decrease of R_{sl}. Even the impedance spectra showed only one semicycle when the working electrodes were charged to 4.4 V. This means that the surface layer is easily formed in the higher voltage state, but the lithium ion extraction could destroy the surface layer.

3.4 Conclusions

Single phase electroactive $LiCo_xMn_yNi_{1-x-y}O_2$ compounds were obtained from lithium compounds and $Co_xMn_yNi_{1-x-y}(OH)_2$ precursor by heating at 850-900 °C. The synthesized $LiCo_xMn_yNi_{1-x-y}O_2$ has good micromorphology and uniform particle size. $LiCo_{0.2}Mn_{0.2}Ni_{0.6}O_2$ has the best electrochemical characteristics among the three materials studied and has an initial discharge capacity of 150 mAh/g.

Chapter 4

Preparation and properties of spherical $LiNi_{0.75}Co_{0.25}O_2$ as a cathode for Lithium Ion Batteries

4.1 Introduction

In order to improve the specific energy and reduce the materials cost of lithium ion battery, $LiNiO_2$ and its derivatives have been extensively studied as a cathode material to replace $LiCoO_2$, which is widely used for commercial lithium-rechargeable batteries. The electrochemical properties of Li_zNiO_2 depend strongly on the stoichiometry of Li, i.e., deviation of the value of z from unity. Unlike Li_zCoO_2, a small deviation from z = 1 in Li_zNiO_2 is reported to induce cation mixing, which means that some Li^+ ions go into the 3b sites of the Ni layer and some Ni^{3+} ions go into the 3a sites of the Li layer. Such a structural disorder is believed to be a main cause of the unsatisfactory electrochemical performance of Li_zNiO_2 [Thomas, David et al. 1995; Kanno, Kubo et al. 1994; Morales, Perez-vicente et al. 1990; Rossen, Jones et al. 1993; Dutta, Manthiram et al. 1992]. To solve these problems, a great deal of effort has been concentrated on doped materials that may possess properties superior to $LiNiO_2$. Recently, $LiNi_{1-x}M_xO_2$, where M is one of the transition metals, has been studied extensively in order to solve these problems by stabilizing the structure of $LiNiO_2$ [Okada, Takahashi et al. 1997; Nitta, Okamura et al. 1995; Arai, Okada et al. 1997; Nayoze, Ansart et al. 2001; Pouillerie, Croguennec et al. 2000].

The results have shown that, in these substituted compounds, cobalt substitution sharply decreases the non-stoichiometry of lithium nickel oxide and thus stabilizes the alternating layered structure. So $LiCo_xNi_{1-x}O_2$ has been identified as one of the most attractive materials [Caurant, Baffier et al. 1996; Yoshio, Noguchi et al. 2000].

Spherical nickel hydroxides are widely used as positive electrode materials in Ni-Cd and Ni-MH batteries. This is because spherical shaped powder particles have a high packing density and a homogeneous micromorphology. When those powders with spherical shaped particles are used as electrode materials, more active materials can be loaded on the electrode. Therefore, the energy density of the batteries can be significantly improved. Similar principle can be applied to lithium-ion batteries when using spherical electrode materials. Recently, spherical $LiCo_xNi_{1-x}O_2$ has become much more attractive due to its high tap density and highly uniform morphology [Cho, Kim et al. 1999]. In this chapter, the spherical $LiNi_{0.75}Co_{0.25}O_2$ compounds were synthesized by using spherical $Ni_{0.75}Co_{0.25}(OH)_2$ and $LiOH{\cdot}H_2O$ as precursors. The physical and electrochemical properties of spherical $LiNi_{0.75}Co_{0.25}O_2$ cathodes were systematically tested.

4.2 Synthesis and structural analysis of spherical $LiNi_{0.75}Co_{0.25}O_2$

The spherical $Ni_{0.75}Co_{0.25}(OH)_2$ precursor powders were synthesized by chemical co-precipitation and controlled crystallization. The reagents $NiSO_4{\cdot}6H_2O$ (99%, Aldrich) and $CoSO_4{\cdot}7H_2O$ (99.9%, Aldrich) were dissolved in deionized water and

homogeneously mixed. A mixture of NaOH and NH_4OH solution was added to precipitate the hydroxide. The pH (= 10-11) value, temperature and pressure were strictly controlled. The precipitate was then aged in a pressurized vessel at 60 – 80 °C for a few hours to allow the spherical crystals to grow. The resultant crystals were thoroughly washed using deionized water and then dried in a vacuum oven to yield spherical $(Ni_{0.75}Co_{0.25})(OH)_2$ powders. The spherical $(Ni_{0.75}Co_{0.25})(OH)_2$ and $LiOH{\cdot}H_2O$ precursor powders were intimately mixed with a molar ratio of $Ni_{0.75}Co_{0.25}$: Li = 1:1.04 (due to evaporation of Li during high temperature sintering) by mortar and pestle. The mixture was then sintered at high temperature between 650 and 850 °C for 12 h under flowing oxygen to obtain spherical $LiNi_{0.75}Co_{0.25}O_2$ compounds. Non-spherical $LiNi_{0.75}Co_{0.25}O_2$ compounds were also prepared by sintering the precursors Li_2CO_3, NiO and CoO at 750 °C under flowing oxygen.

$Ni_{0.75}Co_{0.25}(OH)_2$ is a cobalt-doped derivative of $Ni(OH)_2$. Fig. 4-1 shows the X-ray diffraction pattern of spherical $Ni_{0.75}Co_{0.25}(OH)_2$ powders. The $Ni_{0.75}Co_{0.25}O_2$ compounds adopted the β-$Ni(OH)_2$ phase. All diffraction lines were indexed based on a hexagonal structure (SG: p-3m1). No impurity phases were detected by x-ray diffraction. This clearly demonstrates that Co^{2+} can partially substitute for Ni^{2+} in the β-$Ni(OH)_2$ structure. An SEM image of the as-prepared $Ni_{0.75}Co_{0.25}O_2$ precursor powder is presented in Fig. 4-2. The $Ni_{0.75}Co_{0.25}O_2$ particles have a spherical shape and an average particle size of a few microns.

The precursor mixtures of spherical $Ni_{0.75}Co_{0.25}O_2$ and $LiOH{\cdot}H_2O$ were sintered together at different temperatures, 650, 700, 750, 800 and 850 °C, respectively. Fig. 4-3 shows the x-ray diffraction patterns of $LiNi_{0.75}Co_{0.25}O_2$ obtained by sintering at different temperatures. When sintered at low temperature, eg. 650, 700, and 750 °C, some impurity phases were detected. However, when sintered above 800 °C, pure $LiNi_{0.75}Co_{0.25}O_2$ was obtained.

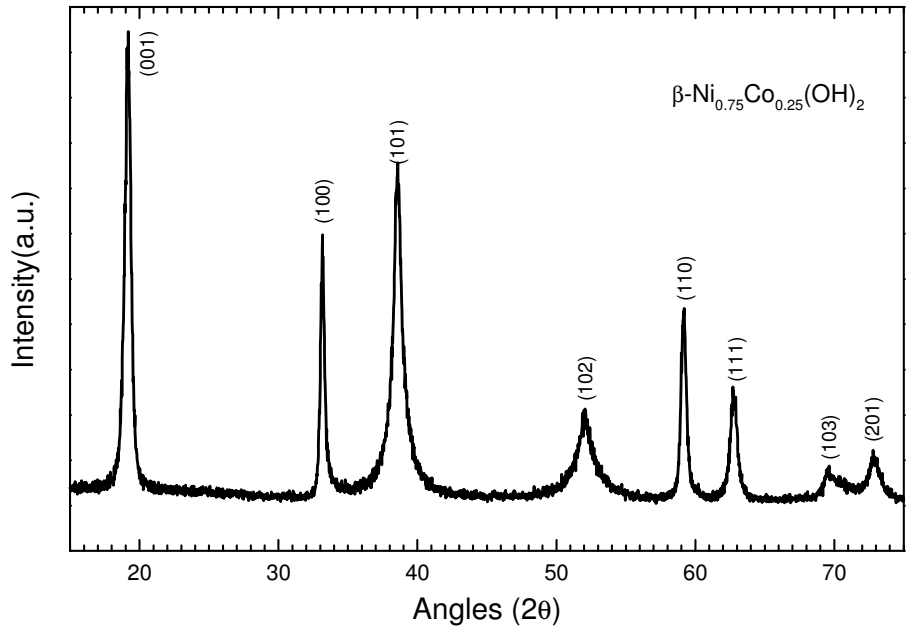

Fig. 4-1 X-ray diffraction pattern of β-$Ni_{0.75}Co_{0.25}(OH)_2$.

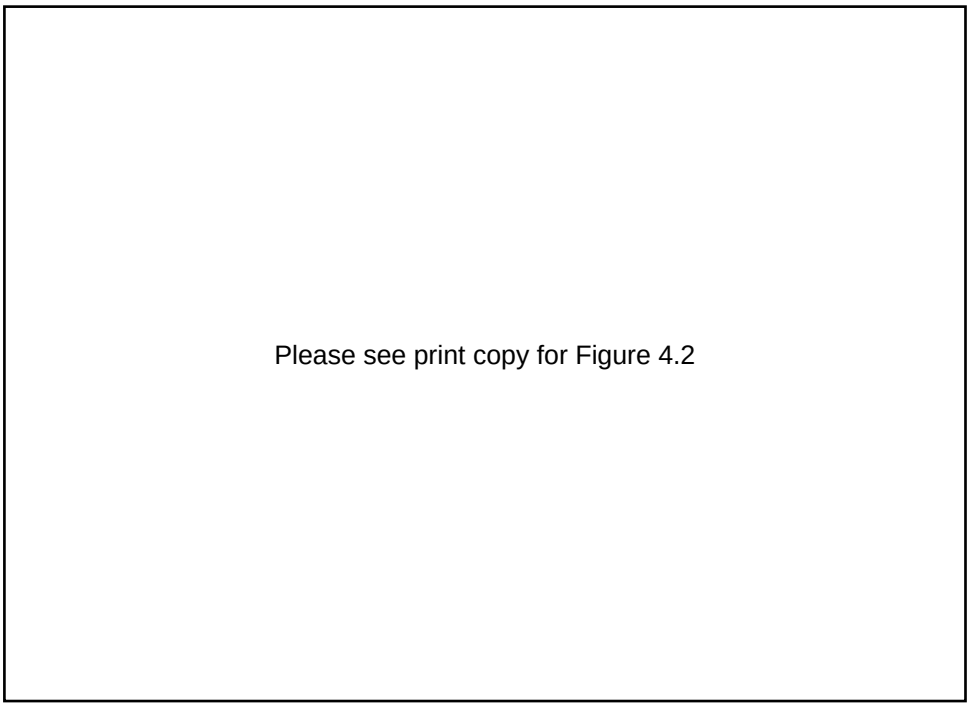

Fig. 4-2 SEM image of the spherical $Ni_{0.75}Co_{0.25}(OH)_2$ precursor.

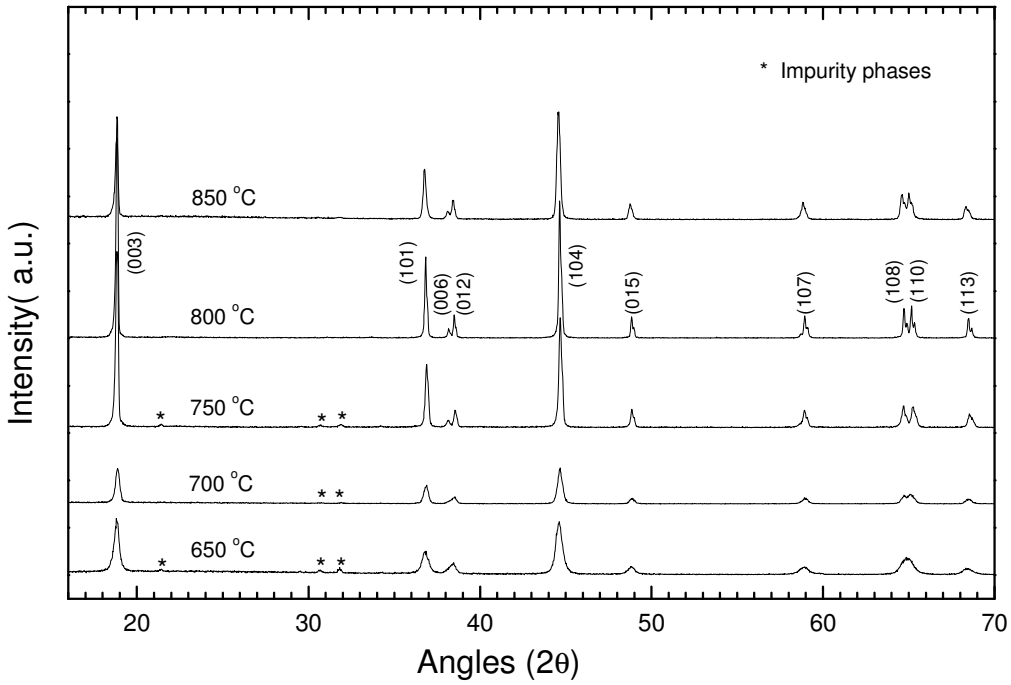

Fig. 4-3 X-ray diffraction patterns of $LiNi_{0.75}Co_{0.25}O_2$ compounds sintered at different temperatures.

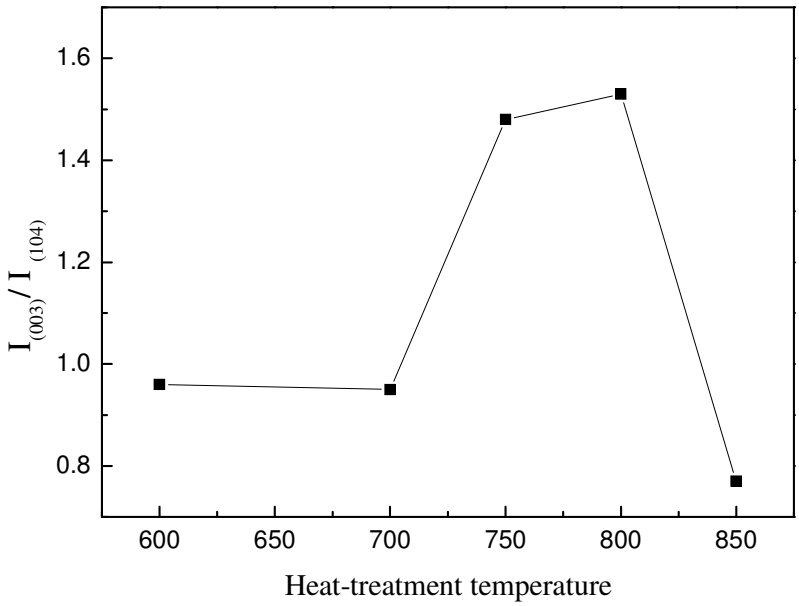

Fig. 4-4 Variation of integrated intensity ratios of (003) to (104) ($I_{(003)} / I_{(104)}$) of $LiNi_{0.75}Co_{0.25}O_2$ compounds as a function of heat-treatment temperature.

In Fig. 4-3, the diffraction lines were indexed based on a hexagonal α-$NaFeO_2$ structure (R3m). The peak intensity ratios of (003) to (104) of the XRD spectra shown in Fig. 4-3 are plotted against heat-treatment temperature for spherical $LiNi_{0.75}Co_{0.25}O_2$ compounds (Fig. 4-4). The intensity ratio increased as the reaction temperature increased up to 800 °C. However, the intensity ratio decreased when the temperature was further increased to 850 °C. Cho and Kim et al. have reported that the intensity ratio of (003) to (104) peaks of their $LiNi_{1-x}Co_xO_2$ increased as the reaction temperature was elevated [2000]. In their preparation technique, the highest temperature used was 750 °C. This observation on the trend of the intensity ratio is

consistent with our present observation. The intensity ratio has been reported to be closely related to the undesirable cation mixing, which is reduced as the value of the ratio is increased [Ohzuku, Ueda et al. 1993]. Therefore, it is reasonable to conclude that the extent of cation mixing in the spherical $LiNi_{0.75}Co_{0.25}O_2$ decreased as the temperature increased up to 800 °C. Further increases in the heat-treatment temperature could cause structural disorder due to the evaporation of Li at high temperature. The other related observations are that the splits in the (006)/(012) and (108)/(110) doublets both become sharper with the temperature increases, which indicates that a highly ordered layered structure is formed when the temperature is between 750 and 800°C. The lattice parameters *a* and *c* of $LiNi_{0.75}Co_{0.25}O_2$ synthesized at 800°C are 2.859 Å and 14.164 Å.

Fig. 4-5 shows SEM images of as-prepared $LiNi_{0.75}Co_{0.25}O_2$ powder sintered at 800 °C. A general view of $LiNi_{0.75}Co_{0.25}O_2$ particles is shown in Fig. 4-5(a). The $LiNi_{0.75}Co_{0.25}O_2$ particles retain the spherical shape. Fig. 4-5(b) shows a magnified view of a single spherical $LiNi_{0.75}Co_{0.25}O_2$ particle, which consists of many small crystals. During the sintering process, the spherical shape of the precursor $Ni_{0.75}Co_{0.25}O_2$ particles is maintained. Therefore, we can deduce that the formation of $LiNi_{0.75}Co_{0.25}O_2$ phase is a diffusion process during which Li^+ ions diffuse into spherical β-$Ni(OH)_2$ precursor particles at high temperature. The final product retains the spherical shape of the precursor particles.

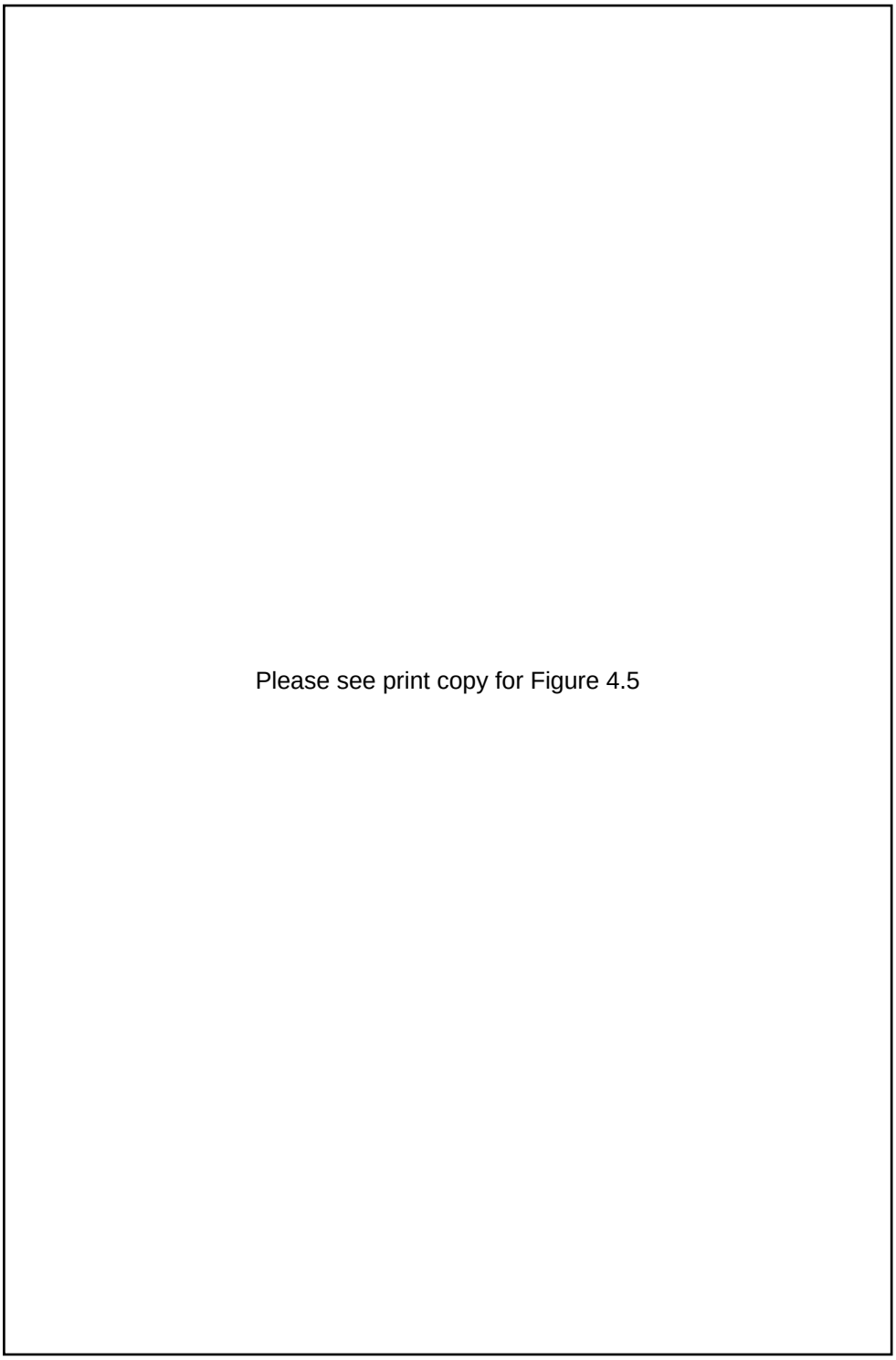

Fig. 4-5 SEM images of spherical $LiNi_{0.75}Co_{0.25}O_2$ particles. (a) General view of spherical particles; (b) a single spherical particle.

Temperature-dependent magnetic susceptibility measurements of the spherical $LiNi_{0.75}Co_{0.25}O_2$ powders were performed in a dc field of 1000 G using a Quantum Design Magnetometer (PPMS, USA). Fig. 4-6 shows the temperature dependence of the magnetic mole susceptibility of spherical $LiNi_{0.75}Co_{0.25}O_2$ powders. As a comparison, the mole susceptibility of non-spherical $LiNi_{0.75}Co_{0.25}O_2$ is also presented in Fig. 4-6. The magnetic susceptibility of the spherical and non-spherical $LiNi_{0.75}Co_{0.25}O_2$ powders obeys the Curie-Weiss law: $\chi = C/(T - \theta)$, where χ is magnetic susceptibility, C is the Curie constant and θ is the paramagnetic Curie temperature. The spherical $LiNi_{0.75}Co_{0.25}O_2$ powders have a negative paramagnetic Curie temperature θ = -25 K, indicating antiferromagnetic behavior below T_c, while, non-spherical $LiNi_{0.75}Co_{0.25}O_2$ powders have a positive paramagnetic Curie temperature θ = 19 K, indicating ferromagnetic interactions of the magnetic centers (Ni^{3+} and Co^{3+}) [Hirota, Nakazawa et al. 1991; Yamaura, Takano et al. 1996; Spahr, Novak et al. 1998].

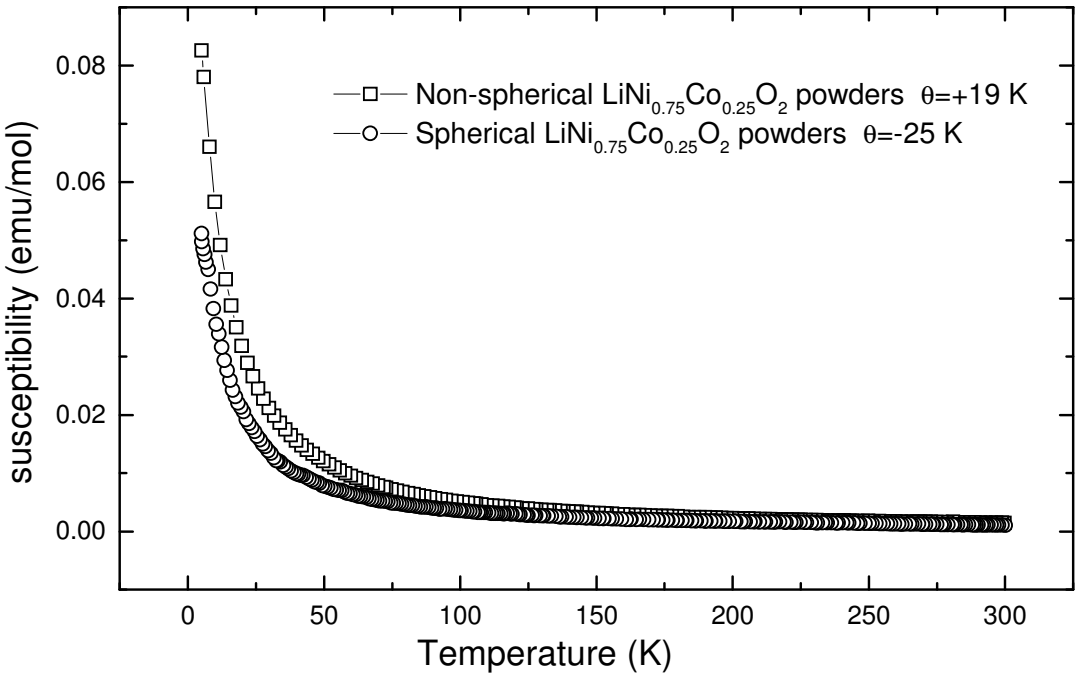

Fig. 4-6 The mole magnetic susceptibility χ vs. T (K) for $LiNi_{0.75}Co_{0.25}O_2$ compounds.

$LiNi_{0.75}Co_{0.25}O_2$ compounds have a rhombohedral-layered structure ($R\bar{3}m$), in which Li^+, Ni^{3+} /Co^{3+}, and O^{2-} ions occupy the 3a, 3b and 6c sites, respectively [Guilmard 2003]. Both Ni^{3+} ($3d^7$, low spin) and Co^{3+} ($3d^6$, low spin) are magnetic ions. Non-magnetic Li^+ layers alternate with magnetic Ni^{3+}/Co^{3+} layers. Therefore, magnetic correlations between Ni^{3+}/Co^{3+} ions in the ideal $LiNi_{0.75}Co_{0.25}O_2$ crystal structure are considered to be two-dimensional (Ni^{3+}/Co^{3+} (3b) - Ni^{3+}/Co^{3+} (3b)). Once there are magnetic Ni^{3+}/Co^{3+} ions in 3a (Li^+) sites, a three-dimensional magnetic interaction between Ni^{3+}/Co^{3+} (3b) - Ni^{3+}/Co^{3+} (3a) layers will be created, which usually causes ferromagnetic anomalies. The ferromagnetism observed for

non-spherical $LiNi_{0.75}Co_{0.25}O_2$ indicates cation disorder in its layered structure. In contrast, the spherical $LiNi_{0.75}Co_{0.25}O_2$ powders demonstrate strong antiferromagnetism, which could result from a frustrated antiferromagnetism of the trigonally arranged Ni^{3+}/Co^{3+} ions within one layer [Ott, Endres et al. 1998; Rosenberg, Stelmaszyk et al. 1994]. Therefore, the spherical $LiNi_{0.75}Co_{0.25}O_2$ powders have a more ordered layered structure than that of non-spherical $LiNi_{0.75}Co_{0.25}O_2$ compounds.

4.3 Electrochemical characteristics of spherical $LiNi_{0.75}Co_{0.25}O_2$ cathodes

Cyclic voltammetry measurement were performed on a spherical $LiNi_{0.75}Co_{0.25}O_2$ (heat-treated at 800 °C) electrode at a sweep rate of 0.1 mV/s. Fig. 4-7 shows the CV curve of the $LiNi_{0.75}Co_{0.25}O_2$ electrode, in which a pair of well-defined redox reaction peaks were observed. The main oxidation peak was observed at 4.15 V, and the main reduction peak was located at 3.85 V. During the anodic and cathodic scanning process, a pair of additional oxidation and reduction peaks appeared in the CV profile, which are located at 4.25 and 4.18 V, respectively. The operating potential, which is related to the Fermi energy of the electrons in the 3d orbital, varies as: CoO_2 ($3d^5/3d^6$) > NiO_2 ($3d^6/3d^7$) [Ueda, Ohzuku 1994]. If Ni^{3+} cations in the $LiNi_{0.75}Co_{0.25}O_2$ cathode mainly contribute to the redox reaction during Li^+ insertion/extraction, these additional redox peaks observed at high potentials could be present because of the participation of Co^{3+} in the redox reaction since Co^{3+}/Co^{4+} has a higher potential than

that of Ni^{3+}/Ni^{4+}.

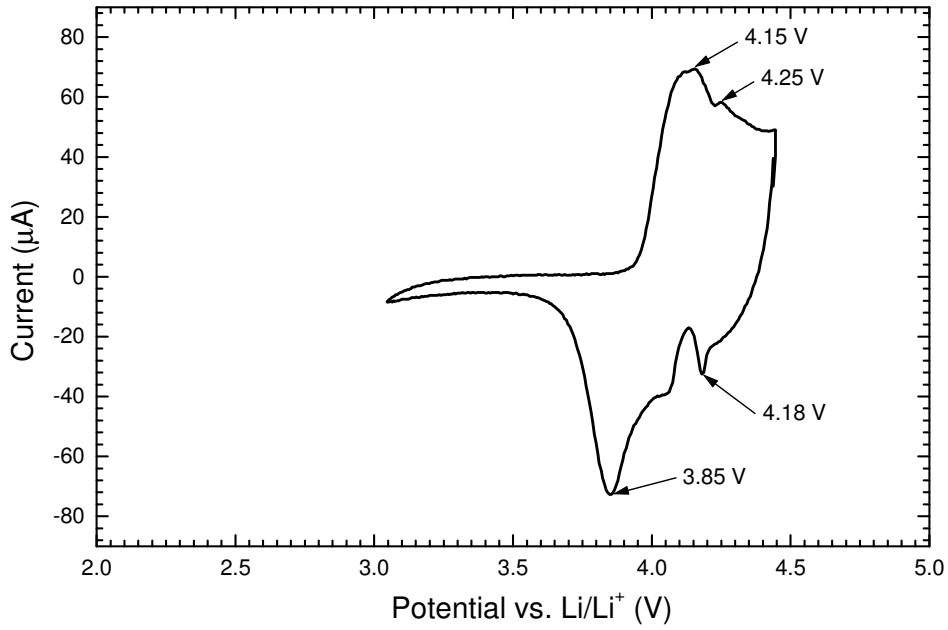

Fig. 4-7 Cyclic voltammogram of spherical $LiNi_{0.75}Co_{0.25}O_2$ cathode.

The first charge/discharge curve of the spherical $LiNi_{0.75}Co_{0.25}O_2$ cathode is shown in Fig. 4-8. The electrode was cycled in the voltage range of 3.0 - 4.3 V at a constant current density of 0.4 mA/cm^2. In the first cycle, the $LiNi_{0.75}Co_{0.25}O_2$ cathode delivered a reversible discharge capacity of 167.4 mAh/g, which is much higher than that of a $LiCoO_2$ cathode. There is a 40.6 mAh/g irreversible capacity in the first cycle. This irreversible capacity could be utilized to compensate for the lithium consumption on the surface of the carbon anode to form the SEI during the first charging process in commercial lithium ion batteries.

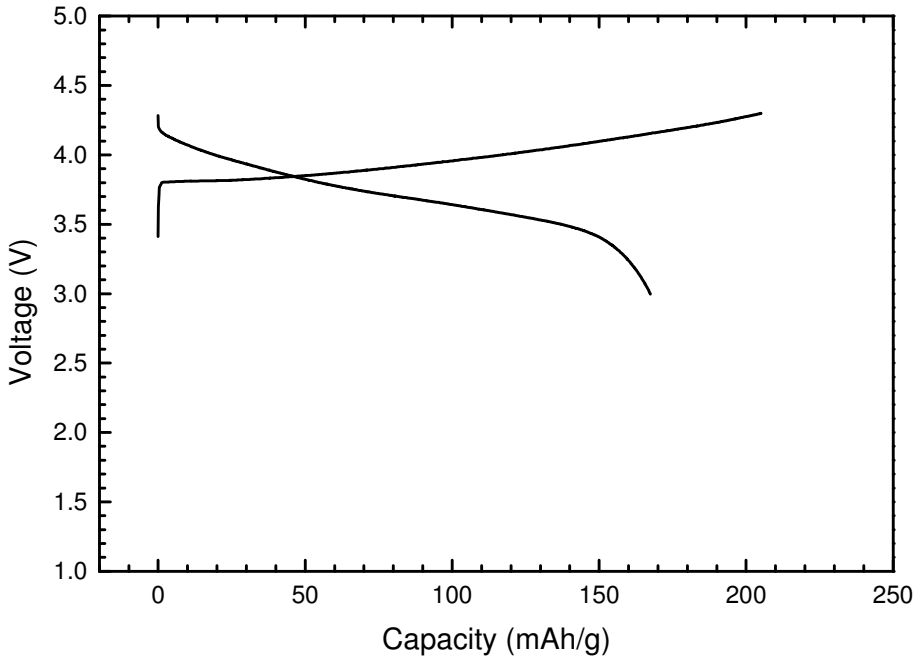

Fig. 4-8 The first charge/discharge curves of $LiNi_{0.75}Co_{0.25}O_2$ cathode.

In order to determine the cyclability of the spherical $LiNi_{0.75}Co_{0.25}O_2$ cathode materials, a $LiNi_{0.75}Co_{0.25}O_2$ cathode was cycled for 50 cycles. Fig. 4-9 shows the results of the cycling test. The spherical $LiNi_{0.75}Co_{0.25}O_2$ cathode materials demonstrated a stable cyclability over charge/discharge cycling. In our synthesis process, the spherical β-$Ni_{0.75}Co_{0.25}(OH)_2$ precursor was prepared by a solution route, in which Ni^{2+} and Co^{2+} ions were homogeneously mixed on the atomic level. When forming $LiNi_{0.75}Co_{0.25}O_2$ compounds, Ni^{2+} and Co^{2+} ions should distribute themselves uniformly in the crystal structure. The results of the magnetic susceptibility measurements confirmed that the spherical $LiNi_{0.75}Co_{0.25}O_2$ compounds have a highly ordered layered structure. These physical characteristics could contribute to the good electrochemical performance of the spherical $LiNi_{0.75}Co_{0.25}O_2$ cathode materials.

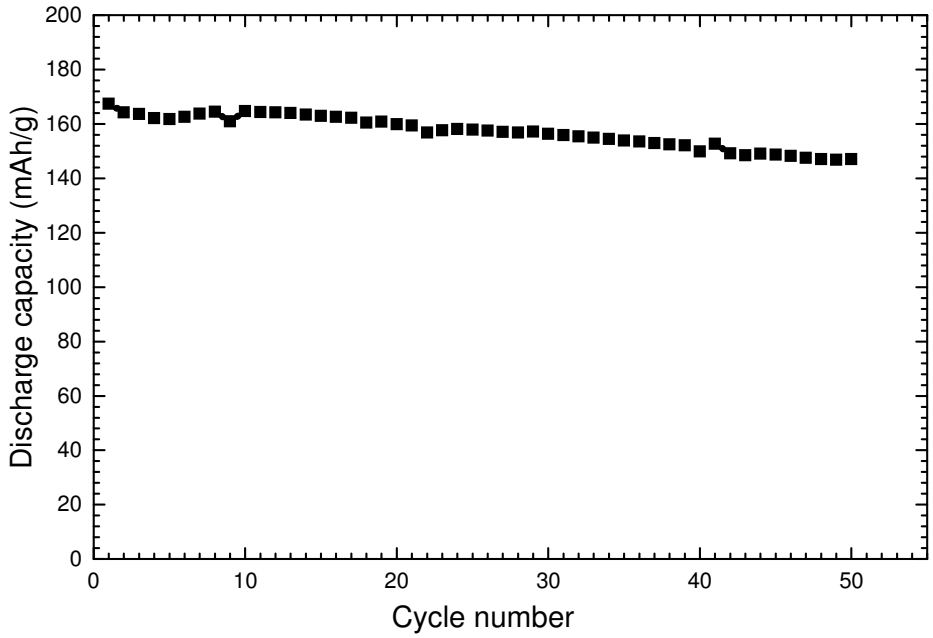

Fig. 4-9 The discharge capacity of $LiNi_{0.75}Co_{0.25}O_2$ cathode versus cycle number.

4.4 Conclusions

Single-phase spherical $LiNi_{0.75}Co_{0.25}O_2$ cathode materials were successfully synthesized by sintering $LiOH{\cdot}H_2O$ and spherical $Ni_{0.75}Co_{0.25}(OH)_2$ precursors at high temperature. The XRD and magnetic susceptibility measurements show that the spherical $LiNi_{0.75}Co_{0.25}O_2$ compounds sintered at 800 °C have a highly ordered layered structure. The spherical $LiNi_{0.75}Co_{0.25}O_2$ cathode materials which was heat-treated at 800 °C, demonstrated a high reversible capacity of 167 mAh/g and stable cyclability. When these spherical cathode materials are used as cathodes in lithium-ion batteries, high energy densities could be achieved.

Chapter 5

Carbon coated $LiFePO_4$ as cathode materials for Li-ion batteries

5.1 Introduction

Lithium-ion batteries have a great potential to be used as power sources for electric vehicles (EVs) and hybrid electric vehicles (HEVs). However, the cost, safety and environmental friendliness of cathode materials are major concerns for the applications of large-scale lithium-ion batteries due to the use of cobalt based oxides. The discovery of polyanion compounds with the general formula $Li_xM_y(XO)_z$ (M = transition metal, X = P, S, As, Mo or W), provides a new class of cathode materials for lithium-ion batteries [Padhi, Najundaswamy et al. 1997]. Among them, lithium iron phosphates have attracted particular interest. $LiFePO_4$ has a theoretical capacity of 170 mAh/g. It is inexpensive, non-toxic, and environmentally friendly. $LiFePO_4$ has an ordered olivine structure (SP: Pnma), in which FeO_6 octahedra share common corners in the bc plane. In the $LiFePO_4$ crystal structure, the oxygen atoms are arranged in a distorted, hexagonal close-packed arrangement, in which the lithium and iron atoms occupy octahedral sites, while the phosphorous atoms occupy tetrahedral sites. The strong P-O covalency stabilizes the anti-bonding Fe^{3+}/Fe^{2+} state through the Fe-O-X inductive effect to generate high operating potential [Streltsov, Belokoneva et

al. 1993; Andersson, Thomas 2001]. Therefore, $LiFePO_4$ has a high lithium intercalation voltage of 3.4 V versus lithium metal. However, $LiFePO_4$ suffers from low electronic conductivity, limiting its capacity and rate capacity.

The electronic conductivity of lithium iron phosphates can be improved by many different material processing approaches such as reducing the crystal size of $LiFePO_4$ [Prosini, Carewaka et al. 2002; Franger, Cras et al. 2002; Prosini, Carewaka et al. 2003; Takahashi, Tobishima et al. 2001], carbon addition [Bewlay, Wang et al. 2004; Deoff, Hu et al. 2003; Huang, Yin et al. 2001; Franger, Bourbon et al. 2004; Barker, Saidi et al. 2003; Bauer, Bellitto et al. 2004; Prosini, Zane et al. 2001], metal powder addition [Croce, Epifanio et al. 2002; Park, Son et al. 2004], and doping with supervalent ions [Wang, Bewlay et al. 2005; Chung, Blocking et al. 2002]. Therefore, the electrochemical performance of lithium iron phosphates can be significantly enhanced through the improvement of the electronic conductivity of the materials. In this investigation, carbon-included lithium iron phosphates were prepared via a sol-gel method and a carbon aerogel synthesis process, respectively, through which lithium iron phosphate and amorphous carbon are formed simultaneously. The electrochemical properties of as-prepared $LiFePO_4$-carbon composites as cathodes in lithium-ion cells were measured via various types of electrochemical testing.

5.2 Nanocrystalline $LiFePO_4$ synthesized via a sol-gel process

Sol-gel synthesis is one of the most promising solution-based methods and has been

widely used to synthesize materials with good battery activity. Many cathode materials, such as $LiCoO_2$[Fey, Chen et al. 1997], $LiNiO_2$ [Choi, Pyun et al. 1998], and $LiMn_2O_4$ [Sun, Jin et al. 1998], which were synthesized using the sol-gel process have shown an improved electrochemical performance. This kind of synthesis allows a better control of the morphology and texture of solid particles.

5.2.1 Synthesis and structural analysis of C-$LiFePO_4$

$FeC_2O_4 \cdot 2H_2O$, $Li(CH_3COO) \cdot 2H_2O$, H_3PO_4, and citric acid were used as the starting materials. The metal compounds were first dissolved in phosphoric acid and deionized water. This solution was mixed until homogeneous, and citric acid was added while stirring, until the molar ratio of citric acid to metal ions was 2:1. Ammonium hydroxide was added to the solution to adjust the pH to between 8 and 9. The solution was then heated to 80 ˚C under N_2 until a gel formed. After that, the gel was transferred to an alumina boat and heated under argon at various temperatures from 600 ℃ to 800 ℃ for 10 h.

Fig. 5-1 shows the x-ray diffraction data collected for $LiFePO_4$ compounds sintered at different temperatures. All samples were pure single phase as indexed with the orthorhombic pnmb space group, in which the oxygen atoms are arranged in a slightly distorted, hexagonal close-packed structure. No Bragg peaks related to carbon were detected.

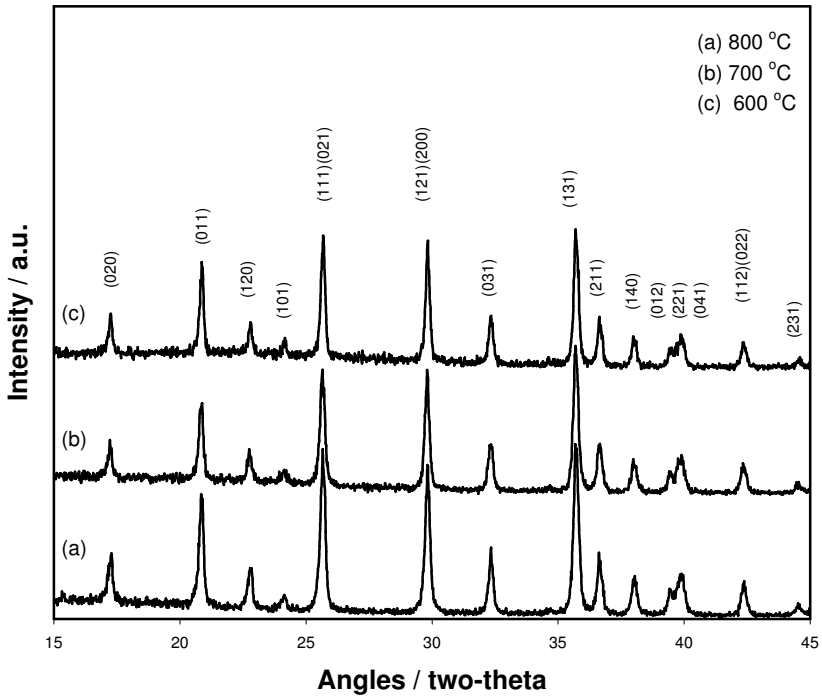

Fig. 5-1 X-ray diffraction patterns of C-$LiFePO_4$ compounds sintered at different temperature.

A TEM image of the $LiFePO_4$ powders is shown in Fig. 5-2(a). The powders have a primary crystal size ranging from 40 to 150 nm, and the crystals form loose agglomerates. The low crystallinity and porous agglomerate structure allow easy penetration of the electrolyte and provide a short pathway for lithium diffusion in the active material crystals. In order to examine the fine structure of the synthesized lithium iron phosphates, high resolution electron transmission spectroscopy (HRTEM) was performed on the powder samples. Fig. 5-2(b) shows a HRTEM image of a $LiFePO_4$ crystal edge. Spot EDX analysis confirmed that the outside layers are amorphous carbon and the inside crystallites are lithium iron phosphates. It clearly demonstrated that a thin layer of amorphous carbon formed a coating on the surface of

the $LiFePO_4$ crystals. During the synthesis process, the gel complexes and precursors were sintered in an inert atmosphere. Carbon was formed from the decomposition of the acetate and oxalate precursors as well as citric acid.

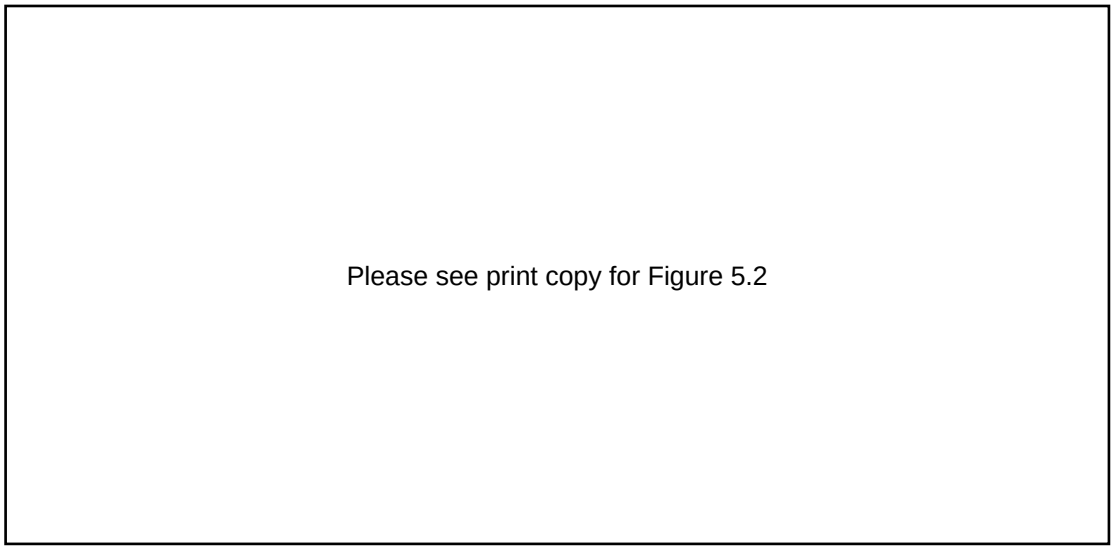

Fig. 5-2 (a) Typical TEM image of the $LiFePO_4$ powders obtained; (b) HRTEM image of single $LiFePO_4$ crystal.

The carbon content was determined by thermogravimetric (TG) and chemical analysis. The lithium iron phosphates prepared by the sol-gel process contain ~ 7.5 wt% carbon, much lower than the amount of carbon in the carbon-containing precursor compounds. Most of the carbon originating from carbon-containing precursors is released as gaseous products during calcination. Because the individual lithium iron phosphate crystals are connected together by the coated carbon layer, it was expected that the carbon coating on the lithium iron phosphate crystals would dramatically increase the

electronic conductivity of the electrodes. We pressed the doped and undoped lithium iron phosphates into disk-shaped pellets. The electronic conductivities were measured by the two-point d.c. method. All pellets exhibited a high electronic conductivity of approximately 10^{-3} S/cm at room temperature. Such a high electronic conductivity mainly comes from the carbon coating.

5.2.2 Electrochemical behavior

Fig. 5-3 shows the charge/discharge voltage profiles of C-$LiFePO_4$ electrodes in the first cycle ($LiFePO_4$ powder sintered at 600°C). The cell was charged and discharged at the C/8 rate. The initial capacity of C-$LiFePO_4$ electrode is 160 mAh/g (approaching the theoretical capacity of 170 mAh/g). A flat charge/discharge profile over a large voltage range indicates that the two-phase redox reaction proceeds via a first–order transition between $FePO_4$ and $LiFePO_4$. Also, a comparatively small polarization is obtained. The differential capacity data are shown in Fig. 5-4 and confirm the outstanding reversibility of the lithium extraction/insertion reactions. The main lithium extraction process is centered at a potential of 3.45 V vs Li, while the corresponding lithium insertion reaction is located at a voltage of 3.40 V vs Li. The voltage separation, $\triangle$V, amounts to just 0.05V, a very small value considering the diffusional polarization of the Li/C-$LiFePO_4$ system.

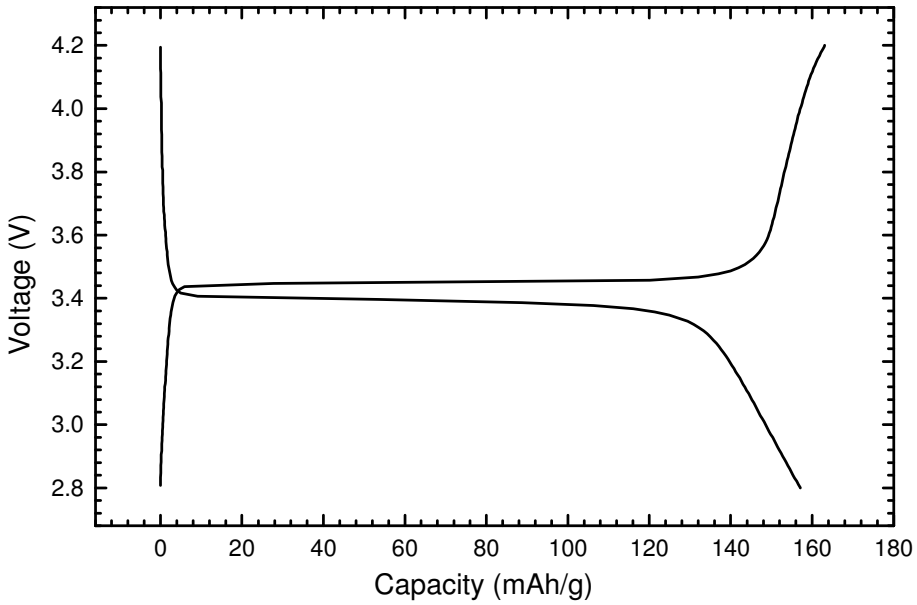

Fig. 5-3 Charge/discharge curve in the first cycle for C-$LiFePO_4$ electrode.

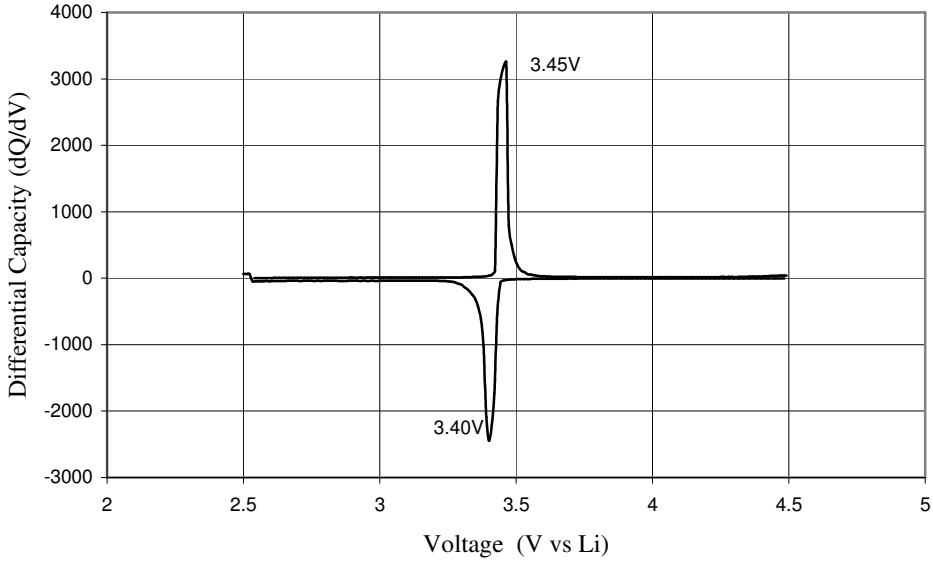

Fig. 5-4 Differential capacity profile for a typical Li/ C-$LiFePO_4$ cell.

The small polarization of the lithium iron phosphate compound synthesized in our work is because: (1) a unique microstructure and small particle size were achieved by the sol-gel synthesis; (2) the high surface-area carbon decomposed from acetate, oxalate precursor and citric acid, which induces the high electronic conductivity of the materials. The carbon coating can dramatically increase the surface electronic conduction.

5.3 Carbon coated $LiFePO_4$ prepared via a carbon aerogel synthesis process

5.3.1 Preparation and structure of carbon coated $LiFePO_4$

$Li(OH)\cdot H_2O$ (99.9%, Aldrich), $FeC_2O_4\cdot H_2O$ (99%, Aldrich) and $NH_4H_2PO_4$ (97%, Aldrich) were used as raw chemicals. The stoichiometric reactants were dissolved in de-ionised water, in which diluted nitric acid was added to accelerate the dissolving of $FeC_2O_4\cdot H_2O$. A typical carbon gel was formed by mixing 0.29 M resorcinol and 0.57 M formaldehyde. The $LiFePO_4$ reactant solution and the carbon gel solution were mixed and the pH value was adjusted to be in the range of 6.5 – 7.4. Then, the mixture solution was put in an ampoule, sealed and heated on a hot plate. The temperature was maintained at 85 °C. When the solution became viscous, the ampoule was moved to an oven and kept at 85 °C for 10 h. The carbon aerogel was then formed with the reactants Li^+, Fe^{2+} and $[PO_4]^{3-}$ dispersed inside. The gel was first decomposed at 450 °C and then sintered at 750 °C for 12 hours under flowing argon to yield carbon

coated $LiFePO_4$. The carbon content was analysed by thermal gravimetric analysis (TGA) to be 20 wt %.

Under an appropriate pH environment and warm temperature, resorcinol reacts with formaldehyde to initially form chains of hydroxymethyl derivatives, which then further react with each other to form a crosslinked 3-dimensional network (called an R/F gel). Fig. 5-5 shows a schematic diagram of the reaction of resorcinol with formaldehyde. Through cross-linking, R/F carbon gel forms an interconnected bead structure [Pakala 1989; Werstler 1986]. The ingredient ions Li^+, Fe^{2+} and $[PO_4]^{3+}$ are homogeneously distributed inside the carbon aerogel. After heat-treatment at 750 °C, the carbon gel was carbonized to become amorphous carbon. Simultaneously, $LiFePO_4$ crystals were formed.

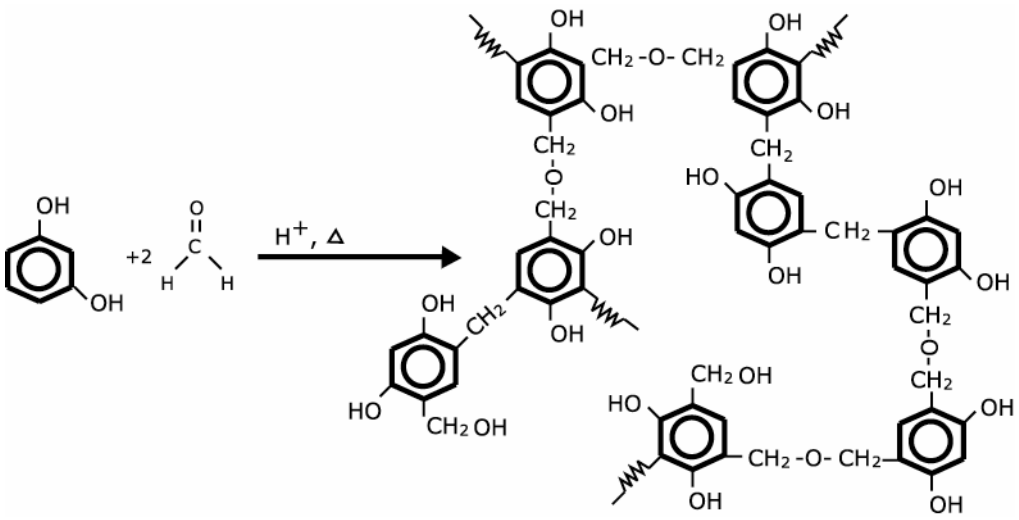

Fig. 5-5. A schematic diagram of the R-F gel formation.

The x-ray diffraction pattern of C-$LiFePO_4$ is shown in Fig. 5-6. All diffraction peaks are indexed with an orthorhombic crystal structure (SP: Pnma). No impurity phases were detected by x-ray diffraction. Thermal gravimetric analysis (TGA) and ICP analysis have identified that approximately 20 wt% carbon is included in the $LiFePO_4$. However, no diffraction line from crystalline carbon (graphite) appears in the diffraction pattern. Therefore, we can conclude that the carbon generated from carbon gel carbonization is amorphous carbon.

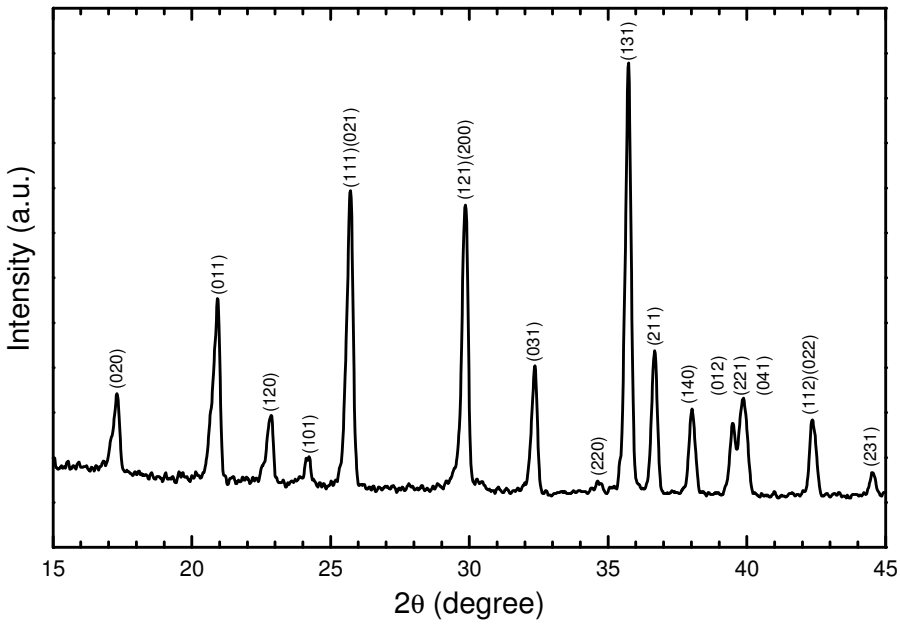

Fig. 5-6 X-ray diffraction pattern of C-$LiFePO_4$.

Fig. 5-7 shows a SEM image of $LiFePO_4$ powders. $LiFePO_4$ powders have a small average crystal size that is less than 1 μm. Fibrous amorphous carbons are present in the SEM photograph. These amorphous carbons can significantly enhance the electronic conductivity of $LiFePO_4$ materials. We pressed the as-prepared lithium iron phosphates into disk-shaped pellets. The electronic conductivity was measured by the two-point d.c. method. The $LiFePO_4$ pellets exhibit high electronic conductivity in the range of 10^{-1} S/cm at room temperature. The included carbons contribute to the high electronic conductivity of the $LiFePO_4$ materials.

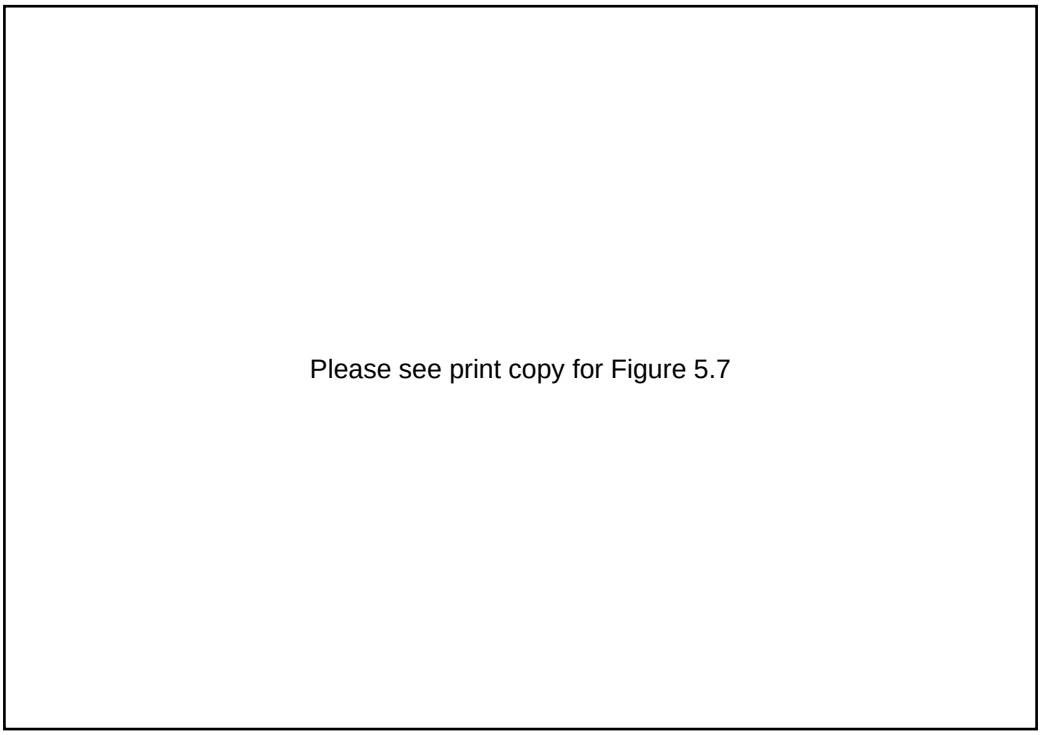

Fig. 5-7 SEM image of C-$LiFePO_4$ powders.

5.3.2 Electrochemical characterization of carbon-coated $LiFePO_4$

Cyclic voltammetry measurements were performed on C-$LiFePO_4$ electrodes using a scanning rate of 0.1 mA/s. Fig. 5-8 shows typical cyclic voltammograms (CV) of a C-$LiFePO_4$ electrode. During the anodic sweep, lithium ions are extracted from the $LiFePO_4$ structure. An oxidation peak is located at 3.51 V versus Li/Li^+. When the potential was scanned from 4.4 V to 2.5 V, a reduction peak occurred at 3.32 V, corresponding to lithium insertion into the $LiFePO_4$ structure. The sharp lithium insertion and extraction peaks in the CV curves indicated high reactivity of the carbon-included $LiFePO_4$ electrode. After 20 scanning cycles, the redox peaks remain of a similar magnitude, indicating good stability of the electrode.

In order to determine the capacity and cyclability of C-$LiFePO_4$ electrode, we performed charge/discharge cycling tests on C-$LiFePO_4$ electrodes at different rates. Fig. 5-9 shows the charge/discharge voltage profiles in the first cycle for a $LiFePO_4$ electrode at the C/5 rate. The as-prepared $LiFePO_4$ electrode demonstrated a high specific discharge capacity of 159 mAh/g in the first cycle, approaching the theoretical capacity of 170 mAh/g. The high capacity delivered by the $LiFePO_4$ electrode should be attributed the enhanced electronic conductivity of the materials due to carbon coating. Since the individual $LiFePO_4$ particles are connected by a carbon network, the active $LiFePO_4$ materials can be fully utilized for lithium extraction and insertion reactions. Fig. 5-10 shows the results of cyclability tests of $LiFePO_4$ electrodes at different charging and discharging rates.

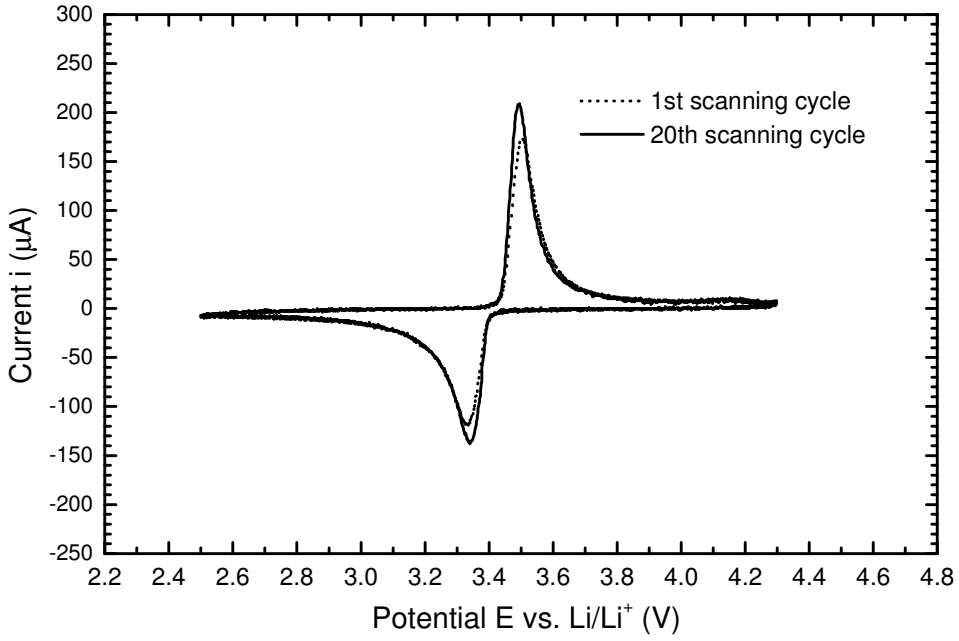

Fig. 5-8 Cyclic voltammograms of a C-$LiFePO_4$ electrode.

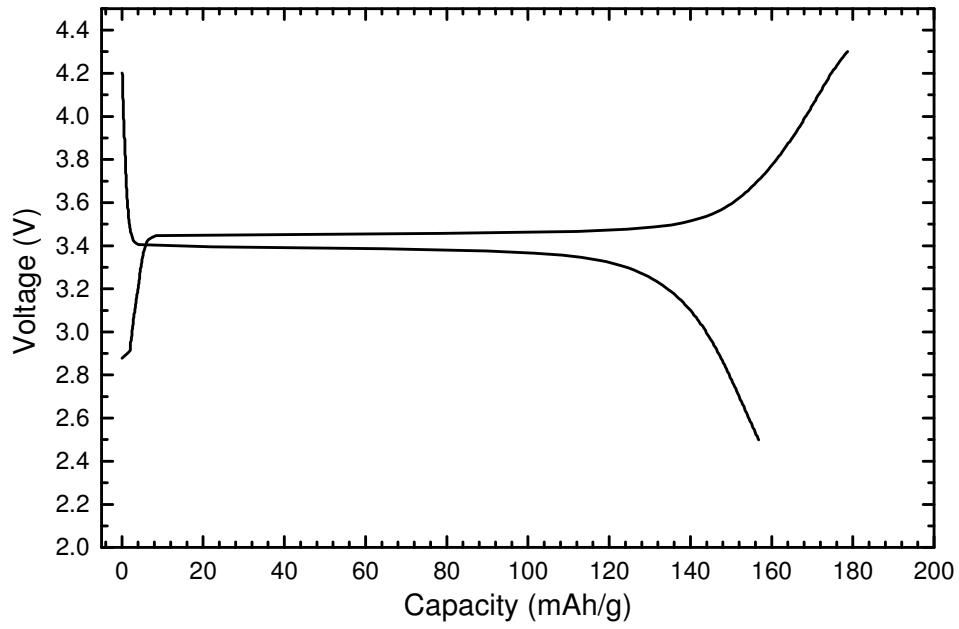

Fig. 5-9 Charge/discharge profiles of a C-$LiFePO_4$ electrode at the C/5 rate.

Although the specific capacity decreases with increasing charge/discharge rate, the capacity retention remains very good for all the different rates. Therefore, the carbon-included $LiFePO_4$ electrodes demonstrated high capacity and good cyclability.

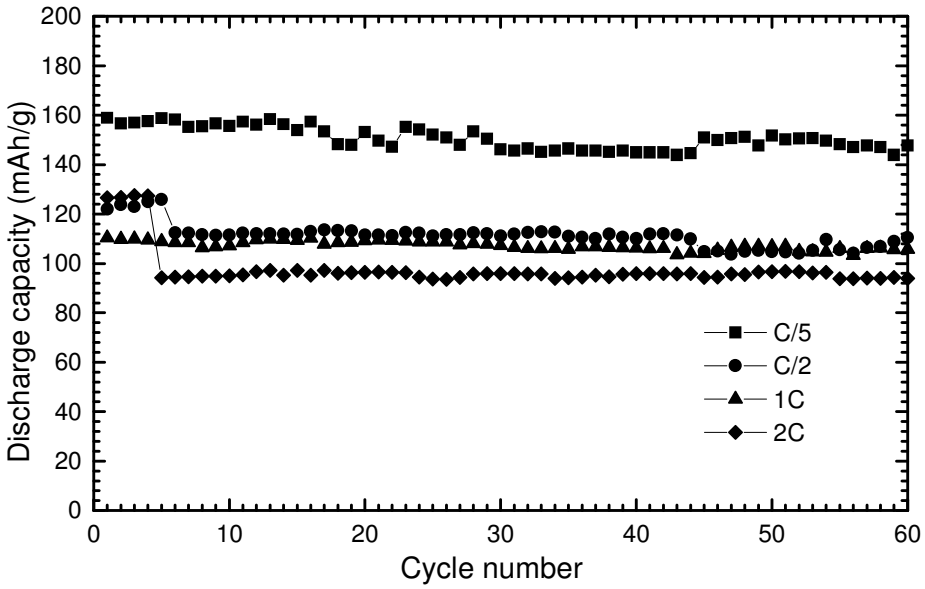

Fig. 5-10 Discharge capacity vs. cycle number for $LiFePO_4$ electrodes at different charge/discharge rates.

5.4 Summary

Nanocrystalline $LiFePO_4$ was synthesized by the sol-gel method. A layer of carbon was laid down as a coating on the surface of the lithium crystals, which is known to dramatically enhance the electronic conductivity. The sol-gel synthesis induces

nanocrystallinity, which could provide short paths for lithium diffusion. In addition, the R/F carbon gel synthesis process has been used to prepare carbon coated $LiFePO_4$. This process can produce fine $LiFePO_4$ embedded in amorphous carbon. The electronic conductivity of $LiFePO_4$ materials can be dramatically enhanced via the carbon inclusion. The cyclic voltammetry tests show the high reactivity of the as-prepared $LiFePO_4$ electrodes. A high capacity of 160 mAh/g at the C/5 rate has been demonstrated for the $LiFePO_4$ electrode. These electrodes also exhibited good cyclability at different charge/discharge rates.

Chapter 6

An Investigation of Cobalt Oxides as Anode Materials for Li-ion Batteries

6.1 Introduction

Lithium-ion batteries have been emerging as the most popular choice of power sources for modern electronics because lithium-ion batteries have the highest energy density among all the rechargeable batteries and have no memory effect. The current commercial lithium-ion batteries use $LiCoO_2$ or $LiMn_2O_4$ as the cathode materials and graphite or carbonaceous materials as anode materials [Nagaura, Tozawa 1990]. Graphite anode materials have a theoretical gravimetric capacity of 372 mAh/g or a volumetric capacity of 820 mAh/cm^3 [Billand, Henry et al. 1993; Dahn, Zheng et al. 1995; Megahed, Scrosati 1994]

In recent years, a worldwide effort has been made to search out alternative anode materials to replace graphite as anode materials for lithium-ion batteries. Idota and Kubota et al. [1997] have reported a new type of high capacity anode materials which consists of tin-based amorphous oxides. The lithium reaction mechanism relies on the formation of Li-Sn alloys. Since then, tin based oxides have been intensively investigated [Goward, Leroux et al. 1999; Courtney, Dahn et al. 1997; Morales, Sanchez 1999]. However, a large irreversible capacity prevents tin-based oxide anode materials from having any practical applications. This is because the source of the Li is cathode material, eg. $LiCoO_2$, which is limited in Li-ion cells. Therefore the irreversible capacity of the anode must be as small as possible.

Rock salt structured MO-type (M = Fe, Co, Ni, Cu, ……) transition metal oxides react reversibly with lithium in a lithium cell below 1.5 V [Poizot 2000]. It has been reported that the MO type oxides demonstrate large capacity (700 mAh/g), long cycle life, and high recharging rates. These brilliant properties make them promising candidates for use as anode materials for Li-ion batteries. Among them, cobalt oxide is a particularly interesting material due to its electrochemical, magnetic, and catalytic applications. The mechanism of the Li reaction differs from the Li insertion/extraction in graphite anode or Li-alloying processes in tin-based oxides. A new mechanism for the formation and decomposition of Li_2O with the reduction and oxidation of metal nano particles has been proposed [Poizot, Laruelle et al. 2000].

In the work described in this chapter, a series of cobalt oxides were prepared as anode materials. Their electrochemical properties were systematically tested. Cobalt oxide anode materials demonstrated high lithium storage capacity and reasonably good cyclability.

6.2 Synthesis of cobalt oxides by the thermal decomposition method and characterization as an anode material for Li-ion batteries

6.2.1 Preparation and structure of cobalt oxides

CoO was synthesised by decomposition of $CoCO_3$ in argon atmosphere at 850 °C for 12 hours, and Co_3O_4 was obtained by decomposition of $CoCO_3$ in air at 900 °C for 12 hours. This type of Co_3O_4 is called HT-Co_3O_4. Fine Co_3O_4 powders were also prepared by heating $Co(OH)_2$ at low temperature 250 °C under oxygen flow for 20 hours, and are thus called LT-Co_3O_4. Superfine Co_3O_4 powders were prepared by high energy ball milling. The ball milling was

performed in a planetary ball-milling machine (Pulverisette-5, LABTECHNICS, Australia) for 120 hours at a rotation rate of 200 rpm.

The three different types of Co_3O_4 powders were characterised by x-ray diffraction and SEM observation. The XRD patterns of Co_3O_4 are shown in Fig. 6-1(a). The Co_3O_4 prepared via high temperature decomposition consists of highly crystalline powders, which have strong and sharp diffraction peaks.

The SEM photograph (Fig. 6-2(a)) shows needle-shaped HT-Co_3O_4 crystals. During the high temperature heating process, the Co_3O_4 crystals grew preferentially along a particular direction. It appears that there liquid phase exists in the crystal boundary at high temperature. The low temperature decomposed Co_3O_4 powders have poor crystallinity with very broad diffraction lines. The SEM photograph of LT-Co_3O_4 (Fig 6-2(b)) shows spherical agglomerates with pores inside the agglomerate. When the $CoCO_3$ precursor was heated at low temperature, $CoCO_3$ was decomposed to cobalt oxide and carbon dioxide. Due to the blowing effect of the CO_2 gas, tiny pores were formed inside the Co_3O_4 particles. At 250 °C, the Co_3O_4 crystals can not could not go on growing, so, those pores were permanently trapped inside the particles to form porous material. After high energy ball milling, the strongly crystalline HT-Co_3O_4 becomes a cotton-shape agglomerate with poor crystallinity (as shown in Fig 6-2(c)). This is typically demonstrated by its XRD pattern (Fig. 6-1(a)), which shows broad diffraction peaks. Cobalt monoxide was obtained by heating $CoCO_3$ at 900 °C under flowing argon. Its x-ray diffraction pattern is shown in Fig. 6-1 (b). A small amount of cubic Co_3O_4 (Fd3m) is present in mono cobalt oxide as an impurity phase. The SEM image demonstrates that CoO powders easily form agglomerates with very fine crystals. Its crystal morphology is quite different from that of HT-Co_3O_4.

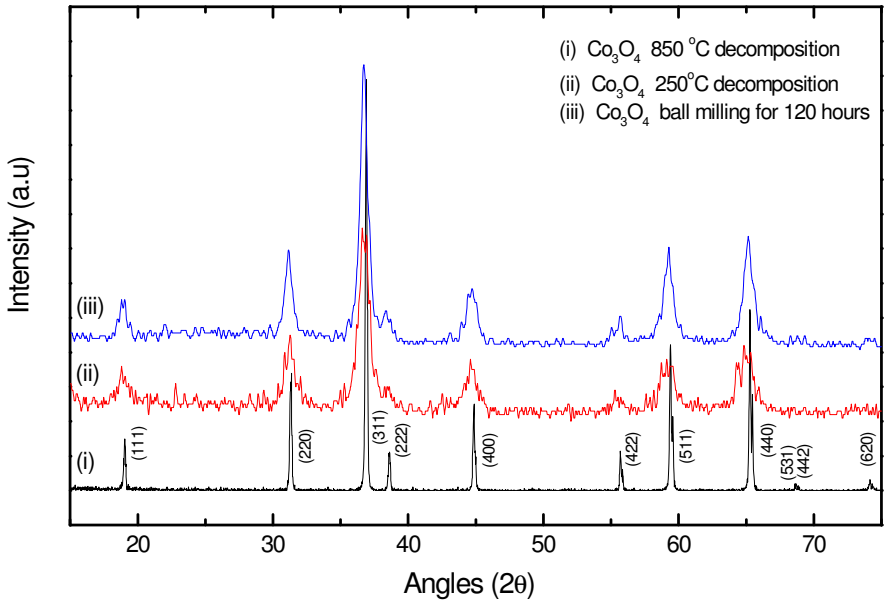

(a)

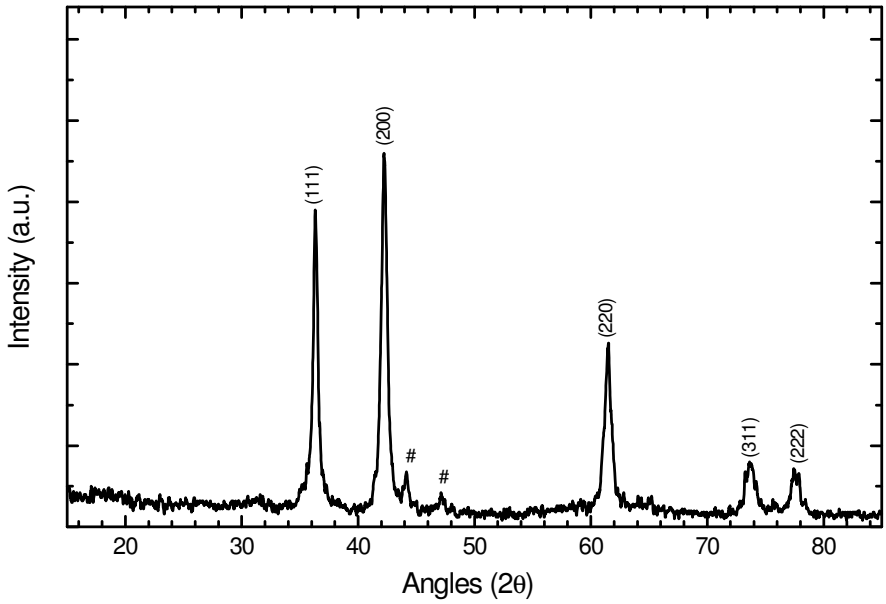

(b)

Fig. 6-1 X-ray diffraction patterns of cobalt oxides (a) Co_3O_4 ; (b) CoO.

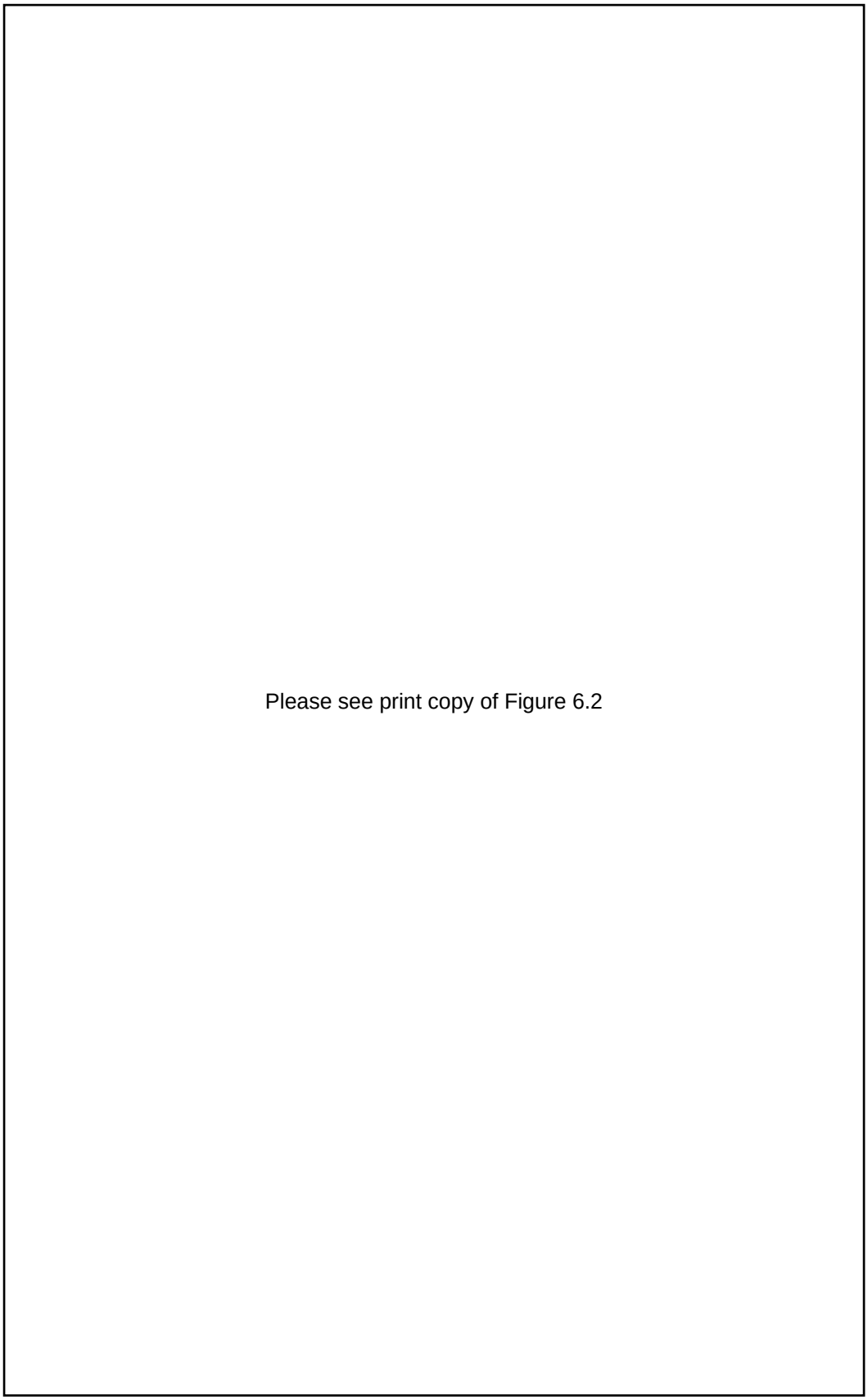
Please see print copy of Figure 6.2

The particle sizes of the as prepared cobalt oxides were measured by using a Mastersizer. The average particle sizes (D(v, 0.5)) of the cobalt oxides are 30 μm, 16 μm, 4.65 μm and 26 μm for HT-Co_3O_4, LT-Co_3O_4, ball-milled Co_3O_4, and CoO, respectively. The measured particle size is the agglomerate size. The real crystalline size is much smaller, in the range of a few micrometers.

6.2.2 Electrochemical characterization of cobalt oxides

The electrochemical properties of cobalt oxides as anodes in Li-ion cells were tested via charge/discharge measurements versus cycle number and cyclic voltammetry (CV). The cycling and CV testing were performed in the voltage range of 0.01 – 3.0 V versus a Li/Li^+ counter electrode. Fig. 6-3 shows the discharge curves of cobalt oxide electrodes in Li-ion testing cells. When discharging, the potentials of cobalt oxide electrodes promptly drop to less than 1.25 V and then slope down to the cut-off voltage. For Co_3O_4 electrodes, a discharge plateau exists between 1.0 and 0.75 V whereas the discharge plateau for CoO electrode is in the range of 0.75 – 0.25 V, which is lower than that of Co_3O_4 electrode. These phenomena are further demonstrated in cyclic voltammograms of cobalt oxide electrodes. For ball-milled Co_3O_4 electrode, there exists a large discharge plateau at ~ 1.0 V as shown in Fig. 6-3(c), which is related to the formation of a SEI (solid electrolyte interface) on the surface of the electrode, because ball-milled Co_3O_4 has a large surface area. It is almost certain that a passivation film was formed during the first discharge process. From the second cycle, this discharge plateau disappeared. The lithium consumed to form SEI is not reversible. The capacity retention with cycling of different oxide electrodes is shown in Fig. 6-4. The ball-milled Co_3O_4 electrode demonstrated the highest irreversible capacity in the first cycle and the most rapid capacity decay rate. The LT-Co_3O_4 and CoO electrodes have good capacity retention. In particular, CoO

electrode retained about a 300 mAh/g discharge capacity after the fifth cycle. This makes mono cobalt oxide very promising for use as a lithium storage material.

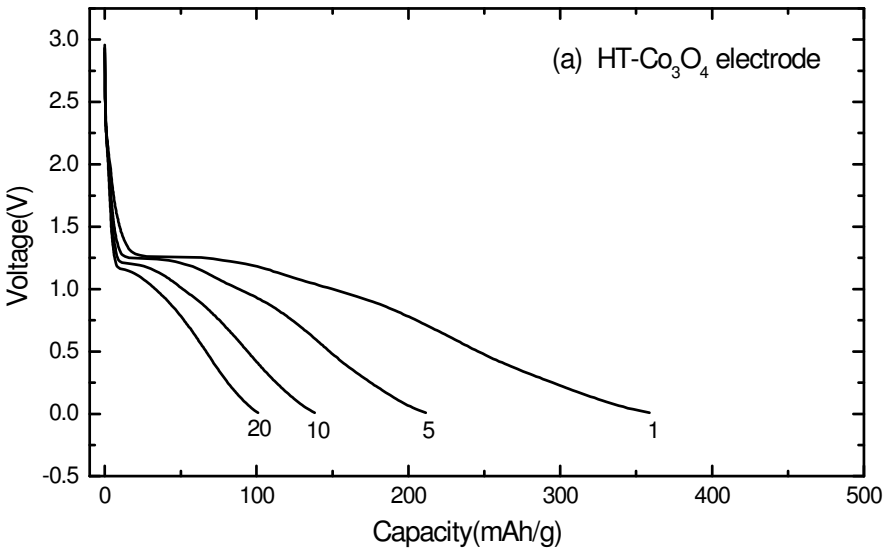

(a)

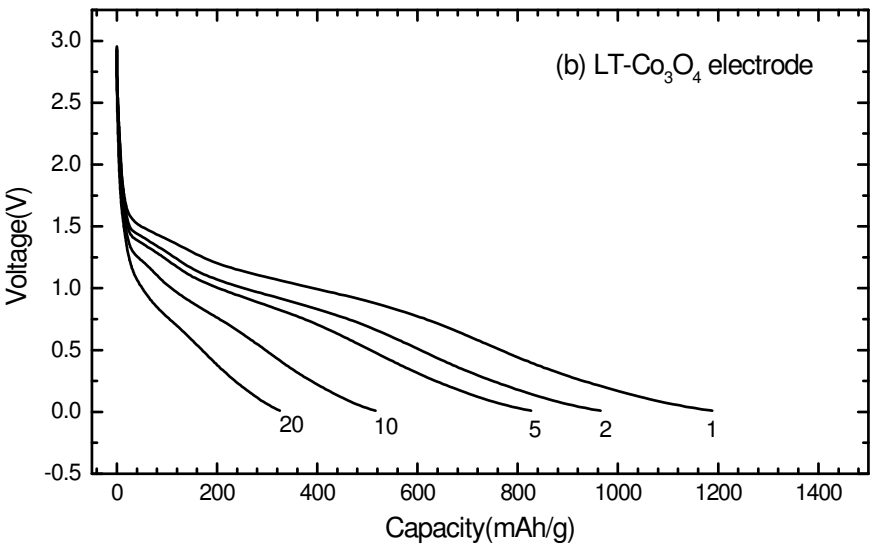

(b)

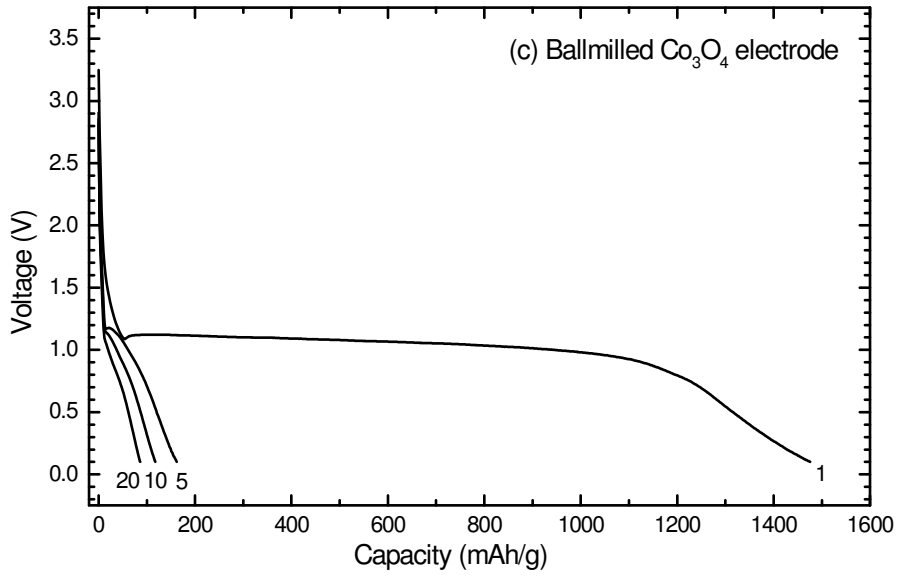

(c)

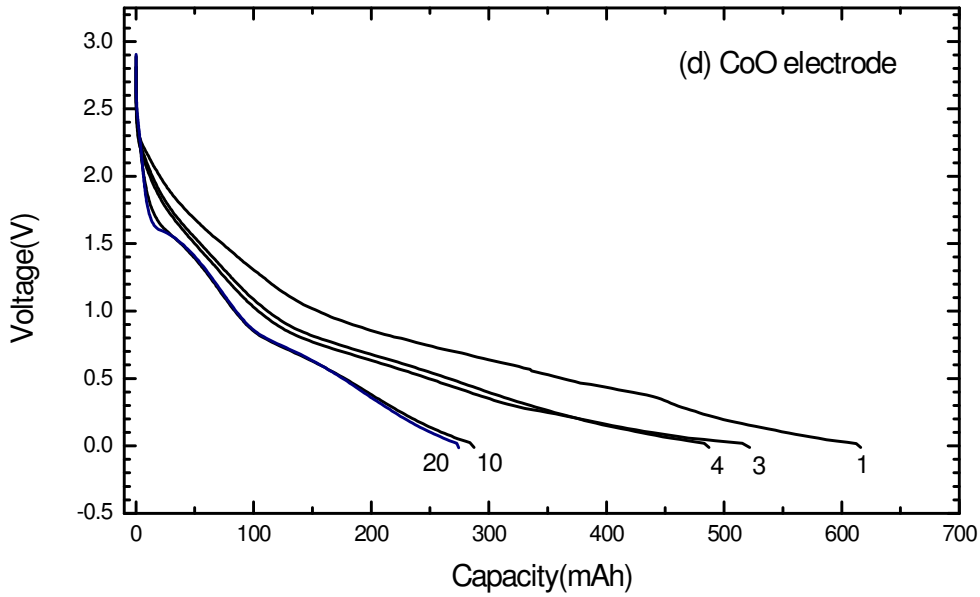

(d)

Fig. 6-3 The discharge profiles of cobalt oxide electrodes in Li-ion testing cells.

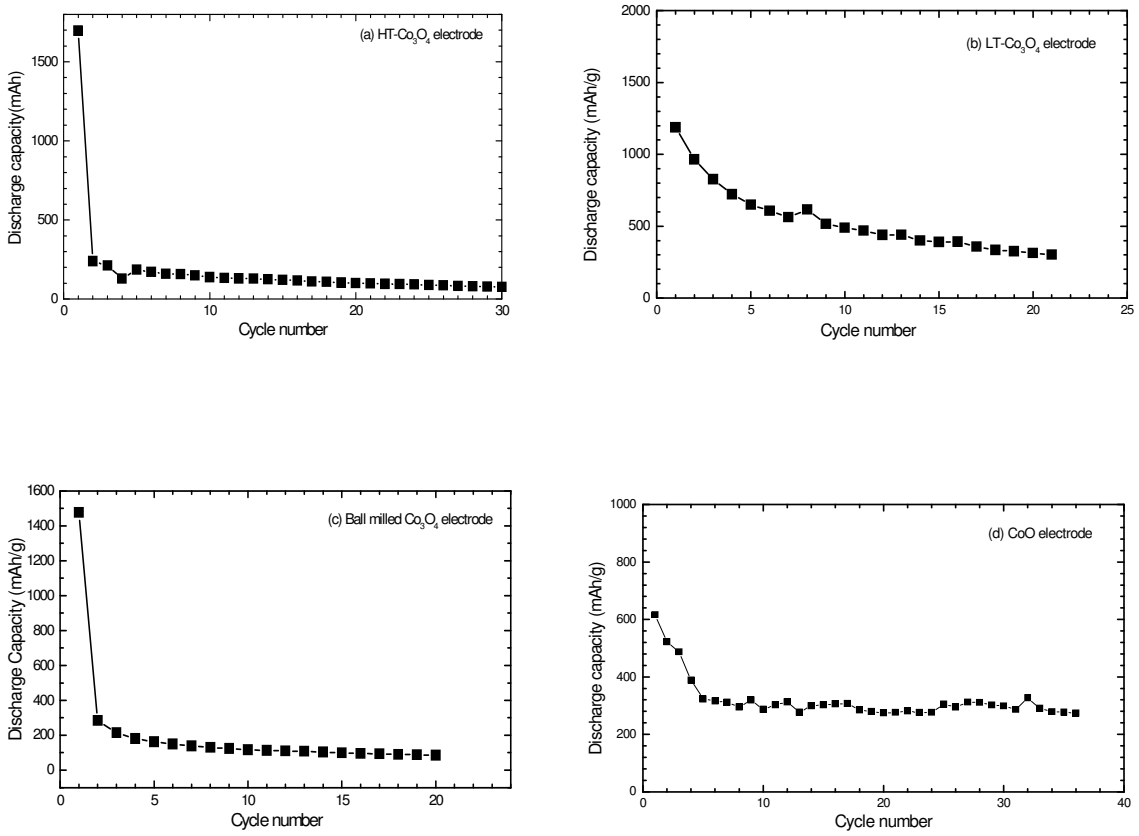

Fig. 6-4 The discharge capacity of cobalt oxide electrodes versus cycle number.

Fig. 6-5 shows the CV curves of four different types of cobalt oxide electrodes. All cobalt oxide electrodes show one reduction and one oxidation peak in the potential range of 0.01 V – 3.0 V versus Li/Li^+, indicating that only one redox reaction is ongoing during Li-ion insertion and extraction. In cyclic voltammograms, the redox peaks of HT-Co_3O_4 and LT-Co_3O_4 electrodes are at the same voltage positions. However, the reduction peaks of ball-milled Co_3O_4 and CoO electrodes are shifted to lower potential. This phenomenon means that the process of lithium

reaction in HT-Co_3O_4 and LT-Co_3O_4 is different from that of ball-milled Co_3O_4 and CoO electrodes. The oxidation peaks for all four types of cobalt oxide electrodes remain unchanged. All the cobalt oxide electrodes exhibited hysteresis between the lithiation and delithiation processes, which is similar to what occurs in tin oxide anode materials [Foster, Wolfenstine et al. 2000; Morimoto, Tatsumisago et al. 2001]. The different types of cobalt oxide electrodes exhibited different electrochemical behaviours in Li-ion cells. Therefore, the electrochemical performance of cobalt oxides is sensitive to the crystallinity, morphology, and microstructure.

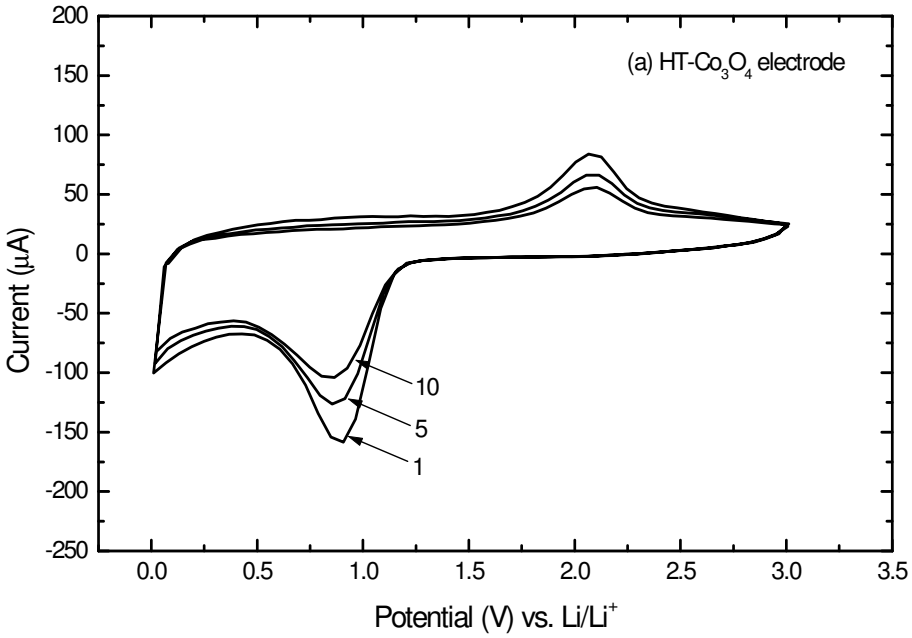

(a)

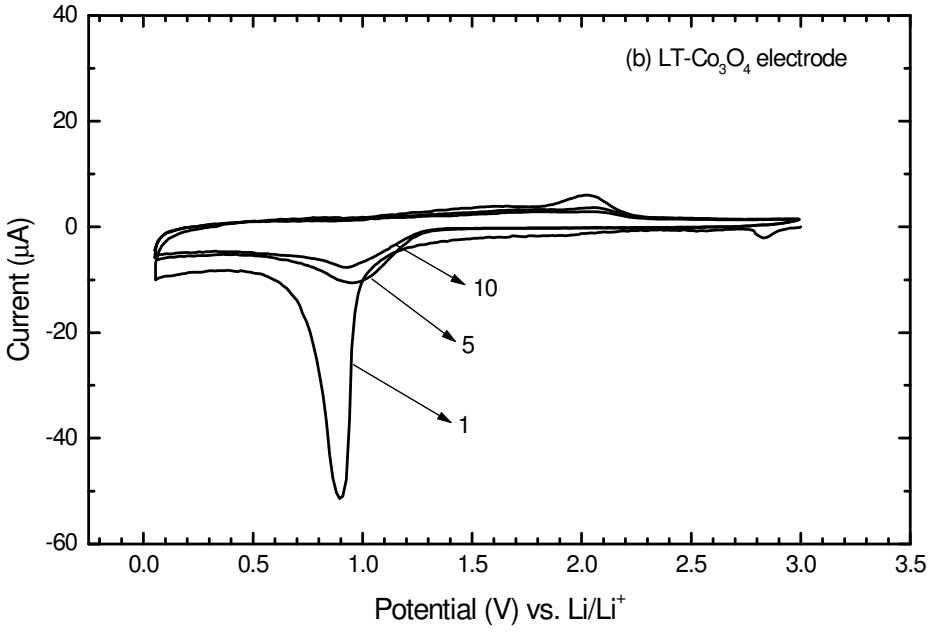
(b) LT-Co_3O_4 electrode
Current (μA)
Potential (V) vs. Li/Li^+
10
5
1

(b)

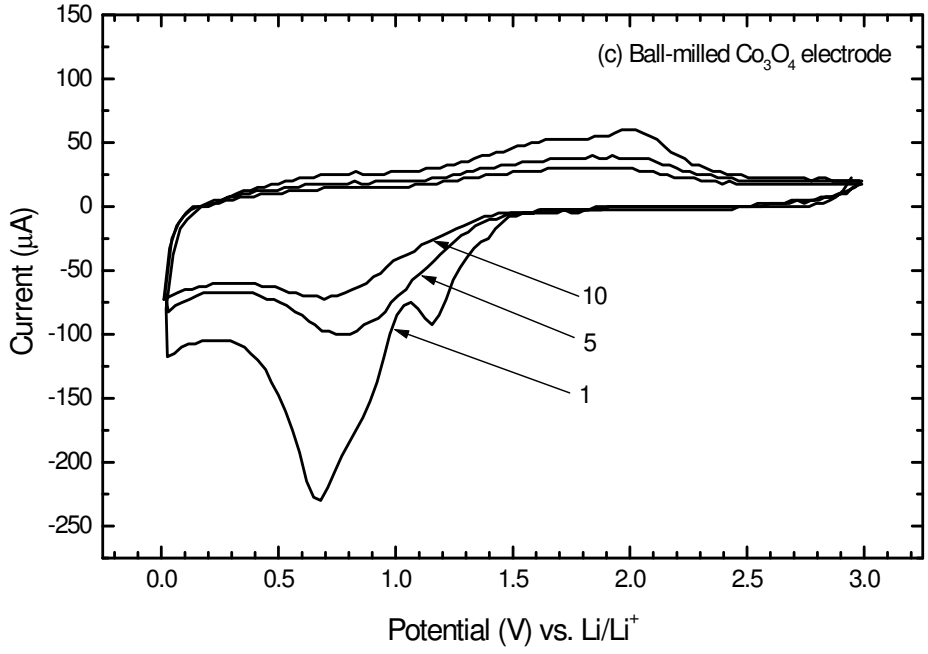
(c) Ball-milled Co_3O_4 electrode
Current (μA)
Potential (V) vs. Li/Li^+
10
5
1

(c)

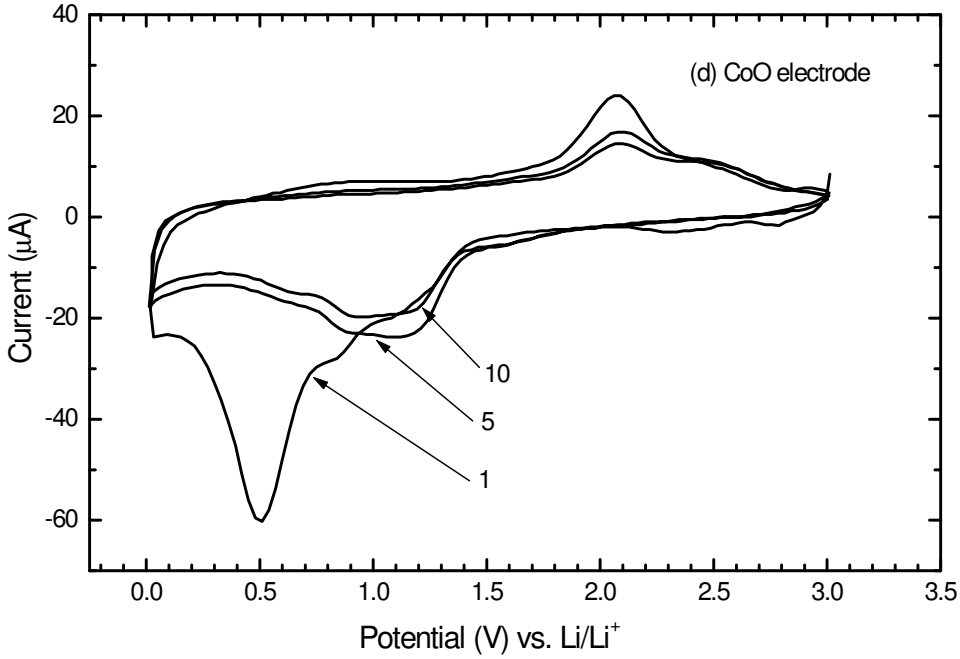

(d)

Fig. 6-5 Cyclic voltammograms of cobalt oxide electrodes in Li-ion cells, scanning rate: 1 mV/s. Cycle numbers are indicated by the arrows.

It has been proposed that the reaction mechanism of cobalt oxide with lithium in Li-ion cells is a displacive redox reaction:

$$CoO + 2Li^+ + 2e \longrightarrow Li_2O + Co$$

$$2Li \longleftarrow 2Li^+ + 2e^-$$

$$CoO + 2Li \rightleftharpoons Li_2O + Co$$

The reaction of lithium ions with cobalt oxide to form lithium oxide and cobalt is thermodynamically feasible. However, Li_2O is electrochemically inactive. Therefore, to extract

lithium from Li_2O is thermodynamically impossible. J.-M. Tarascon [Poizot, Laruelle et al. 2000] argued that both chemical and physical phenomena are strongly affected when dealing with nanosized materials. Electrochemically formed Li_2O and Co are nanoparticles by nature. With decreasing particle size, an increasing proportion of the total number of atoms lies near or on the surface, making the electrochemical reactivity of the nano particles more and more important. In this investigation, *ex-situ* x-ray diffraction was performed on HT-Co_3O_4 electrode in both the fully lithiated and the fully delithiated state. To obtain the fully lithiated state, the freshly assembled Co_3O_4 / Li cell was galvanostatically discharged to 0.01 V and then potentiostatically held at 0.01 V for 4 hours. Similarly, the fully delithiated state was obtained by galvanostatically charging the Co_3O_4 / Li cell to 3.0 V and then potentiostatically holding at 3.0 V for 4 hours. The test cells were disassembled in a glove box. The Co_3O_4 electrodes were then taken out, and the electrolyte on the surface of the electrode was wiped off using dry cotton. The electrodes were then sealed using polyethylene plastic film for x-ray diffraction.

The *ex-situ* XRD patterns are shown in Fig. 6-6, in which only the diffraction peaks from the copper substrate can be identified. For the fully lithiated state, the lithiation products would be Li_2O and Co, but in the fully delithiated state, cobalt oxide should exist. However, neither Li_2O nor Co or Co_3O_4 have been detected. This is evidence that the cobalt oxide had lost crystallinity and that the electrochemically formed lithiation products Li_2O and Co are nanoparticles in nature. These nanoparticles possibly make the extraction of Li from Li_2O feasible. Therefore, cobalt oxide electrode demonstrates a certain reversible lithium storage capacity.

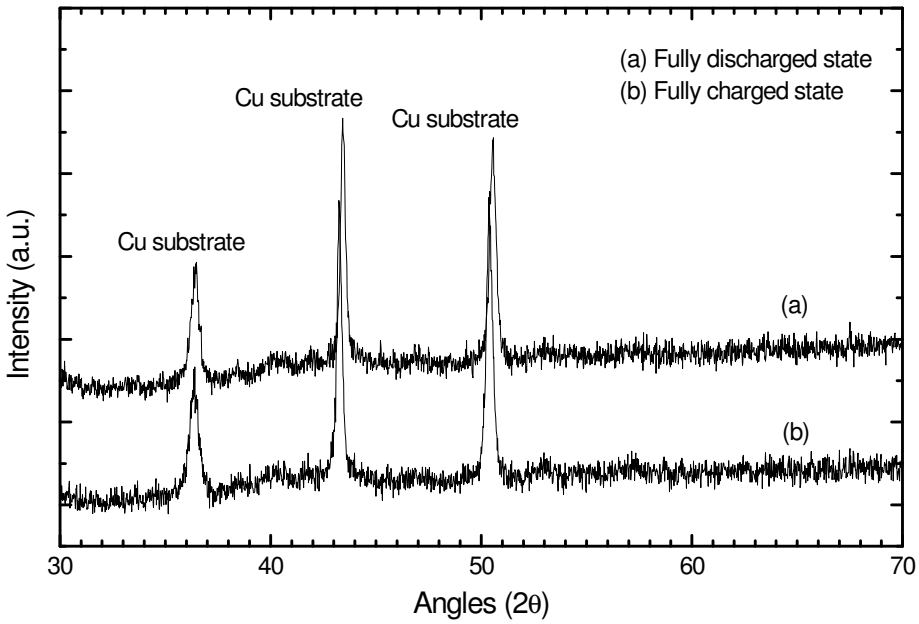

Fig. 6-6 The ex-situ x-ray diffraction patterns of (a) HT-Co_3O_4 electrode in the fully discharged state; (b) HT-Co_3O_4 electrode in the fully charged state.

6.3 Nanosize Co_3O_4 synthesized by chemical decomposition of cobalt octacarbonyl in toluene at low temperature

6.3.1 Preparation and physical characterization

Nanosize Co_3O_4 powders were prepared by a chemical decomposition approach. Cobalt octacarbonyl ($Co_2(CO)_8$) compounds were initially dissolved in toluene to form a solution. The solution was heated at 130 °C in a glove box with oxygen flow. The homogeneous nucleation and growth of nano cobalt oxide crystals were achieved by bubbling oxygen gas through the solution mix during the heating process. The oxygen bubbling effect not only can enhance the oxidation of cobalt, but also disperses the cobalt oxide nanocrystals and prevents the formation of agglomerates. This technique is well known for preparing nanocrystalline self-assembled

materials [Papirer, Horny et al. 1983; Chen, Whittingham 1997; Yin, Wang et al. 1999]. For comparison, normal crystalline cobalt oxides (Co_3O_4) were also prepared by decomposition of $CoCO_3$ at high temperature.

The Co_3O_4 powders were characterised by X-ray diffraction and SEM observation. The XRD patterns of Co_3O_4 powders are shown in Fig. 6-7. The Co_3O_4 powders prepared by decomposition of $Co_2(CO)_8$ show very broad diffraction lines, indicating poor crystallinity. Using the diffraction peak (311) and the Scherrer formula: $d = k\lambda/\beta\cos\theta$, where λ is the X-ray wavelength, θ is the Bragg angle, and β is the half-peak width in radians, the grain size was calculated to be about 5 nm by employing the (311) diffraction peak. In contrast, Co_3O_4 obtained via high temperature decomposition is a highly crystalline powder, which have strong and sharp diffraction peaks.

SEM observation reveals the micromorphological characteristics of Co_3O_4 powders. Fig. 6-8 shows the SEM images of Co_3O_4 powders. The Co_3O_4 powders obtained by decomposing cobalt carbonyl show a cotton shaped morphology with poor crystallinity. Since these Co_3O_4 powder were obtained at low temperature, the crystals remained very small, so that these tiny crystals tend to form agglomerates. The agglomerates consist of small grain particles, whereas, the Co_3O_4 prepared by high temperature sintering shows a needle shaped morphology with good crystallinity (Fig. 6-2(a)). It is obvious that Co_3O_4 crystals grow along a preferred direction, so that it appears as if a liquid phase exists in the crystal boundaries at high temperature. Therefore, nanosize Co_3O_4 powders can be prepared by decomposing organo-cobalt compounds at low temperature. The as-prepared Co_3O_4 powders have poor crystallinity and easily form agglomerates. Co_3O_4 powders prepared via low temperature

decomposition are thus called nanosize Co_3O_4, and those obtained via high temperature sintering are called normal crystalline Co_3O_4.

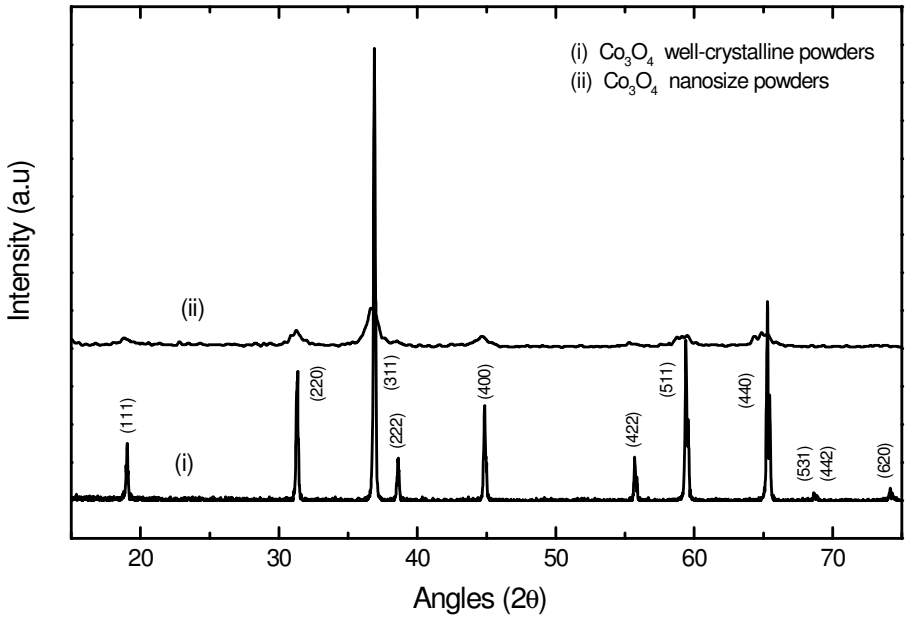

Fig. 6-7 X-ray diffraction patterns of Co_3O_4 powders.

Please see print copy for Figure 6.8

Fig. 6-8 SEM image of nanosize Co_3O_4 powders prepared by chemical decomposition of cobalt octacarbonyl in toluene at 130°C.

6.3.2 Electrochemical performance

The electrochemical properties of cobalt oxides as anodes in Li-ion cells were tested via charge/discharge cycling and cyclic voltammetry (CV) measurements. The cycling and CV testing were performed over the voltage range of 0.01 – 3.0 V versus a Li/Li^+ counter electrode. Fig. 6-9 shows the CV curves of nanosize and normal crystalline Co_3O_4 electrodes. For the nanosize Co_3O_4 electrode, two reduction peaks exist at around 0.7 V and 1.3 V during the lithium insertion process, and two oxidation peaks at 1.4 V and 2.1 V during the lithium extraction process. The intensity of the second pair of redox peaks gradually decreases in the subsequent scanning cycles. By comparison, only one pair of redox peaks appears on the CV curve for normal crystalline Co_3O_4, indicating that only one reduction and one oxidation reaction occur during lithium insertion and extraction. The second pair of redox peaks on the CV curve for nanosize Co_3O_4 electrode should be related to the formation of a SEI film (solid electrolyte interface) on the surface of the electrode, because nanosize Co_3O_4 powders have a large surface area and tend to be more reactive in the organic electrolyte. During the initial lithium insertion process, it is almost certain that a passivation film was formed due to the decomposition of the organic electrolyte. The Co_3O_4 electrodes exhibit hysteresis between the lithium insertion and extraction processes, which is similar to the situation for tin oxide anode materials [Foster,Wolfenstine et al. 2000; Morimoto, Tatsumisago et al. 2001].

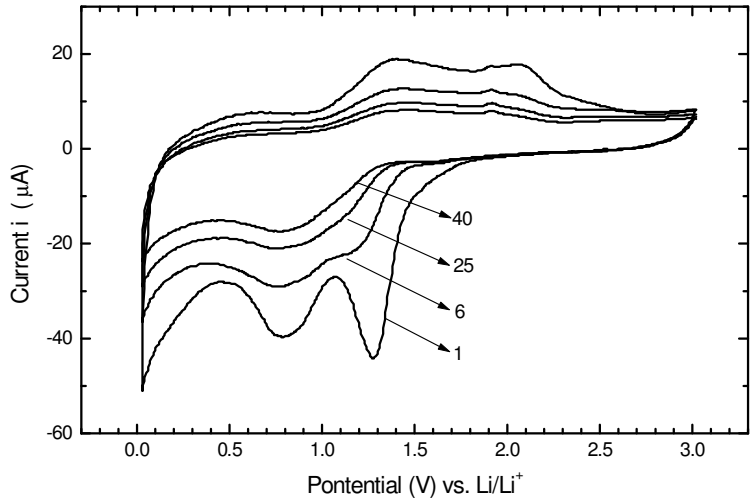

(a)

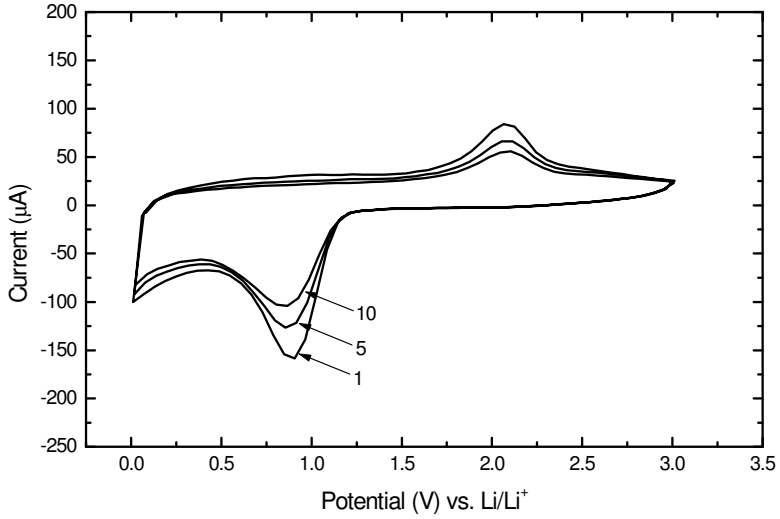

(b)

Fig. 6-9 Cyclic voltammograms of Co_3O_4 electrodes (a) nanosize Co_3O_4 electrode; (b) normal crystalline Co_3O_4 electrode.

The discharge curves of nanosize Co_3O_4 electrode are shown in Fig. 6-10. When discharging, the potentials of Co_3O_4 electrodes promptly drop to less than 1.25 V and then slope down to the cut-off voltage of 0.01 V. The nanosize Co_3O_4 electrode exhibited a larger irreversible capacity

during the first cycle than the normal crystalline Co_3O_4 electrode (Fig. 6-3(a)). However, after the first cycle, nanosize Co_3O_4 electrode demonstrated stable cyclability. The capacity retention with cycling of two different types of Co_3O_4 electrodes is shown in Fig. 6-11. The nanosize Co_3O_4 electrode retained a lithium storage capacity of about 360 mAh/g after thirty cycles, which is very promising for the use of nanosize Co_3O_4 as an anode material for lithium-ion batteries. The nanosize Co_3O_4 particles provide high reactivity to the lithium insertion, which possibly contributes to the large lithium storage capacity. On the other hand, a stable passivation film may form on the surface of the nanosize Co_3O_4 electrode, which may enhance the stability of the electrode on cycling.

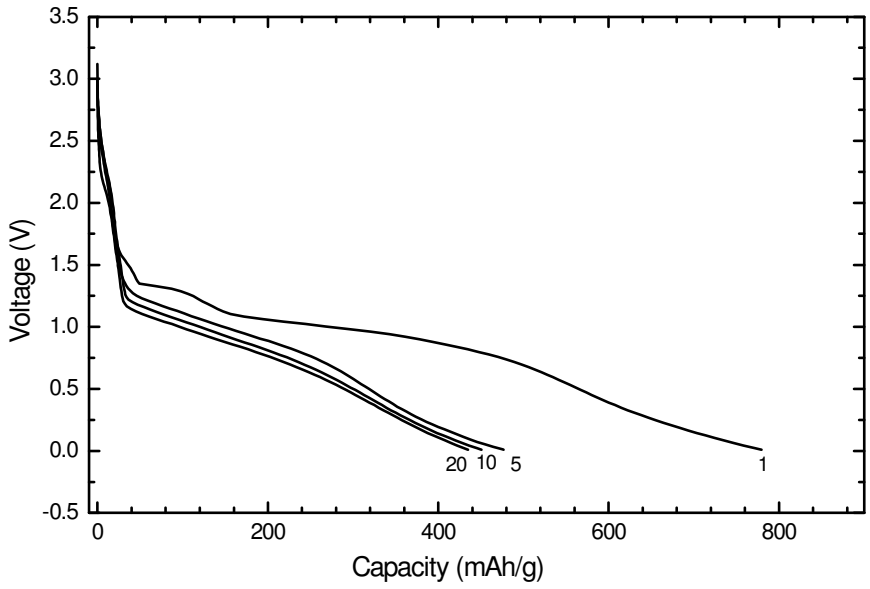

Fig. 6-10 The discharge profiles of nanosize Co_3O_4 electrode in Li-ion cells. Cycle number is given for each profile.

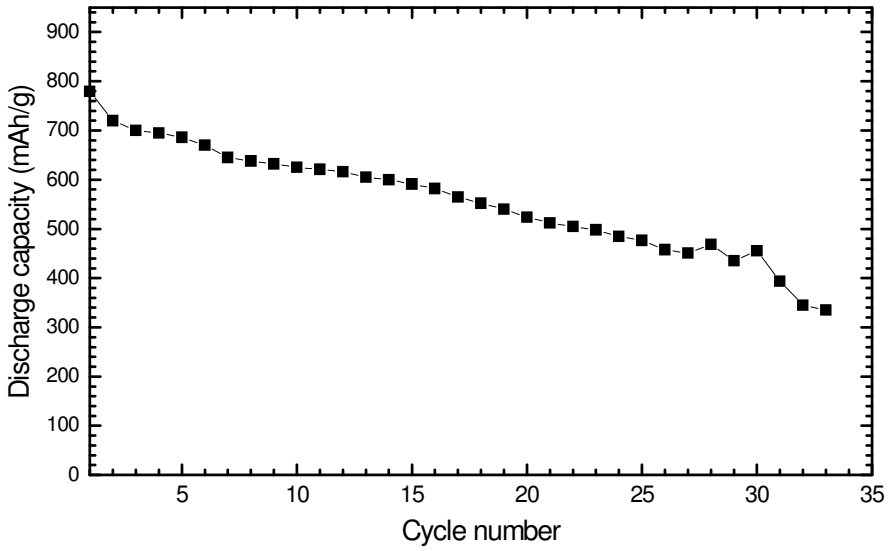

Fig. 6-11 The discharge capacity of nanosize Co_3O_4 electrode versus cycle number.

6.4 Conclusions

Five different types of cobalt oxides were investigated as lithium storage materials in Li-ion cells. Electrochemical testing demonstrated that cobalt oxide electrodes have the capability to react reversibly with lithium to a certain extent. The LT-Co_3O_4, the CoO, and the nanosize Co_3O_4 powders prepared by decomposing organo-cobalt compounds at low temperature show good capacity retention on charge/discharge cycling, which is promising for their use as anode materials in Li-ion cells. The results of *ex-situ* XRD on Co_3O_4 electrode established that the lithiation products Li_2O and Co are nanoparticles. The electrochemical properties of cobalt oxides are sensitive to the crystallinity, morphology and particle size. Further optimisation of the microstructure of cobalt oxides can improve their electrochemical performance.

Chapter 7

Synthesis of nanocrystalline Ag and SnO_2 materials via a reverse micelle approach and their characterization as anodes for Li-ion batteries

7.1 Introduction

Tin-based alloys and composite anode materials have recently attracted worldwide attention due to their high lithium storage capacity [Idota, Kubota et al. 1997; Wang, Appleby et al. 2000; Ulus, Rosenbery et al. 2002; Beaulieu, Dahn 2000]. This class of anode materials relies on the formation of Li_xSn alloys and their subsequent dealloying for reversible lithium storage. However, this alloying process is always accompanied by a significant volume change, which has detrimental effects on the electrode performance. Several strategic approaches have been developed to overcome this problem: (1) using nanosize tin-based anode materials to reduce the volume change associated with the alloying and dealloying processes in the local domain; (2) embedding active tin-based anode materials in an inactive matrix to buffer the volume variation.

On the other hand, nanosize materials have attracted dramatic interest due to their special physical and chemical properties, which are significantly different from those

of bulk and microcrystalline materials. Nanocrystalline noble metal materials such as gold, platinum and silver have potential applications in electronics and biological technologies [Fendler 1987]. For example, it is expected that noble metal particles can be used as an efficient material for DNA probing, the control of DNA hybridization, nanoscale drug delivery systems, and nanoscale biological sensors [Schifferli 2002; Klarreich 2001; Quintana 2002]. The applications of nanocrystalline metal oxides and inorganic compounds vary from semiconductors, optics, and electronics to energy storage and conversion [Fendler, Tricot et al. 1984; Alivisatos 1996; Colvin, Schlamps et al. 1994; Lu and Dahn et al. 2003].

Many techniques have been developed for preparing metallic or inorganic nanopowders, such as chemical vapour condensation (CVC) [Deki, Akamatsu et al. 1999], sol-gel synthesis [Roy, Roy et al. 1984], high energy ball milling [Koch 1993], spray conversion processing [Kear, McCandlish 1993], etc. The grain size, morphology, and texture can be varied by suitably modifying/controlling the process parameters in each method. A technique using a water-in-oil microemulsion solution, so-called reverse micelles, is one efficient approach to synthesis of nanoparticles. This technique has been extensively used to prepare nanoparticles of various materials, including metals, oxides, hydroxides and some inorganic compounds [Lin, Zhou et al. 2001; Carpenter, Kumbhar et al. 2000; Anuradna, Ranganathan et al. 1999; Lu and Dahn et al. 2003; Zhang, Sun et al. 2002; Chen, Yeh et al. 1999]. In this study, we prepared nanosize Ag powders and SnO_2 powders via a reverse micelle synthesis

technique. The physical and electrochemical properties of the as-prepared Ag and SnO_2 nanopowders were then characterized.

7.2 Synthesis and electrochemical characterization of Ag nanopowders

Reverse micelles A consist of 0.5 M $AgNO_3$ solution, cetyltrimethylammonium bromide (CTAB) as surfactant, 1-Butanol as co-surfactant, and octane as organic matrix. The ratio of the ingredient chemicals in reverse micelles A is 0.5 M $AgNO_3$: CTAB : 1-Butanol : octane = 16 : 24 : 18 : 42 by weight percentage. Reverse micelles B consist of 1 M $NaBH_4$ solution, cetyltrimethylammonium bromide (CTAB) as surfactant, 1-Butanol as co-surfactant, and octane as organic matrix. The ratio of the ingredient chemicals in reverse micelles B is 1 M $NaBH_4$: CTAB : 1-Butanol : octane = 16 : 24 : 18 : 42 by weight percentage.

The reactant chemical for each type of reverse micelle were mixed together by stirring to form reverse micelles A and B, initially with a magnetic bar and then with high speed mechanical stirring, to achieve a homogeneous micro emulsion. After that, the separate reverse micelles A and B were mixed together slowly with vigorous stirring. The colour of the solution changed from yellow to dark grey, indicating that Ag^+ ions were reduced to Ag inside the aqueous droplets. The reacted solution was then centrifuged at 4000 rpm for 60 minutes to precipitate the Ag nano powders. The precipitates were then washed with methanol several times. The washed powders

were dried in vacuum at 80 °C for 5 hours.

When a water based solution is mixed with an organic matrix, two completely separate phases will be formed. However, if appropriate surfactant is added and mechanical stirring is applied, a dispersion system will be formed, in which water-based droplets will be dispersed in the organic matrix through microemulsion. These droplets are also called reverse micelles. Fig. 7-1 shows a schematic of the reverse micelles.

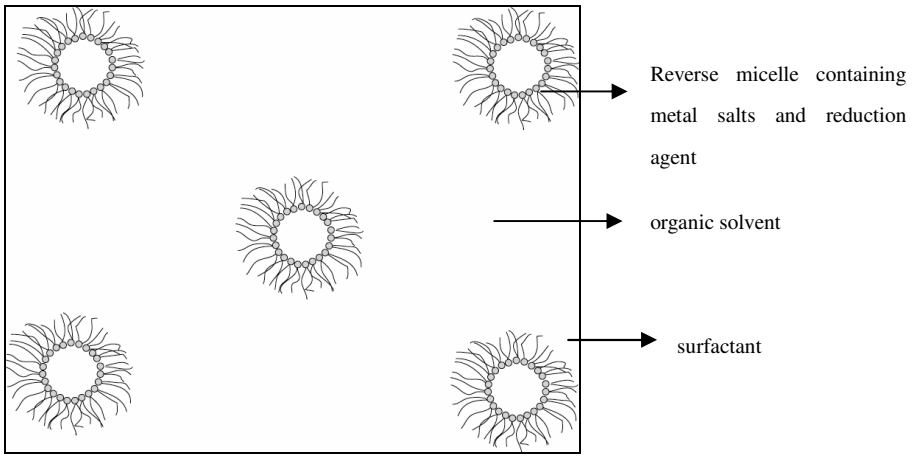

Fig. 7-1 A schematic diagram of the reverse micelles.

We used high speed mechanical stirring and ultrasonic treatment, so that nanosized water droplets were obtained. In the case of synthesizing Ag and Pt nanosize powders, the ratio of water to organics in the micellar system is fixed at $W_{H2O} : W_{org} = 1 : 5$ by

weight. Excess reduction agent $NaBH_4$ was used to ensure that all Ag^+ ions were reduced to elemental Ag. When the reverse micelles A and B were mixed, the two types of reverse micelles were merged to form a new type of reverse micelle. The newly formed reverse micelles contained metal salts and reduction agents. The Ag colloidal particles were immediately nucleated and grown into nanocrystals. Fig. 7-2 shows a schematic of the formation of the reverse micelle nanoreactors.

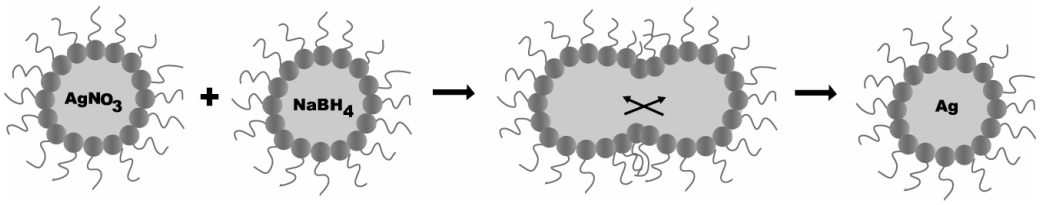

Fig. 7-2 Schematic of the formation of the reverse micellar nano-reactor.

Fig. 7-3 shows an x-ray diffraction pattern of the as-prepared Ag powders. The Ag powders have very good crystallinity and are phase pure.

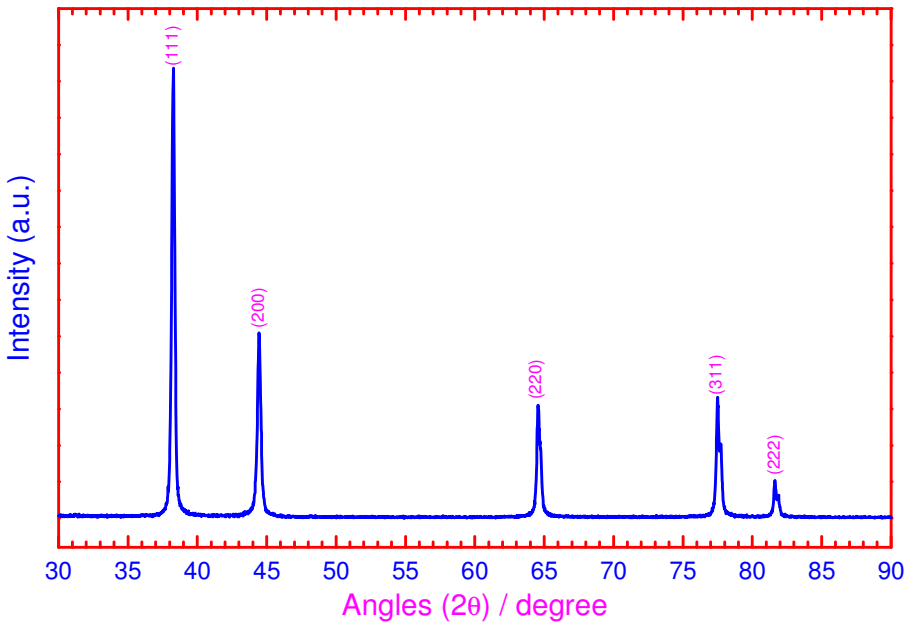

Fig. 7-3 X-ray diffraction pattern of Ag nano powders.

All diffraction peaks can be indexed as cubic phase (S.G.: Fm3m). No AgBr impurity phase is present in the XRD pattern. Therefore, the reaction inside a reverse micelle nanoreactor can be expressed as:

$$4\,Ag^{+} + BH_4^{-} + H_2O \quad \rightarrow \quad 4Ag + H_2BO_3^{-} + 4H^{+} + H_2$$

The excessive surfactants and reductant were thoroughly washed away, leaving us with pure Ag powders. The diameter of the Ag nanopowders is strongly influenced by the concentration of $NaBH_4$ inside the reverse micelles. Fig. 7-4 shows the variation of Ag particle size with the concentration of $NaBH_4$. The mean particle size of the Ag nanopowder decreases as the concentration of $NaBH_4$ increases, indicating that the particle size can be varied through altering the concentration of the reduction agent in aqueous solution.

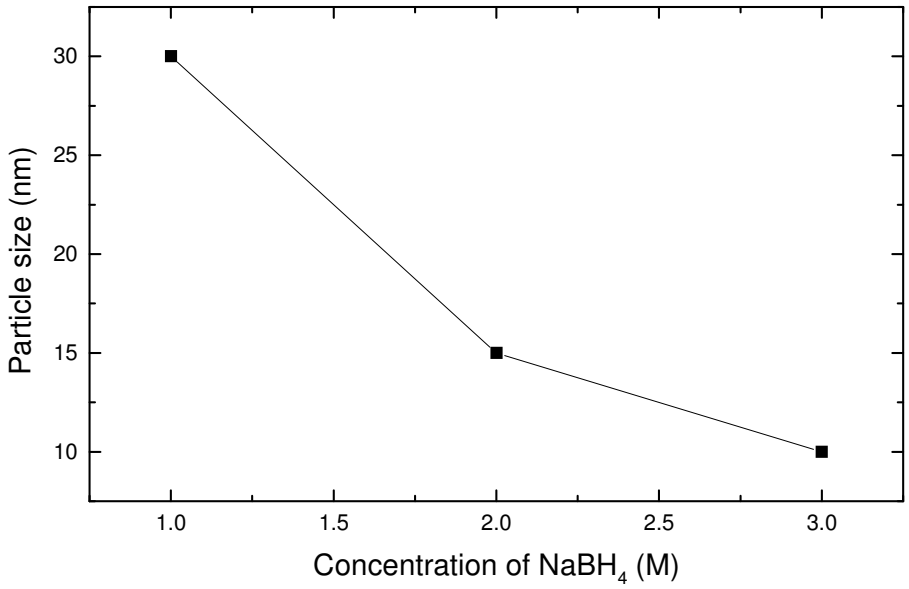

Fig. 7-4 Variation of Ag particle size with the concentration of $NaBH_4$.

A typical TEM image of the Ag powders is shown in Fig. 7-5. The Ag particles have a spherical shape with a crystal size ranging from 5 to 50 nm. The individual Ag nano particles are very well separated. Through micro-emulsion, we successfully obtained nanosize Ag powders.

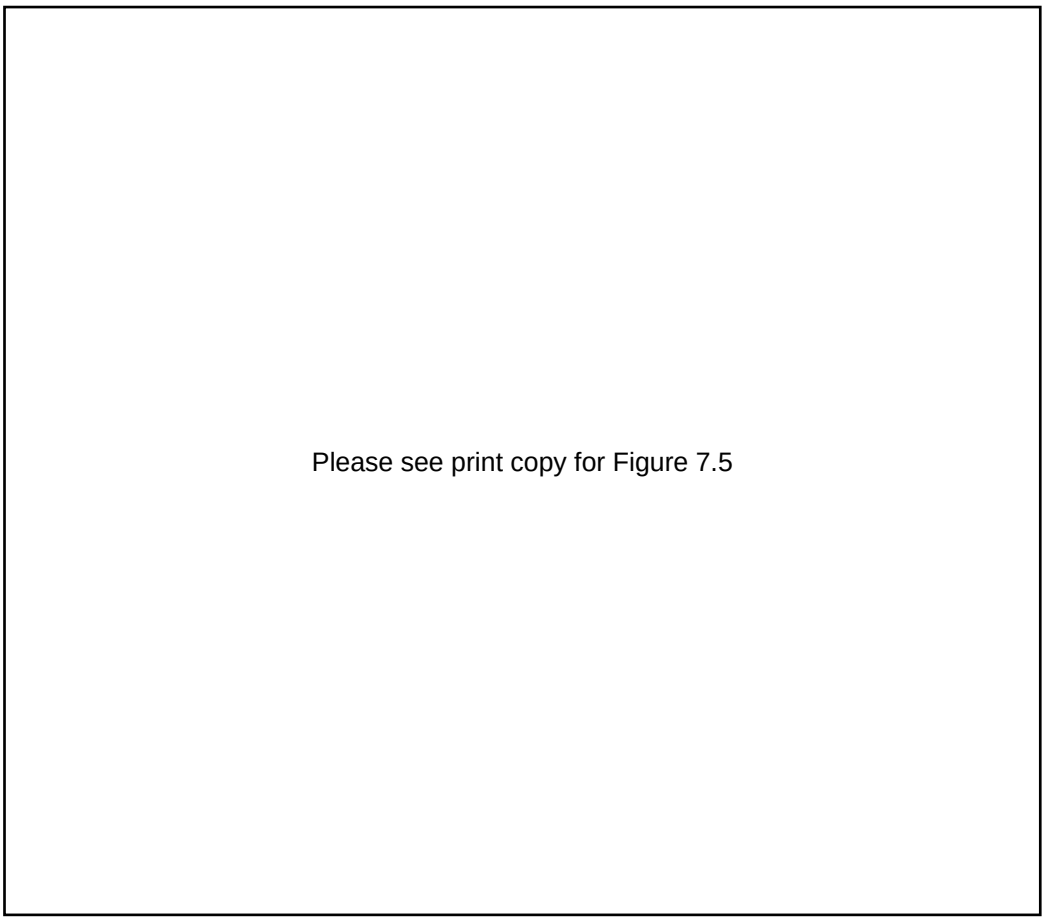

Fig. 7-5 A typical TEM image of Ag nano powders.

The electrochemical properties of Ag nanopowders as anodes in lithium-ion cell s were measured via coin-cell testing. Ag has a theoretical capacity of 820mA h/g when forming $Li_{3.3}Ag$ alloys.

$$3.3\ Li + Ag \leftrightarrow Li_{3.3}Ag$$

This alloying reaction is reversible, but accompanied by substantial volume change. The reduced particle size can decrease volume expansion in the local domain when forming Li_xAg alloys. The lithium storage capacity and cyclability of a nano Ag powder electrode is shown in Fig. 7-6. The Ag nano powder electrode demonstrated

an initial lithium storage capacity of 524 mAh/g. However, its capacity decreased significantly in the first cycle. From the second cycle, the capacity became stabilized. Therefore, Ag nano powder can not be used in a stand-alone situation. However, it can be used as an additive in carbon anode materials to enhance lithium storage capacity and electronic conductivity.

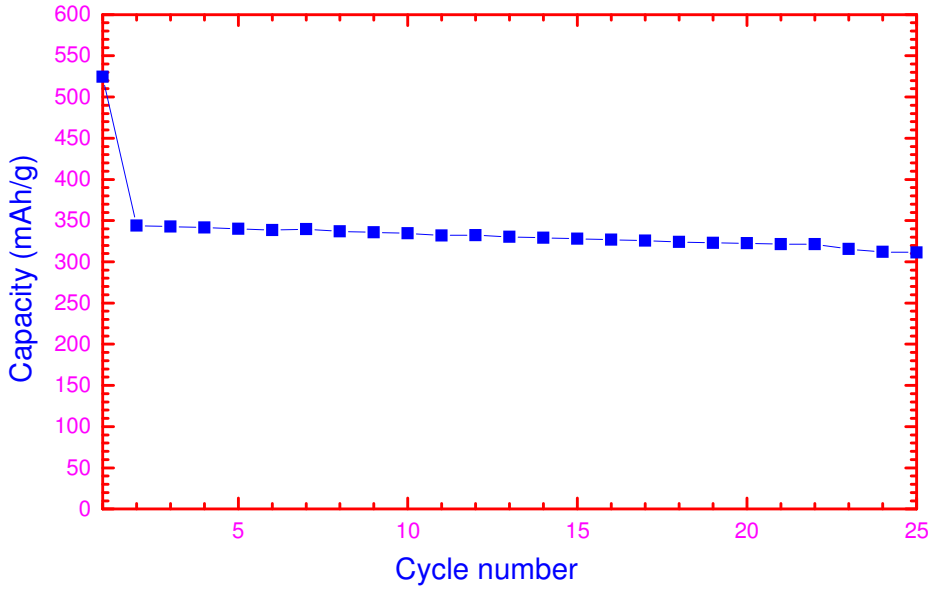

Fig. 7-6 The discharge capacity of Ag nano powder electrode versus cycle number.

7.3 Preparation and electrochemical characteristics of SnO_2 nanopowders

The reverse micelles A consisted of 1M $SnCl_4$ solution, 1M $NH_3 \cdot H_2O$ solution, AOT ($C_2OH_{37}NaO_7S$) as surfactant and n-heptane (C_7H_{16}) as organic matrix. The ratio of the ingredient chemicals in the reverse micelles is 1 M $SnCl_4$: 1M $NH_3.H_2O$: AOT :

n-heptane = 15 : 24 : 18 : 42 by weight percentage. Reverse micelles B consisted of 1M NH_4OH solution, AOT ($C_2OH_{37}NaO_7S$) as surfactant and n-heptane (C_7H_{16}) as organic matrix. The reverse micelles were mixed by stirring the reactant chemicals together with magnetic stirring and high speed stirring. The reactant product $Sn(OH)_4$ was formed inside the reverse micelles. The reacted solution was then centrifuged at 4000 rpm for 60 minutes to precipitate $Sn(OH)_4$ powders. The precipitated product was washed using methanol 4 times and then dried in vacuum at 80 °C for 5 hours. The dried $Sn(OH)_4$ powders were then sintered at 600 °C to convert them to SnO_2 nanopowders.

During the synthesis of SnO_2 nanosize powders, $Sn(OH)_4$ precipitates were formed inside the reverse micelles, which were then converted to SnO_2 through sintering at 450-600 °C. Because the sintering temperature is low, the tin dioxide remains nanocrystalline. The reverse micelles act as a nanoreactor. Fig. 7-7 shows the x-ray diffraction pattern of the final SnO_2 nano powders. All diffraction lines were indexed to tetragonal phase. Fig. 7-8(a) shows a TEM image of the SnO_2 powders. The as-prepared SnO_2 nanoparticles have a particle size in the range of 40 – 80 nm. There are some nanorods present in Fig.7-8(a). More highly magnified TEM image of these SnO_2 nanorods is shown in Fig. 7-8(b). The SnO_2 nanorods could be derived from $Sn(OH)_2$. In the process of forming merged reverse micelles, reverse micelles A containing $SnCl_4$ and reverse micelles B containing NH_4OH could form elongated reverse micelles and then self-assemble to rod-like micelles. The $Sn(OH)_4$ could

nucleate and grows into nanorods inside the rod-like micelles. The process for forming rod-like reverse micelles is shown in Fig. 7-9. After sintering, $Sn(OH)_4$ nanorods were converted into SnO_2 nanorods. This demonstrates that a 1D structure can be synthesized through the reverse micelle process.

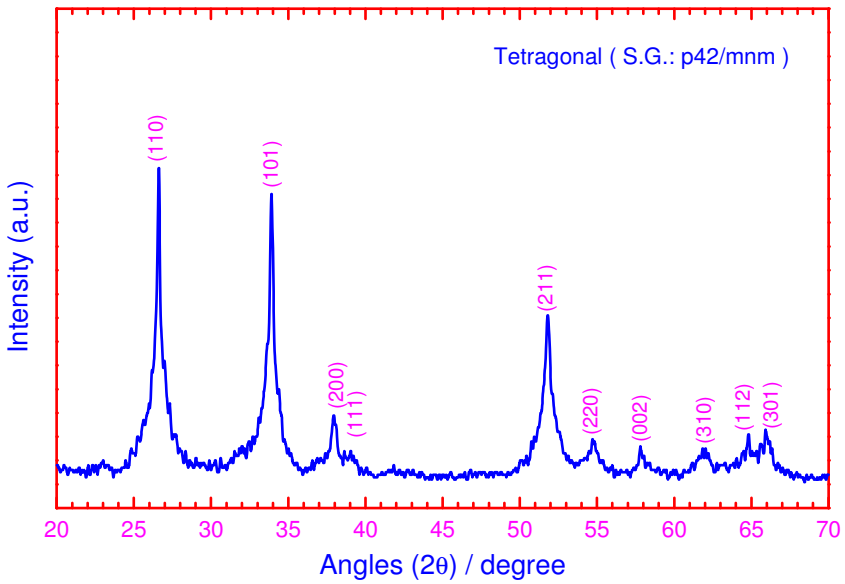

Fig. 7-7 X-ray diffraction pattern of SnO_2 nano powders.

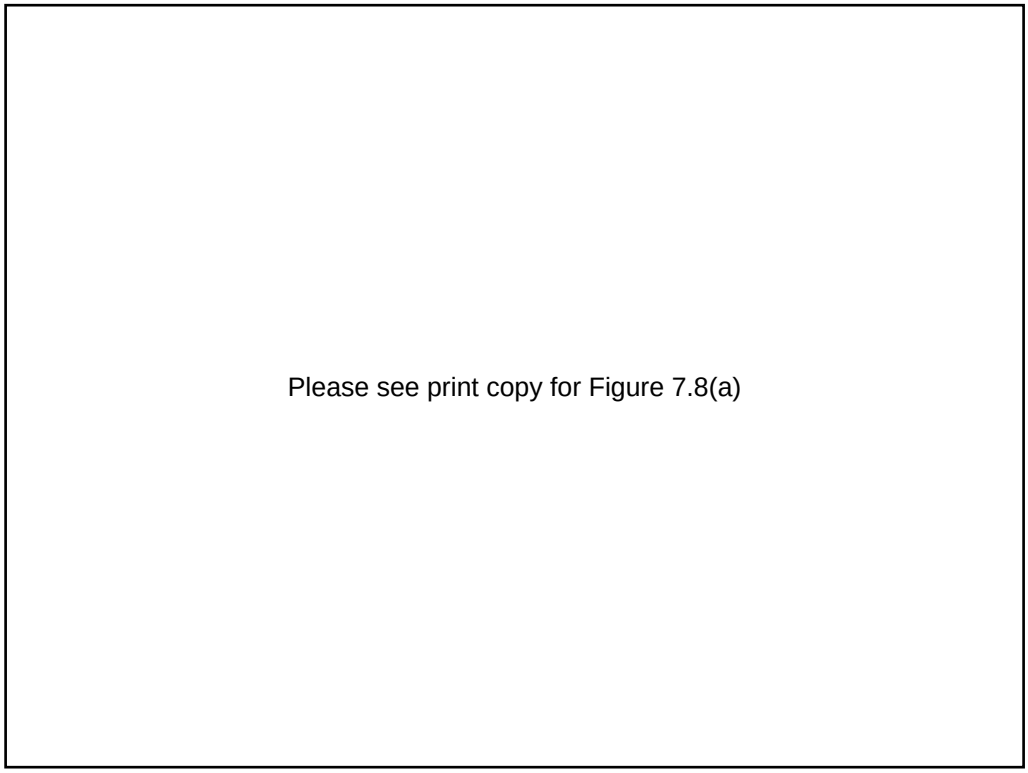

Fig. 7-8(a) TEM image of SnO_2 nanopowders.

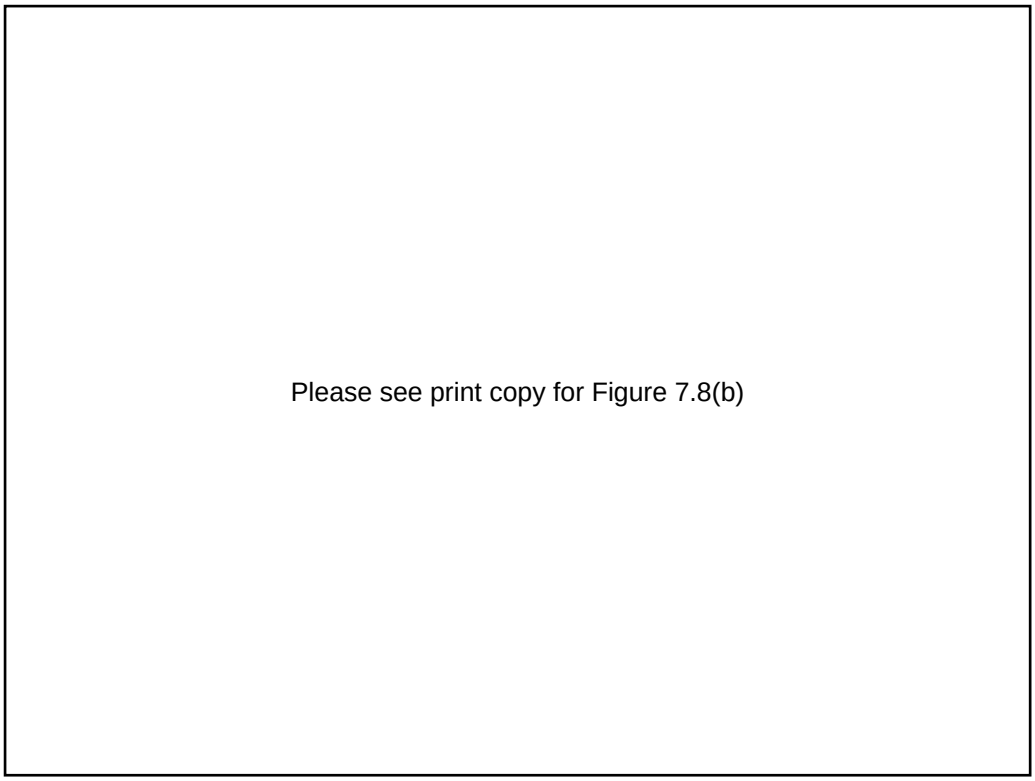

Fig. 7-8(b) TEM image of SnO_2 nanorods.

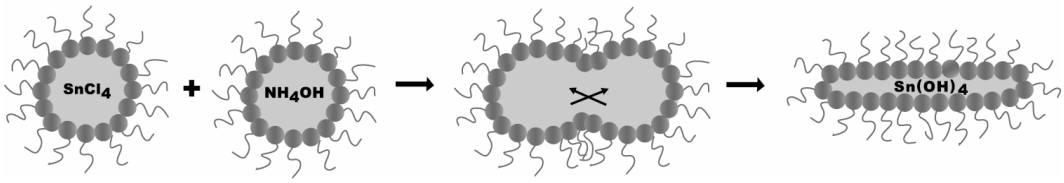

Fig. 7-9 Schematic of the formation of rod-like reverse micelles.

SnO_2 has recently emerged as a new anode material for reversible lithium storage [Idota, Kubota et al. 1997]. Nanosize SnO_2 powders are more desirable due to their small volume variation in the process of lithium insertion and extraction [Beaulieu, Dahn 2000]. The electrochemical properties of as-prepared SnO_2 powder anodes in lithium-ion cells were examined through cyclic voltammetry and charge-discharge measurements. Fig. 7-10 shows cyclic voltammograms of SnO_2 electrode. In the first scanning cycle, three lithiation peaks appear, which correspond to the formation of different Li_xSn alloys. From the second scanning cycle, only one pair of redox peaks occurs. The overall reactions for SnO_2 electrode in Li-ion cell are:

$$SnO_2 + 8.4\ Li \leftrightarrow Li_{4.4}Sn + 2Li_2O \quad (2)$$

$$Li_{4.4}Sn \leftrightarrow Sn + 4.4\ Li \quad (3)$$

When forming $Li_{4.4}Sn$ alloys, there is a 300 % volume increase. Therefore, it is a

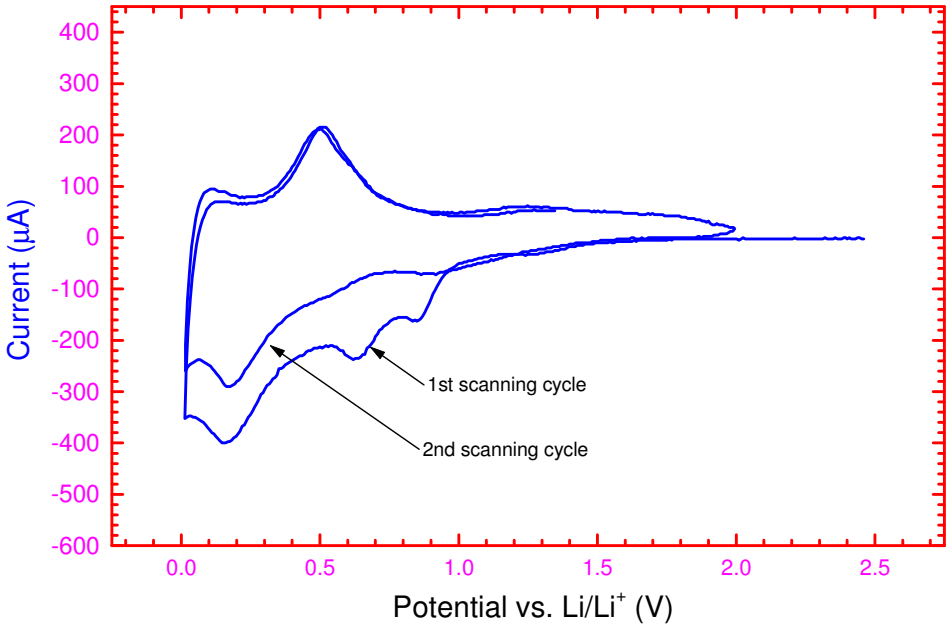

Fig. 7-10 Cyclic voltammograms of SnO_2 nano powder electrode. Scanning rate: 0.1 mV/s.

significant advantage to use nanosize SnO_2 powders to reduce the volume change in local sites. The Li_2O generated in the first cycle can act as a matrix to buffer such volume expansion. The cyclability of a nanosize SnO_2 electrode is shown in Fig. 7-11. In the first cycle, the SnO_2 electrode had a lithium storage capacity of about 900 mAh/g. Some of this capacity was used to form a passivation film due to the large surface area of the nano-powders. A stable reversible lithium storage capacity of about 380 mAh/g was achieved under repeated lithiation and delithiation cycling.

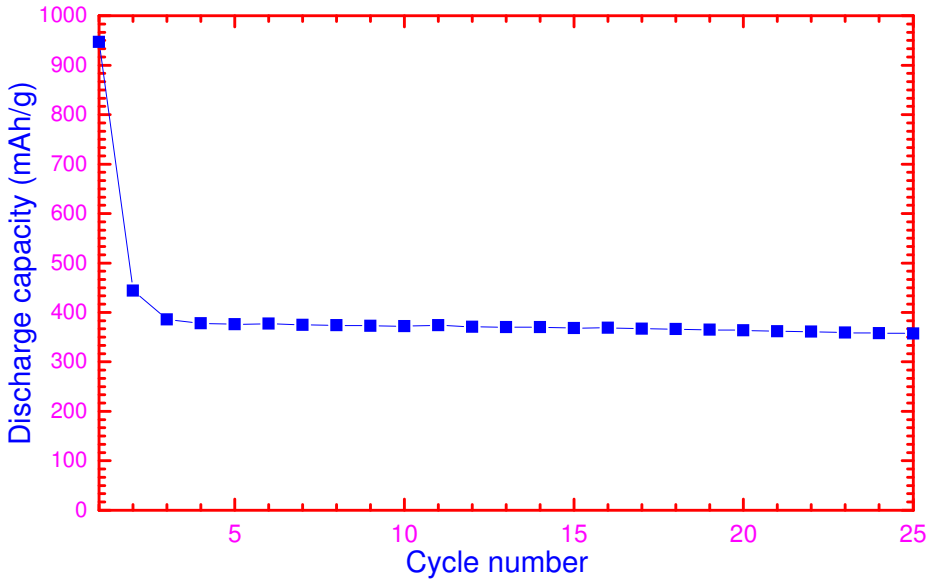

Fig. 7-11 Discharge capacity of SnO_2 nano powder electrode versus cycle number.

7.4 Conclusions

The reverse-micelle synthesis technique is a universal approach for preparing nanocrystalline metals, oxides and inorganic compounds. Nanosize Ag and SnO_2 nano powders were successfully synthesized by using the reverse-micelle technique. The synthesized Ag powders are very strongly crystalline with a crystal size in the range of 5 – 50 nm. The size of the Ag nanoparticles can be influenced by the concentration

of the reduction agent. The SnO_2 powders have a particle size of a few tens of nanometers. 1D structured SnO_2 nanorods were observed in SnO_2 nanopowders, which are formed in the process of reverse micelle synthesis. The electrochemical performance of nano Ag and SnO_2 powders as anodes in lithium-ion cells was measured. SnO_2 nanopowder electrodes show high electrochemical reactivity toward lithium in Li-ion cells. These nanocrystalline anode materials could have significant applications for lithium energy storage and conversion.

Chapter 8

General conclusions and suggestions for future study

8.1 Review of the study

Investigations on electrode materials for lithium ion batteries have been presented in the previous chapters. These studies include the following aspects:

(1) Improvement of the electrochemical performance and tap density of $LiNi_{1-x}Co_xO_2$ by using high tap density spherical $Ni_{1-x}Co_x(OH)_2$ as the precursors;

(2) Detailed studies on stability improvement of the $LiNiO_2$ structure by Co and Ni co-doping;

(3) Electrochemical performance improvement of $LiFePO_4$ cathode materials by novel preparation routes, such as the sol-gel method and the carbon aerogel synthesis method;

(4) Studies of the influences of crystallinity, morphology, and particle size on the electrochemical performance of cobalt oxides;

(5) Synthesis of nanocrystalline transition metals and oxides by using a reverse micelle approach and their characterization as anodes for lithium ion batteries.

Studies of the above five aspects have been summarized in the previous chapters. Based on the summaries, general conclusions are presented below:

1. Electrode fabricated from electroactive $LiCo_xMn_yNi_{1-x-y}O_2$ powder prepared from lithium compounds and $Co_xMn_yNi_{1-x-y}(OH)_2$ precursors by heating at 850-900 °C delivered a high reversible capacity of 150 mAh/g. The lattice parameters, *a* and *c*, and the unit cell volume decreased with increasing cobalt content. The hexagonal unit cell dimensions shrink with an increase in the Co doping level, which may be induced by the difference in size between trivalent cobalt and divalent nickel ions (r^{2+}_{Ni}=0.69 Å and r^{3+}_{Co}=0.545 Å).
2. High density spherical $LiCo_{0.25}Ni_{0.75}O_2$ compounds have been obtained from lithium compounds and spherical $Co_{0.25}Ni_{0.75}(OH)_2$ precursor by heating in oxygen at 750°C and 800°C for 12 hrs. It was found that the spherical $LiCo_{0.25}Ni_{0.75}O_2$ compounds have a highly ordered layered structure with reduced cation mixing, which probably is the reason for their high reversible capacity (~167 mAh/g) and stable cyclability.
3. Carbon-enriched $LiFePO_4$ compounds were prepared by the sol-gel method and the R/F carbon gel method. The organic groups in the precursors work as a particle size growth inhibitor as well as a carbon source. Fine $LiFePO_4$ compounds embedded in amorphous carbon were obtained. The electronic conductivity of $LiFePO_4$ can be dramatically enhanced via the carbon inclusion. Electrochemical evaluation of the $LiFePO_4$ reveals a lithium insertion plateau

around 3.4 V vs. Li together with a specific capacity of over 160 mAh/g at the C/5 rate. Differential capacity data confirm the two-phase nature of the insertion reactions as well as outstanding ionic reversibility.

4. Five different types of cobalt oxides were investigated as lithium storage materials in lithium ion cells. It was found that the electrochemical properties of cobalt oxides are sensitive to the crystallinity, morphology, and particle size of the materials. When the as-prepared nanosize Co_3O_4 powders were used as anode materials in lithium cells, they demonstrated high lithium storage capacity and good cyclability. This is promising for commercial use as anode materials in lithium-ion batteries. Results of *ex situ* X-ray diffraction on the crystalline Co_3O_4 electrode verified that the lithiated products Li_2O and Co are nanoparticles. Further optimisation of the microstructure of cobalt oxides can improve their electrochemical performance.
5. Nanocrystalline transition metals and oxides are very attractive anode materials for lithium-ion batteries due to their higher lithium storage capacity compared to graphite, which is currently the most common commercial anode material used in lithium ion batteries. In my study, Ag and SnO_2 were synthesized by using a reverse-micelle synthesis technique, which is a universal approach for preparing nanocrystalline metals, oxides, and inorganic compounds. The synthesized Ag powders are very strongly crystalline with a crystal size in the range of 5 – 50 nm. The size of the Ag nanoparticles can be influenced by the concentration of the reduction agent. The SnO_2 powders have a particle size of a few tens of

nanometers. 1D structured SnO_2 nanorods were observed in the SnO_2 nanopowders, which were formed by the process of reverse micelle synthesis. The SnO_2 nanopowder electrodes show high electrochemical reactivity toward lithium in Li-ion cells. These nanocrystalline anode materials could have significant applications for lithium energy storage and conversion.

8.2 Suggestions for future study

Although a series of studies on the physical, structural, and electrochemical properties of $LiCo_xMn_yNi_{1-x-y}O_2$, $LiCo_{0.25}Ni_{0.75}O_2$, $LiFePO_4$, Co_3O_4, CoO, Ag, and SnO_2 has been carried out in the present work, it is of note that the characterisation of the electrode performance has focused on the specific capacity and cycle life. Other parameters and properties of the electrode such as rate capability, high temperature behavior, and thermal stability have not been considered. It is therefore suggested that efforts should be made to study the parameters mentioned above in order to further understand and improve the performance of the electrodes.

In Chapter 4, the reason for the improved cycling stability of the spherical $LiCo_{0.25}Ni_{0.75}O_2$ prepared from spherical $Co_xMn_yNi_{1-x-y}(OH)_2$ precursors can be further investigated by using *in-situ* synchrotron x-ray diffraction. This will give direct evidence of intermediate compounds during charge/discharge cycling and provide valuable insight into the spherical $LiCo_{0.25}Ni_{0.75}O_2$ structure. For other materials prepared in this project, more detailed structural and kinetic tests are also

needed to clearly understand the mechanism behind the reactions.

In Chapter 5, element (such as Mg) substitution into $LiFePO_4$ using the sol-gel and R/F carbon gel methods is very promising in terms of improving its conductivity and electrochemical performance. Further research using element doping should lead to higher performance cathode materials for lithium ion batteries.

REFERENCES

Alcantara R., Jimenez J.M., Lavela P., Morales J., Tirado J.L., Mater. Sci. Eng. B, 39, 216(1996).

Alcantara R., Lavela P., Tirado J.L., Stoyanova R., Zhecheva E., J. Electrochem. Soc., 145, 730 (1998).

Alcantara R., Madrigal F.J.F., Vicente C.P., Tirado J.L., Jumas J.C., Fourcade J.O., Chem. Mater., 12, 3044 (2000).

Alcantara R., Jimenez-Mateos J.M., Tirado J.L., J. Electrochem. Soc., 149, 201 (2002).

Alivisatos A.P., Science 271, 933 (1996).

Ammundsen B., Desilvestro J., Groutso T., Hassell D., Metson J.B., Regan E., Steiner R., and Pickering P., J. Electrochem. Soc., 147, 4078 (2000).

Anderson Anna S., Haffstrom Lennart, Kalska Beata, Thomas John O., Solid State Lett., 3, 66 (2000).

Anderson Anna S., Kalska Beata, Haggstrom Lennart, Thomas John O., Solid State Ionics, 130, 41 (2000).

Anderson A.S., Thomas J.O., J. Power Sources 97-98,498 (2001).

Antaya M., Dahn J.R., Preston J.S., Rossen E., and Reimers J.N., J. Electrochem. Soc. 140, 575 (1993).

Anuradha T.V.; Ranganathan S., Nanostructured Materials, 12, 1063 (1999).

Arachi Y., Kobayashi H., Emura S., Nakata Y., Tanaka M., Asai T., Chem. Lett., 32, 60 (2003).

Arai T., J. Phys. Soc. Jpn. 15, 916 (1960).

Arai H., Okada S., Sakurai Y., and Yamaki J., J. Electrochem. Soc. 144, 3117 (1997).

Armstrong A.R., Bruce P.G., Nature, 381, 499 (1996).

Armstrong A.R., Robertson A.D., Bruce P.G., Electrochim. Acta, 45, 285 (1999).

Arora P., Popov B.N., White R.E., J. Electrochem. Soc. 145,807 (1998).

Auborn J.J., Baberio Y.L., J. Electrochem. Soc., 134, 638 (1987).

Barker J., Saidi M.Y. and Swoyer J.L., Electrochem. Solid-State Lett. 6, A53 (2003).

Banov B., Bourikov J., Mladenov M., J. Power Sources 54,268 (1995).

Bauer E.M., Bellitto C., Pasquali M., Prosini P.P.and Righini G., Electrochem. Solid-State Lett. 7, A85 (2004).

Beaulieu L.Y., Dahn, J.R., J. Electrochem. Soc., 147, 3237 (2000).

Beaulieu L.Y., Eberman K.W., Turner R.L., Krause L. J., Dahn J.R., Electrochem. Solid State Lett., 4, A137 (2001).

Besenhard J.O., Hess M. and Komenda P., Solid State Ionics 40/41, 525 (1990).

Besenhard J.O., Yang J., Winter M., J. Power Sources, 68, 87 (1997).

Bewlay S.L., Konstantinov K., Wang G.X., Dou S.X., Liu H.K., Materials Letters, 58, 1788 (2004).

Billand D., Henry F.X., Willmann P., Mat. Res. Bull. 28, 477 (1993).

Bohnke C., Bohnke O., Fourquet J.L., J. Electrochem. Soc. 144,115 (1997).

Bonino F., Brutti S., Reale P., Scrosati B., Gherghel L., Wu J. and Mullen K., Advanced Materials, 17, 743 (2005).

Boukamp B.A., Lesh G.C., Huggins R.A., J. Electrochem. Soc., 128, 725 (1981).

Brouselly M., Perton F., and Labat J., J. Power Sources, 43-44, 209 (1993).

Brouselly M., Lithium Battery Discussion, Bordeaux-Arcachon (2001).

Brousse T., Retoux R., Herterich U., Schleich D.M., J. Electrochem. Soc., 145, 1 (1998).

Carpenter E.E.; Kumbhar A.; Wiemann A.J.; Srikanth H.; Wiggins J.; Zhou W.L.; O'Connor C.J., Materials Science and Engineering A 286, 81 (2000).

Caurant D., Baffier N., Garcia B., Pereira-Ramos J.P., Solid State Ionics 91,45 (1996).

Ceder G., Chiang Y.M., Sadoway D.R., Aydinol M.K., Jang Y.I., Huang B., Nature, 392, 694 (1998).

Ceder G., Meng Y.S., Yang S.H., Grey C.P., 12th International Meeting on Lithium Batteries; Electrochemical Society; Pennington, vol12, Abstract 22 (2004).

Chen D.H., Yeh J.J., and Huang T.C., J. Colloid and Interface Science 215, 159 (1999).

Chen J.P., Sorensen C.M., and Klabunde K.J., Physics Review B 51, 527 (1997).

Chen R., Whittingham M.S., J. Electrochem. Soc. 144, L64 (1997).

Chen Z., Dahn J.R., J. Electrochem. Soc., 149, A1184 (2002).

Chen Z., Dahn J.R., Electrochim. Acta, 49, 1079 (2004).

Chiang Y. M., Jang Y. _II, Wang H., Huang B., Sadoway D.R. Ye P., J. Electrochem. Soc., 145, 887 (1998).

Cho J., Kim G., Ekectricgen. Solid State Lett. 2, 253 (1999).

Cho J., Kim G., and Lim H.S., J. Electrochem. Soc. 146, 3571 (1999).

Cho J., Kim C., Yoo S.I., Electrochem. Soid State Lett. 3, 362 (2000).

Cho J., Kim Y.J., Park B., Chem. Mater., 12, 3788 (2000).

Cho J., Kim Y.J., Park B., J. Electrochem. Soc., 148, A1110 (2001).

Cho J., Kim Y.J., Kim J.T., Park B., Angew. Chem. Int. Ed. 40, 3367 (2001).

Cho J., Park B., Lithium Battery Discussion Electrode Materials, Bordeaux, Abstract 1 (2003).

Choi Y.M., Pyun S.I., Moon S.I., Hyung Y.E., J. Power Sources,72,83(1998).

Chouvin J., Fourcade J.O., Jumas J.C., Simon B., Godiveau O., Chem. Phys. Lett. 308, 413 (1999).

Chouvin J., Branci C., Sarradin J., Olivier-Fourcade J., Jumas J.C., Simon B., Biesan P., J. Power Sources, 81-82, 277 (1999).

Chung Sung-Yoon, Blocking Jason T., and Chiang Yet-Ming, Nature Materials, 1, 123 (2002).

Colvin V.L.; Schlamps M.C.; Alivisatos A.P., Nature, 370, 354 (1994).

Courtney I.A., Dahn J.R., J. Electrochem. Soc. 144, 2045 (1997).

Courtney I.A., Tse J.S., Mao O., Hafner J. Dahn J.R., Phys. Rev. B 58, 15583 (1998).

Courtney I.A., Dunlap R.A., Dahn J.R., Electrochim. Acta 45, 51 (1999).

Courtney I.A., McKinnon W.R., Dahn J.R., J. Electrochem. Soc., 146, 59 (1999).

Croce F., Epifanio A.D., Hassoun J., Deptula A., Olczac T., and Scrosati B., Electrochem. Solid-State Lett., 5, A47 (2002).

Croguennec L., Pouillerie C., Delmas C., Solid State Ionics, 135, 259 (2000).

Crosnier O., Brousse T., Schleich D.M., Ionics, 5, 311 (1999).

Cushing B.L., Goodenough J.B., Solid State Sci., 4, 1487 (2002).

Davidson I.J., McMillan R.J., Slegr H., Luan B., Kargina I., Murray J.J., J. Power Sources, 81-82, 406 (1999).

Dahn J.R., Zheng T., Liu Y.H., and Xue J.S., Science, 270, 590 (1995).

Dahn J.R., Xing W., Gao Y., Carbon, 35, 825 (1997).

Davis S.R., Chadwick A.V., Wright J.D., J. Mater. Chem., 8, 2065 (1998).

Deki S.; Akamatsu K; Hatakennaka Y; Mizuhata M; Kajinami A.. Nanostructured Mater., 11, 59 (1999).

Delacourt C., Poizot P., Morcrette M., Tarascon J.M., Masquelier C., Chem. Mater. 16, 93 (2004).

Delmas C., Saadoune I., Solid State Ionics, 53-56, 370 (1992).

Delmas C., Saadoune I., Rougier A., J. Power Sources 89,43 (1996).

Deoff M.M., Richardson T.J., Kepley L. J. Electrochem. Soc., 143, 2507 (1996).

Deoff M.M., Richardson T.J., Hwang K.T., Anapolsky A., ITE Battery Lett. 2, B (2001).

Deoff M.M., Hu Y., McLarnon F., Kostecki R., Electrochem. Solid State Lett. 6, A207 (2003).

Dolle M., Poizot P., Dupont L., Tarascon J.M., Electrochem. Solid-State Lett., 5, A18 (2002).

Dominko R., Gaberscek M., Drofenik J., Bele M., Pejovnik S., Electrochem. Solid State Lett., 4, A187 (2001).

Driksson T.A., Lee Y.J., Hollisworth J., Reimer J.A., Cairns E.J., Zhang X.F., Doeff M.M., Chem. Mater. 15, 4456 (2003).

Dunlap R.A., Small D.A., MacNeil D.D., Obrovac M.N., Dahn J.R., J. Alloy Compd. 289, 135 (1999).

Dutta G., Manthiram A., Goodenough J.B., and Grenier J.C., J. Solid State Chem., 96, 123 (1992).

Ehrlich G.M., Durand C., Chen X., Hugener T.A., Spiess F., Suib S.L., J. Electrochem. Soc. 147, 886 (2000).

Fendler J.H.; Tricot Y.M., J. Am. Chem. Soc. 106, 7359 (1984).

Fendler J.H., Chem. Rev. 87, 877 (1987).

Fey G.T.K., Hsieh M.C., Jaw H.K., and Lee T.J., J. Power Sources, 43-44, 673 (1993).

Fey G.T.K., Chen K.S., Huang B.J., Lin Y.L., J. Power Sources,68,519 (1997).

Foster D.L., Wolfenstine J., Read J.R. and Behl W.K., Electrochemical and Solid-state Letters 3, 203 (2000).

Foster M.S., Crouthamel C.E., Wood S.E., J. Phys. Chem., 70, 3042 (1966).

Franger S., Cras F. Le, Bourbon C., and Rouault H., Electrochem. Solid-State Lett., 5, A231 (2002).

Franger S., Bourbon C., Cras F.L., J. Electrochem. Soc. 151, A1024 (2004).

Frank U., Muller W., Schafer H., Z. Natursforsch B 30, 1 (1975).

Frank U., Muller W., Schafer H., Z. Natursforsch B 30, 6 (1975).

Frank U. Muller W., Z. Natursforsch B 30, 316 (1975).

Gabrisch H., Yazimi R., Fultz B., J. Electrochem. Soc. 151, A891 (2004).

Garcia B., Farcy J., Pereira-Ramos J.P., Perichon J. and Baffier N., J. Power Sources, 54, 373 (1995).

Goodenough J.B., Mizuchima K., U.S.Patent 4, 302, 518 (1981).

Goward G.R., Leroux F., Power W.P., Ouvrard G., Dmowski W., Egami T., Nazar L.F., Electrochem. Solid State Lett. 2, 367 (1999).

Gratz J., Ahn C.C., Yazami R. and Fultz B., Electrochem. Solid-state Lett. 6, A194 (1996).

Grugeon S., Laruelle S., Herrera-Urbina R., Dupont L., Poizot P., Tarascon P.J.M., J. Electrochem. Soc., 148, A285 (2001).

Guilmard M., Pouillerie C., Croguennec L., Delmas C., Solid State Ionics, 160, 39 (2003).

Guilmard M., Rougier A., Grune M., Croguennec L., Delmas C., J. Power Sources, 115, 305 (2003).

Gummow R.J., Thackeray M.M., Solid State Ionics, 53-56, 681 (1992).

Gummow R.J. and Tachkeray M.M., J. Electrochem. Soc. 140, 3365 (1993).

Guo Z.P., H. Liu, H.K. Liu and S.X. Dou, J. New Mater. Electro. Sys.,6,263(2003).

Guo Z.P., Z.W. Zhao, H.K. Liu and S.X. Dou, J. Power Sources, 146, 190 (2005).

Hamad-Schifferli K.; Schwartz J.J.; Santos A.T.; Zhang S.G.; Jacobson J.M., Nature, 415, 152 (2002).

Hansen D.A., Chang L.J., Acta Cryst. B 25, 2392 (1978).

Herle P.S., Ellis B., Coombs N., Nazar L.F., Nature Materials, 3, 147 (2004).

Hewston T.A., Chamberland B.L., J. Phys. Chem. Solids, 48, 97 (1987).

Hirota K., Nakazawa Y., and Ishikawa M., J. Phys. Condens. Matter., 3, 4721 (1991).

Honbo K., Muranaka Y., Yishikawa M., in: 39th Battery Symposium in Japan Sendai, pp. 311 (1998).

Hosoya M., Takahashi K., Fukushima Y., Patents JP2002-75356, EP1184920, EP1193787, US2002114754 (2002).

Howing J., Gustafsson T., Thomas J.O., Acta Crystallogr. B59, 747 (2003).

Huang S., Kavan L., Exnar I., Gratzel M., J. Electrochem. Soc., 142, L142 (1995).

Huang H., Rao G.V., Chowdari B., J. Power Sources, 81-82, 690 (1999).

Huang H., Yin S.C., and Nazar L.F., Electrochem. Solid-State Lett., 4, A170 (2001).

Huggins R.A., Solid State Ionics, 113-115,57 (1998).

Huggins R.A., J. Power Sources, 81-82, 13 (1999).

Hwang S., Lee H., Jang S., Lee S.M., Lee S.J., Baik H., Lee J., Electrochem. Solid-State Lett., 4, A97 (2001).

Idota Y., US Patent, 5478671 (1995)

Idota Y., Kubota T., Matsufuju A., Maekawa Y., Miyasaka T., Science, 276, 1395 (1997).

Imanishi N., Fujiyoshi M., Takeda Y., Yamamoto Y., Tabuchi M., Solid State ionics, 118, 121 (1999).

Jang Young-II, Huang Biying, Chiang Yet-Ming and Sadoway Donald R., Electrochem. Solid State Lett., 1, 13 (1998).

Jang Y-II, Wang H., Chiang Y. M., J. Mater. Chem., 8, 2761 (1998).

Jang Y._II., Huang B., Wang H., Sadoway D.R., Ceder G., Chiang Y.M., Liu H. Tamura H., J. Electrochem. Soc., 146, 862 (1999).

Jang Young-II, Moorehead W. Douglas, Chiang Yet-Ming, Solid State Ionics, 149, 201 (2002).

Johnson C.S., Kim J.S., Kropf A.J., Kahaian A.J., VaugheyJ.T. and Thackeray M.M., Electrochem. Comm., 4, 492 (2002).

Kalyani P. Kalaiselvi N., Renganathan N.G., Raghavan M., Mater. Res. Bull., 39, 41 (2004).

Kang S.H., Kim J., Stoll M.E., Abraham D., Sun Y.K., Amine K., J. Power Sources, 112, 41 (2002).

Kanno R., Kubo H., Kawamoto Y., kamiyama Y., Izumi F., Takeda Y., and Takano M., J. Solid State Chem., 110, 216 (1994).

Kear B.H.; McCandlish L.E. Nanostructured Mater., 3, 19 (1993).

Kepler K.D., Vaughey J.T., Thackeray M.M., J. Power Sources, 81-82, 383 (1999).

Kepler K.D., Vaughey J.T., Thackeray M.M., Electrochem. Solid-State Lett. 2, 307 (1999).

Kim II.S., Kumta P.N., and Blomgren G.E., Electrochem. Solid-State Lett. 3,493 (2000).

Kim II.S., Blomgren G.E., Kumta P.N., Electrochem. Solid-State Lett. 6,A157 (2003).

Kim J.M., Chung H.T., Electrochim. Acta, 49, 937 (2004).

Klarreich E., Nature, 413, 450 (2001).

Kobayashi H., Sakaebe H., Kageyama H., Tatsumi K., Arachi Y., Kamiyama T., J. Mater. Chem., 13, 590 (2003).

Koyama Y., Makimura Y., Tanaka I., Adachi H., Ohzuku T., J. Electrochem. Soc., 151, A1499 (2004).

Koch C.C., Nanostructured Mater., 2, 109 (1993).

Larcher D., Beaulieu L.Y., Mao O., George A.E., Dahn J.R., J. Electrochem. Soc., 147, 1703 (2000).

Larcher D., Beaulieu L.Y., MacNeil D.D., Dahn J.R., J. Electrochem. Soc., 147, 1658 (2000).

Lacher D., Sudant G., Leriche J.B., Chabre Y., Tarascon J.M., J. Electrochem. Soc., 149, A234 (2002).

Lazzari, M. Sacrosati B., J. Electrochem. Soc. 127, 773 (1980).

Lecerf A., Brpisse;u M., and Gabano J.P., USpatent 4,980,080 (1989).

Levasseur S., Menetrier M., Suard E., Delmas C., Solid State Ionics, 128, 11 (2000).

Li G., Ikuta H., Uchida T., Wakihara M., J. Electrochem. Soc., 143, 178 (1996).

Li G., Azuma H., Tohda M., Electrochem. Solid State Lett., 5, A135 (2002).

Li H., Huang X., Chen L.Q., J. Power Sources, 81-82, 340 (1999).

Li H., Huang X.J., Chen L.Q., Zhou G.W. and Liang Y., Electrochem. Solid-State Lett. 2, 547 (1999).

Lin J.; Zhou W.L.; O'Connor C.J., Materials Letters 49, 282 (2001).

Liu Z., Yu A., Lee J.Y., J. Power Sources, 81-82, 416 (1999).

Liu Y., Hanai K., Yang J., Imanishi N., Hirano A. and Takeda Y., Solid State Ionics, 168, 61 (2004).

Lu C.H.; Wang H.C., J. Eur. Ceram. 23, 865 (2003).

Lu Z., Dahn J.R., Chem. Mater. 12, 3583 (2000)

Lu Z., MacNeil D.D., Dahn J.R., Electrochem. Solid State Lett., 4, A191 (2001).

Lu Z. Dahn J.R., Chem. Mater., 13, 1252 (2001).

Lu Z. Dahn J.R., Chem. Mater., 13, 2078 (2001).

Lu Z., Dahn J.R., J. Electrochem. Soc., 148, A237 (2001).

Macneil D.D., Lu Z. Dahn J.R., J. Electrochem. Soc., 149, A1332 (2002).

Maleki H., Deng G. Anani A., Howard J., J. Electrochem. Soc., 146, 3224 (1999).

Mao O., Dahn J.R., J. Electrochem. Soc., 146, 423 (1999).

Mao O., Turner R.L., Courtney I.A., Fredericksen B.D., Buckett M., Krause L.J., Dahn J.R., Electrochem. Solid-State Lett., 2, 3 (1999).

Masquelier C., Wurm C., Morcrette M., Gaubicher J., International Meeting on Solid State Ionics, Cairns, Australia, July 9-13, 2001 ; The International Society of Solid State Ionics, paper A-IN-06 (2001).

Makimura Y., Ohzuku T., J. Power Sources, 119-121, 156 (2003).

Megahed S. and Scrosati B., J. Power Sources 51, 79 (1994).

Mehrota R.C., J. Non-Cryst. Solids 121, 1 (1990).

Mitsuharu Tabuchi, Kazuaki Ado, Christian Masquelier, Ichiro Matsubara, Hikari Sakaebe, Hiroyuki Kageyama, Hironori Kobayashi, Ryoji Kanno and Osamu Nakamura, Solid State Ionics, 89, 53 (1996).

Morales J., Perez-vicente C., Tirado J.L., Mater. Res. Bull. 25, 623 (1990).

Morales J., Sanchez L., J. Electrochem. Soc., 146, 1640 (1999).

Morgan D., Vanderven A., Ceder G., Electrochem. Solid State Lett., 7, A30 (2004).

Morimoto H., Tatsumisago M. and Minami T., Electrochemical and Solid-state Letter 4, A16 (2001).

Moshtev R.V., Zatilova P., Manew V., Sato A., J. Power Sources, 54, 329 (1995).

Muller W., Schafer H., Z. Natursforsch B 28, 246 (1973).

Muller W., Z. Natursforsch B 29, 304 (1974).

Nagaura T., Tozawa K., Prog. Batter. Solar Cells 9, 209 (1990).

Nakai I., Nakagome T., Electrochem. Solid State Lett., 1, 259 (1998).

Nayoze C., Ansart F., Laberty C., Sarrias J., Rousset A., J. Power Sources 99,54 (2001).

Ngala j.K., Chernova N.A., Ma M., Mamak M., Zavalij P.Y., Whittingham M.S., J. Mater. Chem., 14, 214 (2004).

Nitta Y., Okamura K., Haraguchi K., Kobayashi S., Ohta A., J. Power Sources, 54, 511 (1995).

Niu J. and Lee J.Y., Electrochem. Solid-state Lett. 5, A107 (2002).

Ohara S., Suzuki J., Sekine K., Takamura T., J. Power Sources 119-121, 591 (2003).

Ohzuku T., Kitagawa M., Hirai T., J. Electrochem. Soc., 137, 769 (1990).

Ohzuku T., Ueda A., Nayayam M., Iwakishi I., Komori H., Electrochim Acta, 38, 1159 (1993).

Ohzuku T., Ueda A., and Nagayama M., J. Electrochem. Soc. 140, 1862 (1993).

Ohzuku T., Ueda A., Kouguchi M., J. Electrochem. Soc. 142, 4033 (1995).

Ohzuku T., Yanagawa T., Kouguchi M., Ueda A. J. Power Sources, 68, 131 (1997).

Ohzuku T., Nakura K., Aoki T. Electrochim. Acta, 45, 151 (1999).

Ohzuku T., Makimura Y., Chem. Lett., 744 (2001).

Ohzuku T., Makimura Y., Chem. Lett., 642 (2001).

Okada M., Takahashi K., and Mouri T., J. Power Sources 68, 545 (1997).

Orel B., Lavrencic-Strangar U., Crnjak-Orel Z., Bukovel P., Kosec M., J. Non-Cryst. Solids 167, 272 (1994).

Ott A., Endres P., Klein V., Fychs B., Jäger A., Mayer H.A., Kemmler-sack S., Praas H.W., Brandt K., Filoti G., Kunczer V., Rosenberg M., J. Power Sources 72, 1 (1998).

Ouyang C., Shi S., Wang Z., Huang X., and Chen L., Chem. Phys. Rev. B, 69, 104303 (2004).

Padhi A.K., Najundaswamy K.S., Goodenough J.B., J. Electrochem. Soc., 144, 1188 (1997).

Padhi A.K., Nanjundaswamy K.S., Masquelier C., Okada S. and Goodenough J.B., J. Electrochem. Soc., 144, 1609 (1997).

Papirer E., Horny P., Balard H., Authore R., Petipas C. and Martinet A., Journal of Colloid and Interface Science 94, 207 (1983).

Park K.S., Son J.T., Chung H.T., Kim S.J., Lee C.H., Kang K.T.and Kim H.G., Solid State Communications 129, 311 (2004).

Patoux S., Doeff M.M., Electrochem. Comm., 6, 767 (2004).

Pekala R.W., J. Mater. Sci. 24, 3221 (1989).

Pietro B.D., Patriarca M., Scrosati B., J. Power Sources, 8, 298 (1982).

Poizot P., Laruelle S.,Grugeon S., Dupont L.,Tarason J.M., Nature 407,496 (2000).

Pouillerie C., Croguennec L., Delmas C. Solid State Ionics, 132, 15 (2000).

Pouillerie C., Croguennec L., Biensan P., Willmann P., and Delmas C., J. Electrochem. Soc. 147, 2061 (2000).

Pouillerie C., Perton F., Biensan P., Peres J.P., Brouselly M., Delmas C. J. Power Sources, 96, 293 (2001).

Pralong V. , Leriche J.B. , Beaudoin B. , Naudin E., Morcrette M. and Tarascon J.M., Solid State Ionics, 166, 295 (2004).

Prosini P., Zane D., Pasquali M., Electrochem. Acta, 46, 3517 (2001).

Prosini Pier Paolo, Carewaka Maria, Scaccia Silvera, Wisniewski Pawel, Passerini Stefano, and Pasquali Mauro, J. Electrochem. Soc., 149, A886 (2002).

Prosini P.P., LiSi M., Zane D., and Pasquali M., Solid State Ionics, 148, 45 (2002).

Prosini P.P., Carewska M., Scaccia S., Wisniewski P., Passerini S.and Pasquali M., Electrochimica Acta 48, 4205 (2003).

Quintana A., et al. Pharm. Res. 19, 1310 (2002).

Ravet N., Goodenough J.B., Besner S., Simoneau M., Hovington P., Armand M., Electrochem. Soc. Abstract, 99-2, 127 (1999).

Ravet N., Besner S., Simoneau M., ALLEE a., Armand M., Magnan J.F. (Hydro-Quebec European Patent 1049181A2 (2000).

Retoux R., Brousse T., Schleich D.M., J. Electrochem. Soc. 146, 2472 (1999).

Rosenberg M., Stelmaszyk P., Klein V., Kemmler-Sack S., Filoti G., J. Appl. Phys. 75,6813 (1994).

Rossen E., jones C.D.W., Dahn J.R., Solid State Ionics, 57, 311 (1992).

Rossen E., Reimers J.N., Dahn J.R., Solid State Ionics, 62, 53 (1993).

Rossen E., Jones C.D., and Dahn J.R., Solid State Ionics, 67, 123 (1993).

Rousse G., Carvajal J.R., Patoux S., and Masquelier C., Chem. Mater., 15, 4082 (2003).

Roy R. A.; Roy R., Mater. Res. Bull., 19, 169 (1984).

Saadoune I., Delmas C., J. Mater. Chem., 6, 193 (1996).

Saardoune I., Menetrier M., Delmas C., J. Mater. Chem., 7, 2505 (1997).

Santillli C.V., Pulcinelli S.H., Brito G.E.S., Briois V., J. Phys. Chem. B, 103, 2660 (1999).

Shaju K.M., Subbarao G.V., Chowdari B.V.R., Electrochim. Acta, 48, 2691 (2003).

Shaju K.M., SubbaRao G.V., Chowdari B.V.R., Electrochim. Acta, 49, 1565 (2004).

Shannon R.D., Prewitt G.T., Acta Crystallogr.,Sect.B 25,925 (1969).

Sharma R.A. and Seefurth R.N., J. Electrochem. Soc., 123,1763(1976).

Shimakawa Y., Murata T., Tabuchi J., J. Solid State Chem., 131, 138 (1997).

Song Y., Zavalij P.Y., Whittingham M.S., J. Electrochem. Soc., 152, A721 (2005).

Spahr M.E., Novak P., Schnyder B., Haas O., Nesper R., J. Electrochem. Soc., 145, 1113 (1998).

Streltsov V.A., Belokoneva E.L., Tsirelson V.G., Hansen N., Acta Cryst. B49,147 (1993).

Sun Y.K., Jin S.H., J. Mater. Chen. 8, 2399(1998).

Sun Y.K., Yoon C.S., Lee Y.S., Electrochim Acta, 48, 2589 (2003).

Sun Y., Ouyang C., Wang Z., Huang X., Chen L., J. Electrochem. Soc., 151, A504 (2004).

Takahashi Y., Wada Y., J. Electrochem. Soc., 137, 267 (1990).

Takahashi M., Tobishima S., Takei K., Sakurai Y., J. Power Sources 97-98, 508 (2001).

Tomyama H. Jpn. Patent, 07-029608 (1995).

Thackeray M.M., Backer S.D., Adendorff K.T., Solid State Ionics, 17, 175 (1985).

Thackeray M.M., Johnson C.S., Kahaian A.J., Kepler K.D., Vaughey J.T., Yang S.H., Hackney S.A. ITE Battery Lett. 1, 26 (1999).

Thackeray M.M., Johnson C.S., Kahaian A.J., Kepler K.D., Vaughey J.T., Yang S.H., Hackney S.A., J. Power Sources, 81-82, 60 (1999).

Thackeray M.M., Vaughey J.T., Kahaian A.J., Kelper K.D., Benedek R., Electrochem. Commu. 1, 111 (1999).

Thomas M.G., David W.I., and Goodenough G.B., Mater. Res. Bull., 20, 1137 (1985).

Tirado J.L., Materials Science and Engineering R, 40, 103 (2003).

Ueda A. and Ohzuku T., J. Electrochem. Soc. 141, 2010 (1994).

Ulus A., Rosenberg Y., Burstein L., and Peled E., J. Electrochem. Soc. 149, A635 (2002).

Vaughey J.T., Kelper K.D., Benedek R. Thackeray M.M., Electrochem. Commu.1, 517 (1999).

Vaughey J.T., Hara J.O., Thackeray M.M., Electrochem. Solid State Lett., 3, 13 (2000).

Venkatraman S., Manthiram A., Chem. Mater., 15, 5003 (2003).

Wang C.S., Appleby A.J., Little F.E., Solid State Ionics 147, 13 (2000).

Wang G.X., Bewlay S.L., Konstantinov K., Liu H.K., Dou S.X., Ahn J.H., Electrochimica Acta, 50, 443 (2004).

Wang Y., Sakamoto J., Huang C.K., Surampudi S., Greenbaum S.G., Solid State Ionics, 110, 167 (1998).

Wen C.J., Huggins R.A., J. Electrochem. Soc., 128, 1181 (1981).

Werstler D.D., Polymer 27, 757 (1986).

Weydanz W.J., Wohlfahrt-Mehrens, Huggins R.A., J. Power Sources, 81-82, 237 (1999).

Wilson A.M.and Dahn J.R., J. Electrochem. Soc. 142, 326 (1995).

Winter M., Besenhard J.O., Electrochim. Acta, 45, 31 (1999).

Wolfenstine J., J. Power Sources, 79, 111 (1999).

Xia Y. Sakai T., Fujieda T., Wada M., Yoshinaga H., J. Electrochem. Soc. 148, A471 (2001).

Xing W., Xue J.S. and Dahn J.R., J. Electrochem. Soc. 143, 3046 (1996).

Yamada A. Chung S.C., and Hinokuma K., J. Electrochem. Soc., 148, A224 (2001).

Yamada A., Chung S.C., J. Electrochem. Soc., 148, A960 (2001).

Yamaura K., Takano M., Hirano A., and Kanno R., J. Solid State Chem., 127, 109 (1996).

Yang J., Winter M., Besenhard J.O., Solid State Ionics, 90, 281 (1996)

Yang J. Takeda Y., Imanishi N., Yamamoto O., J. Electrochem. Soc., 146, 4009 (1999).

Yang J., Takeda Y., Imanishi N., Ichikawa T., Yamanoto O., J. Power Sources, 79, 220 (1999).

Yang J. Wachtler M., Winter M., Besenhard J.O., Electrochem. Solid-State Lett. 2, 161 (1999).

Yang S., Zavalij P.Y., Whittingham M.S., Electrochem. Commu., 3, 505 (2001).

Yang S., Song Y., Zacalij P.Y., and Whittingham M.S., Electrochem. Commu., 4, 239 (2002).

Yang S. Song Y. Ngala K., Zacalij P. Y., Whittingham M.S., J. Power Sources, 119, 239 (2003).

Yang X.Q., McBreen J., Yoon W.S., Grey C.P., Electrochem. Comm., 4, 649 (2002).

Yazami R., Lebrun N., Bonneau M. and Molteni M., J. Power Sources, 54, 389 (1995).

Yin J.S. and Wang Z.L., J. Mater. Res. 14, 503 (1999).

Yoon Won-Sub, Kee Kyung-Keun, and Kim Kwang-Bum, Electrochem. Solid-State Lett., 4, A35 (2001).

Yoshio M., Noguchi H., Tominaga K. and Tanaka H., Progress in Batteries and Battery Materials, Vol. 11 (ITE-JECS press, Inc., OH, USA), pp. 158 (1992).

Yoshio M., Noguchi H., Itoh J., Okada M., Mouri T., J. Power Sources 90,176 (2000).

Yoshio M., Todorov Y., Yamato K., J. Power Sources 74,46 (1998).

Yoshio M., Noguchi H. Itoh J.I., Okada M., Mouri T., J. Power Sources, 90, 176 (2000).

Yoshio M., Wang H., Fukuda K., Umeno T., Dimov N.and Ogumi Z., J. Electrochem. Soc. 149, 1598 (2002).

Yuan L., Guo Z.P., Konstantinov K., Wang J.Z., Liu H.K., Electrochimica Acta, 51, 3680 (2006).

Yuan Z.G., Huang F., Feng C.Q., Sun J.T., and Zhou Y.H., Material Chemistry and Physics, 79, 1 (2003).

Zhang F., Ngala K., Whittingham M.S., Electrochem. Commun. 2, 445 (2000).

Zhang J., Sun L.D., Liao C.S., Yan C.H., Solid State Communications 124, 45 (2002)

Zhang X., Patil P.K., Wang C., Appleby A.J., Little F.E. and Cocke D.L., J. Power Sources, 125, 206 (2004).

Zhecheva E. Stoyanova R. Solid State Ionics, 66, 143 (1993).

List of symbols

A.c. impedance	Alternative current impedance spectroscopy
Å	Angstrom
Atm	Atmospheric pressure
BET	Brunauer-Emmet-Teler surface area
C_{dl}	Double layer capacitance
C_f	Capacitance of the passive film
CPE	Constant phase elements
CV	Cyclic voltammetry
D	Diffusion coefficient
F	Faraday constant
ICP	Inductively coupled plasma spectrometer
i_0	Exchange current density
mAh/g	Milli-ampere-hour per gram
mol%	Molar percent
OCV	Open circuit voltage
R_{ct}	Charge transfer resistance
R_f	Resistance of the passive film
R_{sl}	Insertion-ion resistance
R_e	Solution resistance
C_{sl}	Surface-layer capacitance

C_{dl}	Double-layer capacitance
Z_w'	Constant phase angle element
Z_w	Warburg impedance
S	Active surface area
SEM	Scanning Electron Microscope
EDS	Energy Dispersive X-ray Spectroscopy
TEM	Transmission Electron Microscope
V_M	Molar volume
W_s	Shortcircuited Warburg diffusion impedance
wt%	Weight percent
$\triangle E$	Potential change of reaction
$\triangle G$	Free energy change of reaction
XPS	X-ray photoelectron spectroscopy

List of Figures

List of Tables

Publications during PHD studies

1. **Yao Chen**, G.X. Wang, J.P. Tian, K. Konstantinov and H.K. Liu, "Preparation and properties of spherical $LiNi_{0.75}Co_{0.25}O_2$ as a cathode for lithium-ion batteries", *Electrochimica Acta, 50, 435 (2004).*

2. **Yao Chen**, G. X. Wang, K. Konstantinov, H. K. Liu and S. X. Dou, "Synthesis and characterization of $LiCo_xMn_yNi_{1-x-y}O_2$ as a cathode material for secondary lithium batteries ", *Journal of Power Sources, 119-121, 184 (2003).*

3. **Y. Chen,** G.X. Wang, K. Konstantinov, J.H. Ahn, H.K. Liu, and S.X. Dou," Studies of the electrochemical properties of nanosized Co_3O_4 oxide as an anode material for lithium ion batteries", J. Metasable and Nanocrystallline Mat. 15-16, 625-628 (2003).

4. G.X. Wang, L. Yang, **Y. Chen**, J.Z. Wang, Steve Bewlay and H.K. Liu, "An investigation of polypyrrole-$LiFePO_4$ composite cathode materials for lithium-ion batteries ", *Electrochimica Acta, 50, 4649 (2005).*

5. G.X. Wang, **Y. Chen**, L. Yang, Jane Yao, Scott Needham, H.K. Liu and J.H. Ahn, "Synthesis of nanocrystalline transition metal and oxides for lithium storage ", *Journal of Power Sources, 146, 487 (2005).*

6. G.X. Wang, L. Yang, S.L. Bewlay, **Y. Chen**, H.K. Liu and J.H. Ahn, "Electrochemical properties of carbon coated $LiFePO_4$ cathode materials ", *Journal of Power Sources, 146, 521 (2005).*

7. G. X. Wang, Steve Bewlay, Jane Yao, **Y. Chen**, Z. P. Guo, H. K. Liu and S. X. Dou, "Multiple-ion-doped lithium nickel oxides as cathode materials for lithium-ion batteries ", *Journal of Power Sources, 119-121, 189 (2003).*

8. G. X. Wang, **Y. Chen**, K. Konstantinov, Jane Yao, Jung-ho Ahn, H. K. Liu and S. X. Dou, "Nanosize cobalt oxides as anode materials for lithium-ion batteries", *Journal of Alloys and Compounds, 340, L5 (2002).*

9. G. X. Wang, **Y. Chen**, K. Konstantinov, Matthew Lindsay, H. K. Liu and S. X. Dou, "Investigation of cobalt oxides as anode materials for Li-ion batteries", *Journal of Power Sources, 109, 142 (2002).*

10. J. Wang, G.X. Wang, **Y. Chen**, C.Y Wang and H.K. Liu, "A Novel Cureless Pure Lead Oxide Plate for VRLA Battery" *Journal of Applied Electrochemistry,* 34 (2004)1127 – 1133.

11. J. Wang, S.H. Ng, G.X. Wang, J. Chen, L. Zhao, **Y. Chen** and H.K. Liu, Synthesis and Characterization of Nanosize Cobalt Sulfide for Rechargeable Lithium Batteries", *Journal of Power Sources,,* (Accepted in Oct.2005).